Heat transfer enhancement in a cylindrical compression chamber by way of porous inserts and the optimization of compression and expansion trajectories for varying heat transfer capabilities

A THESIS
SUBMITTED TO THE FACULTY OF THE GRADUATE SCHOOL
OF THE UNIVERSITY OF MINNESOTA
BY

Andrew T. Rice

IN PARTIAL FULFILLMENT OF THE REQUIREMENTS
FOR THE DEGREE OF
MASTER OF SCIENCE

Perry Li, Terrence Simon

December, 2011

Acknowledgements

I would like to thank my advisers Perry Li and Terry Simon for their guidance and support, my research colleagues Chao Zhang and Mohsen Saadat for their helpful discussion and collaboration, and the lab manager Tri Nguyen for his insightful suggestions and assistance. You all have been invaluable. I would also like to acknowledge our energy storage research team and the department faculty, students, and staff who have facilitated the progress of this research. Much thanks to my family for their loving encouragement, and to Belinda, who never left my side. Finally, as a creature exploring the workings of creation, I owe everything to the Creator.

Support for this research comes from the National Science Foundation under grant number NSF/EFRI-1038294, the University of Minnesota - Initiative for Renewable Energy and the Environment under project number RS-0027-11, and the Center for Compact and Efficient Fluid Power, a National Science Foundation Engineering Research Center funded under cooperative agreement number EEC-0540834.

Dedication

To Belinda

Abstract

The present work focuses on improving the energy efficiency of an air compressor. The impetus for this work is the open accumulator compressed air energy storage system. This system was designed to address the need for a high energy density storage system that also provides a high-power-density. The open accumulator approach requires a high-efficiency and high-power air compressor/motor. Other applications would also benefit from a more efficient air compressor. This work investigates two complementary approaches for improving compression efficiency, but not at the expense of power.

The first objective of this thesis is to improve the heat transfer rates from the gas being compressed. By preventing heat loss, the compressor efficiency is improved. This is done by introducing a porous medium into the compressor's air space. The main advantages are a large increase in the thermal capacitance of the air space and a much greater available surface area for heat transfer. Two types of porous media are tested: an aluminum mesh and an array of copper minitubes. For the latter, a free-surface liquid-piston compressor was used so that the liquid could flow through the minitubes, thus compressing the air above. It was found that the presence of the porous media enhanced heat transfer rates. For the case of the minitubes, the efficiency (i.e. energy stored vs. work input) improved by about 30% over compression without the minitubes but at the same power. Simple thermodynamic and heat transfer analyses are used to model the gross behavior of the flow. The model results adequately represent the measured data when using the mesh. However, a single, average temperature is inadequate for modeling the temperature in the minitubes due to the large disparity of temperatures in the different regions.

The second objective of this thesis is to optimize the pressure-volume compression trajectory. It is shown that the manner in which the air is compressed is very influential in determining efficiency and power. One key assumption of the analysis is that the product of the heat transfer coefficient and the surface area available for heat transfer, hA, is a function of air volume. It is found that the optimized trajectory takes the form fast-slow-fast, where the slow section exhibits temperature changes proportional

to the inverse root of the hA product. Sample results demonstrate potential order-of-magnitude improvements in compression storage power over more conventional linear- or sinusoidal-shaped trajectories, at the same efficiency.

It is concluded that a porous structure inserted into the air space of an air compressor is a promising means of achieving enhanced heat transfer rates. Substantial efficiency gains also seem available via the manipulation of the compression trajectory. It is recommended that future work should be conducted to optimize the porous structure for compression and experimentally or numerically validate the gains promised by the optimal compression trajectory.

Contents

Acknowledgements **i**

Dedication **ii**

Abstract **iii**

List of Tables **ix**

List of Figures **x**

1 Introduction **1**

1.1 Objectives of the program 1

1.2 Objectives of the present thesis project 2

1.3 Outline of thesis 3

2 General Background **5**

2.1 Common energy storage strategies 5

2.2 The Open Accumulator 7

2.3 Compression heat transfer 11

2.3.1 Compression heat transfer from engine research 11

2.3.2 Compression heat transfer from accumulator studies 20

2.4 Improving heat transfer 20

2.4.1 An overview of heat transfer augmentation strategies 21

2.4.2 Review of steady-state heat transfer with mesh-type inserts . . . 21

2.4.3 Review of heat transfer in minitubes 24

2.5 Trajectory optimization 25

3 System model **29**

3.1 System model 29
3.2 Figure of merit 35
3.3 Governing equations 37
3.3.1 Assumptions 38
3.4 Modeling heat transfer 44
3.4.1 Mesh experiments 45
3.4.2 Minitube array experiments: no minitube array 46
3.4.3 Minitube array experiments: with minitube array 47

4 Test facilities **52**

4.1 Mesh experiments 52
4.1.1 Apparatus 52
4.1.2 Instrumentation 59
4.1.3 Control, data acquisition, and data processing 61
4.2 Minitube experiments 62
4.2.1 Apparatus 62
4.2.2 Instrumentation 70
4.2.3 Control, data acquisition, and data processing 73

5 Test program **74**

5.1 Mesh experiments 74
5.1.1 Data reduction 76
5.1.2 Uncertainty analysis 77
5.2 Minitube experiments 77
5.2.1 Data reduction 79
5.2.2 Uncertainty analysis 79

6 Results **81**

6.1 Mesh experiment and model 81
6.1.1 Results from experiment 81

6.1.2 Results from model . . . 91
6.2 Minitube experiment and model . . . 99
6.2.1 Results from experiment . . . 99
6.2.2 Results from model . . . 106

7 Discussion **118**
7.1 Mesh experiments . . . 118
7.2 Minitube experiments . . . 120

8 Trajectory Optimization: Problem Statement **123**
8.1 Overview of Solution Method . . . 124
8.2 Modeling of the heat transfer . . . 125
8.3 Problem statement . . . 125

9 Trajectory Optimization: Solution **127**
9.1 Optimal compression and expansion trajectories . . . 127
9.2 Optimal expansion and compression profiles . . . 134

10 Trajectory Optimization: Results **136**
10.1 Results . . . 136
10.2 Discussion . . . 148

11 Conclusion and Discussion **149**

References **152**

Appendix A. Nomenclature **163**

Appendix B. Establishing the flow regime in the minitube array **168**
B.0.1 Kinematic viscosity . . . 169
B.0.2 Hydraulic diameter . . . 170
B.0.3 Air velocity . . . 171
B.0.4 Calculating Re . . . 172
B.0.5 The effect of various interface velocities . . . 172

Appendix C. Apparatus detail **173**
C.1 Mesh Experiments 173
C.1.1 Appartus details 173
C.1.2 Instrumentation details 175
C.2 Minitube Array Experiments 176
C.2.1 Apparatus 176
C.2.2 Instrumentation 177

Appendix D. Thermocouple data **178**

Appendix E. Additional Results **180**
E.0.3 Experimental results 180

Appendix F. Optimal compression trajectory for a constant hA product **193**
F.0.4 Introduction 193
F.0.5 Sketch of Proof 193

Appendix G. A high-power case study **196**

List of Tables

3.1 Experimentally determined compressibility factors for air [1] 39
6.1 Peak temperature change for varying compression speeds and mesh masses. 86
6.2 Storage power in Watts for varying compression speeds and mesh masses. 91
6.3 Efficiency for varying compression speeds and mesh masses. 91
6.4 Values of best fit h's in W/m^2-K used in the analytical models. 92
F.1 The sign of s is determined from the sign of three factors. In all eight scenarios, s is positive. 195

List of Figures

2.1 A schematic of the open accumulator compressed air energy storage system. 8

2.2 The open accumulator has a much higher pressure compression ratio, so the total energy stored during a single stroke, $(P_{i,\mathrm{op}}, V_{i,\mathrm{op}})$ to (P_f, V_f), becomes much greater than the energy stored for a closed, conventional accumulator: $(P_{i,\mathrm{cl}}, V_{i,\mathrm{cl}})$ to (P_f, V_f). 10

3.1 Air is compressed from initial (expanded) conditions, left, to final (compressed) conditions, right). During the compression, heat transfer occurs between the heated air and the bounding surfaces, all at ambient temperature T_0. 30

3.2 Air is compressed from initial (expanded) conditions, left, to final (compressed) conditions, right. During compression, heat transfer occurs between the heated air and the bounding surfaces plus mesh. The walls are at ambient temperature T_0. The mesh temperature varies in time. The mesh is confined between the piston and the endwall. 31

3.3 Air is compressed from initial (expanded) conditions, left, to final (compressed) conditions, right. During compression, heat transfer occurs between the heated air and the bounding surfaces plus minitubes. The walls are at ambient temperature T_0. The minitube temperature is allowed to vary with time. Water flows through the minitubes so the surface area of the minitube array is not constant in time. 32

3.4 Compressing the air in different ways will require different amounts of work. In this example, compression along the dashed line will take more work than compressing along the solid line. This is evident on a P-V diagram by comparing the area under the curves. 34

3.5 P-V diagram showing compression (ζ_c) and expansion (ζ_e) trajectories. The shaded area under the curves represent the work input (vertical lines) and work output (added horizontal lines). Isothermal compression and expansion follows the dashed black trajectory. The change in total energy stored is the area under the thick dashed isothermal curve. Reducing the area between ζ_c and the isothermal curve increases compression efficiency. Reducing the area between the isothermal curve and ζ_e increases expansion efficiency. 36
4.1 The hydraulic circuit for the low-power porous mesh experimental program. 53
4.2 A photograph of the hydraulic circuit of figure 4.1. The MicroMo motor and black Haldex pump are at the left hand side of the photo. At the bottom of the photo is the 3-2 valve. The blue 4-3 valve is in the center. The black Oildyne pump is on the right. The very bottom of the compression cylinder can be seen at the top of the photo. The reservoir is off-screen at the top. 54
4.3 A photograph of the tandem piston (foreground) and reservoir (background, left). The Oildyne pump is in the bottom right corner. Additional polycarbonate shielding encases the compressor for safety. 55
4.4 A diagram (not to scale) of the tandem piston-in-cylinder compressor for the low-power porous mesh experimental program. 57
4.5 A photograph of the tandem piston-in-cylinder compressor for the low-power porous mesh experimental program. 58
4.6 A photograph of the two meshes used in the low-power, dual-pump solid-piston experiments. 59
4.7 A photograph of the end cap. The Kulite pressure sensor is inserted into the top of the cap. Two other ports may be used for thermocouples or to replenish fresh air. 60
4.8 The hyraulic circuit for the water piston circuit used with the porous minitube array. 63

4.9 A photograph of the circuit of figure 4.8. The pump and motor are at the bottom of the photo on the blue mount. The Danfoss relief valve and directional valve is in the foreground in the center of the photo. The Bürkert control valve is black and downstream of the Danfoss valve. The piston is top center. 64
4.10 A diagram (not to scale) of the water piston compressor used with the porous minitube array and without the minitube array (right). Porous plugs bound the inlet and exit of the minitube array. 65
4.11 A photograph of the water piston sketched in figure 4.10. The Bürkert control valve can be seen to the left of the mount. The hose protruding from the front of the mount is the water discharge port. 66
4.12 A photograph of the two compression cylinders. The compression cylinder on the left was packed with 210 copper minitubes. 67
4.13 A photograph of the porous disk on top of the minitube structure. This disk prevented water from impacting the thermocouple measurements. The screw functioned as a handle so the disk could be removed. Before operation, the edges were sealed by hot glue. 69
4.14 A photograph of the end cap from the top. The pressure sensor and thermocouples can be seen. The yellow components are Omega Quick disconnect sockets. 71
4.15 A photograph of the end cap from the bottom. The pressure sensor is flush with the end wall. The thermocouples junctions are between 4 and 6 mm from the cap surface. 72
6.1 Volume data with no mesh in the air space. 82
6.2 Pressure data with no mesh in the air space. 83
6.3 Pressure data with a flow rate of 4 cc/s during compression. 84
6.4 Calculated temperature profiles with no mesh. Compression begins at the 60 second marker. The four ending times are approximately 81, 86, 115, and 167 seconds. 85
6.5 Calculated temperature profiles with a flow rate of 4 cc/s during compression. Compression begins at 60 seconds and ends at about 170 seconds. 86

6.6 Calculated heat transfer rate as a function of time with no mesh in the airspace. Compression begins at the 60 second marker. The four ending times are approximately 81, 86, 115, and 167 seconds. 87
6.7 Calculated heat transfer rate as a function of time with a flow rate of 4 cc/s during compression. Compression begins at 60 seconds and ends at about 170 seconds. 88
6.8 Calculated hA values as functions of time with a flow rate of 4 cc/s during compression. Compression begins at 60 seconds and ends at about 170 seconds. 89
6.9 Calculated heat transfer coefficients as functions of time with a flow rate of 4 cc/s during compression. Compression begins at 60 seconds and ends at about 170 seconds. 90
6.10 Air volume vs. time with the 1.70 g mesh and 4 cc/s flowrate. Experimental data is compared to simulation output for various constant h's. 93
6.11 Air pressure vs. time with the 1.70 g mesh and 4 cc/s flowrate. Experimental data is compared to simulation output for various constant h's. 94
6.12 Figure 6.11 zoomed in to show the good fit. See figure 6.11 for the legend. 95
6.13 Calculated air temperature vs. time with the 1.70 g mesh and 4 cc/s flowrate. Experimental data is compared to simulation output for various constant h's. 96
6.14 Figure 6.13 zoomed in to show the good fit. See figure 6.13 for the legend. 97
6.15 Mesh temperature vs. time with the 1.70 g mesh and 4 cc/s flowrate. Experimental data for air temperature is compared to simulation output for various constant h's. 98
6.16 Pressure vs. time with and without the porous insert. These data were taken without the thermocouples or porous disks. 100
6.17 Air pressure data with and without the porous minitube array. 102
6.18 Air pressure data during compression with and without the porous minitube array. 103

6.19 Local air temperature data from the four thermocouples with and without the porous minitube array. 104
6.20 Local air temperature data during compression from the four thermocouples with and without the porous minitube array. 105
6.21 Local air temperatures from the four thermocouples (solid lines) and the volume-averaged temperature (dashed lines) during the compression event and shortly following. Results are shown with and without the porous minitube array. 107
6.22 Local air temperatures from the four thermocouples (solid lines) and the volume-averaged temperature (dashed lines) during the constant-volume cooling. Results are shown with and without the porous minitube array. 108
6.23 The measured pressure and simulated pressure for the compression event. 109
6.24 The local measured temperatures from the four thermocouples and the simulated volume-averaged air temperature and minitube temperature for the compression event. The dashed line provides the magnitude of the measured peak volume-averaged temperature. 110
6.25 The measured pressure and simulated pressure for the compression event. 111
6.26 The local measured temperatures from the four thermocouples and the simulated volume-averaged air temperature and minitube temperature for the compression event. The dashed line provides the magnitude of the measured peak volume-averaged temperature. 112
6.27 The modeled heat transfer rates as a function of time. The heat transfer to the outer surface of the minitubes is artificially high due to the uniform air temperature assumption. 114
6.28 The modeled heat transfer coefficients as a function of time. The constant values are based on equations (3.43)–(3.45). The heat transfer coefficient for the plenum is based on Hohenberg's correlation as in equation (3.34). 115
6.29 The measured pressure and modified simulated pressure for the compression event. 116

6.30 The local measured temperatures from the four thermocouples and the modified simulated volume-averaged temperature and minitube temperature for the compression event. The dashed line provides the magnitude of the measured peak volume-averaged temperature. 117
9.1 A compression trajectory is broken up into N adjacent volume intervals, each with a constant hA. Over each interval the optimal form of the compression trajectory is adiabatic-isothermal-adiabatic. 128
9.2 Optimal compression for a continuously varying hA product consists of three stages: adiabatic compression; hA-dependent compression; adiabatic compression. The slow hA-dependent curve is determined by the parameter λ_c. After the air is moved to the accumulator, the air volume is further reduced by isobaric cooling. 132
9.3 Determining the optimal trajectory for a given power 134
10.1 The optimal volume profile consists of an instantaneous compression, slow hA-dependent compression, then another stage of instantaneous compression. More efficient trajectories take longer and more of the compression occurs in the middle stage. 137
10.2 The optimal pressure profile consists of an instantaneous compression, slow hA-dependent compression, then another stage of instantaneous compression. The initial and final pressures are the same for each case, but more efficient trajectories will not include as much adiabatic compression. 137
10.3 The optimal temperature profile consists of an instantaneous compression, slow hA-dependent compression, then another stage of instantaneous compression. The initial temperature is the same for each case, but the final temperature depends on the time allowed for heat transfer. More efficient trajectories take longer in general, to prevent temperatures from rising too high. The difference in final temperature can be very significant, as shown here. 138

10.4 The compression efficiency, for given heat transfer characteristics, decreases as the overall temperature rise increases (left). The power absorbed during compression, for given heat transfer characteristics, increases as the overall temperature rise increases (right). 139
10.5 The optimal volume profile consists of an instantaneous expansion, slow hA-dependent expansion, then another stage of instantaneous expansion. The initial volume is the same for each case, but the final volumes differ depending on how the air is expanded. More efficient trajectories will be nearer to isothermal, so the final volume will be larger. 139
10.6 The optimal pressure profile consists of an instantaneous expansion, slow hA-dependent expansion, then another stage of instantaneous expansion. The initial and final pressure is the same for each case. Different efficiencies are due to where the expansion occurs. More efficient trajectories take longer, but at the expense of power. 140
10.7 The optimal temperature profile consists of an instantaneous expansion, slow hA-dependent expansion, then another stage of instantaneous expansion. For the chosen function of hA, this profile allows the air to heat back up during the slower hA-dependent stage. 140
10.8 The expansion efficiency, for given heat transfer characteristics, decreases as the overall temperature change increases (left). The power provided by expansion, for given heat transfer characteristics, increases as the overall temperature change increases (right). 141
10.9 Normalized volume profiles are plotted as functions of normalized compression time. Intuition suggests that a fast-slow-fast type trajectory would be optimal. 142
10.10 Normalized volume profiles are plotted as a function of normalized expansion time. 142
10.11 Compression efficiency is plotted as a function of power for the varying-hA optimal trajectory, constant-hA optimal trajectory, sinusoidal trajectory, and linear trajectory using the hA product defined in equation (10.1). The varying-hA optimal trajectory performs best, and is Pareto frontier for compression. 143

10.12Compression efficiency is plotted as a function of power for the varying-hA optimal trajectory, constant-hA optimal trajectory, sinusoidal trajectory, and linear trajectory using a **constant** hA product. The varying-hA optimal trajectory reduces to the constant-hA optimal trajectory when hA is constant. 144
10.13Expansion efficiency is plotted as a function of power for the varying-hA optimal trajectory, constant-hA optimal trajectory, sinusoidal trajectory, and linear trajectory using the hA product defined in equation (10.1). The varying-hA optimal trajectory performs best, and is Pareto frontier for expansion. 145
10.14Expansion efficiency is plotted as a function of power for the varying-hA optimal trajectory, constant-hA optimal trajectory, sinusoidal trajectory, and linear trajectory using a **constant** hA product. The varying-hA optimal trajectory reduces to the constant-hA optimal trajectory when hA is constant. 146
10.15Compression efficiency vs power. The advantage of the varying-hA optimal trajectory is more significant for this case than for the simple example shown in figure 10.11 148
B.1 A diagram of a representative packing arrangement in the minitube array. Three different flow channels, labeled A, B, and C, are shaded. 171
D.1 Temperature vs time traces taken by a single thermocouple (wire diameter 0.001 inches) at a location 2.5 cm from the cap near the centerline. 179
E.1 Calculated temperature profiles with a flow rate of 4 cc/s during compression. Compression begins at 60 seconds and ends at about 170 seconds.181
E.2 Calculated temperature profiles with a flow rate of 8 cc/s during compression. Compression begins at 60 seconds and ends at about 115 seconds.181
E.3 Calculated temperature profiles with a flow rate of 16 cc/s during compression. Compression begins at 60 seconds and ends at about 87 seconds.182
E.4 Calculated temperature profiles with a flow rate of 20 cc/s during compression. Compression begins at 60 seconds and ends at about 81 seconds.182

E.5 Calculated temperature profiles with no mesh. Compression begins at the 60 second marker. The four ending times are approximately 81, 86, 115, and 167 seconds. 183
E.6 Calculated temperature profiles with a 1.7 g mesh. Compression begins at the 60 second marker. The four ending times are approximately 81, 87, 115, and 167 seconds. 183
E.7 Calculated temperature profile with a 5.48 g mesh. Compression begins at the 60 second marker. The four ending times are approximately 81, 87, 116, and 172 seconds. 184
E.8 Calculated heat transfer coefficient as a function of time with a flow rate of 4 cc/s during compression. Compression begins at 60 seconds and ends at about 170 seconds. 184
E.9 Calculated heat transfer coefficient as a function of time with a flow rate of 8 cc/s during compression. Compression begins at 60 seconds and ends at about 115 seconds. 185
E.10 Calculated heat transfer coefficient as a function of time with a flow rate of 16 cc/s during compression. Compression begins at 60 seconds and ends at about 87 seconds. 185
E.11 Calculated heat transfer coefficient as a function of time with a flow rate of 20 cc/s during compression. Compression begins at 60 seconds and ends at about 81 seconds. 186
E.12 Calculated air temperature vs time with no mesh and 4 cc/s flowrate. Experimental data compared to simulation output for various constant h's. 187
E.13 Calculated air temperature vs time with no mesh and 8 cc/s flowrate. Experimental data compared to simulation output for various constant h's. 187
E.14 Calculated air temperature vs time with no mesh and 16 cc/s flowrate. Experimental data compared to simulation output for various constant h's. 188
E.15 Calculated air temperature vs time with no mesh and 20 cc/s flowrate. Experimental data compared to simulation output for various constant h's. 188
E.16 Calculated air temperature vs time with the 1.70 g mesh and 4 cc/s flowrate. Experimental data compared to simulation output for various constant h's. 189

E.17 Calculated air temperature vs time with the 1.70 g mesh and 8 cc/s flowrate. Experimental data compared to simulation output for various constant h's. 189
E.18 Calculated air temperature vs time with the 1.70 g mesh and 16 cc/s flowrate. Experimental data compared to simulation output for various constant h's. 190
E.19 Calculated air temperature vs time with the 1.70 g mesh and 20 cc/s flowrate. Experimental data compared to simulation output for various constant h's. 190
E.20 Calculated air temperature vs time with the 5.48 g mesh and 4 cc/s flowrate. Experimental data compared to simulation output for various constant h's. 191
E.21 Calculated air temperature vs time with the 5.48 g mesh and 8 cc/s flowrate. Experimental data compared to simulation output for various constant h's. 191
E.22 Calculated air temperature vs time with the 5.48 g mesh and 16 cc/s flowrate. Experimental data compared to simulation output for various constant h's. 192
E.23 Calculated air temperature vs time with the 5.48 g mesh and 20 cc/s flowrate. Experimental data compared to simulation output for various constant h's. 192
F.1 Diagram of isothermal-adiabatic-isothermal (ζ) and adiabatic-isothermal-adiabatic (ζ^*) profiles. 194
G.1 Schematic of the compressor with liquid piston and porous mesh for the case study. 196
G.2 Sample profiles of the optimal trajectory for various efficiencies. Volume, normalized by the maximum volume, is shown as a function of time, scaled by total compression time. Sinusoidal, linear, and AIA trajectories are provided for comparison. 198
G.3 Compression efficiency vs power. There is no other trajectory that allows more power to be absorbed at a given efficiency than the optimal trajectory. Sinusoidal, linear, and AIA trajectories are provided for comparison. 199

G.4 Expansion efficiency vs power. There is no other trajectory that allows more power to be produced at a given efficiency than the optimal trajectory. Sinusoidal, linear, and AIA trajectories are provided for comparison. 199

Chapter 1

Introduction

1.1 Objectives of the program

Recent trends indicate a growing emphasis on sustainability. The impact on energy generation, distribution, and consumption is substantial. Renewable energy sources, such as wind and solar, are beginning to play a larger role as they mature and become viable larger-scale options. The "smart grid" concept is slowly transforming power transmission infrastructure, and consumers are becoming more conscientious when it comes to energy choices. One key piece in the sustainability puzzle is energy storage. The ability to store energy helps smooth the intermittent nature of many renewable energy sources, improving reliability. It provides increased flexibility for load balancing. It enables more efficient production. The benefits are manifold. The drawback is the present absence of a cheap, efficient, and power-dense energy storage system. One system that could contribute to the energy storage solution is the open accumulator infrastructure, a compact compressed air energy storage system. This system, which will be discussed herein, is best applied to mechanical-type energy sources, such as a rotating turbine (wind, hydroelectric, geothermal), and is best used before conversion to electricity since the storage medium is compressed air.

The impetus for the current research program is off-shore wind power energy storage. An advantage of offshore wind turbines is the promise of huge rotor spans and, therefore, immense power, approaching 10 MW. Of course, lacking the storage, this prospect has a steep drawback: the generator and transmission must be sized for the peak power

in order to justify such large wind turbines in the first place. The problem becomes worse when one considers the disproportionate cost for the huge components in light of the fraction of time the wind turbine will be operating at peak power. Energy storage offers a solution: size the generator and transmission based on mean power demand, not installed peak power. When supply exceeds demand, store the excess energy prior to generating electricity. When demand exceeds supply, augment the current output of the wind turbine with energy stored previously. This may be done using the open accumulator concept.

1.2 Objectives of the present thesis project

However, while the open accumulator is plausible, concerns linger over the capability of the system to absorb the high power generated by the wind turbine yet operating at high efficiency. Since the energy storage medium is compressed air, the enabling technology is the air compressor. The research reported in this thesis seeks to scope out the capability of an air compressor to achieve both high efficiency and high power. It is recognized that two different, but complementary, thrusts are in play. This thesis considers both.

First, the heat transfer rate during compression must be suitable. A basic compressor not only compresses the air, but also heats the air. Spending power toward heating the air is a significant cause of inefficiency for an compressor. Preventing air temperatures from rising (i.e. improving heat transfer rates) improves compression efficiency. Thus, a key objective is to enhance, augment, or in some way improve, the heat transfer rate. There are numerous techniques for enhancing heat transfer between the air being compressed and a heat sink. This thesis focuses on one strategy that offers many benefits: the use of high thermal capacity material in the air space. Experiments, to be discussed herein, consider two scenarios. In one, a deformable porous mesh is put between the piston and the end wall of a conventional piston-in-cylinder compressor. In the other, the solid piston is replaced with a free-surface liquid piston, and a rigid honeycomb-like minitube structure is inserted into the compression chamber. These experiments are performed to demonstrate the change in temperature during compression with and without added porous media. Lower air temperatures indicate higher

heat transfer rates and therefore higher efficiencies. Simple models are created to simulate the compression process and predict the gross behavior of pressure, volume, and temperature changes. These models may be used in system-level optimization.

Second, given the heat transfer characteristics, the manner in which the air is compressed must be optimized. It is shown that the pressure-volume trajectory influences efficiency and power. Optimization of the pressure-volume trajectory, presented herein, is an analytical problem studied under the assumption that the heat transfer rate is a function of air temperature and air volume. This form for the heat transfer rate emphasizes the role of the heat transfer area (generally correlated with air volume), which is appropriate when considering the additional surfaces associated with porous inserts. The objective of the optimization is to determine how to best compress an ideal gas to maximize the power absorption for a given efficiency, or equivalently, maximize the efficiency for a given power.

To summarize, this thesis has the following objectives.

1. Demonstrate experimentally a means for reducing temperature rise by chosen modes of enhanced heat transfer.

2. Create simple and flexible mathematical models which describe the compression of air in a compression chamber in which porous media have been added for heat transfer improvement.

3. Validate the mathematical models with experimental results.

4. Optimize the compression trajectory, given the heat transfer characteristics.

It should be noted that while the motivation for this work derives from a specific application, the results are by-and-large applicable to air compressors in general.

1.3 Outline of thesis

The thesis is organized into three parts. The first part, consisting of the first three chapters, is the introduction, general background, and system model. Chapter 2 introduces energy storage strategies including the open accumulator, heat transfer augmentation

strategies, and reviews of research pertaining to the experiments and optimization presented herein. Chapter 3 describes the system model, develops the governing equations, and defines important parameters.

The second part, consisting of chapters 4 through 7, describes and discusses the experimental facilities, experimental program, and results. Chapter 4 details the experimental prototypes and the two types of porous media used in the experiments: first, aluminum wool made of fine strands that deform and always stay within the airspace ("a mesh"); second, thin copper minitubes packed into a honeycomb-like pattern oriented with axes parallel to the axis of the compression cylinder (a "minitube array"). Chapter 5 outlines the experimental program. Chapter 6 provides experimental results, comparing them to results predicted from the system model and modified governing equations. Chapter 7 offers a discussion of the results and the comparison with the modeled results.

The third part, consisting of chapters 8 through 10, describes the trajectory optimization problem. Chapter 8 introduces the problem statement. Chapter 9 develops the problem solution. Chapter 10 presents results for a selected case study and discusses the practicality of implementing the solution.

Chapter 11 concludes by discussing the key results and implications.

Chapter 2

General Background

The intent of this chapter is to establish the context of the present research. First, section 2.1 introduces common energy storage systems and how their functions and capabilities differ from those of the open accumulator. In section 2.2 the open accumulator concept for compressed air energy storage is developed, and its advantages described. As regards the heat transfer problem, section 2.4 provides a broad overview of potential heat transfer augmentation strategies as well as a review of pertinent literature on heat transfer during compression, heat transfer using meshes or mesh-like media, and heat transfer in minitubes. Finally, section 2.5 reviews previous investigations into trajectory optimization.

2.1 Common energy storage strategies

Energy storage is a relatively new concern and an active topic of research as renewable energy sources increase their market penetration and efforts are made to increase power grid efficiency. As such, there is no consensus on how to utilize energy storage technology. This section summarizes common energy storage technologies and their relation to the content of this thesis. For more extensive reviews, the reader may consult Hadjipaschalis, et al. [2], Bradbury [3], Yang, et al. [4], Ibrahim, et al. [5], and Chen, et al. [6]. For a study which focuses on the economic viability of energy storage with regards to wind energy, see Barton and Infield [7]. Storage concepts will now be discussed.

- **Batteries**

  Batteries are currently the most often utilized energy storage technology. Current residential-scale and mid-scale wind energy and photovoltaic systems usually use banks of batteries as the energy storage system. They have also been considered for large-scale use [8][9]. However, for high power applications such as large wind turbines, batteries do not offer the advantages afforded by a hydraulic system since generators and components must still be sized for peak power and batteries have relatively low power density. Shorter life, higher cost, and disposal issues are other disadvantages. The advantages of batteries are their energy density and the ease in which they may be integrated with the grid. In some cases, portability may be another benefit.

- **Pumped hydro/reverse pumped hydro**

  Pumped hydro stores energy by increasing the potential energy of a volume of water. Typically, this involves pumping water from a lower reservoir to a higher reservoir. When the mechanical energy needs to be regenerated, the water flows from the upper reservoir to the lower, passing through a water turbine. The greater the elevation change, the greater the energy density. Reverse pumped hydro operates similarly, but usually involves submerging a vessel under water. Energy is stored by pumping water out of the chamber and regenerated by running the water back into the vessel. In both these technologies, the energy density is low. Problematic are the elevation and volume requirements, limiting deployment.

- **Compressed air energy storage**

  Compressed air energy storage can take several forms. Large scale compressed air energy storage (CAES) systems typically involve compressing air into a underground cavern, such as a mine or aquifer (e.g. [10]). CAES is often proposed as a viable and economical means to integrate intermittent renewable energy sources, such as wind [11][12][13]. One disadvantage of large scale CAES is that deployment of the system is limited by the storage options. Smaller scale CAES use a fabricated storage vessel or accumulator, which allows more flexible deployment. An advanced smaller scale approach that proposes near-isothermal compression using liquid pistons and porous media is mentioned in [14], although not discussed

in detail. The open accumulator system, discussed below, is another example of an advanced compressed air energy storage system[15] which may also use a liquid piston as described in [16]. The present research is applicable to the CAES storage option, when near-isothermal compression is desirable.

- **Supercapacitors**
  Supercapacitors have been proposed as a promising short-term energy storage system for wind energy applications (see e.g. [17]). Advantages include high power and energy density, high efficiency, and better life expectancy than batteries. The main drawback is usually cited to be the cost. Supercapacitors offer considerable potential for new technology, such as the electrochemical supercapacitor discussed by Shukla, et al. [18]. They can also be used as complements to other technologies, such as compressed air storage [14].

- **Flywheels**
  Flywheels have high power densities and moderate energy densities. They are most useful for shorter-term storage [19], and, as such, have been proposed as a means of frequency stabilization for wind farms [20].

- **Hydraulic Accumulators**
  Hydraulic accumulators store energy by compressing a fixed quantity of inert gas. Hydraulic fluid is pumped into one compartment of a two-compartment holding vessel, called an accumulator. The other compartment contains the fixed quantity of gas. The divider between the hydraulic fluid and gas is typically a piston or diaphragm, which allows the gas to be compressed as more hydraulic fluid is added to the accumulator. Allowing the air to expand and expel the hydraulic fluid through a hydraulic motor provides energy. Hydraulic accumulators have high power densities but low energy densities. The open accumulator improves the energy density by introducing elements of compressed air energy storage.

2.2 The Open Accumulator

The open accumulator is an energy storage system proposed by Li et al. [15] that combines elements of the hydraulic accumulator and compressed air energy storage. The

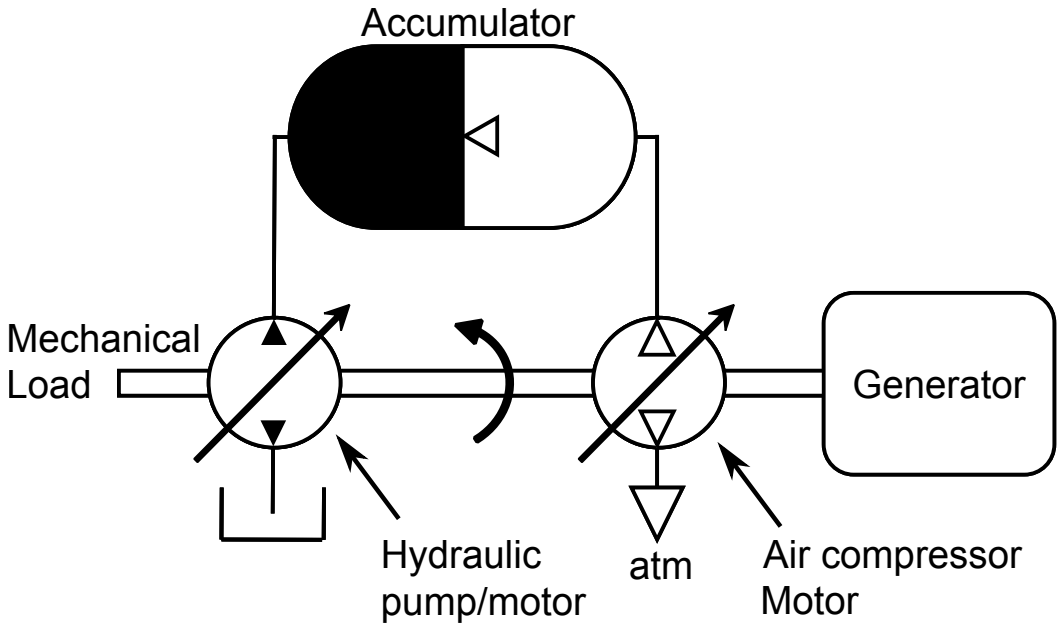

Figure 2.1: A schematic of the open accumulator compressed air energy storage system.

key components are an air compressor/motor, a pump/motor, and an accumulator containing the pressurized air and liquid. Figure 2.1 shows the relationship between these components. Two operational modes are possible: a preferred base mode and a high-power mode. Basic operation maintains a constant accumulator vessel pressure. To store additional energy, ambient air is compressed using the air compressor and moved into the accumulator. Simultaneously, a quantity of liquid equal to the volume of the added air is bled from the liquid side of the accumulator, thus maintaining the accumulator pressure. To regenerate energy, pressurized air passes through the air motor, and simultaneously liquid is added to the accumulator to maintain constant pressure. It can be seen that in the basic operational mode the quantity of stored energy is represented by the volume of the air in the accumulator. This first mode takes advantage of the high energy density of highly-pressurized air. In the second, high-power mode, the pressure of the accumulator is not maintained and liquid is added or removed from the accumulator via the hydraulic pump/motor without changing the quantity of air. Thus, the operation emulates that of a conventional hydraulic accumulator. A hydraulic pump offers superior power characteristics compared to an air compressor/motor, so this

mode would be utilized in situations when transiently high power needs to be supplied or absorbed.

The open accumulator fits naturally with fluid power systems, and as such, becomes an alternative to conventional hydraulic accumulators. It is useful to compare these two technologies. First, it is important to note that hydraulics are characterized by high power density, which makes them attractive for high-power applications, such as wind turbines. However, hydraulic accumulators have traditionally offered relatively poor energy density (by volume)—on the order of 10 kJ/L at 350 MPa (cf. 1 MJ/L for batteries). Actually, compressed air itself has reasonably high energy density; the reason for the low energy density of conventional accumulators (in which the quantity of air is constant) largely rests with the configuration of those systems. In a conventional "closed" accumulator, energy is stored by pumping liquid into a vessel, thereby compressing a fixed quantity of gas. Mechanical energy is regenerated by allowing the compressed gas to expand, thereby forcing the liquid out of the accumulator and through a hydraulic motor. Both high energy and low system volume are desired, but both energy and volume are correlated to the compression ratio. While a larger compression ratio means more energy is stored, it also requires a larger accumulator volume to hold the initial expanded gas. Additionally, a larger volume of liquid is required to compress the gas, and this liquid must also be stored. The result is that maximum energy density occurs when the compression ratio is in the range of 2–3.

The open accumulator addresses these shortcomings by utilizing the ambient as a "reservoir" for the expanded air. This eliminates the requirement that the accumulator be sized for the expanded air, thereby also removing the need for the liquid which would have been required to fill the accumulator. Consequently, these volume savings enable much larger compression ratios. A reasonable peak pressure for hydraulic components is 35 MPa (350 atm), so the compression ratio becomes 350, as opposed to the conventional 2–3. The impact on total energy stored during compression can be seen in figure 2.2. The result is a potential 20-fold improvement in energy density [15].

A key component in the open accumulator design is a compact and efficient air compressor. The air compressor/motor adds air to, or removes air from, the accumulator, corresponding to storing and regenerating energy, respectively. In order for the system to be viable, the power must surpass that of alternative high-energy density options

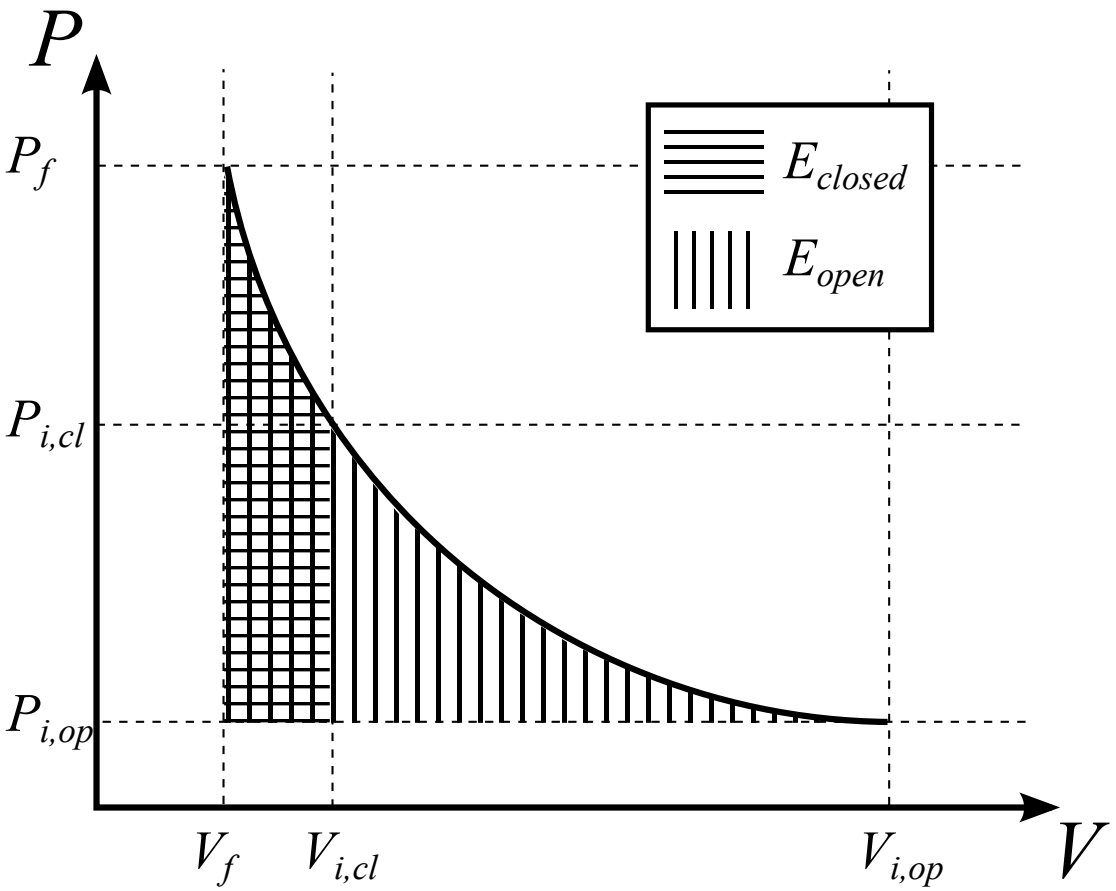

Figure 2.2: The open accumulator has a much higher pressure compression ratio, so the total energy stored during a single stroke, $(P_{i,\mathrm{op}}, V_{i,\mathrm{op}})$ to (P_f, V_f), becomes much greater than the energy stored for a closed, conventional accumulator: $(P_{i,\mathrm{cl}}, V_{i,\mathrm{cl}})$ to (P_f, V_f).

such as batteries. However, efficient conversion of mechanical energy to the pressurized air "potential" energy is required. The primary inefficiency of a compression process is the conversion of the input work to internal energy of the gas—that is, heating the gas. Compression with a constant temperature, isothermal compression, is the most efficient method of compression since no input work is expended to heat the gas. As discussed in the introduction, there are two over-arching strategies that may be used to improve the efficiency: first, improving the heat transfer, thus preventing the temperature rise of the gas; second, modifying the pressure-volume trajectory such that the heat transfer is optimized.

Motivated by the compactness and efficiency requirements for the open accumulator, Hafvenstein [21] conducted research and analyses focusing on the development of a novel diaphragm air compressor. However, thermodynamic and heat transfer models, as well as FLUENT simulations, predicted that the diaphragm compressor would not meet the heat transfer and volume requirements set for the open accumulator. Nevertheless, progress was made in understanding the heat transfer problem for the open accumulator system. The present thesis may, in some ways, be considered an offshoot of Hafvenstein's research, as new strategies for a compact and efficient air compressor are presented and discussed. Specifically, a conventional piston-in-cylinder compressor is considered, but it is modified in that the heat transfer is augmented by porous materials and the motion of the piston optimized. The remaining contents of this chapter review literature relevant to the study of compression in piston cylinders, heat transfer augmentation by porous materials, and trajectory optimization. It should be noted that while there is an extensive archive of literature on both heat transfer during compression and heat transfer in porous media, very little combines the two for the purpose of achieving near-isothermal compression and expansion. Thus, the literature reviewed in this paper will focus on these two sub-topics, separately.

2.3 Compression heat transfer

2.3.1 Compression heat transfer from engine research

Most compression heat transfer literature comes from engine research. These studies are on understanding and modeling the heat transfer during compression. In the present

work the objective is to achieve near-isothermal compression. While engine research does not share that objective, an understanding of the heat transfer during compression as provided by these studies is valuable.

The study of engine heat transfer has a long history, beginning with Nusselt in the 1920's. At the risk of over-simplifying its evolution, this history can be divided into four stages, which will be summarized below: first, quasi-steady heat transfer correlations; then, unsteady correlations; about the same time, multi-zone models; finally, three-dimensional numerical or computational fluid dynamics models. An informative introduction is Borman and Nishiwaki's review of the history of internal combustion engine heat transfer up until 1987. They cover quasi-steady correlations for the heat transfer coefficient (often via the Nusselt number) as suggested by Nusselt (1923), Eichelberg(1937), Briling (1958), Taylor (1960), Oguri (1960), Pflaum (1961), Van Tyen (1962), Annand (1963), Woschni (1967), and others. They also look at multi-zone models which break up the problem into different zones of interest based on physical or geometrical reasoning and determine the heat transfer for each zone. A typical multi-zone model is composed of a one-dimensional thermal boundary layer and an adiabatic core. They also introduce some of the initial findings from three-dimensional computational routines, although as of the time they were writing, the results seem to have been viewed as promising curiosities with limited practical value.

A review by Finol and Robinson [22] published in 2006 provides a more modern perspective. Despite the influx of detailed theoretical and computational models, Finol and Robinson chose not to review them. They were of the opinion that the complexity of computational modeling and concerns about accuracy inhibit their widespread use—designers were (as of that time) unable to justify the time and effort. Thus, the correlations from the 1960s (especially from Woschni and Annand) remain popular, albeit more for their simplicity than their performance. The Finol and Robinson review focuses on these empirical and semi-empirical correlations for the in-cylinder heat transfer coefficient. Three different types of correlations were recognized and cataloged: time- and spatial-averaged correlations, instantaneous and spatial-averaged correlations, and instantaneous local correlations. Interestingly enough, little progress seems to have been made since the 1987 Borman and Nishiwaki review. There is still a logjam of correlations and a lack of consensus on how best to model the heat transfer coefficient.

It should be noted that both experimental and numerical research has looked at the fluid dynamics of the compression process. The most significant feature observed during that start of compression is a corner vortex [23]. Others have focused on the transition to turbulence during compression in the piston of an internal combustion engine. Marc, Boree et al. [24] have published several papers on the topic, including high-speed particle image velocimetry (PIV) data. Numerical studies have been performed by Le Roy and Le Penven [25] and Naitoh et al. [26]. The consensus is that a vortex-type flow field transitions to turbulence through a phenomenon described as a "tumbling vortex" flow. For a compression process, the energy imparted by the piston, and the eventual squishing of the vortices by the piston, are impetuses for transition. While the computational heat transfer models will capture these dynamics at some level, the other heat transfer models do not.

Compression heat transfer: quasi-steady models

Quasi-steady models are models derived from steady-state heat transfer correlations. Among the most enduring are those by Woschni and Hohenberg. Woschni's 1967 paper proclaimed a "universal" correlation for the instantaneous heat transfer to cylinder walls for the internal combustion engine [27]. Woschni assumes that the probable trend of the heat transfer is similar to steady-state correlations for turbulent flow through a pipe:

$$Nu \propto \mathrm{Re}^{0.8} \tag{2.1}$$

where

$$Nu \equiv \frac{hD_h}{k} \tag{2.2}$$

Woschni uses an energy balance to develop a correlation for the scavenging period, then backs out the total heat transfer during compression and expansion. The following correlation was obtained:

$$h = 1.58 D_h^{-0.2} \left(\frac{P}{98100}\right)^{0.8} T^{-0.53} \left[C_1 U + C_2 \frac{V}{nR}\left(P - P_0\right)\right]^{0.8} \tag{2.3}$$

where C_1 is 6.18 during the scavenging period and 2.28 during the compression and expansion strokes, and C_2 is $3.30{\times}10^{0.8}$. The hydraulic diameter, D_h, is the bore, U is the average piston velocity, V is the cylinder volume, and n is the number of moles

of gas at the beginning of combustion. All quantities are in SI units. The brackets contain two convective terms accounting for piston motion and additional gas motion due to combustion. Woschni and others continued to fine-tune the correlation, with Hohenberg's modification one of the better known. Hohenberg [28] offered the following modification of equation (2.3):

$$h = C_1 V^{-0.06} \left(\frac{P}{100000} \right)^{0.8} T^{-0.4} \left(U + C_2 \right)^{0.8} \tag{2.4}$$

finding C_1 and C_2 to be approximately 130 and 1.4, respectively. These two classic quasi-steady correlations for the heat transfer coefficient may be useful for modeling the heat transfer during compression for parameters (e.g. aspect ratio and compression ratio) representative of what might be found in an engine.

Two more recent quasi-steady correlations are reviewed next. Chen and Karim [29] measured the pressure and volume during rapid compression of air and used thermodynamic analysis to determine the instantaneous unsteady heat transfer to the cylinder wall. The authors determined a correlation for Nusselt number that applies for compression ratios in the range of 8.4 to 24.3:

$$\mathrm{Nu} = 0.010 \mathrm{Re}^{1.188} \tag{2.5}$$

where Re is the Reynolds number based on average piston velocity and the cylinder bore. Chen and Karim also ran three-dimensional computational fluid dynamics codes to simulate compression. They found that the Nusselt number is nearly independent of the Reynolds number when defined in terms of the maximum gas velocity and the instantaneous distance between the piston and endwall. Thus, the Nusselt number is nearly constant and h changes inversely with air volume. Hsieh and Wu [30] experimentally determined correlations for the heat transfer coefficient in a high pressure (to 6000 PSI) reciprocating gas compressor. Thermocouples were used to measure the wall temperature and backside wall temperature, from which the authors were able to back out the heat flux. Hsieh and Wu proposed a correlation for the Nusselt number during compression in the form

$$\mathrm{Nu} = C_2 \mathrm{Re}^{C_3} \left(\frac{\mu}{\mu_0} \right)^{C_4} \tag{2.6}$$

where the Reynolds number is based on piston velocity and bore diameter, μ is the

instantaneous viscosity, μ_0 is the viscosity at standard temperature and pressure, and the constants are $C_2 = 0.163$, $C_3 = 1.093$, and $C_4 = 0.484$.

Compression heat transfer: unsteady models

Not all researchers agreed that quasi-steady models are adequate since they are based on steady-state correlations. They maintain that any model must account for the unsteady nature of the compression event. Faulkner and Smith [31] studied the heat transfer between the cylinder walls and a gas during compression and expansion in reciprocating machinery. They wanted to find the instantaneous, spatially-averaged heat transfer for a single, closed cylinder without combustion. The authors tested three different gases (helium, nitrogen, argon), two different volume compression ratios (2.39, 3.99), and three different cylinder liner materials (steel, copper, micarta). They found that the heat loss is correlated with the ratio of specific heats, γ, but is a maximum at an average Reynolds number on the order of 100 for all testing conditions, where the average Reynolds number is based on average density, average velocity, and the cylinder bore. One of their observations was that instantaneous heat transfer is not proportional to the instantaneous temperature difference between the average gas temperature and wall temperature. In fact, heat transfer was greatest when the "driving potential" was near zero. They concluded that an unsteady term would be required to accurately predict instantaneous, spatially-averaged heat transfer.

Similarly, Lawton [32] calculated heat flux to the endwall of a cylinder-in-piston device and found that the heat flux was out of phase with the air-wall temperature difference. Lawton numerically solved the one-dimensional unsteady conduction problem and found that the results were in good agreement with the measurements. However, easy-to-use correlations were much more popular, so using dimensional reasoning, Lawton empirically modified the popular Annand correlation, introducing a steady term. The result, for compression, is

$$q_w = \frac{k}{d}\left[a\mathrm{Re}^b\left(T - T_w\right) - 2.75LT_w\right] \tag{2.7}$$

where T_w is the wall temperature and $0.3 < a < 0.8$ and $b = 0.7$ are Annand's constants.

The unsteady L is a compressibility factor

$$L = (\gamma - 1)\,\frac{\dot{V}}{V}\sqrt{\frac{d^3}{\alpha_0 U}} \tag{2.8}$$

where γ is the ratio of specific heats, V is the air volume, d is the cylinder bore, U is the mean piston velocity, and α_0 is the initial thermal diffusivity (the diffusivity of the inlet air).

Kornhauser and Smith [33] propose the heat flux be modeled as

$$q = \frac{kA}{D_h}\left[\mathrm{Nu}_r\,(T - T_w) + \frac{\mathrm{Nu}_i}{\omega}\frac{dT}{dt}\right] \tag{2.9}$$

where k is the thermal conductivity of the gas, D_h is the hydraulic diameter of the compression chamber, Nu_r and Nu_i are the real and imaginary components of the Nusselt number, T is the volume-averaged gas temperature, T_w is the wall temperature, and ω is the cycle frequency. Kornhauser and Smith conducted experiments for a range of gases (helium, hydrogen, nitrogen, argon), bore/stroke ratios (0.42, 0.67, 1.23), volume ratios (2.0, 4.0, 8.0), and frequencies (0.034 Hz to 16.8 Hz). Using measured heat fluxes, the authors backed out values for both components of the Nusselt number. They found that the imaginary Nusselt number (indicating a phase shift between heat flux and temperature potential) was greatest for higher Peclet numbers, defined as

$$\mathrm{Pe}_\omega = \frac{\omega D_h^2}{4\alpha} \tag{2.10}$$

where α is the thermal diffusivity of the gas. When the Peclet number was in low end of tested values ($10 < \mathrm{Pe}_\omega < 100$), the imaginary Nusselt number was small, particularly for high pressures and low frequencies. Cantelmi et al. [34] developed an analytical model for turbulent heat transfer incorporating the complex Nusselt number discussed by Kornhauser and Smith [33]. Model results predict the trends and general magnitudes seen by experiments.

Compression heat transfer: multi-zone models

The advantage of the quasi-steady and unsteady correlations described above are their ease of use. More complex are the multi-zone models, reviewed next. The multi-zone heat transfer model was spearheaded by Knöös [35] and Isshiki and Nishiwaki [36].

These authors divided the flow into two regions: a one-dimensional thermal boundary layer against the cylinder head, and an adiabatic core flow. One-dimensional thermal boundary layers were used because the dominant temperature gradients occur normal to the wall. The temperature gradients parallel to the wall are relatively insignificant. The authors solved for the heat flux and temperature distribution in the thermal boundary layer. Knöös [35] ran tests using a cylinder with 32.1 mm bore, 240 mm stroke, and volume compression ratio of about 8.6. The test gases were helium and argon. Peak piston velocities were in the range of 15 m/s. Comparisons between the measured pressure curves and the theoretical pressure curves from the one-dimensional boundary layer model were very good. Isshiki and Nishiwaki [36] conducted experiments using nitrogen gas in a single piston with 95 mm bore and 105 mm stroke. Air temperature and pressure were measured, and oblique grid shadowgraphs of the thermal boundary layer at the cylinder head were taken using windows installed into the chamber walls. The temperature distribution in the thermal boundary layer were extracted from the shadowgraph because the refraction of light was related to the temperature and pressure of the gas. Isshiki and Nishiwaki found good agreement between the shadowgraph results and their predictions using a one-dimensional boundary layer model.

Building on the work of Isshiki and Nishiwaki [36], Nikanjam, et al. studied heat transfer to the endwall [37] and Greif, et al. studied heat transfer to the sidewall [38]. Both these studies focused on a single compression stroke. The heat flux was determined using two methods. In one, temperature measurements were taken with compression ratios of 4 (sidewall) and 8 (endwall) and a conduction analysis was performed. In the second, the one-dimensional boundary layer continuity and energy equations were solved, assuming adiabatic compression outside the boundary layer. Using the boundary layer method and assuming that variations in the wall temperature were negligible, the heat transfer coefficient for both the sidewall and end cap was found:

$$h = \frac{1}{T_\infty - T_w(t)} \left(\frac{-k_w \rho_w}{\rho_0 (\pi \alpha_0)^{1/2}} \right) \left[\frac{T_w - T_\infty(t)}{t^{1/2}} + \frac{T_w T_\infty(t)}{2} \int_0^t \frac{T_\infty(t) - T_\infty(\tau)}{(t-\tau)^{3/2}} \mathrm{d}\tau \right] \tag{2.11}$$

where T_∞ is the temperature of the gas outside the boundary layer, k_w is the thermal conductivity of the wall, ρ_w is the density of the wall, ρ_0 is the initial density of the gas, α_0 is the initial thermal diffusivity of the gas, and T_w is the constant temperature

of the wall. In the boundary layer analysis, the authors choose to neglect the effect of mixing due to the corner vortex and the velocity of the gas due to the movement of the piston, both of which would tend to increase h. Further extensions of the two-zone model include those of Polman [39], who considers the effect of changing surface area due to sinusoidal oscillating behavior, Keck [40], who considers a temperature-dependent thermal conductivity, Yang and Martin [41], who consider a turbulent boundary layer, and Buttsworth, et al. [42] who consider non-planar walls and a non-isentropic core region.

Lee and Hochgreb indirectly supported the two-zone scheme in their experimental study of a rapid-compression machine [43]. They observed that two-zone models routinely underestimate heat transfer. The authors suspected that a corner vortex (as seen by, e.g. [23]) induces mixing between the core region and the boundary layer, and that, since this kind of feature is ignored in the two-zone model, it was a candidate for the primary error. They implemented a new piston geometry designed to suppress the corner vortex. With the new piston, experimental results fit the two-zone model assumption much better, suggesting that the author's suspicions were correct. While it is definitely not the intention of this thesis to propose methods of reducing mixing, this study is enlightening in that it seems to validate the boundary layer model as generally correct, and, also, the corner vortex as the primary complication for an empty piston-in-cylinder geometry.

Compression heat transfer: numerical simulations

Now, numerical simulations and computationally-intense models will be commented on briefly. Recktenwald and Patanker [44][45] demonstrated that computational models can provide very different results than simple lumped models. In their study Recktenwald and Patanker used a finite-difference method to solve the differential equations for flow and heat transfer based on the pioneering work by Gosman and Watkins (e.g. [46]). They compared a three-node, bulk properties case with an axisymmetric, three-dimensional, moving-mesh, multi-node case. The three-node case implemented mass and energy balances, assuming spatially uniform pressure and temperature. The computational, multi-node model essentially replaced each node in the three-node model with a multi-element grid. The output of the three-node model was used as input to

the multi-node model to determine inflow and outflow boundary conditions. Conservation equations for mass, x- and r-direction momentum, and energy were solved using a finite-difference method. Comparing the three-node and multi-node models, the authors found that while the pressure was in good agreement, the variations of temperature and heat transfer rate were very different. The three-nodal model underpredicted the average net heat transfer by an order of magnitude (132%) as compared to the multi-node model, resulting in a near-adiabatic cycle. Rectenwald and Patanker's work serves as a caution against putting too much trust in the results of simple models.

More recent simulations have been performed by Catto and Prata [47], who numerically solve continuity and conservation equations for axisymmetric unsteady compressible flow of an ideal gas. They validate their model by matching predicted adiabatic behavior at all speeds and compression ratios. They then run a series of tests looking at volume ratios from 2 to 200, speeds of 100 to 3500 rpm, and three gases (helium, air and R134a). Significantly, a phase shift between the temperature difference and heat flux was observed, corroborating Kornhauser and Smith [31] and Lawton [32]. Catto and Prata observed that the phase shift became less significant for higher speeds and higher compression ratios. However, Kornhauser and Smith [31] showed that the phase shift was less significant for lower speeds and more significant for higher speeds, so more work may need to be conducted to determine where quasi-steady models are acceptable and where unsteady models are required.

Porous media and engines

Finally, engine research has provided some studies combining compression and porous media—a combination also reported in the present thesis. However, while the research in this thesis utilizes porous media for achieving near-isothermal compression, engine research utilizes porous media to enhance the evaporation of fuel by improved mixing and preheating of the air from the energy stored in the media, (e.g. see [48][49]). These studies may be useful for understanding flow fields in a piston containing porous media. A numerical study by Zahi et al. [50] simulated a compression stroke in a cylinder partially filled with a laterally heated saturated porous structure. Their compression cylinder consisted of three regions of interest. The first is the space between the piston and the porous structure. The porous structure is the second region of interest. The

third is the space between the porous structure and the endwall. Zahi found that heat exchange between the porous structure and air was facilitated by increasing Reynolds number, permeability, and porous structure length. Unfortunately, no comparisons were made with a conventional piston. Zahi et al. provides interesting figures demonstrating circulation within the different regions, which may be useful when designing a porous insert.

2.3.2 Compression heat transfer from accumulator studies

Besides air compressors and engines, a third gas-compressing technology is the hydraulic accumulator. As with an air compressor, near-isothermal compression is desired for a hydraulic accumulator to improve efficiency. Otis [51] suggested that plastic foam be put into the accumulator to provide additional heat transfer surface area and thermal capacitance. Experiments showed that by putting a plastic foam into the accumulator, thermal losses can be reduced from 15–25% to 1.4% of the useful energy. Pourmovahed [52] continued the work of Otis, addressing some of the practical concerns of foams, such as durability. Pourmovahed, et al. [53] conducted experiments demonstrating improved efficiency of up to 60% due to the foam. They utilized foam-filled accumulators in a hydraulic energy regeration system which was then able to achieve efficiencies as high as 89%.

Sherman and Karlekar [54] suggested bonding a large number of very thin, highly-conductive metallic strands to the casing of the accumulator. In function, the strands offer benefits similar to a foam: increased surface area and thermal capacitance. They studied the rapid charging and discharging over a pressure range of 6.9 MPa (1000 psi) to 20.7 MPa (3000 psi). They assumed a heat transfer coefficient of 113 W/m^2-K (20 btu/hr-ft^2-°R), and predicted improvements of 15% over adiabatic compression and 43% over an adiabatic-compression, cooling, adiabatic-expansion process.

2.4 Improving heat transfer

As discussed in the introduction, the first major objective in increasing compressor efficiency is to provide suitable heat transfer rates between the air being compressed and a thermal sink. The heat transfer offered by a conventional piston-in-cylinder as

described above is insufficient. Thus, it must be augmented in some way. A brief overview of the larger spectrum of heat transfer augmentation strategies is provided before delving into more specific topics.

2.4.1 An overview of heat transfer augmentation strategies

Several thorough reviews have been written on the state of heat transfer augmentation strategies throughout the years (e.g. Balaras [55], Dewan [56], Bergles [57]). Notably, Arthur E. Bergles has been an active leader in the field heat transfer augmentation and has written numerous papers and several reviews on the topic. His 1995 Max Jakob Memorial Award lecture reviewed augmentation techniques for convective heat transfer [58]. He broke up the various strategies into 14 techniques, discounting compound strategies, divided into passive and active types. The passive techniques are treated surfaces, rough surfaces, extended surfaces, displaced enhancement devices, swirl flow devices, coiled tubes, surface tension devices, and additives for fluids. The active techniques are mechanical aids, surface vibration, fluid vibration, electrostatic fields, suction of injection, and jet impingement. The porous inserts used in the present work fall into the passive category and function as extended surfaces.

2.4.2 Review of steady-state heat transfer with mesh-type inserts

Literature reporting experimental results for heat transfer using porous inserts almost invariably addresses the cooling of heated surfaces in steady-state. With regards to the wall, porous media, and fluid, the object of this thesis is different: the fluid experiences transient heating and the combined porous media and wall are the heat sink. However, the effect of the porous media is similar for both steady and unsteady cases. In the conventional case of steady-state forced convection of a coolant past a heated surface, the porous media may perform a variety of functions. Sometimes, the porous structure essentially extends the wall, increasing surface area. To perform this duty, it is essential that the porous media is a good conductor and that good thermal contact is made with the wall. Another function of the porous insert is that of a mixer. Sometimes, the porous inserts are in the core flow but are physically separated from the wall. A third function is that of a radiative heat exchanger. Due to the high emissivities of the

porous media materials, the heated wall emits thermal radiation to the porous structure which is then dissipated to the coolant, or vice versa in the case that the fluid is hot and the wall is the heat sink [59][60]. The following studies report the heat transfer gains offered by meshes for steady-state situations. The substantial benefits described in these studies motivated the use of a mesh in the transient situation as described in this thesis.

In the 1970's, Megerlin et al. [61] published one of the first studies of porous mesh inserts for the purposes of augmenting heat transfer. The authors brazed felt metal pads constructed from thin stainless steel fibers of 80% porosity to the inner surface of a 0.21 inch diameter heated tube. Pressure drop and temperature measurements were taken for water flowing through the mesh. The authors found that up to 9-fold increase in the heat transfer coefficient was possible, as compared to the empty tube, but caution that the results are highly dependent on the location of the thermocouples.

The use of a wire mesh insert to enhance heat transfer was again studied by Kuzay, Collins, et al. in the 1990's [62][63][64]. In their experimental program [62] they tested two different copper meshes (wire diameter 0.150 mm) and a sintered copper foam brazed to the inner wall of a copper tube. They compared these to an empty, smooth tube and to a commercially-available, enhanced-surface tube. Heating was applied to the outer surface of the copper tube and flowing water was used as the coolant. Of the five options, they found a 6-7-fold increase in heat transfer coefficient over that of a plain tube for press-formed copper mesh surfaces with 85% porosity. For the sintered foam tube, a 5-fold increase in the heat transfer coefficient was seen. The loosely-rolled copper mesh at 90% porosity was judged to be no more effective than the commercial enhanced-surface tube, at 2–3-fold improvement. However, they were not able to attain the augmentation seen by Megerlin et al. . Pahlavanzadeh et al. [65] imitated Megerlin's setup by running water through a 1.9 cm (3/4 inch) heated tube with and without a "medium density" wire mesh. Heat transfer enhancement with the mesh was measured to be only 163-174% over that of plain tubes.

Angirisa [66] looked at heat transfer by forced convection through a fibrous mesh bonded to a heated wall. These numerical studies predicted substantially higher heat transfer rates which increase with Reynolds number, based on channel length and inlet velocity, up to values around 25000, at which point gains level out. The results show

that the optimal configuration of the porous mesh would be to use as small fibers as possible while maximizing the porosity. Angirisa [67] also performed some experiments which showed that a lower porosity leads to lower temperatures due to increased surface area.

Several authors studied forced convection through mesh screens. Pavel and Mohamad performed experimental [68] and numerical [69] studies of the heat transfer enhancement during forced convection of air through a series of circular aluminum screens in a cylinder. They varied screen diameter and separation distance to get different porosities. Reynolds numbers, based on mean velocity and cylinder bore, ranged from 1000 to 4000, including laminar, transitional, and turbulent flow regimes. In each case the wall was heated with a uniform heat flux. The authors found that the Nusselt number tended to be independent of porosity for small screen diameters, but the porosity was very important when the screen diameter equaled the cylinder diameter. Also, when the screen diameter equaled the cylinder diameter, there was the additional benefit of conduction between the screen and the wall. A 6-fold improvement in Nusselt number over plain tubes was reported when the porosity was 98.1%, Reynolds number was 4000, and the screen extended to the wall. When the screen diameter was less than cylinder diameter, the flow resistance caused by the screens forced higher velocities and flow turbulence near the wall which enhanced the heat transfer. Pavel and Mohamad's computational results largely agreed with their experimental results in character, although the computation results predicted poor performance when the screen diameter equaled the cylinder diameter, whereas the experimental results showed that case to have the best performance. The authors attribute descrepancies to several factors, including the inability of the numerical program to model turbulence, radiation, and conduction.

Sarada et al. [70] extended the results of Pavel and Mohamad further into the turbulent regime. Their computational and experimental results exhibit the same trends, namely the Nusselt number improves with Reynolds number and screen diameter. However, the relative enhancement over plain tubes was greatest for the lowest Reynolds number cases tested (Re = 8000), at about a 2-fold improvement. Varshney and Saini [71] also studied heat transfer between wire screens and flowing air. They uncovered a correlation for the heat transfer coefficient that was proportional to $\mathrm{Re}^{0.45}\mathrm{Pr}^{1/3}$, where the proportionality constant was a function of the number of screens, the porosity, the

screen pitch, and the screen wire diameter.

2.4.3 Review of heat transfer in minitubes

Skinny tubes have been suggested as a means to improve the heat transfer during compression [16]. This thesis will investigate the possibility in greater detail. Heat transfer between fluid flowing through conventionally-sized tubes (hydraulic diameters greater than a few millimeters) and the tube surface is already well understood. In general, small diameters are beneficial from a heat transfer perspective. Thus, the use of minitubes and microtubes for heat transfer is becoming increasingly popular. The second experimental program described in this thesis uses a minitube array fabricated from copper tubing with an inner diameter of about 1.5 mm, classifying them as "minitubes." However, there is some concern that conventional theory does not apply to minitubes and microtubes. Literature is discussed, below, to address the question "do heat transfer correlations for conventionally-sized tubes and channels apply on the microscale, and, if not, when do they become invalid?"

A review by Sobhan and Garimella [72] from 2001 compares ten studies reporting correlations for the Nusselt number as a function of Reynolds number in the laminar flow regime. These studies encompassed different fluids, channel sizes, and channel shapes, but the significant scatter in the results did not follow a discernible trend. However, in all cases the Nusselt number increased with Reynolds number more steeply than with a comparable conventional channel correlation. Sobhan and Garimella also compared thirteen studies reporting Nusselt number correlations as a function of Reynolds number in the turbulent regime. Again, the studies encompassed various fluids and geometries, and again, the various groupings were not correlated with these parameters. All reported correlations predict higher Nusselt numbers than the Dittus-Boelter correlation for turbulent flow, except one research group which regularly predicted lower values. Sobhan and Garimella conclude that there is no consensus regarding a heat transfer correlation, and recommend a systematic study to understand the influence of the various parameters. They also don't recognize significant deviation from a continuum assumption and conventional theory for the channels tested, which generally have hydraulic diameters of at least 50 microns.

Subsequent experimental work has continued to affirm that "macro-scale" theory

is applicable on the micro-scale. In 2003 Guo and Li [73][74] reported on the consequences of smaller channels on heat transfer and friction factor. They consider both non-continuum effects as well as aspects of conventional flow that become increasingly important (e.g. viscous dissipation) in small diameter tubes. In 2005, Reynaud et al. [75] reported heat transfer coefficients for minichannels of 1.12 mm to 300 micron thickness. Their results agree with macro-scale correlations. In 2006 Celata, et al. [76] reported on single-phase heat transfer for laminar, liquid flow through microtubes with diameters ranging from 528 microns to 120 microns. They found that the Nusselt number decreases with decreasing diameter, but speculate that this deviation from expected behavior was linked to thermal entrance effects. However, the measured Nusselt number for the largest diameter (528 microns) was very similar to the fully-developed laminar flow value. Li et al. [77] conducted a detailed numerical simulation of forced convection through channels with a hydraulic diameter of 86 microns at Reynolds numbers less than 200. Comparisons with other numerical results and experiments indicate that the assumption of conventional, fully-developed laminar flow was accurate. Owhaib and Palm [78] studied forced convection heat transfer for minitubes with diameters of 1.7, 1.2, and 0.8 mm. Data were taken for Reynolds numbers ranging from 1000 to 17000. They compared the data to both classical macro-scale correlations and newer micro-scale correlations. Owhaib and Palm found that the conventional correlations outperformed the micro-scale correlations. These results seem to indicate that conventional heat transfer correlations are appropriate for minitubes of diameter 1.5 mm as used in the experiments reported herein.

2.5 Trajectory optimization

As discussed in the introduction, the second major objective in increasing compressor efficiency is to optimize the manner in which the air is compressed. This optimization problem could be classified as a problem in finite-time thermodynamics. Finite-time thermodynamics differs from classical thermodynamics in that it is concerned with time. Classical thermodynamics assumes quasi-static reversible processes (i.e. infinite-time); thus, results are applicable only as theoretical limits. As Andresen, Salamon, and Berry explain in their introduction to thermodynamics in finite-time [79], real processes

may have time constraints and irreversibilities. They pose the question "Are reversible limits close enough to real performances to be useful in guiding the improvement of processes?" They propose finite-time thermodynamics (FTT) as an improvement and proceed to highlight some of the current research. A recent review of FTT exposes numerous applications, including heat engines and refrigerators, economics, chemical reactions, and quantum systems, among others [80][81]. The application to optimal control of heat engines [82] comes closest to the topic of the present research and will be looked at more closely to see what can be learned.

Morton Rubin tackled the generic heat engine with finite cycling times. The analysis focused on the case in which the only irreversibility was linear heat conduction between the engine and the environment. The maximum volume rate of change was also limited to finite values. Solutions were worked out for maximum efficiency and maximum power which consist of six branch cycles with isothermal and maximum-power components. This solution reduced to the Carnot cycle when the constraints on time were removed [83]. A more detailed "part II" analysis may be found in [84]. Further analysis with additional constraints on the compression ratio resulted in an eight-branch cycle consisting of isothermal, maximum-power, and isochoric components [85].

Similar work was done by Salamon, Band, and Kafri [86][87][88]. They considered a piston-in-cylinder arrangement with a working fluid coupled to an infinite heat sink and with a constant conductivity, and a rate of heating as might be provided by combustion. They asked "what is the optimal motion of the piston in order to extract the maximum work in a given amount of time?" They used calculus of variations to find that the optimal trajectory for expansion (i.e. the power stroke) between an initial and final volume consists of an initial instantaneous adiabatic jump, followed by expansion along an Euler-Lagrange (EL) arc, completed by a second adiabatic jump to the final volume. When the rate of heating was zero, the EL-arc was replaced by simple isothermal expansion [86]. A more lengthy article considers the same problem, but looked at various permutations of the problem (constraining final volume, final energy, or both), as well as the effects of practical concerns such as heat leaks, friction, limited piston velocity, and finite piston and air masses [87]. The same authors again extended their work to encompass non-ideal gases and non-constant heat sink temperatures [88]. These results

assumed a constant linear conductivity, K, so the heat transfer rate was

$$q\left(t\right) = K\left(T(t) - T_{\text{sink}}\right). \tag{2.12}$$

They did not address the issue of variable heat transfer between the working fluid and its environment. Also, their results focused on the expansion of the gas, as they were intended to be used for the power stroke of a combustion engine.

Mozurkewich and Berry [89][90] optimized the volume trajectory of a working fluid over the Otto cycle while modeling typical losses, such as friction and heat leaks. They determined that maximum work was extracted from the power stroke by instantly accelerating to a high velocity to take advantage of the higher efficiency of the hotter gases, and then by slowing down as the rate of heat loss decreases to reduce frictional losses, thus taking a fast-slow type trajectory. Hoffman, Watowich, and Berry [91] performed a similar analysis on the diesel cycle, in which they found a similar fast-slow result for the piston trajectory. Again, this analysis did not address the varying heat transfer between the working fluid and the heat sink. Heat loss was modeled as a linear function of the temperature difference. Heat leaks were built into the proportionality constant.

Chen et al. [92][93] looked at the effects of different heat transfer laws on the optimal efficiency of a generalized irreversible Carnot cycle. They observed that most studies assume a Newton's law type heat transfer, that is $q \propto \Delta T$, but in non-equilibrium thermodynamics, a different heat transfer model, called the phenomenological law, is sometimes used: $Q \propto (\Delta T)^{-1}$. They did not determine the optimal trajectories, however, and they still assumed a constant proportionality constant.

Sancken and Li [94] addressed the optimization of compression and expansion trajectories in a air motor/compressor with Newton's law type heat transfer. They based their analysis on the open accumulator system and defined efficiency in terms of the maximum possible energy that may be stored. They found that the optimal compression and expansion trajectories were composed of three stages: first, an adiabatic stage; second, a isothermal stage; and third, an adiabatic stage. This result agreed with previous research by Band et al. [86]. During compression an additional isobaric cooling stage was required by the system model which simulated the storage of the air in the accumulator. Sancken and Li found that for a given storage efficiency of 90%, the gains in storage power (defined by stored energy divided by compression time) over linear-

and sinusoidal-shaped trajectories ranged from 300–500%.

Chapters 8–10 of the present work extend the analysis of Sancken and Li by allowing the proportionality constant in Newton's Law, hA, to vary as a function of air volume over the compression and expansion processes.

Chapter 3

System model

The objective of this chapter is to describe the system model and develop the governing equations under appropriate assumptions. The governing equations describe the compression of air with and without a porous medium in the air space. Two porous media are discussed: a mesh and a minitube array. The heat transfer characteristics of each will be considered separately. The objective is to develop simple governing equations and heat transfer models that capture the relationship between air pressure, air volume, air temperature, and porous media temperature.

3.1 System model

This thesis focuses on the role of the air compressor in the open accumulator infrastructure, specifically, the ability to achieve high efficiency while retaining the high power density inherent in fluid power. Throughout the present work the following system model will be employed.

A piston-in-cylinder-type compressor at bottom dead center contains ambient air, assumed to be an ideal gas, with initial pressure, temperature, and volume, P_0, T_0, and V_0 as in figure 3.1 (left side). The piston is a liquid piston and the cylinder is oriented vertically with liquid on bottom and air on top. To compress the air, liquid is added to the bottom of the cylinder. As discussed previously, two types of porous media are used to attain higher heat transfer rates: a mesh and a minitube array. Figures 3.2 and 3.3 show the two situations, which are variations of the basic situation in figure 3.1.

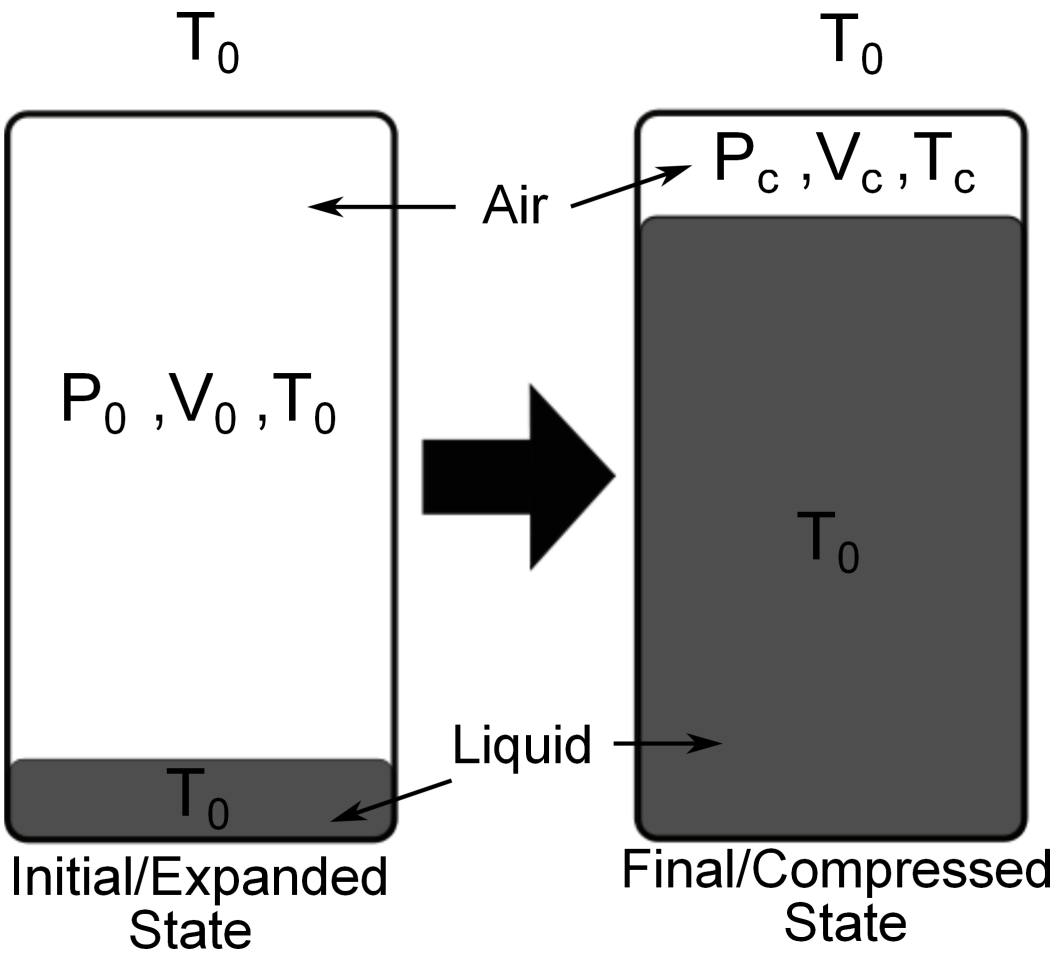

Figure 3.1: Air is compressed from initial (expanded) conditions, left, to final (compressed) conditions, right). During the compression, heat transfer occurs between the heated air and the bounding surfaces, all at ambient temperature T_0.

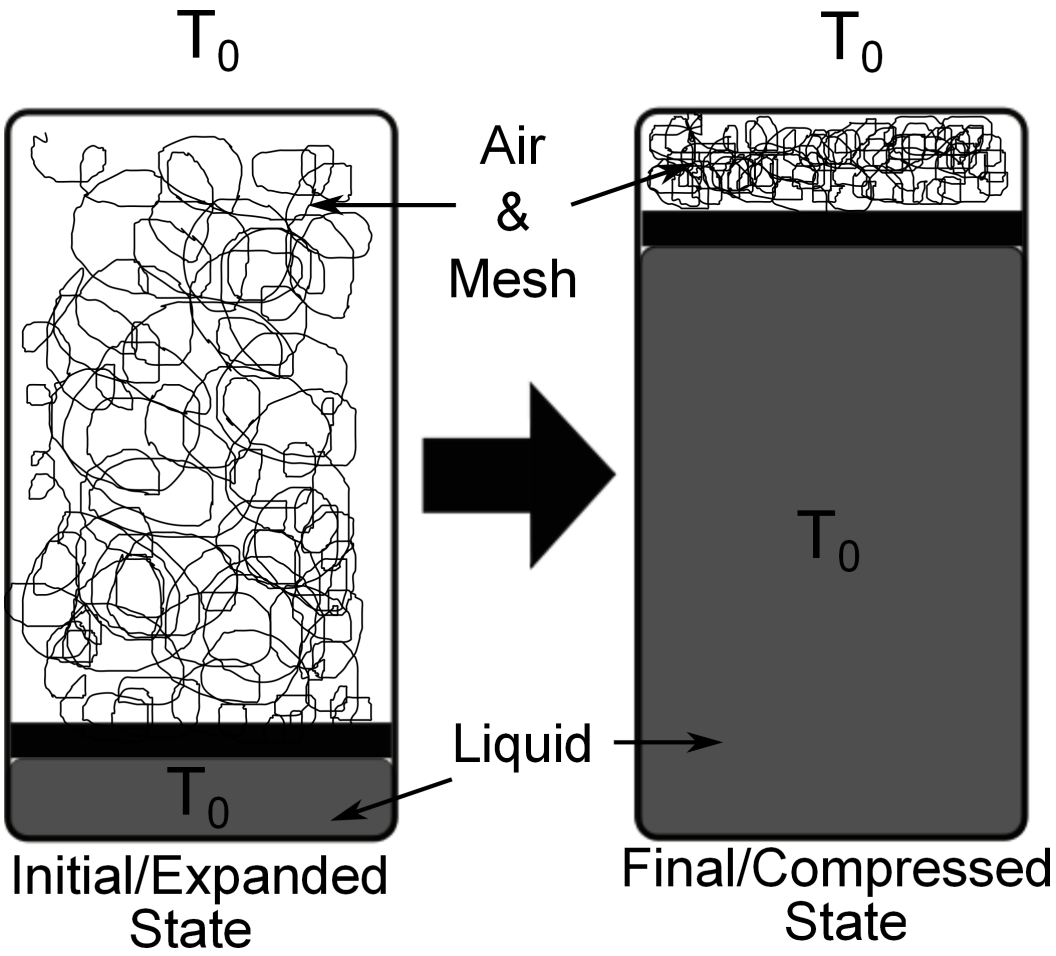

Figure 3.2: Air is compressed from initial (expanded) conditions, left, to final (compressed) conditions, right. During compression, heat transfer occurs between the heated air and the bounding surfaces plus mesh. The walls are at ambient temperature T_0. The mesh temperature varies in time. The mesh is confined between the piston and the endwall.

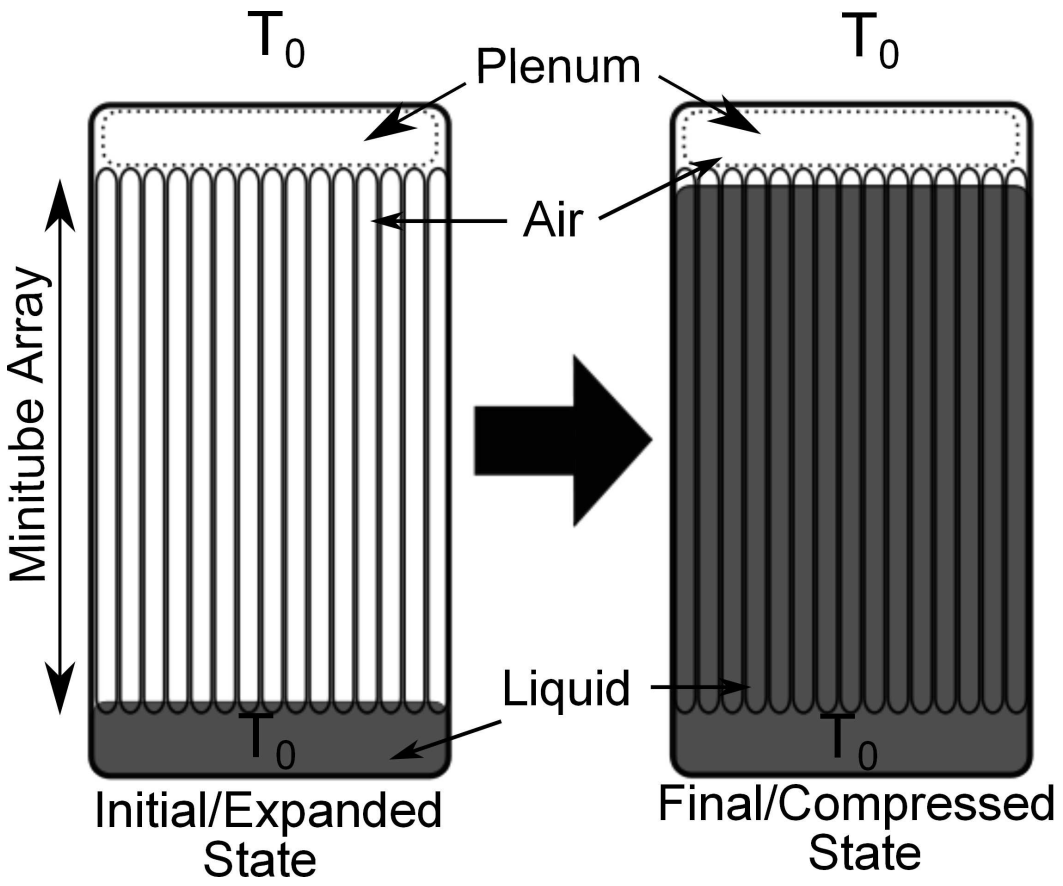

Figure 3.3: Air is compressed from initial (expanded) conditions, left, to final (compressed) conditions, right. During compression, heat transfer occurs between the heated air and the bounding surfaces plus minitubes. The walls are at ambient temperature T_0. The minitube temperature is allowed to vary with time. Water flows through the minitubes so the surface area of the minitube array is not constant in time.

During compression, work, W, is done on the air. Due to the applied work, the air is compressed and the internal energy of the air, U, increases. The increase in internal energy during compression depends on the heat transfer, Q, between the air and the heat sink. The relationship between work, internal energy, and heat transfer is guided by the first law of thermodynamics, discussed in detail in section 3.3.

Compression continues until the final pressure, P_c, is reached. The final pressure is related to the initial pressure by the pressure compression ratio:

$$r = \frac{P_c}{P_0}. \tag{3.1}$$

The final temperature and volume at this point are T_c and V_c, as shown in figure 3.1 (right side). In the open accumulator system, the compressed gas is next moved to storage in the accumulator, where it cools isobarically, returning to the ambient temperature. The assumption that the air has time to return to equilibrium with the environment before expansion is compatible with applications that require storage on the order of hours or longer, and is a conservative assumption in other cases. Further, it is assumed that the work required to move the gas between the compressor and accumulator is negligible, essentially bulk flow at constant volume and pressure. Thus, the total energy stored, E, is equivalent to the work required to compress the air from P_0 to P_c isothermally:

$$E \equiv nRT_0 \left[\ln(r) - 1 + \frac{1}{r} \right]. \tag{3.2}$$

Since the time-scales, and thus heat transfer, for isobaric cooling are not important to study, the experiments forgo that step. However, the heat loss associated with isobaric cooling is included in the definitions of work and efficiency.

During regeneration, the pressurized air expands from initial conditions P_c and T_0 to final pressure and temperature P_0 and T_e within an air motor (or air compressor run in reverse). Expansion will not be studied experimentally, but optimal expansion trajectories are discussed in the chapters 8–10.

As was mentioned, the air is compressed by adding liquid to the compression chamber. Thus, the height of the piston-air interface (which may be solid or a free surface) depends on the flow rate of liquid into the cylinder, $\dot{V}(t)$. This liquid piston system for compressing the air enables a variety of possible interface vs. time trajectories, as opposed to crank-type piston-in-cylinder compressors which only allow sinusoidal-shaped

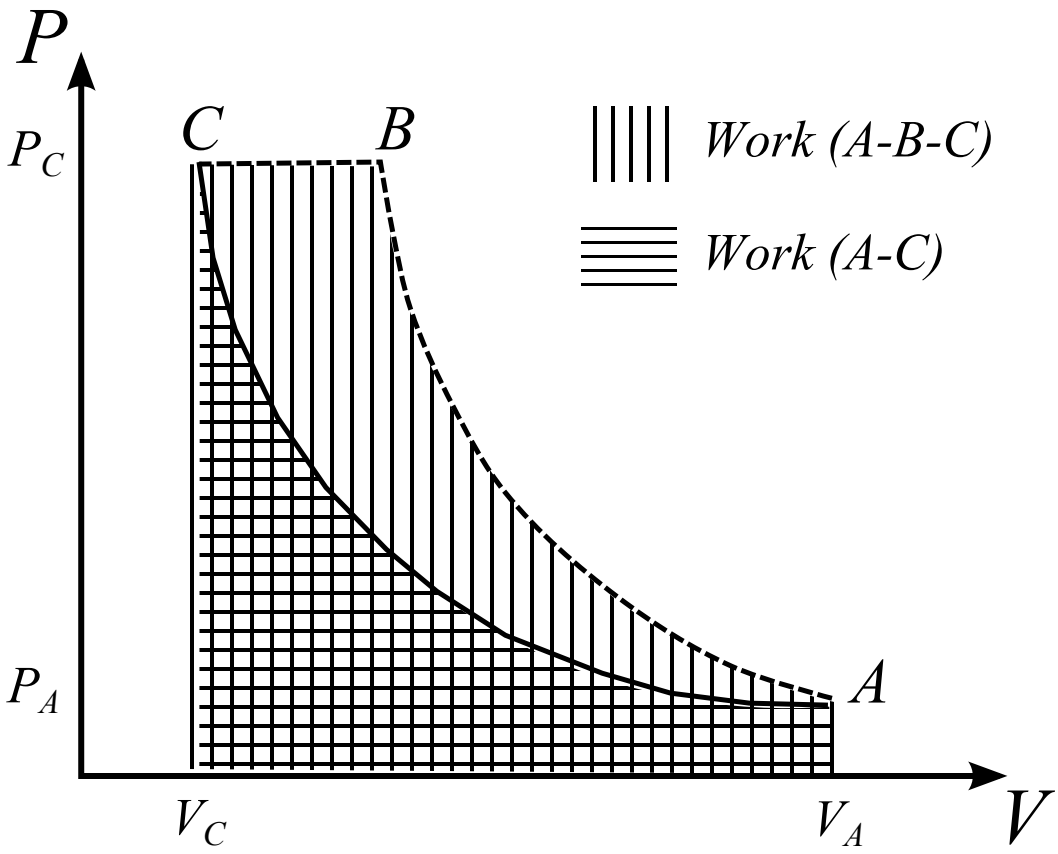

Figure 3.4: Compressing the air in different ways will require different amounts of work. In this example, compression along the dashed line will take more work than compressing along the solid line. This is evident on a P-V diagram by comparing the area under the curves.

trajectories. The pressure-volume curve corresponding to a interface-time trajectories determines the input work required to achieve that trajectory. The pressure-volume trajectory is an unambiguous description of the state of the gas throughout a compression or expansion process, assuming the gas is ideal. Such a process may be plotted in a pressure-volume (P-V) diagram. The area under the P-V curve is the work required to compress the air. Less work corresponds to greater efficiency. Consider the two compression processes in figure 3.4. Both cases start at state A and end at state B. The dashed curve represents a process consisting of fast adiabatic compression to the desired pressure, and then transitioning to isobaric compression at B. The solid curve represents near-isothermal compression from A to C. The relative work required for each process (i.e. the area under the curve) is immediately apparent from the PV diagram. The objective of chapters 8–10 is to discover the optimal pressure-volume compression trajectory.

3.2 Figure of merit

Let the time-dependent pressure-volume trajectory for compression be

$$\zeta_c(t) = (P(t), V(t))$$

and the time-dependent pressure-volume trajectory for expansion be

$$\zeta_e(t) = (P(t), V(t)).$$

The entire process can be mapped onto a P-V diagram as in figure 3.5.

For an arbitrary compression trajectory, ζ_c, the work required to compress the air from (P_0, T_0) to (P_c, T_c) to (P_c, T_0) is

$$W_{\text{in}}(\zeta_c) = -\int_0^{t_c} (P(t) - P_0)\dot{V}(t)\,\mathrm{d}t + nR(1 - 1/r)(T_c - T_0) \tag{3.3}$$

where t_c is the time it takes to compress the air from (P_0, T_0) to (P_c, T_c). The second term describes isobaric cooling from (P_c, T_c) to (P_c, T_0). Due to the heat up of the air during compression and subsequent cooling, W_{in} is larger than the change in stored energy, E, as revealed in figure 3.5.

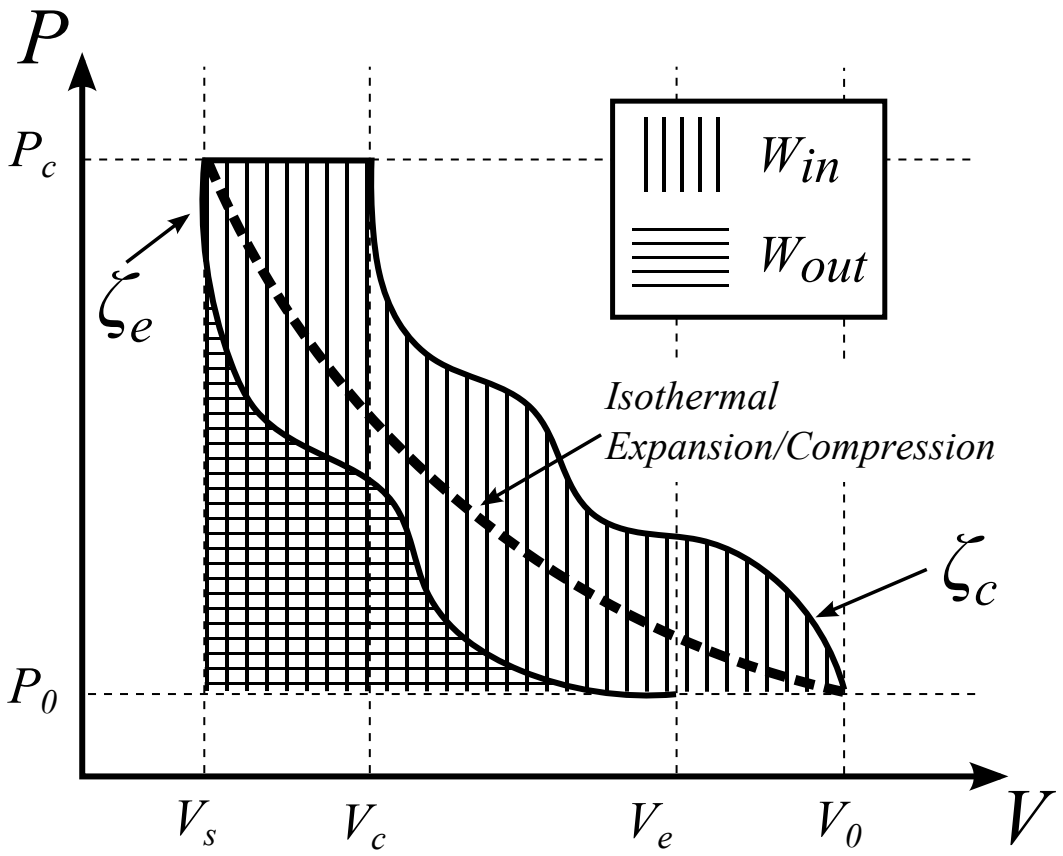

Figure 3.5: P-V diagram showing compression (ζ_c) and expansion (ζ_e) trajectories. The shaded area under the curves represent the work input (vertical lines) and work output (added horizontal lines). Isothermal compression and expansion follows the dashed black trajectory. The change in total energy stored is the area under the thick dashed isothermal curve. Reducing the area between ζ_c and the isothermal curve increases compression efficiency. Reducing the area between the isothermal curve and ζ_e increases expansion efficiency.

For an arbitrary expansion trajectory, ζ_e, the work provided when the air expands from (P_c, T_0) to (P_0, T_e) is

$$W_{\text{out}}(\zeta_e) = \int_0^{t_e} (P(t) - P_0)\dot{V}(t)\,\mathrm{d}t \tag{3.4}$$

where t_e is the expansion time and T_e is the temperature of the cold expanded air after compression. Due to the cooling of the air during expansion, W_{out} is less than the stored energy, E, as shown in figure 3.5. Work is nondimensionalized by E (from equation (3.2)) to obtain compression and expansion efficiencies:

$$\eta_c(\zeta_c) \equiv \frac{E}{W_{\text{in}}(\zeta_c)} \quad \text{and} \quad \eta_e(\zeta_e) \equiv \frac{W_{\text{out}}(\zeta_e)}{E}. \tag{3.5}$$

The overall energy efficiency would be

$$\eta_{overall}(\zeta_c, \zeta_e) \equiv \frac{W_{\text{out}}(\zeta_e)}{W_{\text{in}}(\zeta_c)} = \eta_c \eta_e. \tag{3.6}$$

The rate at which energy is stored or regenerated is the power. Since E represents the change in total energy stored and W_{out} represents the total energy regenerated, the compression power ("absorbed" power) and expansion power ("provided" power) are defined, respectively, as

$$\text{Pow}_c(\zeta_c) \equiv \frac{E}{t_c} \quad \text{and} \quad \text{Pow}_e(\zeta_e) \equiv \frac{W_{\text{out}}(\zeta_e)}{t_e}. \tag{3.7}$$

3.3 Governing equations

Physically, the *air-heat sink system* is described by the first law of thermodynamics. In general,

$$dU_{\text{air}} = \delta Q_{\text{to air}} - \delta W_{\text{by air}} \tag{3.8}$$

and

$$dU_{\text{sink}} = \delta Q_{\text{to sink}} - \delta W_{\text{by sink}} \tag{3.9}$$

where dU is the differential of internal energy of the system, δQ is an infinitesimal transfer of heat to the system, and δW is an infinitesimal amount of work done by the system. For closure, a function that relates air pressure, air temperature, and air volume (an equation of state) will be also be required. Generally, this is in the form

$$f\,(V, P, T) = 0. \tag{3.10}$$

The following section will consider appropriate assumptions for simplifying these equations and putting them in a form which is convenient to use.

3.3.1 Assumptions

- Ideal gas

  There are numerous equations of state for gases. These include the classic ideal gas law and Van der Waals equation of state, as well as more complex equations such as the PengRobinson equation of state [95]. The most simple of the equations of state, and thus the preferred option, is the ideal gas law:

  $$PV = nRT \tag{3.11}$$

  where P is absolute pressure, V is air volume, n is the quantity of air in moles, R is the universal gas constant, and T is the absolute temperature. The ideal gas assumption is appropriate for air at ambient conditions, but as the air temperature and pressure increase, the ideal gas approximation becomes increasingly inaccurate. Since changes in temperature and pressure are inherent in gas compression, the ideal gas assumption will eventually break down. The compressibility factor, Z, is a common means of quantifying the deviation of the ideal gas law from real gas behavior:

  $$Z = \frac{PV}{nRT} \tag{3.12}$$

  The further Z is from unity, the greater the discrepancy. For air, experimentally determined compressibility factors are provided in table 3.3.1. The temperatures and pressures in table 3.3.1 are representative of the values possible in the experiments to be discussed. As can be seen, the worst case deviation is only 0.34%. In fact, pressures must surpass 2 MPa (about 300 psi) before the deviation exceeds 1%. Thus, the ideal gas assumption for air is appropriate for the experiments to be discussed, and the ideal gas law provides the necessary equation of state.

  A second advantage of the ideal gas assumption is that the internal energy of air can now be described as a function of temperature alone, despite the fact that it is compressible:

  $$dU = nc_v dT \tag{3.13}$$

	P=0.1 MPa	P=0.5 MPa	P=1 MPa
T=300 K	0.9999	0.9987	0.9974
T=350 K	1.0000	1.0002	1.0004
T=400 K	1.0002	1.0012	1.0025
T=450 K	1.0003	1.0016	1.0034
T=500 K	1.0003	1.0020	1.0034

Table 3.1: Experimentally determined compressibility factors for air [1]

where n is the quantity of the gas in moles, c_v is the constant volume specific heat on a molar basis, and T is the air temperature. The specific heat, c_v, may be approximated as $5R/2$ to within 0.5% over the pressure range 0.1–1.0 MPa.

- Thermodynamically pure substances

  For simplicity it is assumed that any porous medium put into the chamber is a pure substance. For homogeneous, simple compressible substances that are invariable in composition, any thermodynamic state can be determined by at most two other thermodynamic states. So, the internal energy per mass, u, can be written as a function $u = u(v, T)$, where v is the volume per mass and T is the temperature. Therefore,

$$du = du(v, T) = \left(\frac{\partial u}{\partial v}\right)_T dv + \left(\frac{\partial u}{\partial T}\right)_v dT \tag{3.14}$$

  The constant volume specific heat is defined as

$$c_v = \left(\frac{\partial u}{\partial T}\right)_v . \tag{3.15}$$

  Therefore, for an incompressible substance ($dv = 0$), such as metallic porous media, the internal energy can be written as

$$du = c_v dT \tag{3.16}$$

  or

$$dU = mcdT \tag{3.17}$$

  where m is the mass and $c_v = c_p = c$ is the specific heat on a mass basis for incompressible substances.

- PV work only

  There are several different forces acting on the air, including the piston, friction due to flow along the walls, and gravity. For the compression of air, the piston does work on the air, while work must be expended to overcome friction and gravity. As a crude order-of-magnitude estimate, the total PV work for the experiment will be greater than (1e5 Pa)(1e-4 m^3)=10 J. The work due to friction is roughly (1e-5 kg/m-s)(1 m/s)(0.1 m^2)=1e-6 J. The work against gravity is (1 kg/m^3)(1e-4 m^3)(10 m/s^2)(1 m)=1e-3 J. This clearly demonstrates that for a simple model, only the PV work must be considered for the air. So,

  $$\delta W = PdV \tag{3.18}$$

  where P is the air pressure and V is the air volume.

- Uniform air pressure

  Pressure waves travel through air at the speed of sound, approximately 300 m/s at ambient temperature. In the experiments, the shortest compression event takes one second over a length of about 10 cm. This corresponds to 0.1 m/s, a velocity three orders of magnitude smaller than pressure wave velocity. To capture the gross behavior of the air, the temporal resolution must be high compared to the duration of the compression event, but three orders of magnitude is not necessary. Therefore, spatial variation in pressure during compression will not be noticed. Further, the pressure difference due to compression dominates the pressure variations driving the flow. These differences can be roughly estimated using the Bernoulli equation which says $\Delta P = \rho \frac{U^2}{2}$. For a density about 10 kg/m^3 and velocity an order of magnitude greater than the piston velocity, the pressure differences are about 500 Pa, which is less than 0.01% of the total pressure change due to compression. Therefore, pressure becomes essentially only a function of time.

- Uniform air temperature

  The temperature of the air is not uniform, in general. However, obtaining a spatially-distributed temperature field is a computationally expensive task and does not lend itself well to what purports to be a simple model. A small compromise is made using multi-zone models which typically divide the temperature

field into a core flow region and a 1D thermal boundary layer. However, the zone model doesn't account for mixing, and does not seem reasonable to implement when there is no true "core" flow as is the case when using porous media. Given these drawbacks, it is justifiable to forgo this option as well. Historically, the majority of engine cylinder heat transfer correlations have used some single bulk temperature, with adequate results [96]. Given the substantial simplifications offered by a single air temperature, and its general acceptance, this thesis makes this assumption as well, albeit with reservations. It is expected, of course, that in the proximity of walls and porous media, the air temperature will be somewhat less than the average air temperature. Similarly, the air temperature relatively far from cool surfaces is expected to be somewhat greater than the average air temperature.

- Uniform porous medium temperature

  The Biot modulus is a dimensionless number comparing the thermal resistance at the surface of a body to the thermal resistance inside the body. The Biot modulus is defined as

  $$\mathrm{Bi} = \frac{hL_C}{k} \tag{3.19}$$

  where h is the heat transfer coefficient, L_C is a characteristic length, and k is the thermal conductivity of the body. The characteristic length is commonly defined as the volume per surface area:

  $$L_C = \frac{V_{\mathrm{body}}}{A_{\mathrm{surface}}}. \tag{3.20}$$

  When the thermal resistance within a body is much less than that at the surface, the temperature of the body can be considered spatially uniform and so becomes a function of time only. The commonly cited threshold for a uniform temperature distribution is $\mathrm{Bi} < 0.1$. Both the mesh and the minitube array may be considered spatially uniform in temperature. For the mesh, the characteristic length is

  $$L_C = \frac{V_{\mathrm{mesh}}}{4V_{\mathrm{mesh}}/d_{\mathrm{strand}}} = \frac{d_{\mathrm{strand}}}{4} \tag{3.21}$$

  where V_{mesh} is the volume of the mesh, d_{strand} is the diameter of an individual strand of the mesh, typically around 0.08 mm. The mesh is aluminum, with a

thermal conductivity of 250 W/m-K. To satisfy bulk temperature conditions,

$$\text{Bi} = \frac{h d_{\text{strand}}}{4k} < 0.1 \quad \text{or} \quad h < \frac{4k}{10 d_{\text{strand}}} = 125000. \tag{3.22}$$

It can be safely assumed that h is less than 125 kW/m^2-K, so the lumped temperature assumption is valid for the mesh.

For the minitube array, the characteristic length is

$$L_C = \frac{\pi/4 \left([OD]^2 - [ID]^2 \right)}{\pi \left([OD] + [ID] \right)} = \frac{[OD] - [ID]}{4} \tag{3.23}$$

where $[OD]$ is outer diameter and $[ID]$ is the inner diameter of an individual minitube. In the experiment, the minitube wall thickness, t_{minitube}, is 0.8 mm. The minitubes are copper, with a thermal conductivity of 339 W/m-K. To satisfy bulk temperature conditions,

$$\text{Bi} = \frac{h t_{\text{wall}}}{2k} < 0.1 \quad \text{or} \quad h < \frac{2k}{10 t_{\text{wall}}} = 84750. \tag{3.24}$$

Again, the heat transfer coefficient will not be as high as 84 kW/m^2-K, so the lumped temperature assumption is valid for the minitube array.

- Isothermal compression cylinder walls

  The walls of the compression cylinder are exposed to the ambient on their outer surface and the heated air on their inner surface. The cylinder wall thickness, t_{cylinder}, is 0.32 cm (0.125 inches). The compression cylinder is polycarbonate with a thermal conductivity of 0.2 W/m-k. Again using the Biot modulus, in order for the walls to be uniform temperature,

$$\text{Bi} = \frac{h t_{\text{cylinder}}}{2k} < 0.1 \quad \text{(or)} \quad h < \frac{2k}{10 t_{\text{cylinder}}} = 0.13. \tag{3.25}$$

  This is much lower than the expected values of h, so it is seen that the compression cylinder will see thermal gradients within its polycarbonate walls. Unfortunately, modeling the temperature distribution in the polycarbonate wall requires coupling an additional equation to the governing equations. Furthermore, this equation must be a partial differential equation since the spatial distribution of temperature in the polycarbonate is not uniform. Coupling this PDE into the existing set of

equations leads to much more complexity than this model warrants. Therefore, the compression cylinder walls will be assumed isothermal. The endwall and piston interface (or water interface, where applicable) are also assumed isothermal, for the same reason. Thus, the bounding surfaces of the compressed air, minus the porous insert, become, in essence, an infinite thermal capacity heat sink.

What is the effect of assuming isothermal walls? For nearly adiabatic compression, probably very little, since there will be little heat transfer. Similarly, when the porous medium is inserted into the air space, the thermal capacitance of the porous medium will hold the air temperature rise, and thus, the air to polycarbonate temperature difference, to a minimum. The porous medium becomes the primary heat sink. As more surface area and thermal capacitance is added, the isothermal wall assumption becomes less significant. The greatest errors will be seen with no porous media. Values of h calculated from measured heat fluxes and temperature differences, assuming a isothermal wall, will be artificially small. However, predictions of the heat flux based on this model will be artificially large. Future modeling efforts striving for greater accuracy should take the wall radial temperature gradient into account or use a wall made of a high-conductivity material.

- No Radiative Heat Transfer

  During compression, heat transfer occurs primarily through forced convection as the heated flow transfers heat to the walls. Radiative heat transfer also contributes to the total heat transfer but this contribution is small. Generally, in heat transfer studies in internal combustion engines, radiative heat transfer is ignored during compression, but included during combustion where it may contribute as much as 10% of the heat transfer [96].

- Newton's Cooling Law

  Convective heat transfer rates are often described using a heat transfer coefficient. The heat transfer coefficient, h, is defined as

$$h = \frac{q}{A\left(T_{\text{sink}} - T\right)} \tag{3.26}$$

  where q is the heat transfer rate from the sink to the air, A is the surface area

available for heat transfer, T_{sink} is the temperature of the heat sink (or source), and T is the temperature of the air. Several researchers (e.g. [32][47]) have observed a phase shift between the temperature difference and heat transfer under transient situations. In correlations for engine heat transfer, this phase shift is usually modeled as a function of the instantaneous volume change, $\dot{V}$, which, for the 3000 rpm engine, will be much greater than that of a compressor operating at 30 to 60 rpm. Therefore, there is some question as to whether the phase shift is important at the much slower speeds of the present study. Kornhauser and Smith [33] observed that for low oscillating Peclet number ($10 < \text{Pe}_\omega < 100$), the phase shift was very small and Newton's law of cooling dominates. The Peclet numbers (based on frequency, diameter, and thermal diffusivity) for the experiments presented herein are less than 71, where the cycle time is set to twice the compression time and a estimate of the average thermal diffusivity of air is used. The low Peclet numbers suggest that no unsteady term is required to model the heat transfer using the experimental conditions.

Using these assumptions, equations 3.8 and 3.9 are simplified to

$$nc_v\dot{T} = q_{\text{to air}} - P\dot{V} \tag{3.27}$$

$$mc\dot{T}_{\text{sink}} = q_{\text{to sink}} \tag{3.28}$$

$$PV = nRT \tag{3.29}$$

where the heat transfer rate, q, describes Newtonian convective heat transfer between the air, the porous medium, and the wall. The specific formulations for q will now be investigated for each experiment

3.4 Modeling heat transfer

Given the assumptions above, modeling the heat transfer becomes an issue of determining the heat transfer coefficient, h, and surface area, A, in equation 3.26. This can be done based on empirical or theoretical reasoning.

3.4.1 Mesh experiments

Surface area

To estimate the surface area of the mesh, several strands were randomly selected from the mesh to be used in the experiments. The mean diameter, D_{strand}, was found to be approximately 80 microns. Assuming that the strands have a circular cross-section with typical diameter of 80 microns, the surface area is estimated to be

$$A_{\text{mesh}} = \pi D_{\text{strand}} \frac{V_{\text{mesh}}}{\pi D_{\text{strand}}^2/4} = \frac{4V_{\text{mesh}}}{D_{\text{strand}}}. \tag{3.30}$$

The surface area of the mesh is constant, since it is confined between the piston and the endwall. The surface area of the wall is determined from the air volume:

$$A_{\text{wall}} = \frac{4\left(V - V_{\text{dead}} + V_{\text{mesh}}\right)}{d} + \frac{\pi d^2}{2}. \tag{3.31}$$

The dead volume V_{dead}, refers to any air volume not contained within the cylindrically-shaped chamber, e.g. due to valving, etc. Strictly speaking, the surface area of the dead volume should be included in equation (3.31), however in many cases, such as the experiments described herein, this area is negligible. The dominant term for most of the compression event is the first term in equation (3.31), the area of the side wall. However, as the piston approaches top dead center, the dominant term becomes the second term in equation (3.31), the area of the two end walls.

Heat transfer coefficient

A "first cut" model might use a constant h. The experimental results, to be discussed later, show this to be a good approximation. Further improvements to the heat transfer model for this setup are deemed unnecessary due to a) the good fit afforded by the constant-h model, and b) the limited utility of the mesh experiments, which, because of the very low compression speeds, do not warrant extensive study.

Heat transfer in the mesh experiments

The complete heat transfer rate for the air system is

$$q = -hA_{\text{wall}}\left(T - T_{\text{wall}}\right) - hA_{\text{mesh}}\left(T - T_{\text{mesh}}\right) \tag{3.32}$$

where A_{wall} is the instantaneous wall area (equation (3.31)) and A_{mesh} is the surface area of the mesh (equation (3.30)). The value of h is constant, as discussed, and equal for both heat transfer to the mesh and to the wall. This is a simplifying assumption that seems to work well in practice. Equation (3.32) should be substituted into equation (3.27).

The complete heat transfer rate for the mesh is

$$q = hA_{\text{mesh}} \left(T - T_{\text{mesh}}\right). \tag{3.33}$$

It is assumed that no heat transfer occurs between the wall and the mesh. Although they are in contact during the course of the compression event, the contact is poor and little conduction will occur. Equation (3.33) should be substituted into equation (3.28). For the case with no mesh insert, A_{mesh} is zero, so only equation (3.32) will be used.

3.4.2 Minitube array experiments: no minitube array

As with mesh experiments, the minitube array experimental program is divided into two parts: tests with and without the porous media. Unlike the mesh experiments, the two situations with and without the minitubes are expected to be very dissimilar from geometrical and heat transfer perspectives. These two cases are treated separately.

Surface area

The only heat sink area is the bounding surfaces. As with the mesh experiments, the heat transfer area is described in terms of air volume using equations (3.31).

Heat transfer coefficient

Without the cylinder array insert, the water piston is similar in geometry to some engine cylinders (about 51 mm diameter by 120 mm stroke). As discussed in the introduction, engine heat transfer has been been studied early and often. Many empirical correlations have been suggested. The correlation by Hohenberg [28], based on the well-known Woschni correlation, was found to capture the essence of the data as well as any. The Hohenberg correlation is

$$h = C_1 V^{-0.06} \left(\frac{P}{100000}\right)^{0.8} T^{-0.4} \left(U + C_2\right)^{0.8} \tag{3.34}$$

where C_1 and C_2 are parameters that must be tuned for the particular engine. Hohenberg found that the values of 130 and 1.4, respectively, generally gave good results.

Heat transfer for the empty compression chamber

The complete heat transfer rate is

$$q = -hA_{\text{wall}}\left(T - T_{\text{wall}}\right) \tag{3.35}$$

where A_{wall} is the instantaneous wall area (equation (3.31)) h is from Hohenberg's correlation (equation (3.34)). Equation (3.35) should be substituted into equation (3.27).

3.4.3 Minitube array experiments: with minitube array

When the minitube array is used, there are two distinct regions. First, there is the minitube array. Second, since the minitube array does not extend to the cap, there is a plenum. Within the plenum, the flow field is expected to be turbulent. Within the minitube array the flow field is expected to be laminar. Further, there are several different channels through the minitube array. Due to the very different hydraulic diameters, these channels will be grouped into three representative sizes and shapes. Thus, there are four values of the heat transfer coefficient that are of interest. First, the heat transfer coefficient between air and the inner surface of each minitube. Second, the heat transfer coefficient between air and the outer surface of each minitube. Third, the heat transfer coefficient between the air and the chamber wall. Fourth, the heat transfer coefficient between the air and the cap or plenum wall. These will be referred to as h_{inner}, h_{outer}, h_{wall}, and h_{plenum}. The associated surface areas are A_{inner}, A_{outer}, A_{wall}, and A_{plenum}

Surface Area

The surface area of the plenum (the volume between the end wall and the top of the minitube array as in figure 3.3) is

$$A_{\text{plenum}} = \pi d\delta + \frac{\pi d^2}{2} \tag{3.36}$$

where δ is the height of the plenum. The surface area of the wall along the minitube array is

$$A_{\text{wall}} = \pi d\,(z - \delta) \tag{3.37}$$

where z is the distance between the interface of the water and the endwall. The outer surface area of the minitubes is

$$A_{\text{outer}} = N\pi[OD]\,(z - \delta) \tag{3.38}$$

where N is the number of minitubes. The inner surface area of the minitubes is

$$A_{\text{inner}} = N\pi[ID]\,(z - \delta)\,. \tag{3.39}$$

The water does not exceed the height of the minitube array, assuming the interface rises at the same rate throughout the cross section of the minitube array. If a higher pressure ratio is used, such that the water interface exceeds the height of the minitubes, i.e. $z < \delta$, then the equations for the surface area will have to take that into account.

Heat transfer coefficient

As with the empty compression cylinder, the Hohenberg correlation will be used to model the heat transfer in the plenum. Although the shape of the plenum is not very similar to the empty cylinder, the overall heat transfer should be largely insensitive to the heat transfer within the plenum because of the relatively small surface areas and large hydraulic diameter. So, the value of h_{plenum} is determined by Hohenberg's correlation, given in equation (3.34).

As mentioned already, within the narrow confines of the minitube array the flow field is expected to be laminar. Appendix B lays out a calculation validating this claim. Since water is flowing through the channels, an internal channel flow heat transfer model seems appropriate. There are several obvious differences between channel flow and the compression event occurring in a minitube, however, there is a precedent for using this model, e.g. [16][97]. The pipe flow model is more applicable in the present work than for the works just cited due to the presence of the large plenum at the end of the minitubes. This situation much more closely resembles flow through a pipe than the case in which the minitube is capped at the end, because without the plenum, the air at the end of the pipe is stagnant.

If the flow through the channels can be considered fully developed, then the very simple fully-developed laminar pipe flow correlation may be used. By "fully developed," it is meant that both the velocity and temperature profiles are invariant with position. Since the present work concerns compression in addition to flow through a channel, this definition is not directly applicable. However, lacking an equivalent for a compression problem, the hydrodynamic entry length criterion for laminar flow in a circular pipe will be used. The entry length is roughly

$$x = \frac{\mathrm{Re} D_h}{20} \tag{3.40}$$

where x is the distance from the entrance to the pipe and Re is the Reynolds number. The Reynolds number for flow through a channel is

$$\mathrm{Re} = \frac{\rho U D_h}{\mu} \tag{3.41}$$

where ρ is the density, U is the air velocity, D_h is the hydraulic diameter, and μ is the dynamic viscosity. Using the initial Reynolds number of 34 from above and the inner diameter of the small copper tubes, the entry length is less than 3 mm, which is 1% of the total length of the cylinder array. The thermal entry length, assuming hydrodynamically fully-developed flow, is typically

$$x = \frac{\mathrm{Pr}\mathrm{Re} D_h}{20} \tag{3.42}$$

where Pr is the Prandtl number. For air, this is about 0.7 over the range of temperatures expected in the experiment. Again using the initial Reynolds number of 34 and diameter of 1.55 mm, the entry length is less than 2 mm. The combined entry length should be no longer than 5 mm, less than 2% of the total length, for the flow through the inner diameters of the minitubes. Through the channels with a smaller hydraulic diameter, the entry length is expected to be shorter. With larger hydraulic diameters, it is expected to be somewhat longer, although likely never exceeding 10% of the total length. Therefore, the fully-developed laminar flow assumptions are appropriate, and the heat transfer may be modeled as such.

The analytical solution for the heat transfer coefficient in a cylindrical smooth pipe of inner diameter $[ID]$ with fully-developed laminar flow and with constant temperature walls is

$$h_{\mathrm{inner}} = \mathrm{Nu}\frac{k}{[ID]} \qquad \text{with Nu} = 3.657 \tag{3.43}$$

where k is the thermal conductivity of air and Nu is the Nusselt number. For a pipe with non-circular cross section, the constant Nusselt number is somewhat different. The interstitial spaces are approximately triangular. For pipes with the cross section of an equilateral triangular, the heat transfer coefficient is

$$h_{\text{outer}} = \text{Nu}\frac{k}{D_h} \qquad \text{with Nu} = 2.59. \tag{3.44}$$

The spaces between the cylinders and the wall are also approximately triangular. So, around the circumference of the minitube array, the heat transfer coefficient to the chamber wall is

$$h_{\text{wall}} = \text{Nu}\frac{k}{D_h} \qquad \text{with Nu} = 2.59. \tag{3.45}$$

In all three cases, it is assumed that the heat transfer surface (i.e. the cylinder array or chamber wall) is at a constant, uniform temperature. This is a good assumption, as will be seen in the results section, because the cylinder array has a huge thermal capacitance relative to the air and does not change in temperature by more than a fraction of a degree.

Heat transfer in the minitube array experiments

The complete heat transfer rate for the air system using the values for h, above, is

$$\begin{aligned} q = &-h_{\text{wall}}A_{\text{wall}}\left(T - T_{\text{wall}}\right) - Nh_{\text{inner}}A_{\text{inner}}\left(T - T_{\text{minitube}}\right) \\ &- Nh_{\text{outer}}A_{\text{outer}}\left(T - T_{\text{minitube}}\right) - h_{\text{plenum}}A_{\text{plenum}}\left(T - T_{\text{wall}}\right) \end{aligned} \tag{3.46}$$

where N is the number of minitubes, h_{wall} and A_{wall} are the heat transfer coefficient and instantaneous exposed wall area (equations (3.45) and (3.37)), h_{wall} and A_{inner} are the heat transfer coefficient and the instantaneous exposed surface area of the inside of a minitube (equations (3.43) and (3.39)), h_{wall} and A_{outer} are the heat transfer coefficient and the instantaneous exposed surface area of the outside of a minitube (equations (3.44) and (3.38)), and h_{wall} and A_{plenum} are the heat transfer coefficient and the instantaneous exposed surface area of the plenum region (equations (3.34) and (3.36)). Equation (3.46) should be substituted into equation (3.27).

The complete heat transfer rate for the minitube array using the values for h, above, is

$$q = Nh_{\text{inner}}A_{\text{inner}}\left(T - T_{\text{minitube}}\right) + Nh_{\text{outer}}A_{\text{outer}}\left(T - T_{\text{minitube}}\right) \tag{3.47}$$

where A_{inner} is the instantaneous exposed surface area of the inside of a minitube and A_{outer} is the instantaneous exposed surface area of the outside of a minitube. It is assumed that no heat transfer occurs between the wall and the minitubes because of the poor thermal contact. Equation (3.47) should be substituted into equation (3.28).

Chapter 4

Test facilities

4.1 Mesh experiments

4.1.1 Apparatus

The hydraulic circuit for the compressor prototype is shown in figure 4.1 and photographs 4.2 and 4.3. It consists of a reservoir, a tandem piston-in-cylinder arrangement compression chamber, two pumps, two valves, volume and pressure instrumentation, and peripheral power and circuitry. Two pumps are used for flexibility in controlling the compression trajectory. One pump provides lower flow rates, and one provides higher flow rates. The low flow rate pump is a fixed displacement Parker OilDyne miniature piston pump. The other pump is a Haldex G. C. series gear pump with a fixed displacement that is forty times greater than the OilDyne pump. The 4-3 directional control valve is an electrically-controlled Vickers DG4V-3 valve from Eaton. The state of the 4-3 directional valve determines whether the piston is compressing, retracting, or stationary (in which case the oil returns directly the the reservoir). The electrically-controlled 3-2 valve is from Hydraulic Controls, Inc. part number 4WE6D6X/EG12N9Z5L. As can be seen in the circuit drawing (figure 4.1), the 3-2 valve allows flow from the high-flow Haldex pump to by-pass the compressor. This provides a means to achieve slow compression.

Compression is accomplished by means of dual piston-in-cylinder arrangements extending from opposite faces of an aluminum mount as in figure 4.4. For the purposes

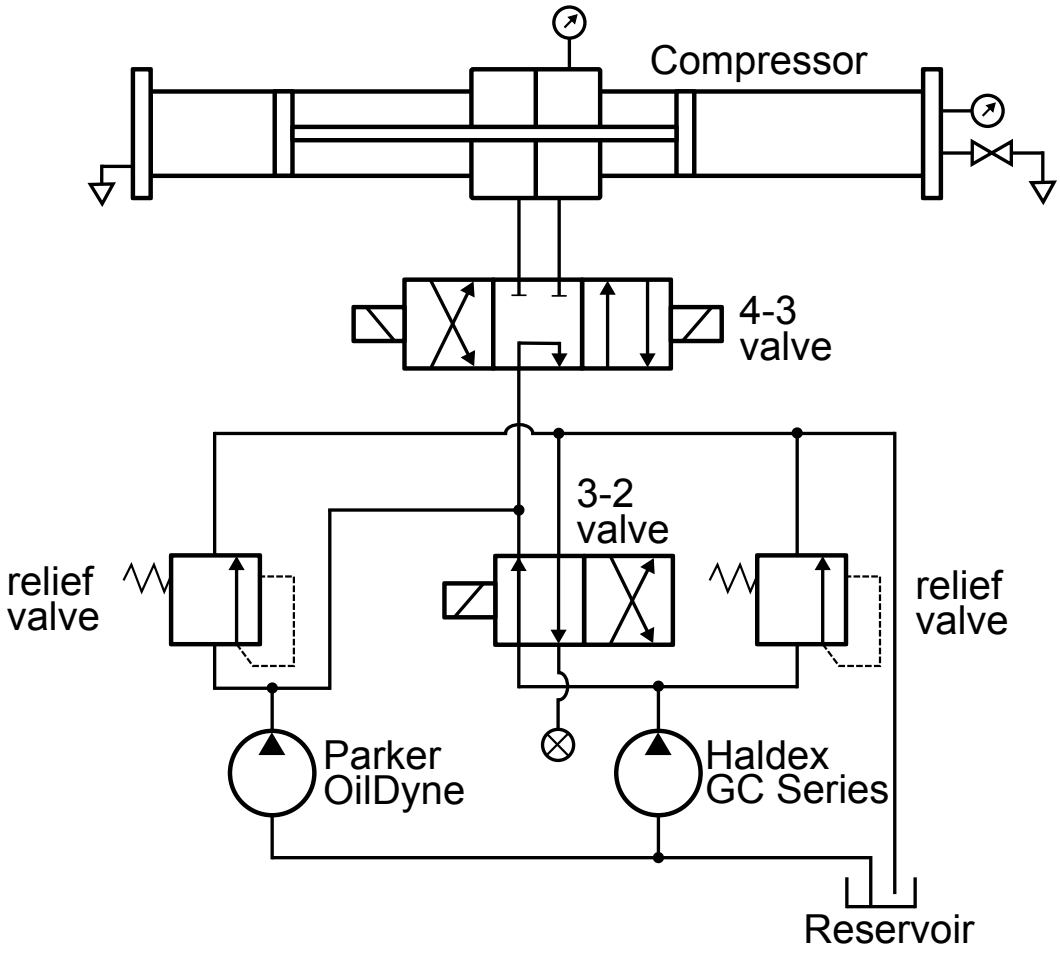

Figure 4.1: The hydraulic circuit for the low-power porous mesh experimental program.

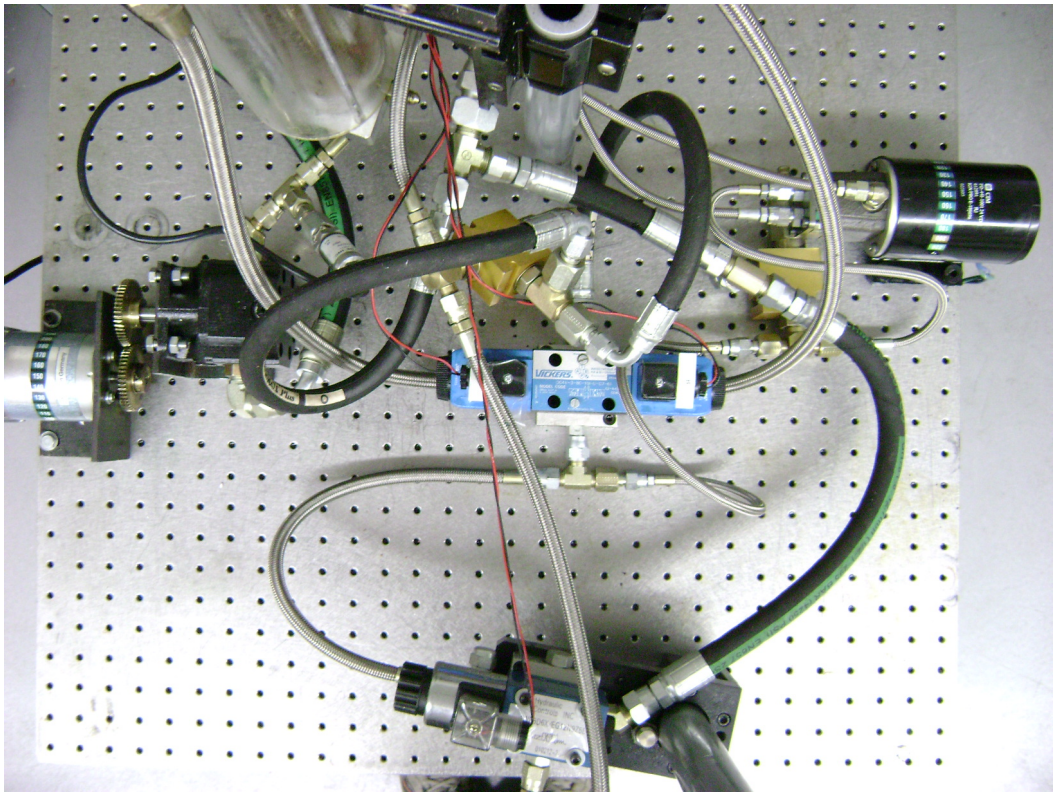

Figure 4.2: A photograph of the hydraulic circuit of figure 4.1. The MicroMo motor and black Haldex pump are at the left hand side of the photo. At the bottom of the photo is the 3-2 valve. The blue 4-3 valve is in the center. The black Oildyne pump is on the right. The very bottom of the compression cylinder can be seen at the top of the photo. The reservoir is off-screen at the top.

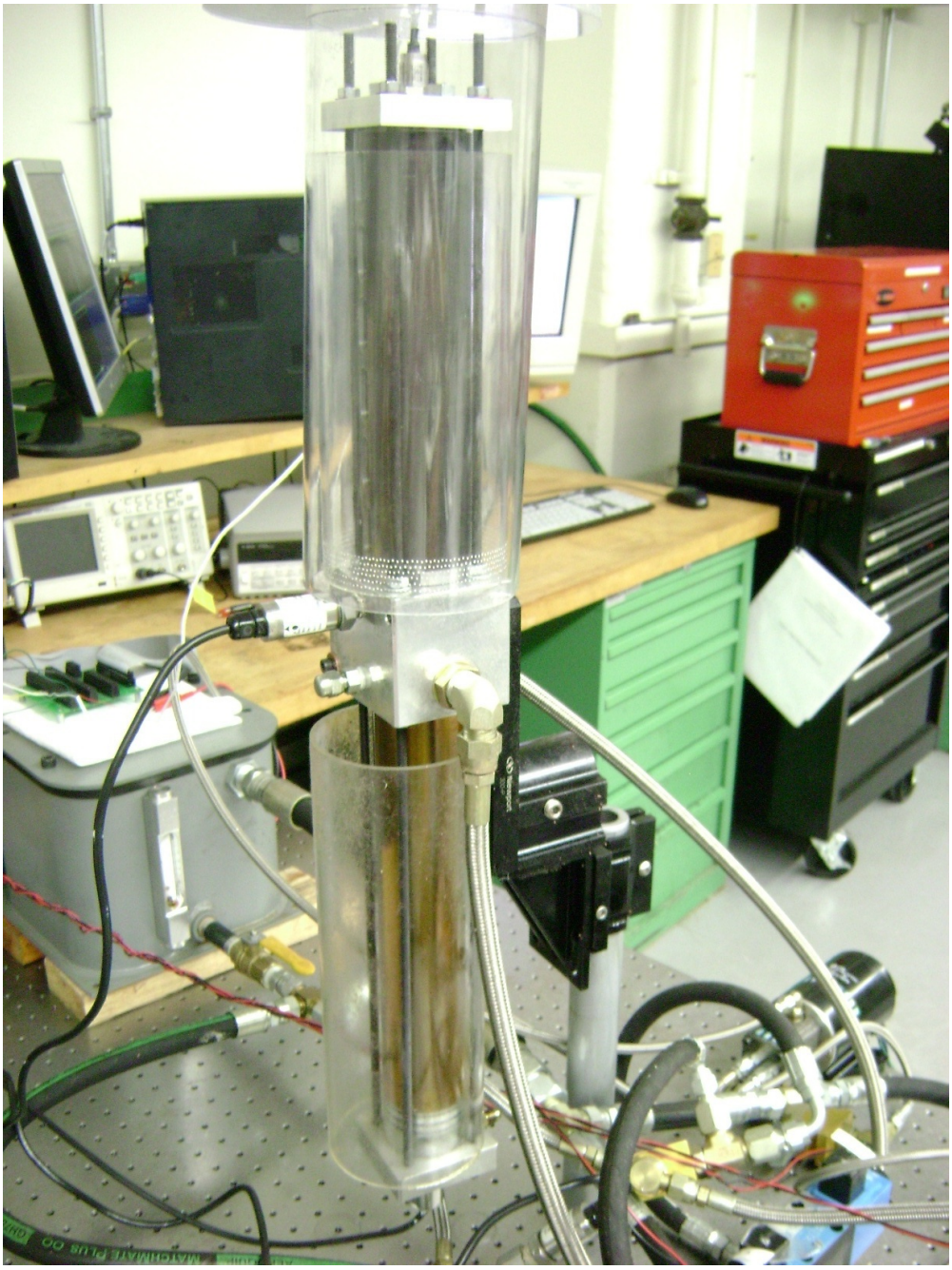

Figure 4.3: A photograph of the tandem piston (foreground) and reservoir (background, left). The Oildyne pump is in the bottom right corner. Additional polycarbonate shielding encases the compressor for safety.

of description, let one arrangement be called the A side and the other be the B side. Pistons A and B are connected by a rod that passes through the aluminum mount. Seals in the mount create two separated chambers: one between piston A and the mount and one between piston B and the mount. Each chamber has a port connected to the 4-3 directional flow valve. In one of the valve states, oil is pumped into chamber A, forcing piston A to move toward the cap. Since the piston B is rigidly connected to piston A, it too will move, but it will be pulled toward the mount. Oil in chamber B is forced to evacuate through port B. Thus compression of the air between piston A and the end cap is accomplished. Changing the state of the 4-3 valve changes the direction of the flow of oil, so that oil is pumped into chamber B. This pushes piston B away from the mount, and pulls piston A toward the mount, allowing the air in cylinder A to expand. The experimental facility only effected compression and expansion in cylinder A, which will be called the compression cylinder.

The compression cylinder was cut from a length of extruded polycarbonate tubing. A second cylinder of the same inner and outer diameter is located between the mount and the lower end cap. The upper cylinder is clad in the steel "exoskeleton." During operation, a polycarbonate shield is placed around the chamber for added safety as in figure 4.3.

The porous medium utilized in the mesh experiments is fine-grade, rustless, aluminum wool. Two meshes were molded, as shown in figure 4.6. The masses were determined to be 1.70 g for the smaller mesh and 5.48 g for the larger mesh. Since the mesh is made of aluminum, which has a known density of 2700 kg/m^3, the volume was calculated to be 0.63 cc for the smaller mesh and 2.03 cc for the larger mesh. The surface area of the small mesh, calculated from equation (3.30), is on the order of 300 cm^2. The surface area of the larger mesh is on the order of 1000 cm^2. Porosity, ϵ, is defined as the ratio of air volume to total volume:

$$\epsilon = \frac{V_{\text{air}}}{V_{\text{total}}}. \tag{4.1}$$

The initial porosity of the smaller mesh is almost 99.9%. The initial porosity for the large mesh is about 99.5%. It should be noted that the porosity is not uniformly distributed over the air volume. The wire mesh (especially the smaller mesh) is concentrated along the cylinder axis, the core region. This is advantageous because the core is (by definition)

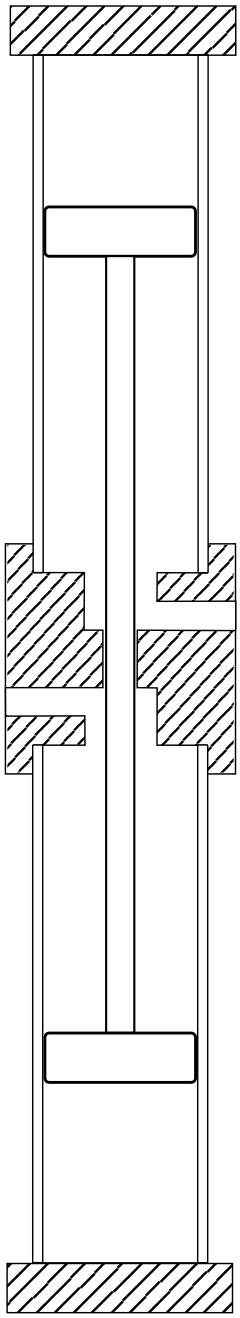

Figure 4.4: A diagram (not to scale) of the tandem piston-in-cylinder compressor for the low-power porous mesh experimental program.

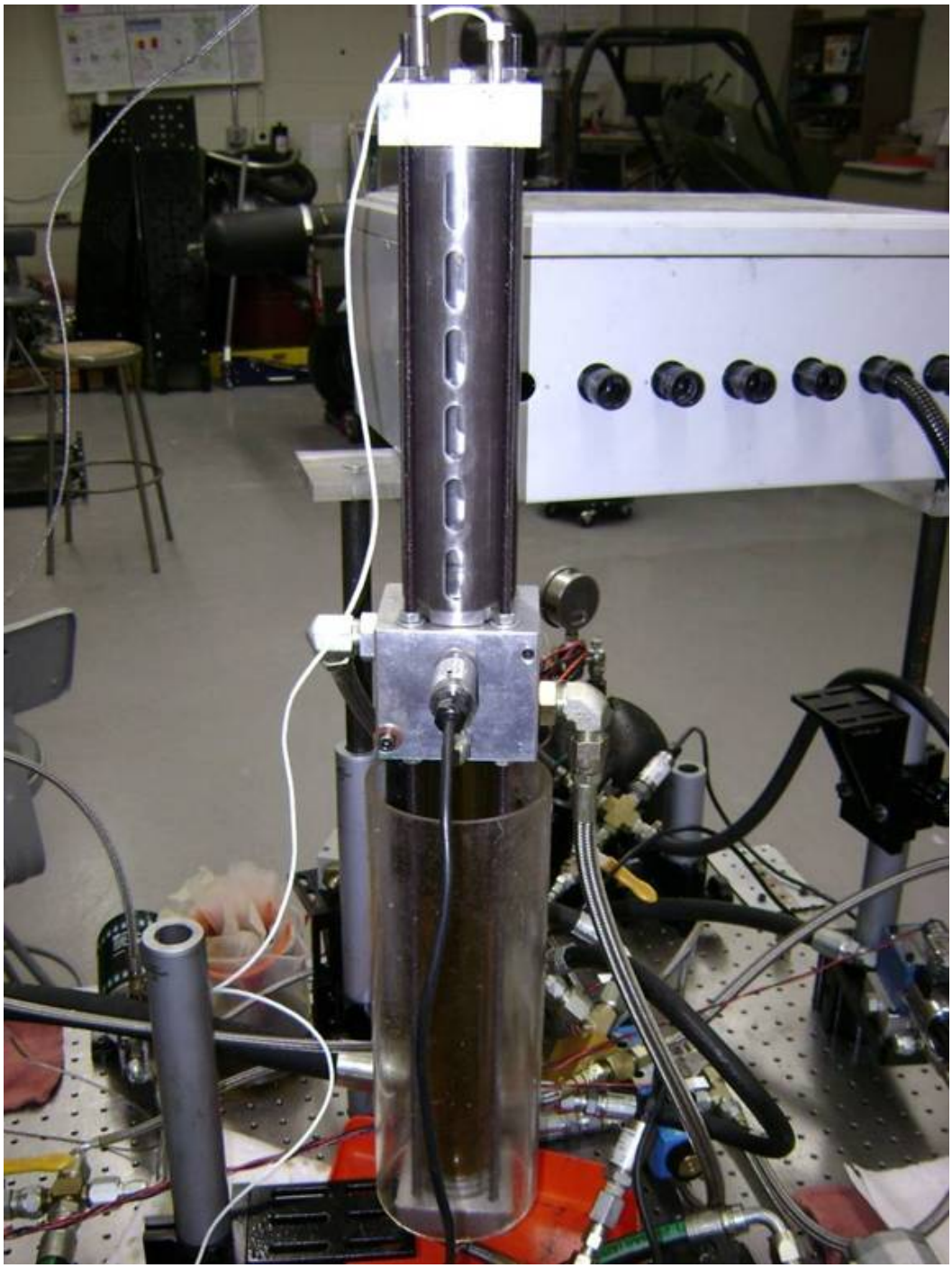

Figure 4.5: A photograph of the tandem piston-in-cylinder compressor for the low-power porous mesh experimental program.

outside the thermal boundary layer.

Figure 4.6: A photograph of the two meshes used in the low-power, dual-pump solid-piston experiments.

4.1.2 Instrumentation

A Kulite ETM-375 pressure transducer was set into the end cap for measuring the air pressure shown in figure 4.7. The sensing element was placed flush with the surface of the end cap. An Omega PX309 series pressure transducer was attached to the aluminum mount to measure the oil pressure. An MTS Tempsonics C-Series core sensor is used to obtain the linear position of the piston, which was calibrated to measure the air volume. Again, more details may be found in appendix C.

Several attempts were made to measure the air temperature by gluing thermocouples into holes drilled through a polycarbonate cap, but they proved unsuccessful. A

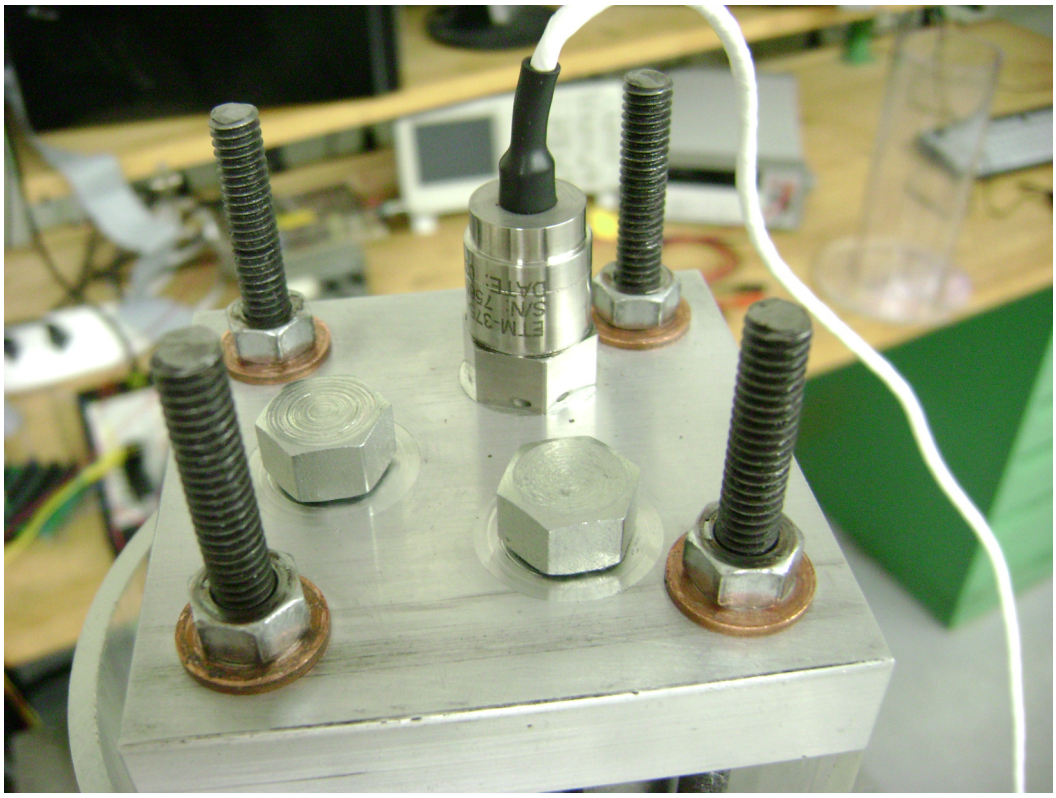

Figure 4.7: A photograph of the end cap. The Kulite pressure sensor is inserted into the top of the cap. Two other ports may be used for thermocouples or to replenish fresh air.

successful reading of the core temperature requires adequate distance between the thermocouple junction and any solid surface to avoid the thermal boundary layer and to minimize conduction error in the thermocouple. However, care must be taken that the piston does not hit the thermocouple at the end of the stroke. Also, in order for the thermocouple to follow the transient compression event, a very thin thermocouple is required. The response from wires 0.254 mm (0.010 inch) seemed sluggish, so very fine 0.025 mm (0.001 inch) wire was tried. However, thin thermocouples are very delicate and sharing the airspace with the porous mesh would inevitably destroy the thermocouple. The use of sacrificial thermocouples was discussed; that is, a thermocouple simply takes measurements until its certain demise. However, the process of drilling holes in the cap and gluing in thermocouples is tedious and encourages air leaks. It was decided that even if temperature data were acquired, the data would be local to the thermocouple junction. Thus, comparisons for validation purposes with calculated or modeled volume-average temperatures would be difficult. It should be mentioned that some successful thermocouple data were taken using the very fine thermocouples for the empty compression chamber (no mesh) and a compression ratio of about 7. The thermocouple junction was located about 2.5 cm away from the cap and near the axis of the compression chamber. These results are provided in appendix D.

For system testing, trouble-shooting, and general investigation, an Agilent 34401A 6.5 digit multimeter and a Tektronix TDS1001B Two-Channel Digital Storage Oscilloscope were used.

4.1.3 Control, data acquisition, and data processing

Control of the compressor was effected through the Mathworks programs Simulink version 7.1 (R2008a) and xPC Target. Simulink allows the modeling of systems as virtual block diagrams. Real-time interaction with the prototype hardware is enabled through xPC Target. A 16-bit PCI-DAS1602/16 multifunction analog and digital I/O board is used to acquire and digitize data. The digital outputs of the board control the states of the valves. Each analog output is sent to an H-bridge associated with a power supply and a variable-speed motor. The H-bridge scales the high voltages from the power supplies with the small voltage signal from the computer. This allows the speed of the motors to be controlled. The valve logic and motor speeds are controlled in Simulink.

A proportional-integral controller was designed and implemented to track the specified volume trajectory.

Data processing and plotting occurs in Matlab version 7.6.0 (R2008a). Matlab and Simulink were run on a Compaq Presario SR2010NX with an AMD Sempron processor 3400+ and 512 MB memory. Pressure and volume data were digitally filtered using a first-order transfer function with a 10 Hz cutoff frequency. Pressure, volume, temperature (when applicable), valve states, motor inputs, target and actual oil flow rates and run time were saved for each recorded time step.

The air pressure signal from the Kulite pressure transducer was filtered and amplified using instrumentation amplifiers (in-amps) before being digitized by the I/O board. The Texas Instruments INA122 was chosen for its high common-mode rejection ratio and the ability to use a single power supply. It was discovered that these in-amps are vulnerable to high out-of-band frequencies caused by the variable speed motors. This high frequency noise is rectified and appears as a DC output error, a problem called radio frequency interference (RFI) rectification. Low-pass RC filters were placed at the signal inputs, power inputs, and signal outputs, as recommended by Analog Digital [98][99].

4.2 Minitube experiments

4.2.1 Apparatus

The hydraulic circuit for the water-piston compressor prototype is shown in figure 4.8. Water was drawn from the water tap through a flexible hose to the pump. The pump was a D-10-I series Hydra-Cell positive displacement diaphragm pump from Wanner Engineering, Inc. The water passed through a Danfoss Power Pack Valve type VPH 15 E which housed both a relief valve and directional control valve. A pressure switch determined the state of the directional control valve. The pressure switch was set to about 1 MPa (150 psi). An electronically-controlled Bürkert proportional solenoid control valve Type 6223 was used to control the flow rate to the compression cylinder. A photograph of the prototype can be seen in figure 4.9.

Two compression cylinders were cut from a length of extruded polycarbonate tubing so they would be compatible with the aluminum mount used in the mesh experiments.

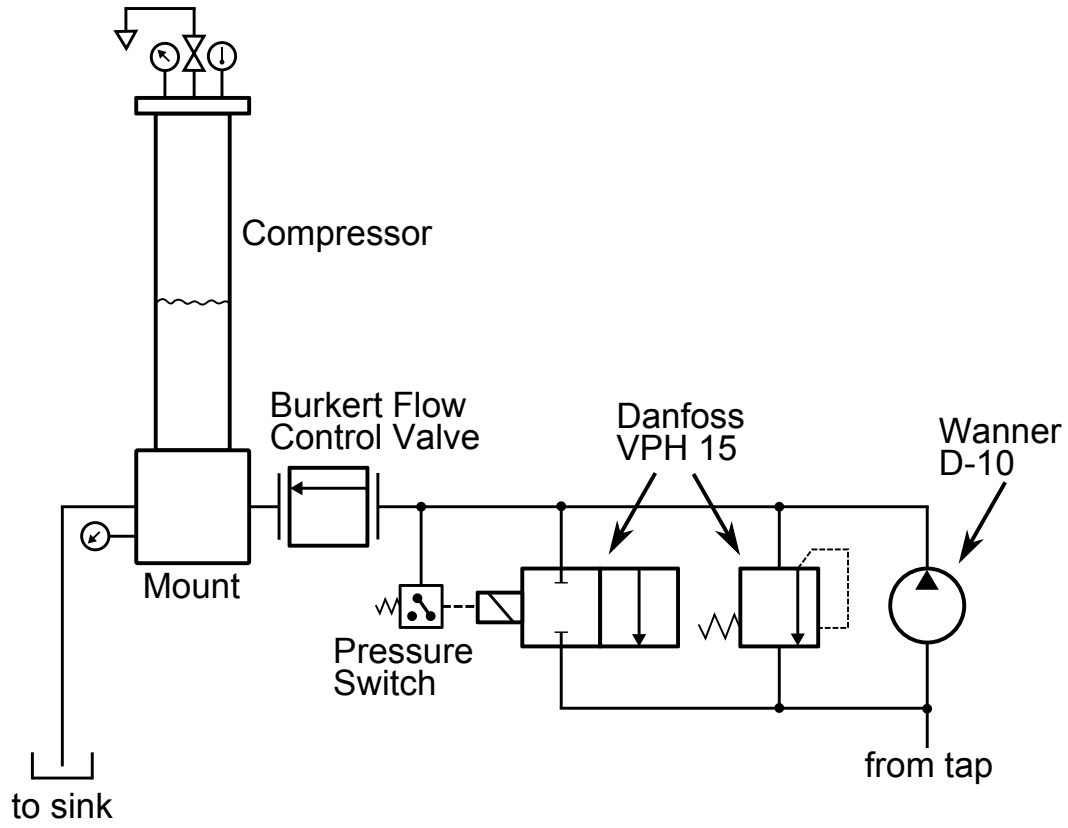

Figure 4.8: The hyraulic circuit for the water piston circuit used with the porous mini-tube array.

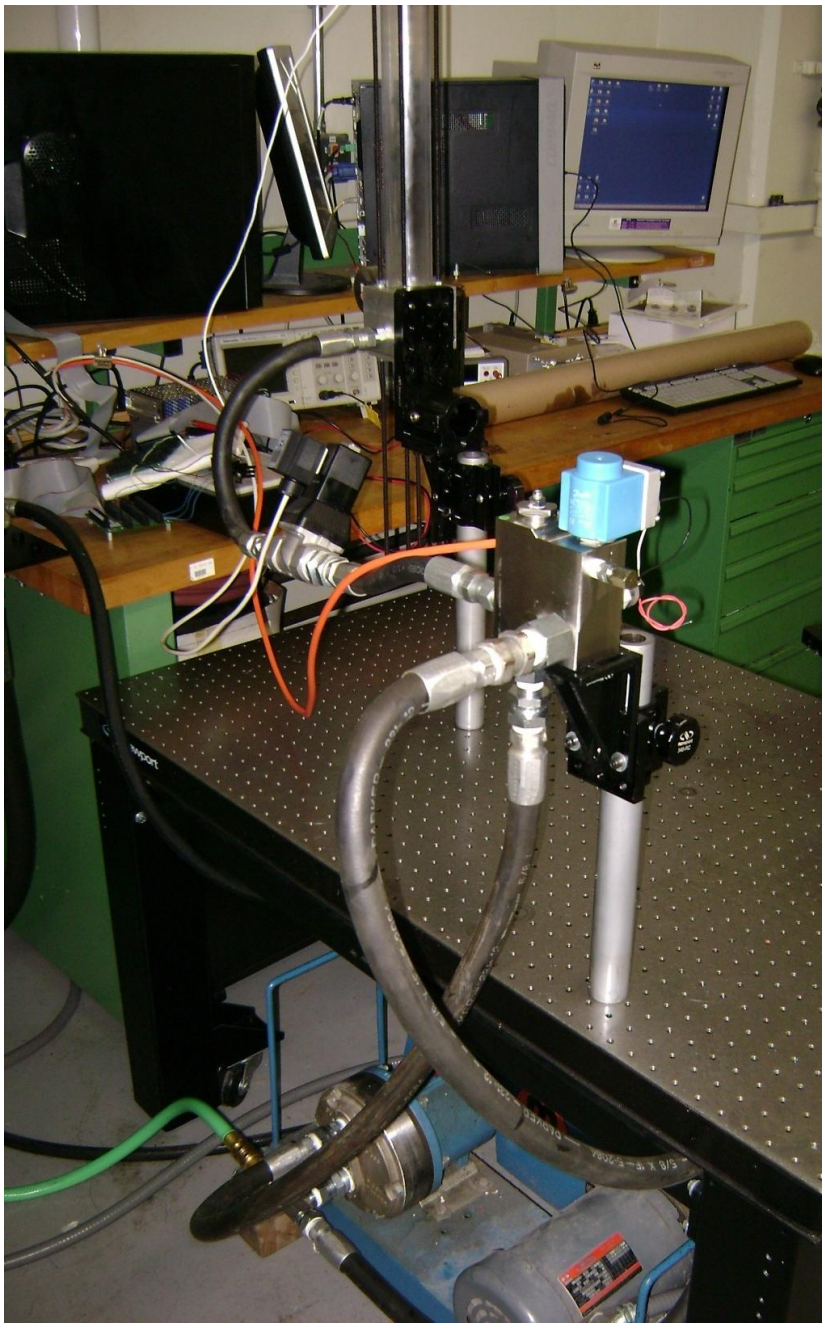

Figure 4.9: A photograph of the circuit of figure 4.8. The pump and motor are at the bottom of the photo on the blue mount. The Danfoss relief valve and directional valve is in the foreground in the center of the photo. The Bürkert control valve is black and downstream of the Danfoss valve. The piston is top center.

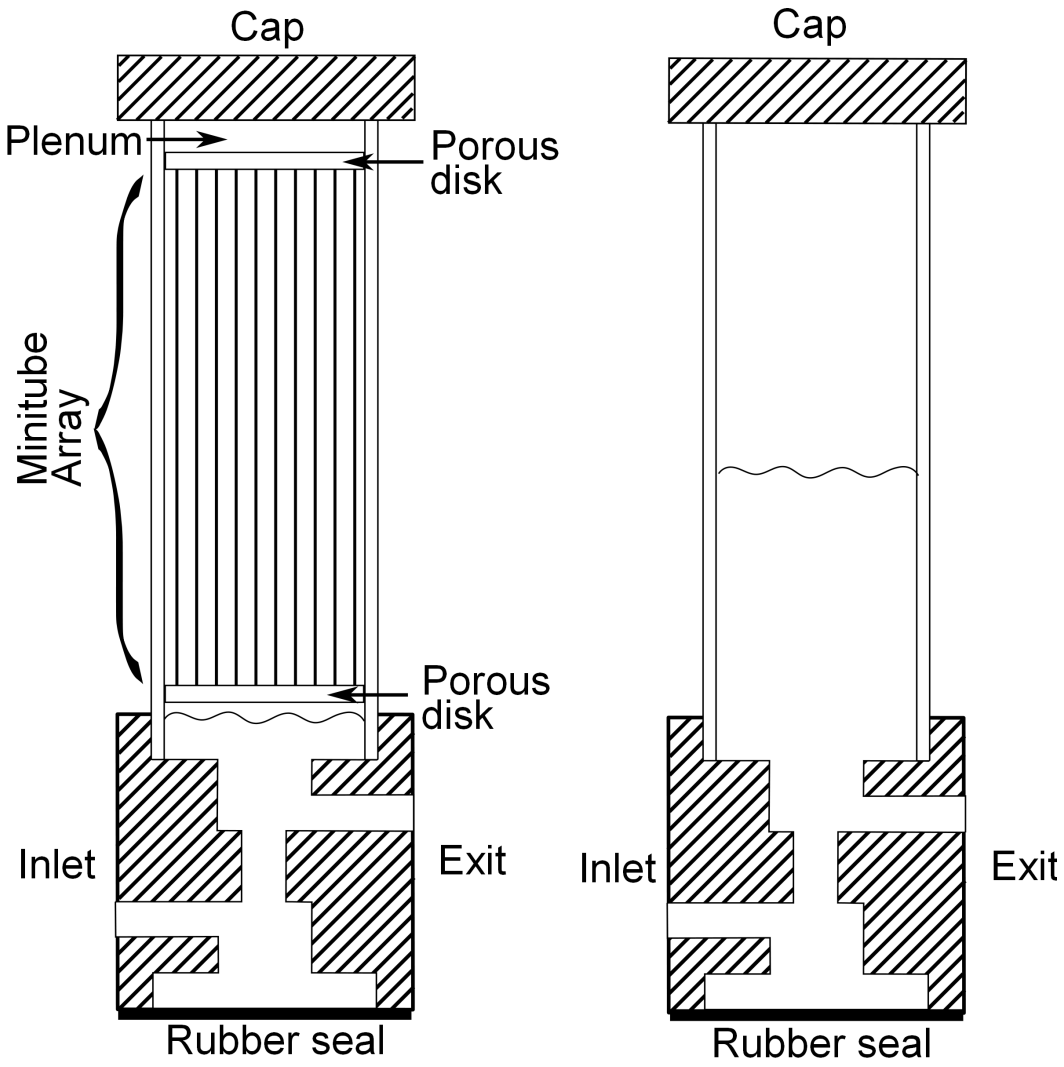

Figure 4.10: A diagram (not to scale) of the water piston compressor used with the porous minitube array and without the minitube array (right). Porous plugs bound the inlet and exit of the minitube array.

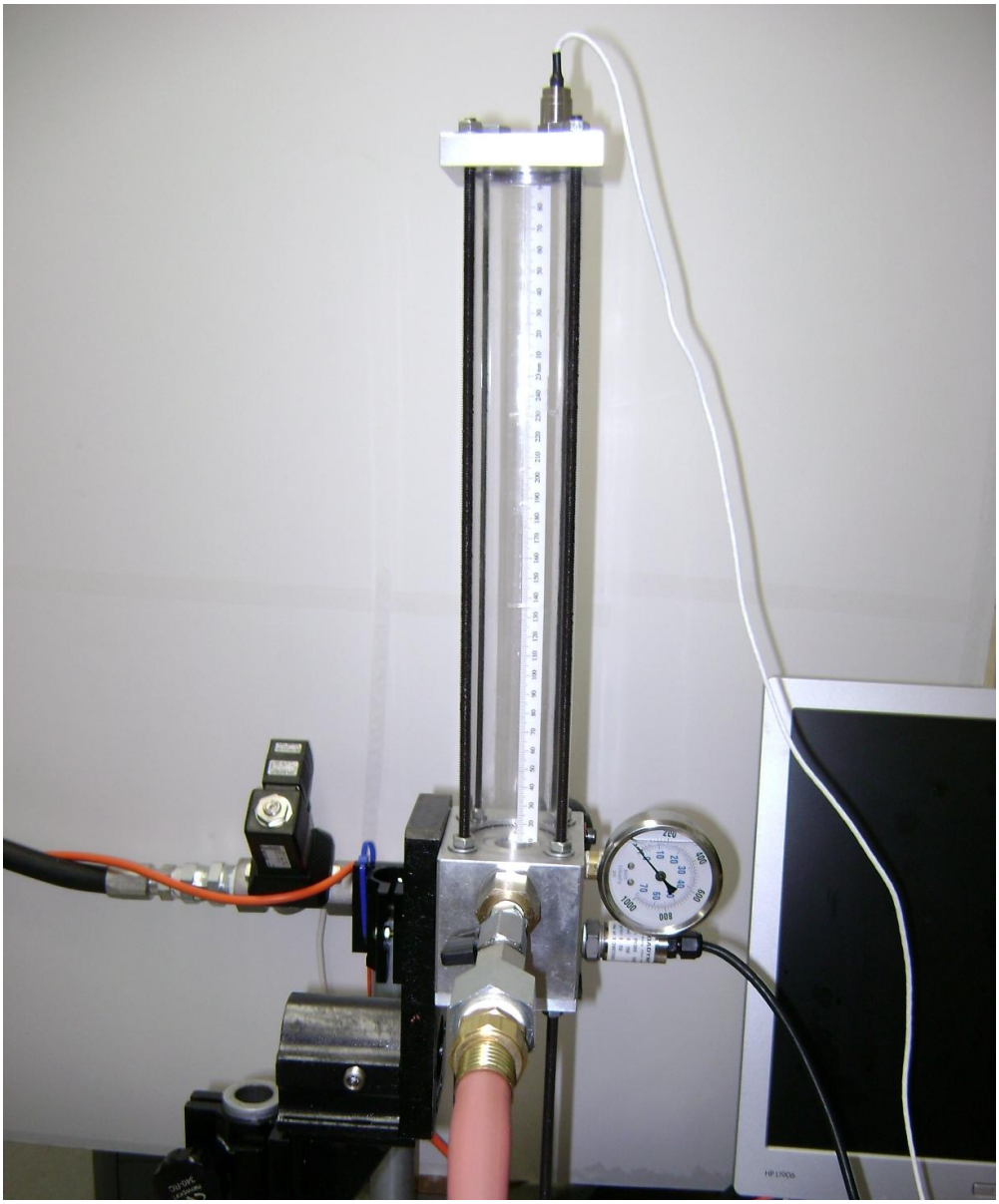

Figure 4.11: A photograph of the water piston sketched in figure 4.10. The Bürkert control valve can be seen to the left of the mount. The hose protruding from the front of the mount is the water discharge port.

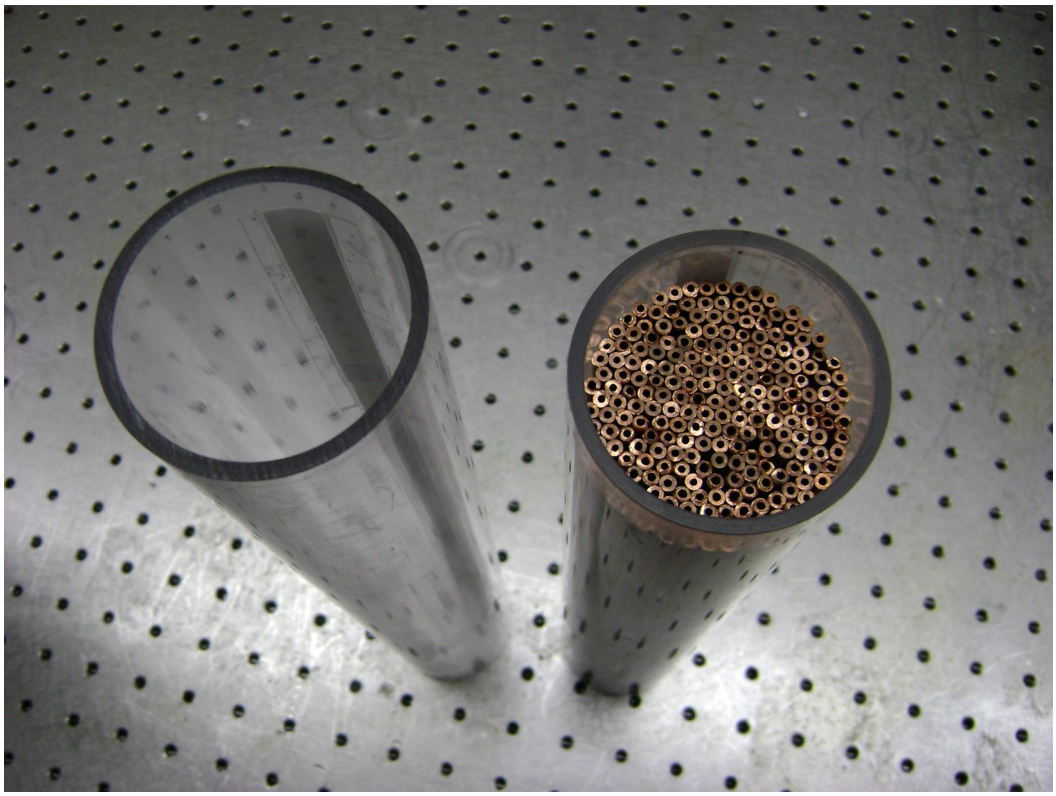

Figure 4.12: A photograph of the two compression cylinders. The compression cylinder on the left was packed with 210 copper minitubes.

One cylinder was packed with the minitube array as seen in figure 4.12. The minitube array was constructed from 210 copper cylinders. Each minitube had a nominal inner diameter of 1.5494 mm (0.061 inches) and an outer diameter of 3.175 mm (0.125 inches). The minitubes were packed in a honeycomb-shaped pattern. Clearances of 1.2 cm and 2 cm were left on either end of the minitube array. A diagram of the compressor assembly is shown in figure 4.10. A photograph of the empty compression cylinder is shown in figure 4.11. Steel exoskeletons were not needed since the target pressure was around 690 kPa (100 psi).

The total mass of the minitube array was 3.429 kg +/- 2 g. Using the known density of the copper alloy of 8.941 g/cc, the volume of copper was computed to be 383.5 cc. This compares favorably with the 380.1 cc volume calculated using the nominal values for inner and outer diameter, the difference being 0.8%. The total air volume enclosed by the polycarbonate cylinder was 683.1 cc, determined using the nominal values for the compression cylinder bore. The maximum air volume was the cylinder volume minus the minitube array, which equaled 299.6 cc. The porosity of the minitube was determined by the cross-section. The cylinder cross section was

$$A_{\mathrm{CS}} = \pi d^2/4 = 20.3 \quad \mathrm{cm}^2 \tag{4.2}$$

where d is the bore of the polycarbonate cylinder. The void area was

$$A_{\mathrm{void}} = A_{\mathrm{CS}} - N\frac{\pi}{4}\left(OD^2 - ID^2\right) = 7.6 \quad \mathrm{cm}^2 \tag{4.3}$$

where N is the number of minitubes, OD is the outer diameter of each minitube, and ID is the inner diameter of each minitube. The porosity is the void area over the total area:

$$\epsilon = \frac{A_{\mathrm{void}}}{A_{\mathrm{CS}}} = 0.375 \quad \mathrm{cm}^2. \tag{4.4}$$

Initial testing demonstrated that the flow resistances through various parallel channels in the minitube array were significantly different from one another. A fountaining effect was observed when flow through some channels reached the top of the minitube array before the compression process was completed. For the purposes of heat transfer, this would be a positive feature; however, thermocouples placed above the minitube array would become wet, leading to inaccurate air temperature measurements. Further, since the thermocouple wires were so thin, they could break if hit forcefully by the water.

Figure 4.13: A photograph of the porous disk on top of the minitube structure. This disk prevented water from impacting the thermocouple measurements. The screw functioned as a handle so the disk could be removed. Before operation, the edges were sealed by hot glue.

In an attempt to equalize the flow resistance, porous disks from Applied Porous, Inc were glued directly below the minitubes. While the fountaining effect was reduced, it was not removed. Therefore, an additional porous disk was glued above the minitubes (figure 4.13). This eliminated the fountaining, so the environment between the porous disk and cap was safe for the thermocouples.

The total air volume in the cylinder must account for the volume of the porous disks. The porous disks were made of sintered 316L stainless steel of density 7.99 g/cc. The mass of the top disk is 58.94 g +/- 0.01 g. This corresponded to a volume of 7.4 cc. The mass of the bottom disk was 45.33 g +/- 1 g for a volume of 5.5 cc. Thus, the maximum air volume in the chamber was 286.7 cc.

4.2.2 Instrumentation

The Kulite ETM-375 pressure transducer measured the air pressure at the cap, and the Omega PX309 series pressure transducer measured the water pressure at the base. Both pressure sensors are described in greater detail in section 4.1. The sensors can be seen in figure 4.11.

Four Omega KMQSS thermocouples are used to measure local air temperatures. The thermocouples have an exposed, beaded junction and 304 stainless steal sheath. The sheath diameter is 0.010 inches (0.254 mm) and the thermocouple wire diameter is 0.0015 inches (0.0381 mm). The thin wire allows the thermocouple to better follow the transient temperature. The response time for a step change in temperature for flowing air at 20 m/s at standard pressure and temperature is estimated from a plot provided by Omega to be on the order of 0.1 seconds. This will be shown to be too slow, and a lag is seen in the thermocouple data. The thermocouple materials meet or exceed the special limits of error supplied by Omega, corresponding to accuracy within 1.1 K or 0.4%, whichever is greater. Figure 4.14 shows the cap with the the four thermocouples. Figure 4.15 shows the distribution of the thermocouple junctions relative to the chamber cross section.

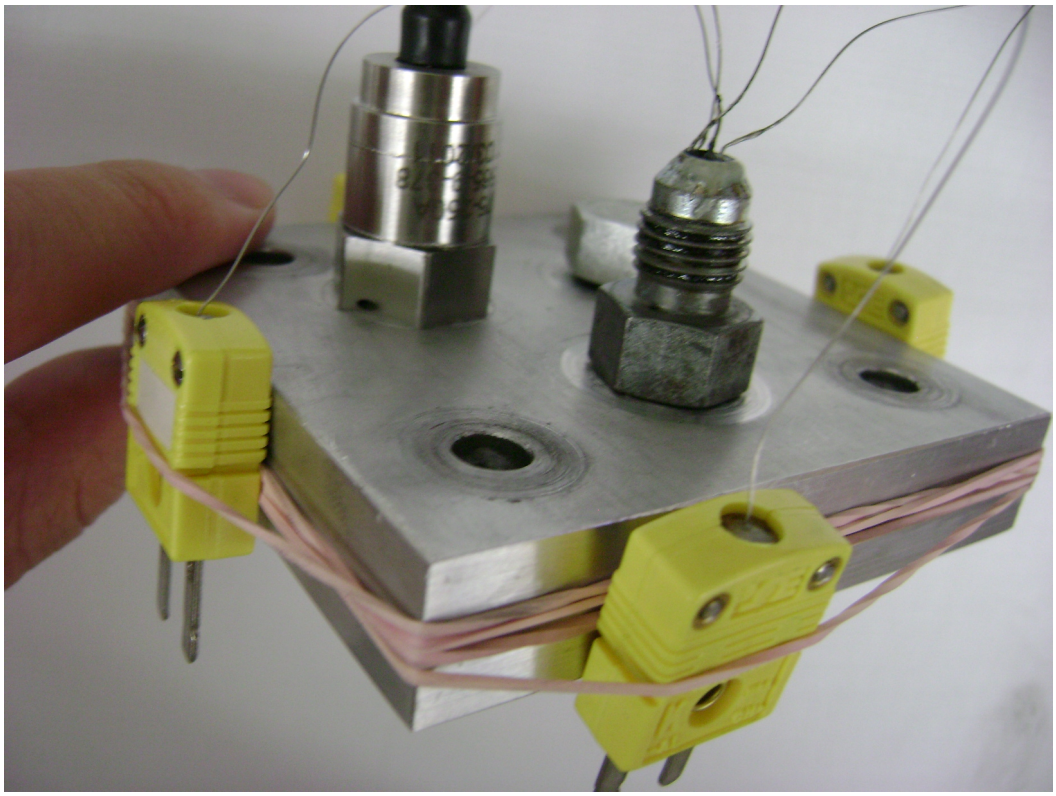

Figure 4.14: A photograph of the end cap from the top. The pressure sensor and thermocouples can be seen. The yellow components are Omega Quick disconnect sockets.

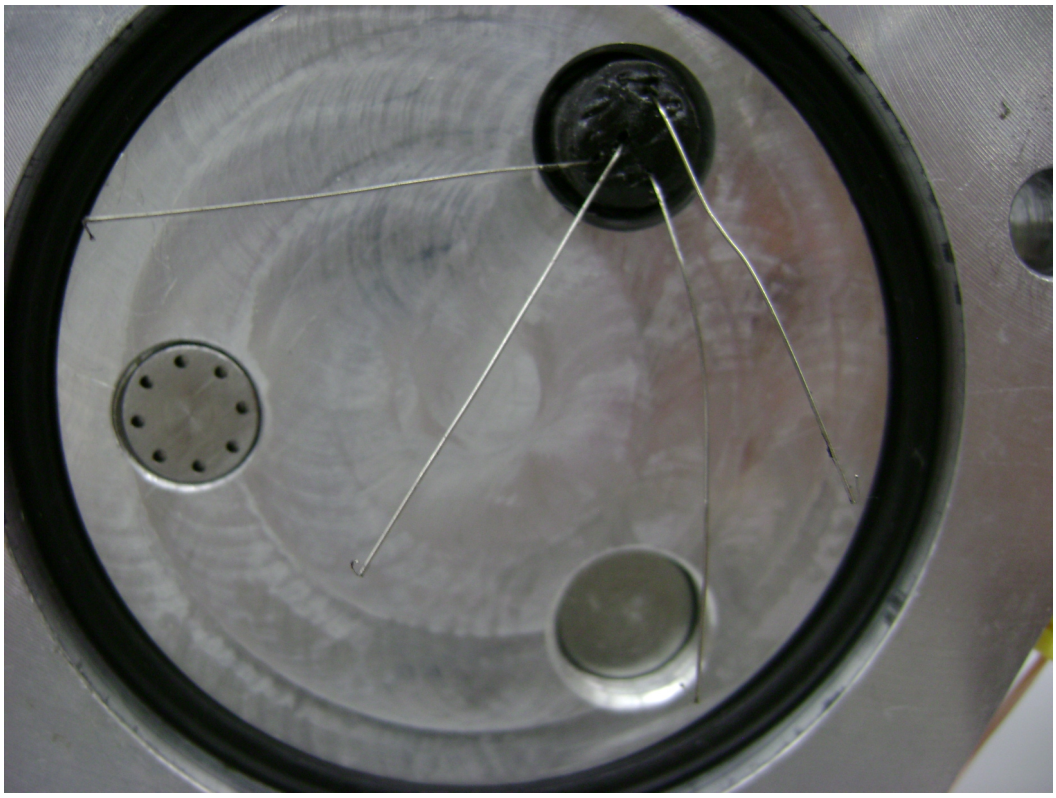

Figure 4.15: A photograph of the end cap from the bottom. The pressure sensor is flush with the end wall. The thermocouples junctions are between 4 and 6 mm from the cap surface.

4.2.3 Control, data acquisition, and data processing

Control of the compressor was achieved through Simulink and xPC Target. A 16-bit PCI-DAS1602/16 multifunction analog and digital I/O board is used to acquire and digitize data. A single analog output is needed for the control valve. A manual switch in Simulink sets the control valve state to fully open (maximum of 0.25 l/s) or fully closed.

Data processing and plotting occurs in Matlab. Five Texas Instruments INA128 instrumentation amplifiers are used to amplify thermocouple signals. Post amplification, an RC filter attenuates high frequency noise that may have been picked up by the thermocouple wires. The cutoff frequency was set to about 100 Hz for the thermocouple data and 20 Hz for the pressure sensor. The data were also digitally filtered using a first-order transfer function with a cutoff frequency of 10 Hz.

Chapter 5

Test program

5.1 Mesh experiments

The objective of the experiments was to compare the temperature difference during the compression of air with and without a metallic mesh in the air space between the piston and the endwall. Initial experiments used a fast-slow type volume profile to qualitatively imitate the optimal compression trajectory, discussed later. High- and low-displacement pumps in combination effected rapid compression, until a specified transition pressure was reached, at which point only the low-displacement pump was used to obtain much slower compression. However, it was decided that for the purposes of the experimental program, a fast-slow trajectory was needlessly complicated. Therefore, a linear compression profile with a constant inlet flow rate was implemented for each trial.

Four flow rates and two meshes were tested, in addition to a base case with no mesh. The volume, initial porosity, and surface area for each mesh are provided in chapter 4, section 4.1. The flow rates were 4 cc/s, 8 cc/s, 16 cc/s, and 20 cc/s. The flow rate was determined by numerically differentiating the volume with respect to time in real time. Feedback to the motors maintained the desired flow rate. The flow rates corresponded to piston velocities of approximately 2 mm/s, 4 mm/s, 8 mm/s, and 10 mm/s. For a stroke length of about 190 mm, compression times ranged from around 19 seconds to over 95 seconds (0.026–0.0053 Hz). These compression times were well below intended target times, largely motivating the construction of a new facility, used

with the minitube experiments below.

The trials were conducted in random order to eliminate false trends due to environmental parameters' temporal effects. The initial air volume was always within 1% of 450 cc. The initial pressure and temperature were equal to the ambient conditions of the lab. The lab pressure ranged from 97.9 kPa to 98.6 kPa (14.2 to 14.3 psi). The lab temperature stayed within a half degree of 298 K (77° F) throughout the process. The final pressure was set to be 690 kPa (100 psi) for a compression ratio of 7. Higher compression ratios were not possible because the high-displacement pump stalled at higher pressures and it was impossible to track a linear compression trajectory at the higher flow rates without it.

Each trial began by holding the air at ambient conditions until 60 seconds was reached, at which point the air was compressed with a constant piston speed until the pressure reached 690 kPa (100 psi). For the faster piston speeds there was some overshoot of the target pressure, but the compression ratio never varied more than 7%. Once the peak pressure was reached, the compressed air was held at a constant volume until the run time reached 300 seconds. A real compressor would immediately push the pressurized air to the accumulator and draw in new air. However, for the purposes of studying the compression, it was found useful to keep the air pressurized for a period of time. It became an opportunity to test for air leaks. It also allowed the pressurized air to return to thermal equilibrium, thus providing a known temperature reference in the middle of the data set that could be used to help validate data reduction. After 300 seconds, the air was allowed to expand to a volume of 450 cc. Data acquisition stopped at 400 seconds, again allowing time for a return to thermal equilibrium.

Preventing leakage was a key objective. O-rings between the cylinder and the mount and the cylinder and the cap provided a good seal. O-rings between the piston and cylinder wall offered a decent seal, but care was needed to ensure that the clearance between the piston and wall was filled with oil so the air volume would be measured correctly. A solution of water and soap was often applied to the seals in the cap. During compression, the soapy water would bubble if air was leaking through the seal.

5.1.1 Data reduction

Voltages from the Kulite pressure sensor are converted to psi by scaling by 50.16 psi/volt and offsetting by -2.47 psi. Voltages from the MTS position sensor are directly converted to air volume according to a calibration curve generated for that particular cylinder. Volume-averaged temperature data were calculated from measured air pressure and air volume using the ideal gas law:

$$T = \frac{T_0}{P_0 V_0} P_{\text{measured}} V_{\text{measured}}. \tag{5.1}$$

The quantity of air in the cylinder was calculated from the measured initial conditions:

$$n = \frac{P_0 V_0}{R T_0}. \tag{5.2}$$

The instantaneous heat transfer was calculated by numerically differentiating temperature and volume and using the first law energy balance:

$$q_i = n c_v \frac{T_i - T_{i-1}}{t_s} - P_i \frac{V_i - V_{i-1}}{t_s} \tag{5.3}$$

where t_s is the sampling time. Numerical differentiation tends to amplify noise. Rigorous n-point smoothing of the data both before and after differentiation was performed in an attempt to extract the underlying trends, with moderate success. The instantaneous value of hA is

$$(hA)_i = \frac{q_i}{T_{\text{sink}} - T_i} \tag{5.4}$$

The instantaneous heat transfer coefficient, h, is

$$h_i = \frac{(hA)_i}{A_i}. \tag{5.5}$$

The instantaneous surface area depends on the instantaneous air volume, V_i, and several constants:

$$A_i = \frac{4\left(V_i - V_{\text{mesh}}\right)}{d} + \frac{\pi d^2}{2} + (SA)_{\text{mesh}} \tag{5.6}$$

where V_{mesh} is the volume of the mesh, d is the diameter of the compression cylinder, and $(SA)_{\text{mesh}}$ is the surface area of the mesh as calculated in equation 3.30.

5.1.2 Uncertainty analysis

Uncertainty in single-sample experiments was calculated by

$$\frac{\delta T}{T} = \left(\left(\frac{\delta V}{V} \right)^2 + \left(\frac{\delta P}{P} \right)^2 \right)^{1/2} \tag{5.7}$$

where δP is the total uncertainty in the pressure and δV is the total uncertainty in the volume. These values were obtained from the instrument specifications or calibration. For the Kulite pressure transducer, the maximum error was reported to be $\delta P = 8.6$ kPa (1.25 psi). For the volume, the uncertainty due to the instrument was dominated by the volume calibration, so $\delta V = 1$ cc. At the peak temperature, the pressure was 690 kPa (100 psi) and the volume was about 65 cc. The relative uncertainty, $\frac{\delta T}{T}$, is 2%. This corresponds to temperature uncertainty of 6.1 K at 310 K and 6.7 K at 340 K.

5.2 Minitube experiments

The objective of the experiments was to compare the temperature difference during the compression of air due to a minitube array in the air space. Initial testing established that the system was working properly and results were repeatable. It was discovered that the pump was not needed to reach the target pressure of 690 kPa (100 psi) within the target compression time of one second—the pressure from the tap supplying the pump was sufficient. This streamlined the control of the experiment.

To facilitate a useful comparison, the compression storage power for both trials, with and without the minitube insert, must be the same. The compression power for the open accumulator is

$$\mathrm{Pow}_c \equiv nRT_0 \frac{\ln(r) + 1/r - 1}{t_c}. \tag{5.8}$$

Here t_c is the total time for compression. The compression efficiency for the open accumulator is

$$\eta \equiv nRT_0 \frac{\ln(r) + 1/r - 1}{W_{\mathrm{in}}}. \tag{5.9}$$

The work in is

$$W_{\mathrm{in}} \equiv -\int_{V_0}^{V_c} (P - P_0)\,\mathrm{d}V + nR\,(1 - 1/r)\,(T_c - T_0) \tag{5.10}$$

where V_c and T_c are the values of air volume and air temperature at the end of the compression event, but before storage (and cooling) in the accumulator. The second term in the definition for the work input is the work associated with isobaric cooling in the accumulator.

As mentioned in chapter 4, section 4.2, when the minitube array was used a fountaining effect occurred during compression. This jetting of water into the plenum was deemed dangerous for the thermocouples. Therefore, several tests were conducted without the thermocouples. For each test, the initial air volume was set to within 1% of 275.7 cc. The appropriate initial interface level was determined by a ruler attached to the cylinder wall. Pressure data were taken and the volume-averaged peak temperature was calculated as described below.

Also, as described in chapter 4, section 4.2, porous disks were eventually placed below and glued above the minitube array, so as to smooth the cross-sectional variation in flow resistance and prevent splashing. This created an environment safe for the thermocouples, so several more trials were run, with and without the minitube array, using the thermocouples. For each trial, the initial air volume was within 1% of 275.7 cc. The initial pressure was 98 kPa (14.2 psi). The ambient temperature ranged from 297 to 299 K over the course of the tests as read by a lab thermometer, but no significant temperature change occured over the course of a single trial. The thermocouples tended to report slightly higher temperatures than the lab thermometer, but this could be attributed to different locations and the 1.1 Kelvin uncertainty band inherent to the thermocouples.

Each trial (with or without the thermocouples) began by holding the air at ambient conditions for 30 seconds. After 30 seconds, the control valve was fully opened and water filled the compression chamber until the air pressure reached 690 kPa (100 psi). Once this pressure was reached, the compressed air was held at a constant volume until the run time reached 120 seconds. During this time, the air cooled back to the ambient temperature while the volume remained constant. At 120 seconds, the discharge port was opened and the compressed air was allowed to expand, forcing water out of the compression chamber. Data acquisition stopped after the run time reached 150 seconds, allowing for a return to thermal equilibrium after expansion.

5.2.1 Data reduction

Voltages from the Kulite pressure sensor were converted to pressure by scaling by 50.16 psi/volt and offsetting by -2.47 psi. Voltages from the thermocouples were converted to temperature using interpolating polynomials from the National Institute of Standards and Technology (NIST). From the ideal gas law,

$$\frac{PV}{T} = \text{constant.} \tag{5.11}$$

When the volume was also constant, as during the isochoric cooling,

$$\frac{P}{T} = \text{constant.} \tag{5.12}$$

After the compressed air returned to thermal equilibrium during the isochoric cooling period, the temperature was known to be equal to the ambient temperature:

$$T_{\text{eq}} = T_0 \tag{5.13}$$

Thus, the volume-averaged temperature throughout the isochoric cooling period was calculated by

$$T = \frac{P}{P_{\text{eq}}} T_{\text{eq}} \tag{5.14}$$

where P is the instantaneous measured pressure and the subscript "eq" refers to values when the temperature is at thermal equilibrium. The peak temperature was calculated by

$$T_{\text{peak}} = \frac{P_{\text{peak}} T_{\text{eq}}}{P_{\text{eq}}}. \tag{5.15}$$

where the subscript "peak" refers to values at the moment of peak pressure.

5.2.2 Uncertainty analysis

Uncertainty in the peak temperature found through equation (5.15) was calculated by

$$\frac{\delta T_{\text{peak}}}{T_{\text{peak}}} = \left(\left(\frac{\delta P_{\text{eq}}}{P_{\text{eq}}} \right)^2 + \left(\frac{\delta T_{\text{eq}}}{T_{\text{eq}}} \right)^2 + \left(\frac{\delta P_{\text{peak}}}{P_{\text{peak}}} \right)^2 \right)^{1/2} \tag{5.16}$$

where δP is the total uncertainty in the pressure sensor and δT is the total uncertainty in ambient room temperature. For the Kulite pressure transducer, the maximum error was

reported in the specifications to be 8.6 kPa (1.25 psi). For the equilibrium temperature (equal to the ambient temperature), the uncertainty was estimated to be 0.5 K. At the peak temperature, the pressure as about 690 kPa (100 psi) and the volume was about 55 cc. The relative uncertainty at the peak temperature, $\frac{\delta T}{T}$, is 2.1%. When the minitube array with porous disks was used the peak temperature is calculated to be 320 K, so the uncertainty at 2.1% is 6.7 K. When the compression cylinder is empty, the peak temperature is calculated to be 400 K, so the 2.1% uncercertainty corresponds to 8.4 K. The Kulite sensor specifications also reported the "typical" error magnitude. Using the typical error instead of the maximum error, the temperature uncertainty for the cylinder with the minitube array and porous disks is reduced to 1.4 K and the uncertainty in temperature for the empty cylinder is reduced to 1.8 K.

Chapter 6

Results

6.1 Mesh experiment and model

Two sets of results are of interest: the experimental results and the model results for comparison. This section summarizes both, starting with the experimental results.

6.1.1 Results from experiment

Representative samples of the volume vs. time measurements are shown in figure 6.1. These curves depict compression using no mesh and four different piston velocities. All volume profiles are of a similar shape, but vary due to differing piston speeds. Each curve is characterized by a constant-volume period at 450 cc, followed by linear compression, followed by a second constant-volume period, followed by expansion, and finishing with a constant-volume period at 450 cc. The volume of the middle constant-volume period varies, depending on how the gas is compressed. Nearly isothermal compression will have a smaller final volume than nearly adiabatic compression.

Representative pressure data are shown in figures 6.2 and 6.3. Each curve has an initial constant pressure period at ambient pressure, followed by compression to 690 kPa (100 psi), followed by a constant volume (isochoric) period, then expansion, and finally a constant pressure period at the ambient pressure. The pressure drop immediately after compression is due to the isochoric cooling, and so indicates the relative air temperature change. Greater cooling corresponds to a larger drop in pressure. Thus, in the pressure curves of figure 6.2, faster piston speeds correspond to larger pressure drops indicating

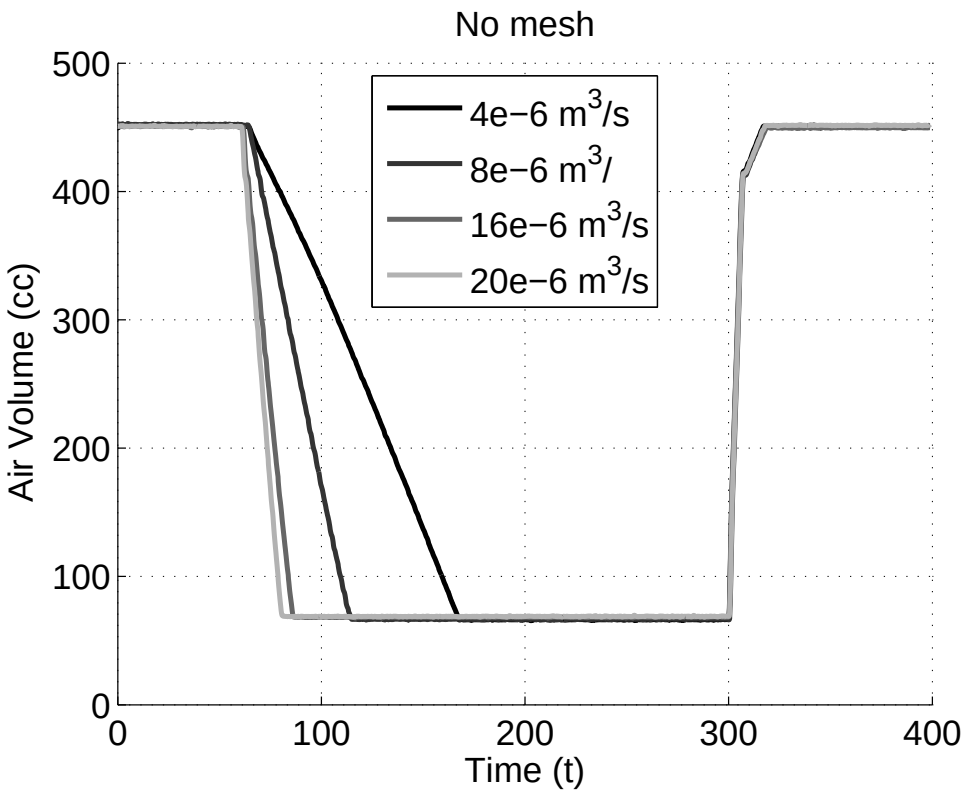

Figure 6.1: Volume data with no mesh in the air space.

more significant cooling. Faster compression means higher temperatures. In figure 6.3, the pressure is shown for a constant-speed but for various mesh sizes. Greater mesh mass (i.e. more surface) corresponds to a smaller drop in pressure, so more mass means lower temperatures.

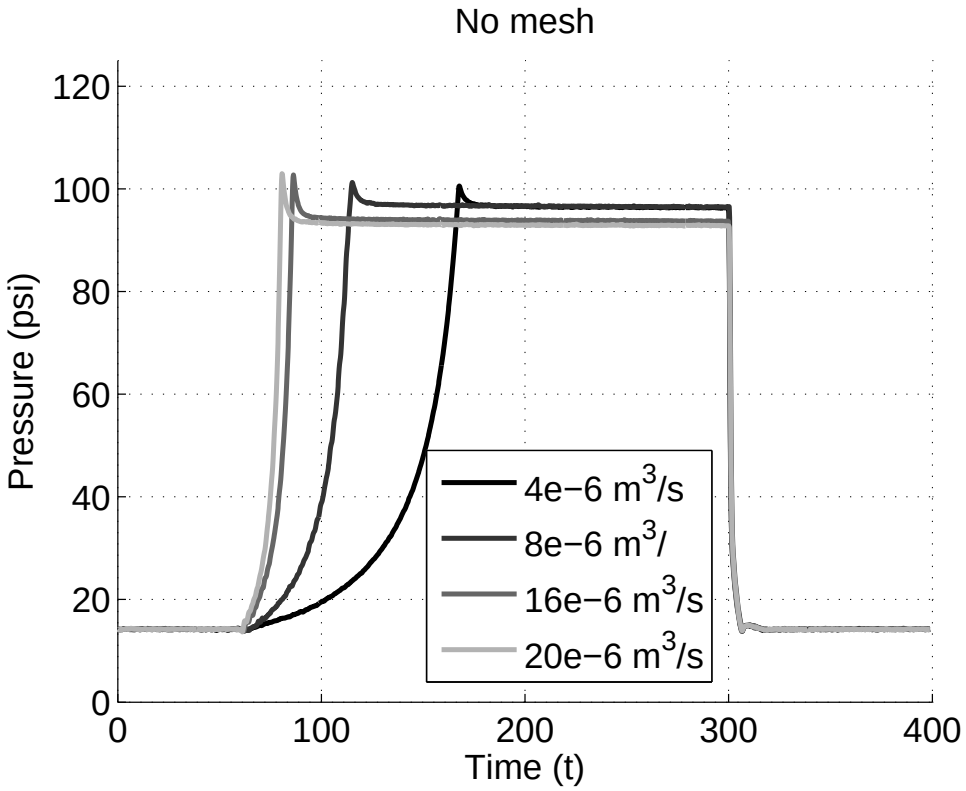

Figure 6.2: Pressure data with no mesh in the air space.

Temperature is calculated from the measured pressure, volume, and initial temperature using equation (5.1). Representative data corresponding to the pressure curves in figures 6.2 and 6.3 are shown in figures 6.4 and 6.5. Here, the temperature changes hinted at in the pressure data are clarified. In the figures, dashed lines indicate the temperatures of 298 K, 293 K, and 303 K. These approximate the ambient temperature, and the lower and upper uncertainty bounds during the isochoric cooling stage equilibrium conditions. However, the exact values vary from trial to trial. The sudden decrease in temperature at 300 seconds was due to the expansion of the gas at that time. The recorded peak temperature differences for all twelve trials (four inlet flow

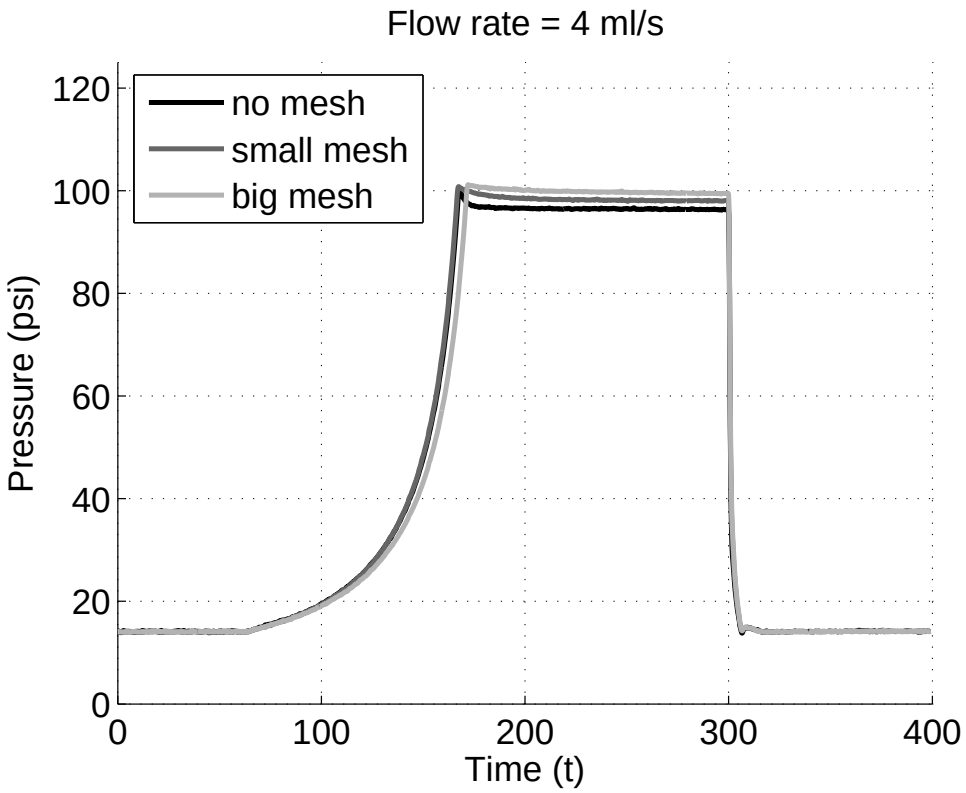

Figure 6.3: Pressure data with a flow rate of 4 cc/s during compression.

rates × three mesh sizes, including no mesh) are tabulated in table 6.1. The two trends observed in the presented plots were true over all the ranges of parameters tested. The peak temperature decreased when the mesh mass increased. Also, the peak temperature decreased when the inlet flow rate (i.e. piston velocity) increased. Appendix E contains the complete set of figures showing temperature variation due to mesh size, holding the compression flow rate constant, and temperature variation due to flow rate, holding the mesh size constant.

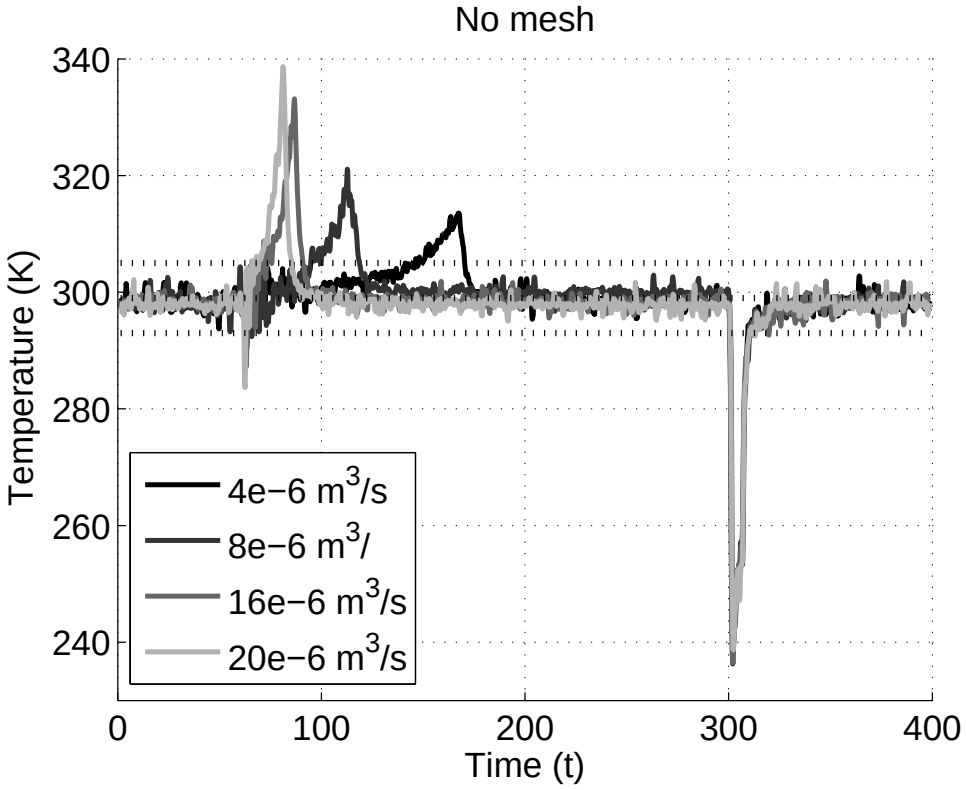

Figure 6.4: Calculated temperature profiles with no mesh. Compression begins at the 60 second marker. The four ending times are approximately 81, 86, 115, and 167 seconds.

Figures 6.6 and 6.7 show the instantaneous overall heat transfer rate vs. time. The heat transfer rate was calculated by equation (5.3). Figure 6.8 shows the instantaneous overall hA product vs. time. The hA product was calculated by equation (5.4). Figure 6.9 shows the instantaneous overall heat transfer coefficient vs. time. The heat transfer coefficient was calculated by equation (5.5). These data exhibit significant noise, largely

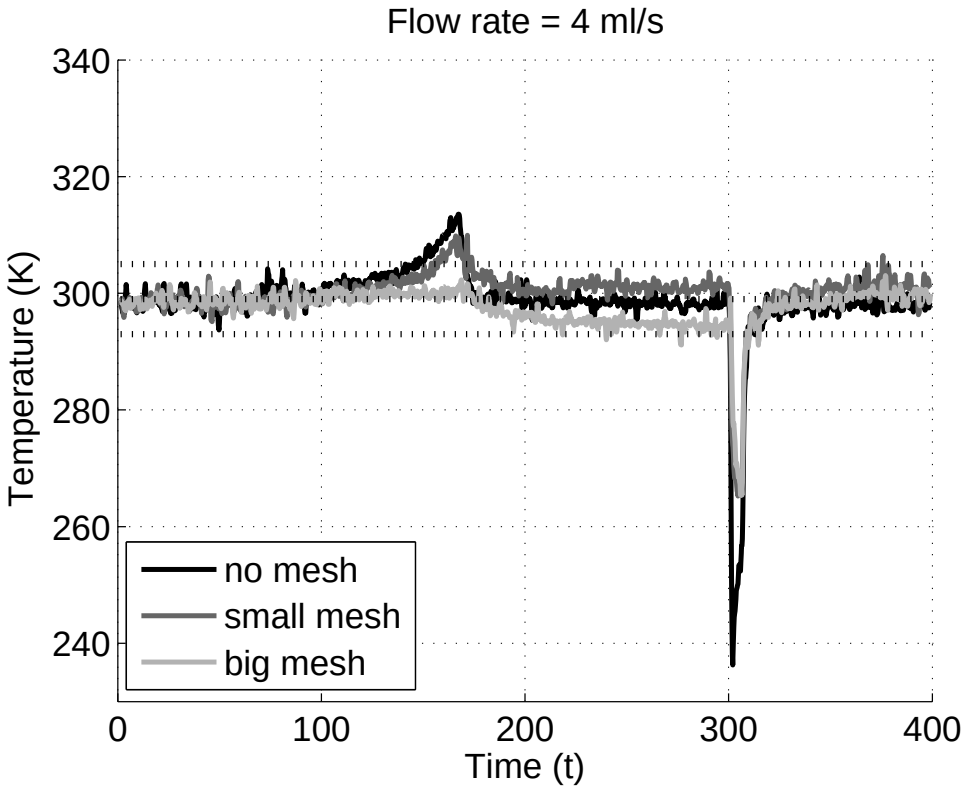

Figure 6.5: Calculated temperature profiles with a flow rate of 4 cc/s during compression. Compression begins at 60 seconds and ends at about 170 seconds.

Table 6.1: Peak temperature change for varying compression speeds and mesh masses.

		Flow Rate (cc/s)			
		4	8	16	20
Mesh Mass (g)	0	15.7	23.0	34.7	41.5
	1.70	9.7	11.2	19.5	19.8
	5.48	7.2	8.5	8.8	12.6

due to the numerical differentiation, which amplifies noise.

Figure 6.9 seems to offer the clearest depiction of the form of the heat transfer coefficient. In this figure it is seen that for all cases, the h is fairly constant, taking values around 30–40 with no mesh, 20 with the 1.70 g mesh, and 15–20 with the 5.48 g mesh. Data from the other trials are more difficult to interpret. The heat transfer coefficient sometimes starts very high before settling down, which is similar to what is seen in the entrance flow of tubes or starting problems. For other runs h starts very low, but the negative values of h discourage literal interpretation of the results. Overall, values ranging from 15–50 W/m^2-K seem to be typical.

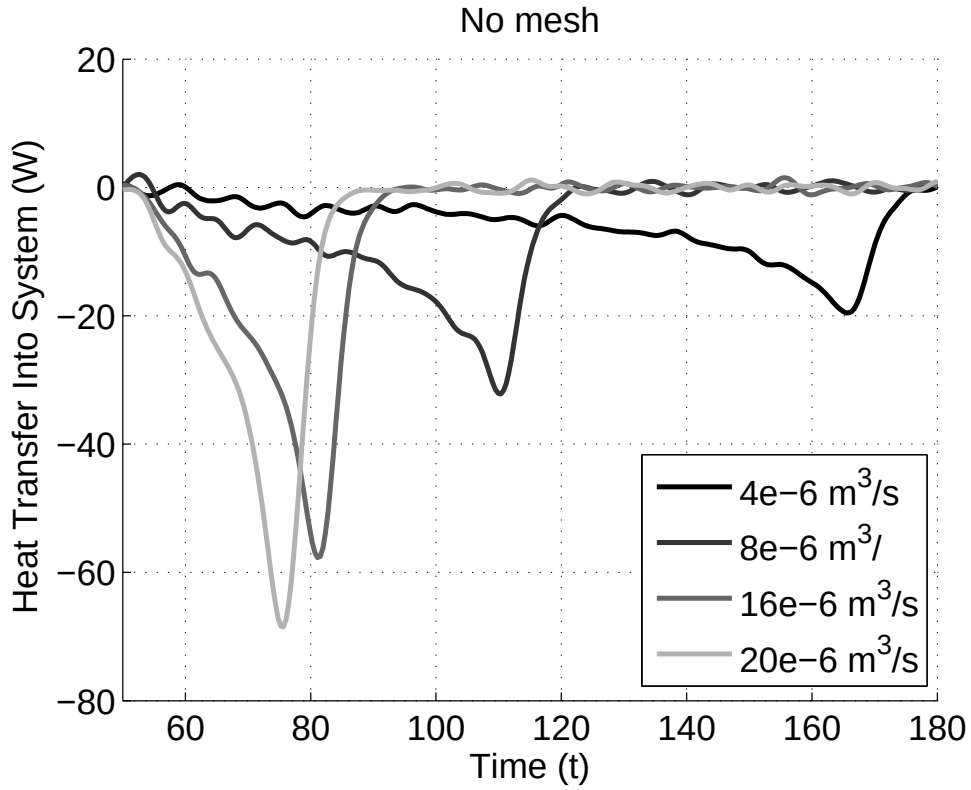

Figure 6.6: Calculated heat transfer rate as a function of time with no mesh in the airspace. Compression begins at the 60 second marker. The four ending times are approximately 81, 86, 115, and 167 seconds.

Work and efficiency can be calculated directly from the pressure data, volume data, and peak temperature using equations (3.2), (3.3), and (3.5). Power is calculated from

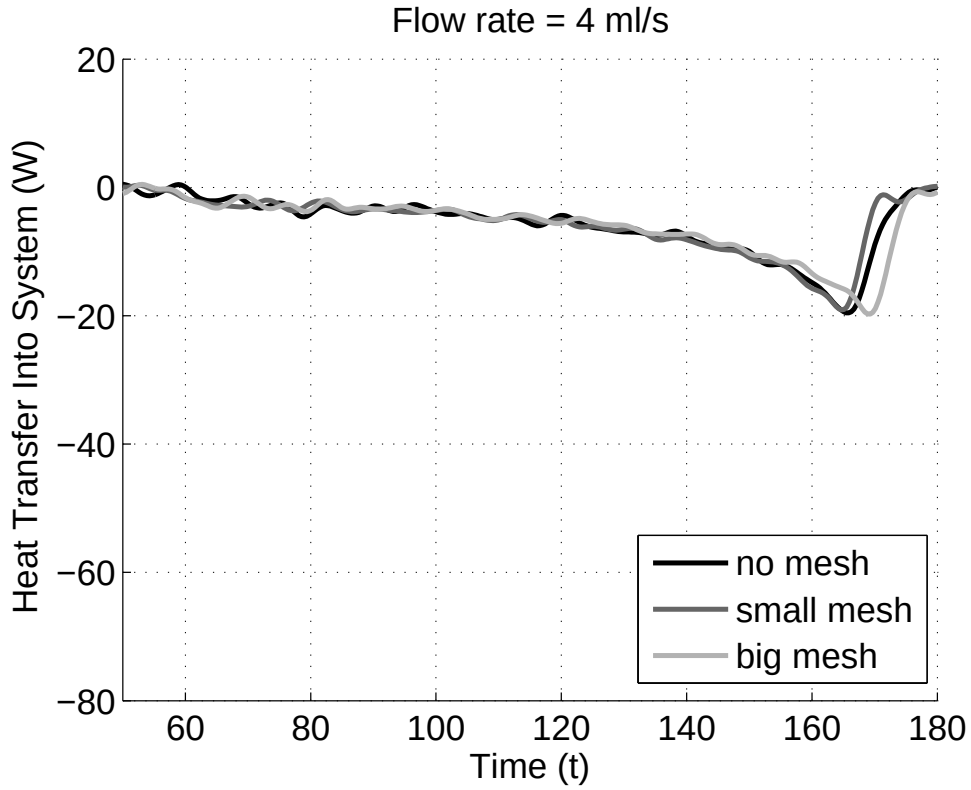

Figure 6.7: Calculated heat transfer rate as a function of time with a flow rate of 4 cc/s during compression. Compression begins at 60 seconds and ends at about 170 seconds.

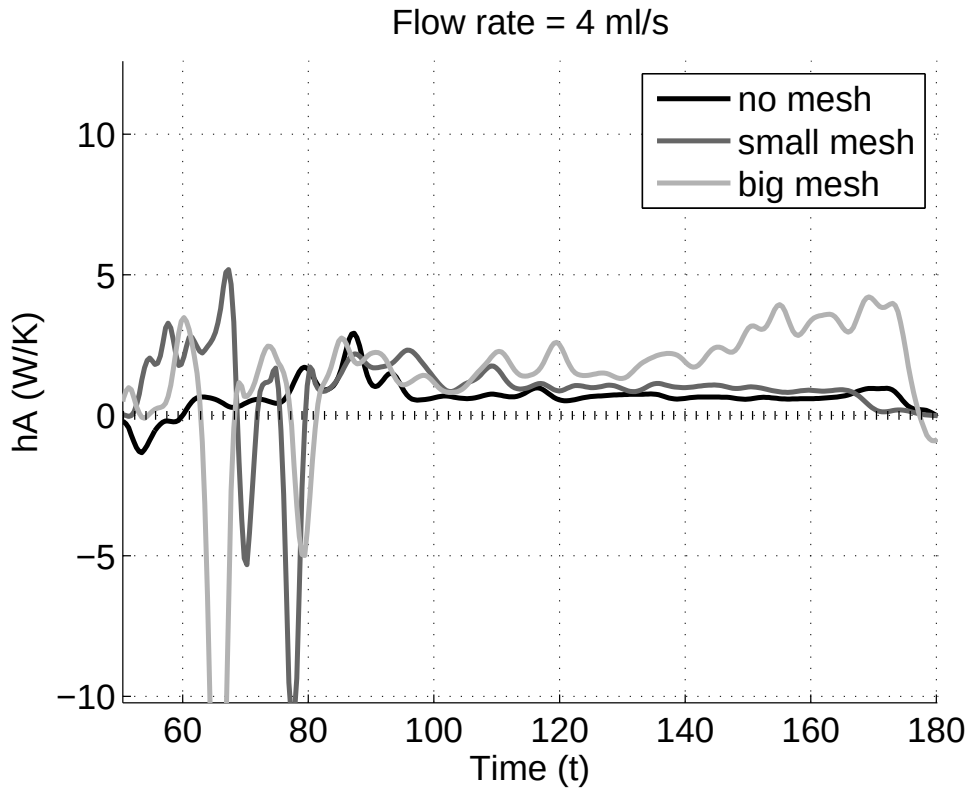

Figure 6.8: Calculated hA values as functions of time with a flow rate of 4 cc/s during compression. Compression begins at 60 seconds and ends at about 170 seconds.

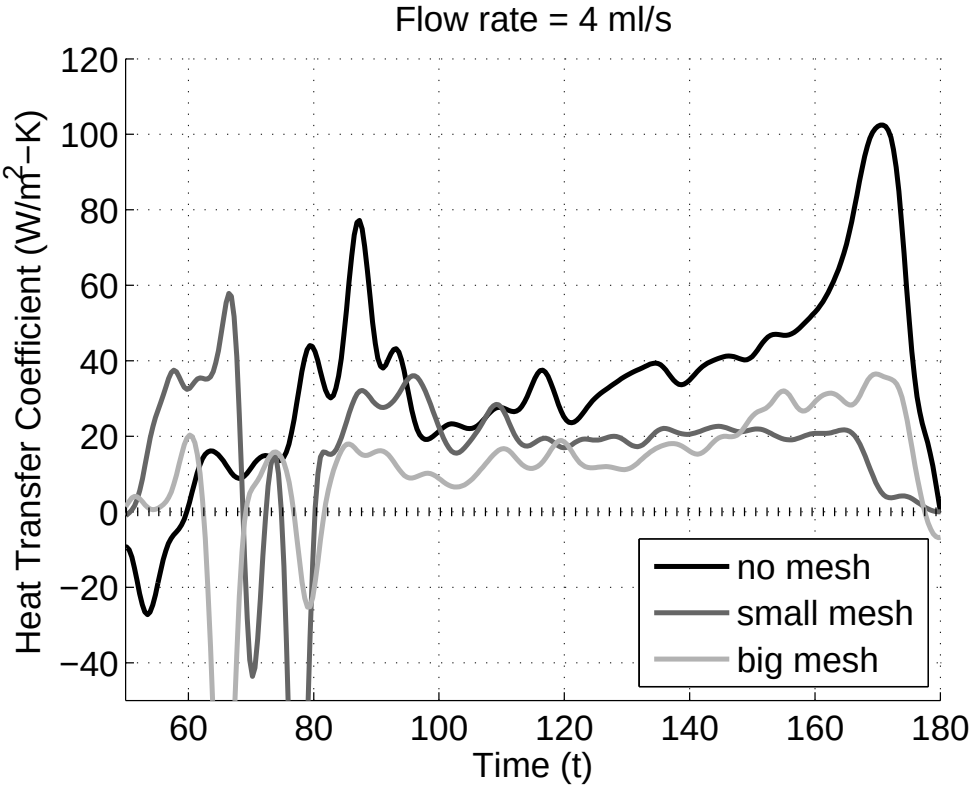

Figure 6.9: Calculated heat transfer coefficients as functions of time with a flow rate of 4 cc/s during compression. Compression begins at 60 seconds and ends at about 170 seconds.

equation (3.7). The results are summarized in tables 6.2 and 6.3. It can be seen that for very similar powers, the efficiency increases when additional mesh mass is added.

Table 6.2: Storage power in Watts for varying compression speeds and mesh masses.

		Flow Rate (cc/s)			
		4	8	16	20
Mesh Mass (g)	0	0.47	0.95	1.98	2.49
	1.70	0.46	0.94	1.94	2.39
	5.48	0.45	0.95	1.92	2.41

Table 6.3: Efficiency for varying compression speeds and mesh masses.

		Flow Rate (cc/s)			
		4	8	16	20
Mesh Mass (g)	0	0.96	0.95	0.92	0.90
	1.70	0.97	0.97	0.96	0.95
	5.48	0.99	0.99	0.99	1.00

6.1.2 Results from model

A constant value for the heat transfer coefficient, as described in chapter 3, was used in the simulation of the compression event. This fits the general trend observed in the experiments. Experimentally measured volume profiles and constant values of h were the inputs to the model. The output is calculated temperature and pressure based on the governing equations and assumptions outlined in section 3. As can be seen in the figures below, four values of h are chosen, $h = 0$ (adiabatic), $h = 0.5$, $h = 2$, $h = 10$, $h = 50$, as well as a "best fit" value. The best fit h is chosen by minimizing the least squares difference between the temperature during compression calculated from the experimental data and from the model. The nearest integer value of h is chosen when using no mesh or the 1.70 g mesh. The least squares method failed to provide an accurate value for trials using the 5.48 g mesh. This was because non-physical oscillations resulted in temperature dips below the ambient temperature that were on the same order of magnitude as the peak temperature difference. Therefore an "eyeball" fit was used to approximate the h and better qualitative fits are achieved. The values of the best fit h's used in the analytic models are given in table 6.4. Initially, the sudden

increase in the heat transfer coefficient for the 5.48 g mesh seems suspicious, but as can be seen in the temperature figures (e.g. figures 6.13 and 6.14, the nearer the process gets to isothermal operation the greater the h must become. The relation between the temperature change and h is not linear. The complete set of plots with best fit curves are available in appendix E. Representative plots are provided in figures 6.10 through 6.15.

Table 6.4: Values of best fit h's in W/m^2-K used in the analytical models.

		Flow Rate (cc/s)			
		4	8	16	20
Mesh Mass (g)	0	16	18	21	22
	1.70	17	25	32	36
	5.48	80	100	130	300

Figures 6.10–6.14 show the experimental results along with analytical results for different choices of a constant h. In these results, the flow rate is 4 cc/s and the 1.70 g mesh is used. These data are are highlighted because the noise level is relatively small, but they are representative of the rest of the results. Figure 6.10 shows the volume profile as a function of time. Since the volume profile is an input to the analytical model, the volume curves match the experimental results regardless of the choice of h. Figure 6.11 shows the measured pressure as well as calculated pressures using different values of h, including the best fit. Figure 6.12 is figure 6.11 zoomed in to show the fit around the peak pressure. Figure 6.13 shows the experimentally derived temperature along with temperature profiles calculated from the analytical model. As with pressure, various values of h are shown. Figure 6.14 is figure 6.13 zoomed in to show the fit around the peak pressure. Figure 6.15 shows the predicted mesh temperature, compared to the measured volume-averaged air temperature. It can be seen that the mesh temperature is predicted to closely follow the air temperature during compression.

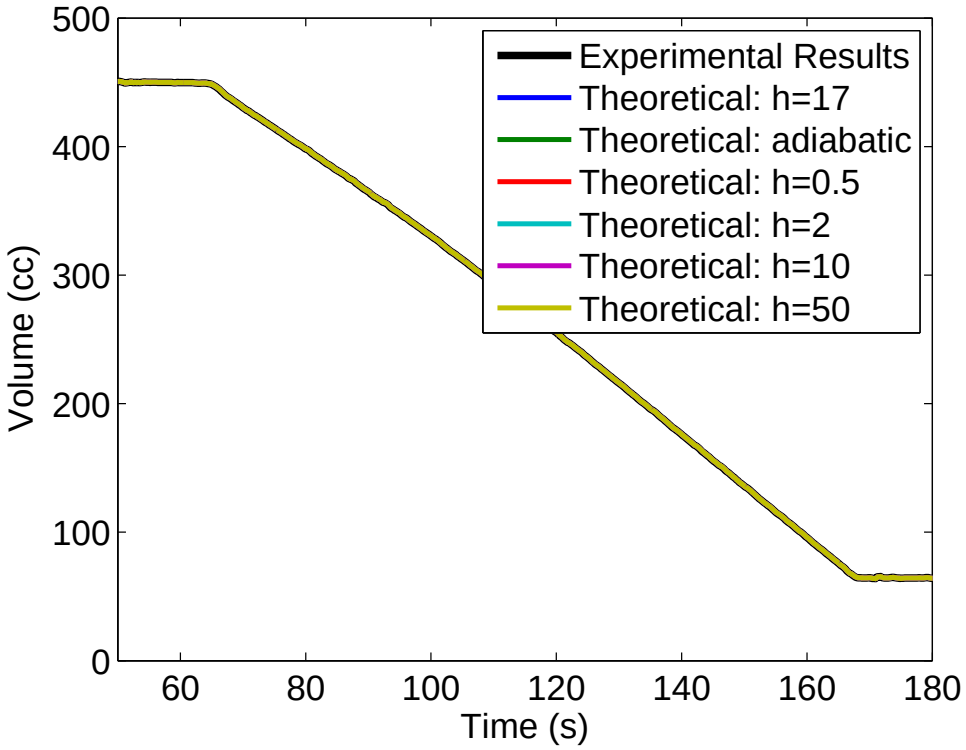

Figure 6.10: Air volume vs. time with the 1.70 g mesh and 4 cc/s flowrate. Experimental data is compared to simulation output for various constant h's.

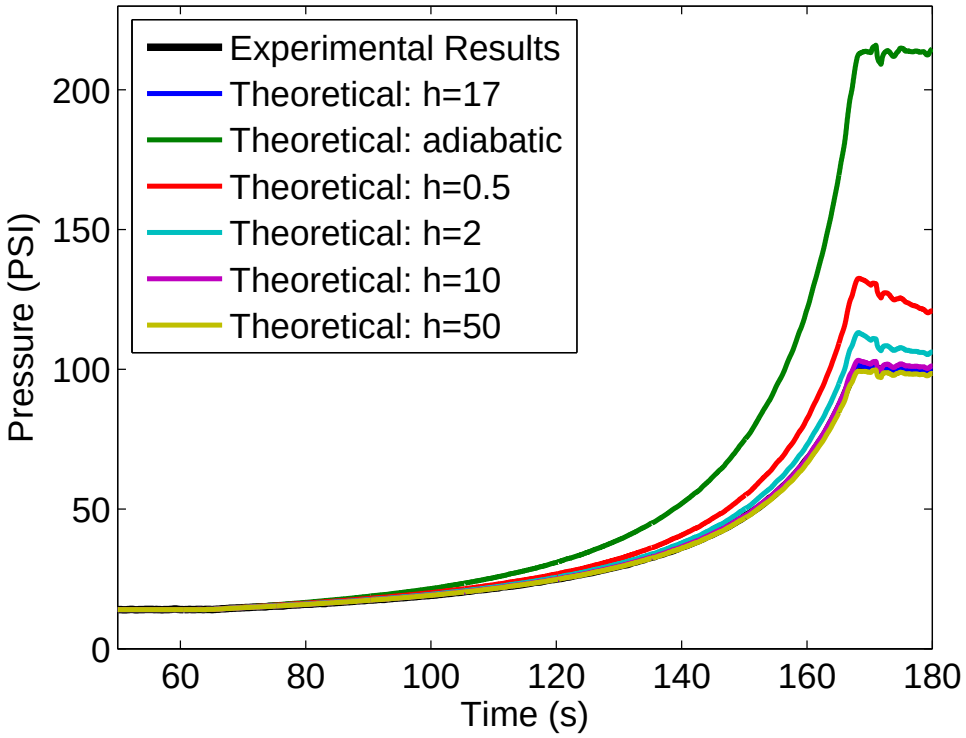

Figure 6.11: Air pressure vs. time with the 1.70 g mesh and 4 cc/s flowrate. Experimental data is compared to simulation output for various constant h's.

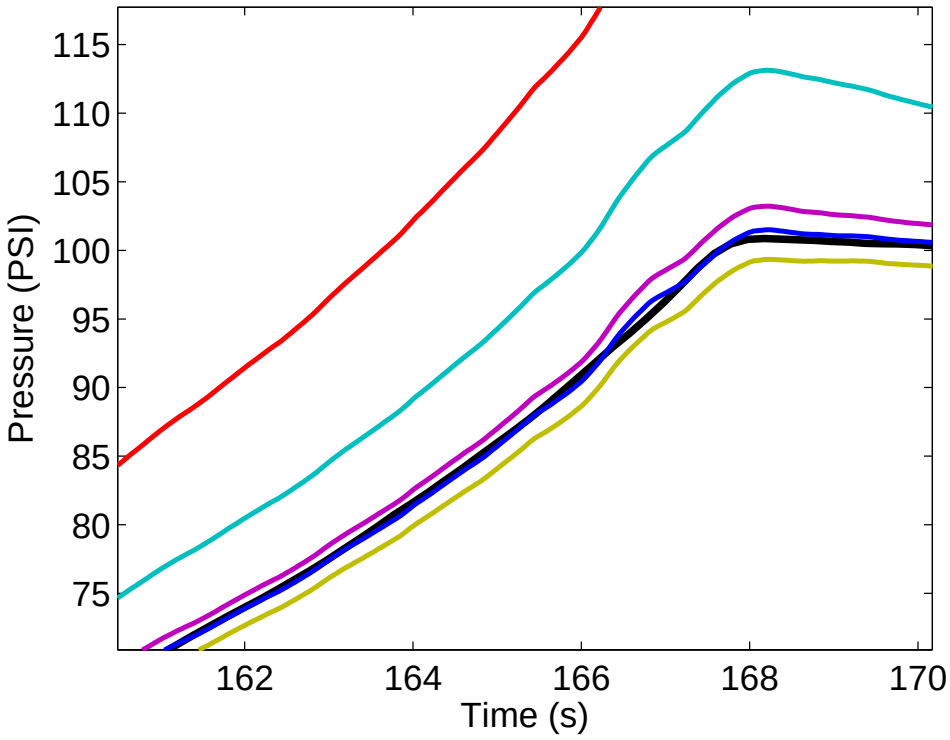

Figure 6.12: Figure 6.11 zoomed in to show the good fit. See figure 6.11 for the legend.

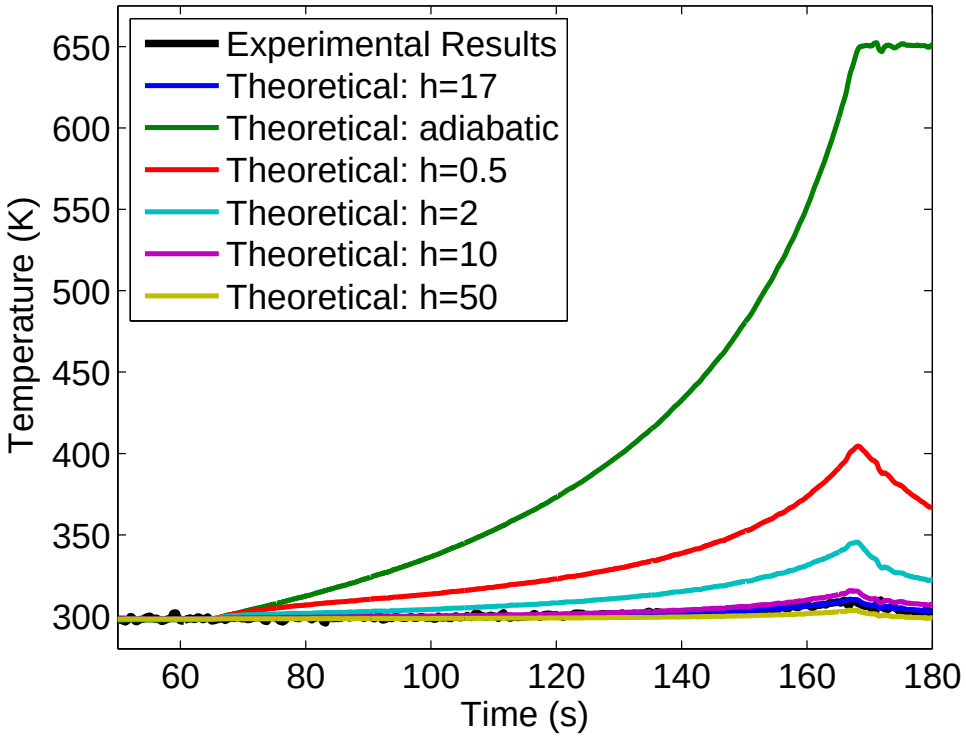

Figure 6.13: Calculated air temperature vs. time with the 1.70 g mesh and 4 cc/s flowrate. Experimental data is compared to simulation output for various constant h's.

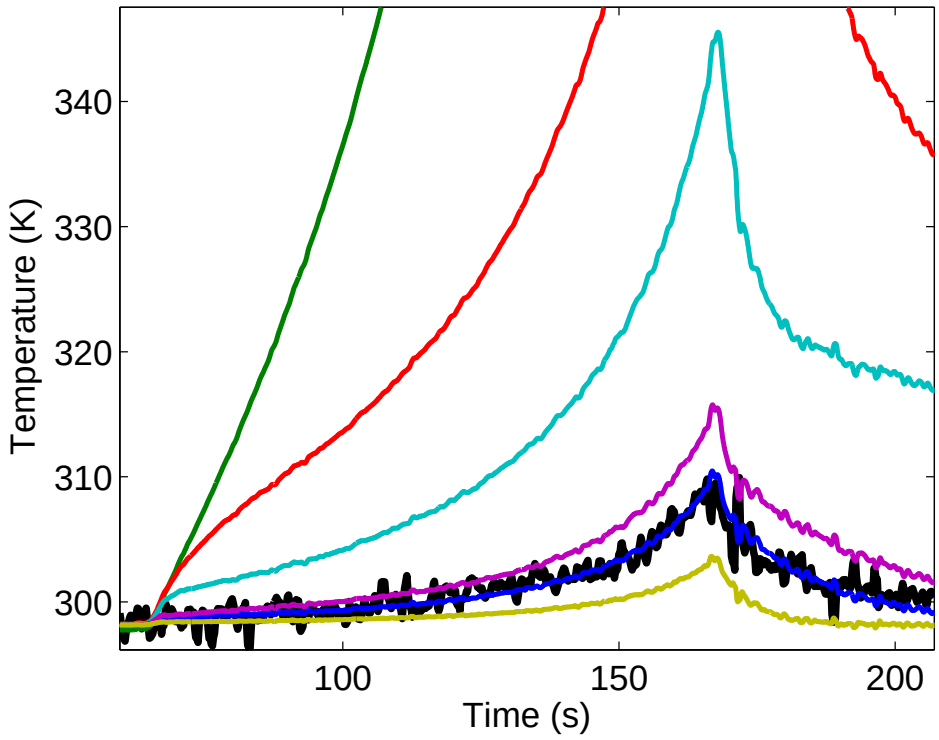

Figure 6.14: Figure 6.13 zoomed in to show the good fit. See figure 6.13 for the legend.

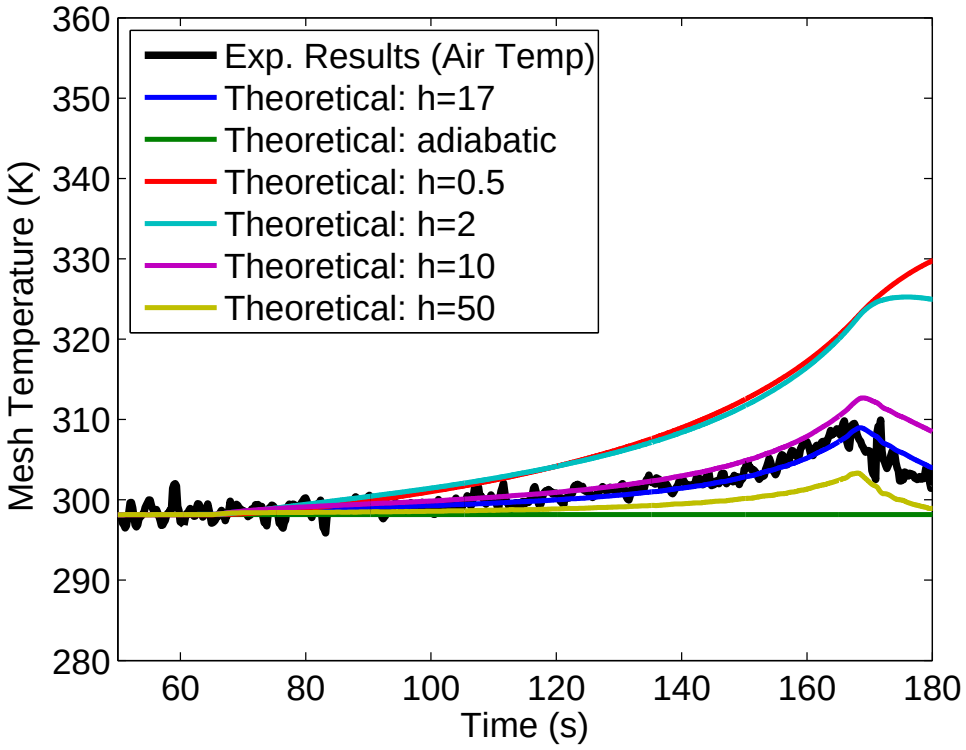

Figure 6.15: Mesh temperature vs. time with the 1.70 g mesh and 4 cc/s flowrate. Experimental data for air temperature is compared to simulation output for various constant h's.

6.2 Minitube experiment and model

As with the mesh experiments, the results are divided into results from the experiments and results from the model for comparison. This section summarizes both, starting with the experimental results.

6.2.1 Results from experiment

From among the data taken without the thermocouples, one trial utilizing the minitube array and one trial without will be presented and discussed. These two data sets were chosen because the compression storage power for each case is nearly identical, isolating the effect of the minitube array on temperature, and consequently, efficiency. Additional data, not reported here, corroborated the trials chosen, but slightly different compression times or compression ratios disqualified them for being the comparison runs because these variations influenced the temperature change. Pressure for the whole trial, as well as initial temperature and initial volume, were recorded for each trial. Pressure profiles during the compression event are plotted in Figure 6.16. The very close match in compression time and compression ratio can be observed. The compression storage power calculated from equation (5.8) is 24.6 W (or 107 kW/kg of air) for both trials. Using equation (5.15), the peak temperature differences, ΔT, with and without the minitube array are calculated to be 108.8 K and 14.6 K. Thus the minitube effects a temperature reduction of 86.6%.

From among the data taken with the thermocouples, one trial utilizing the minitube array and two trials without have been selected for comparison. Again, matching compression storage power was the criteria for selection. The data not selected for comparison agreed in nature with the selected results, but since several variables varied, the influence of the minitube array could not be differentiated from the influence of variation in, e.g., compression time. Pressure, temperature, and initial volume were recorded for each trial. Pressure data for the complete trial are plotted in figure 6.17. Each pressure curve depicts a period at ambient pressure, followed by compression to 676 kPa (98 psi), followed by a constant volume (isochoric) period, then expansion, and finally a period at ambient pressure. The water interface velocity was intended to be constant, but the rounded pressure peak indicates protracted deceleration. An acceleration period also

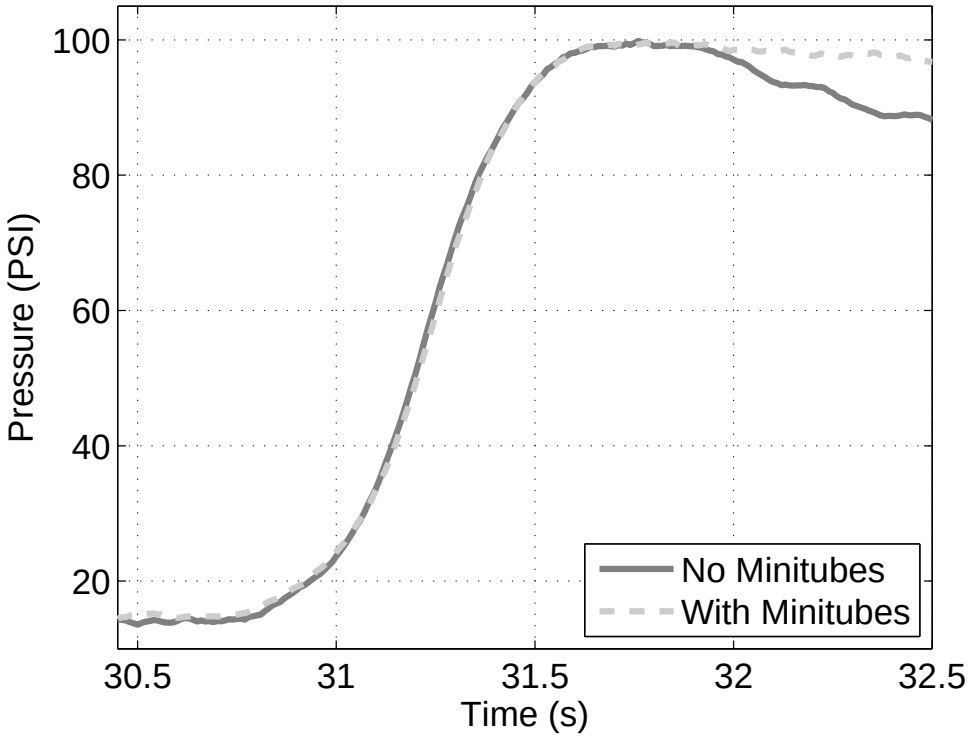

Figure 6.16: Pressure vs. time with and without the porous insert. These data were taken without the thermocouples or porous disks.

seems evident at the beginning. The steep drop off in pressure following compression without the minitubes array indicates the relatively large temperature change during compression. Figure 6.18 shows the same data zoomed in at the compression event. The compression ratios vary by less than 1.5% ($\Delta r < 0.1$), compression times vary by less than 9% ($\Delta t_c < 0.1$), air masses vary by less than 2% ($\Delta m_{\text{air}} < 10mg$), and initial temperatures vary by less than 1% ($\Delta T_0 < 3K$). The compression powers, calculated from these quantities, are 24.7 W and 25.1 W for the trials with no minitubes, and 23.1 W with the minitubes. The power with the minitubes is less by 9%, but it is the closest match from the data taken. The calculated volume-averaged peak temperatures for the two trials without the minitubes and the one trial with are, respectively, 409.2 K (276.9 ° F), 410.3 K (278.9 ° F), and 312.8 (102.8 ° F). These correpond to temperature differences of 108.8 K, 112.3 K, and 15.0 K. Thus, for similar power, the minitube array plus porous disks offer an 86.2% reduction in temperature compared to trial 1 with the empty chamber and 86.6% reduction compared to trial 2. This compares favorably to temperature reduction seen in the case without the thermocouples, above.

The temperature data from the four thermocouples are shown for the whole trial in figure 6.19. Figure 6.20 shows the same runs, zoomed in at the compression event. Peak recorded temperatures for the trial with the minitube array (plus porous disks) are in the range of 315–335 K. Peak recorded temperatures for the two trials without the minitube array are in the range of 370-410 K.

The volume-averaged temperatures during the isochoric cooling period, calculated from equation (5.14), are plotted with the thermocouple data in figures 6.21 and 6.22. For the case with the minitube array, the volume-averaged temperature is significantly less than the temperatures taken at the locations of the thermocouple junctions. This reflects the reality that the majority of the cooled air volume during compression is in the vicinity of a heat sink, but the thermocouples are in the plenum, which is the only region lacking embedded heat transfer surfaces. The volume-averaged temperature is more representative of the temperatures within the minitubes than the temperature within the plenum.

For the case without the minitube array, the volume-averaged temperature depicts rapid cooling, beginning at the time corresponding to the peak pressure. As can be seen in figures 6.21 and 6.22, the volume-averaged temperature passes through, or very

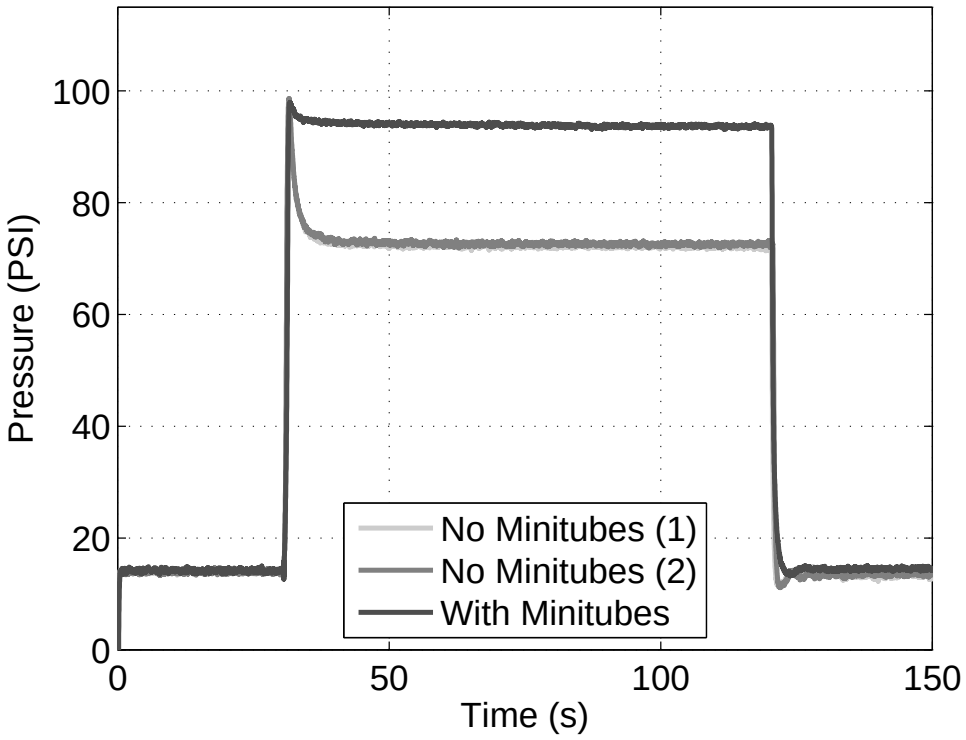

Figure 6.17: Air pressure data with and without the porous minitube array.

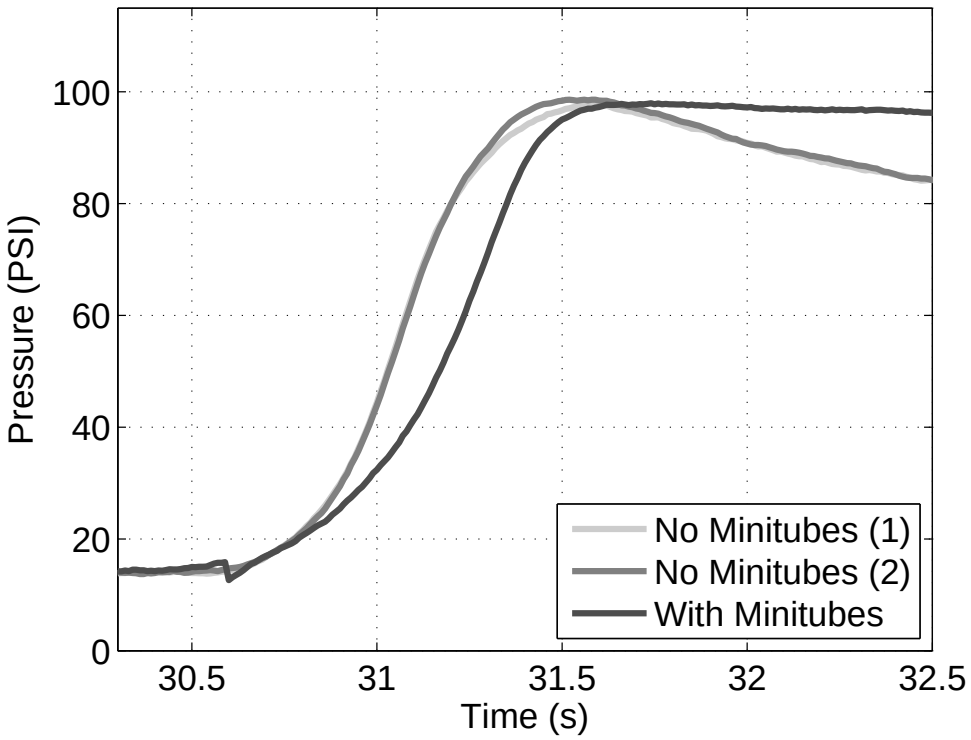

Figure 6.18: Air pressure data during compression with and without the porous minitube array.

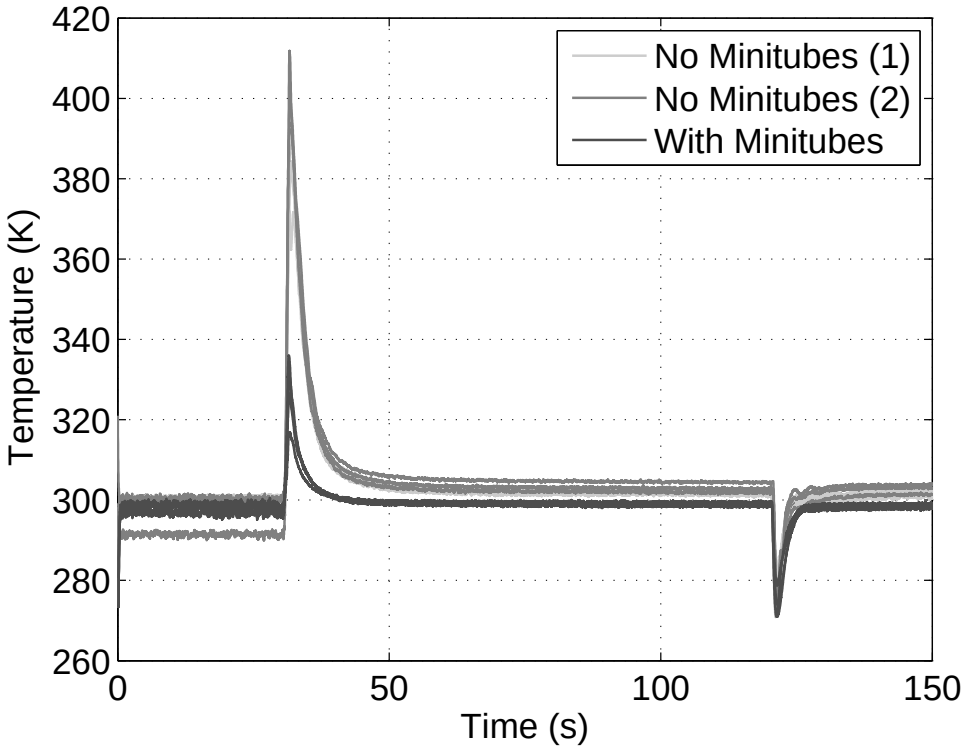

Figure 6.19: Local air temperature data from the four thermocouples with and without the porous minitube array.

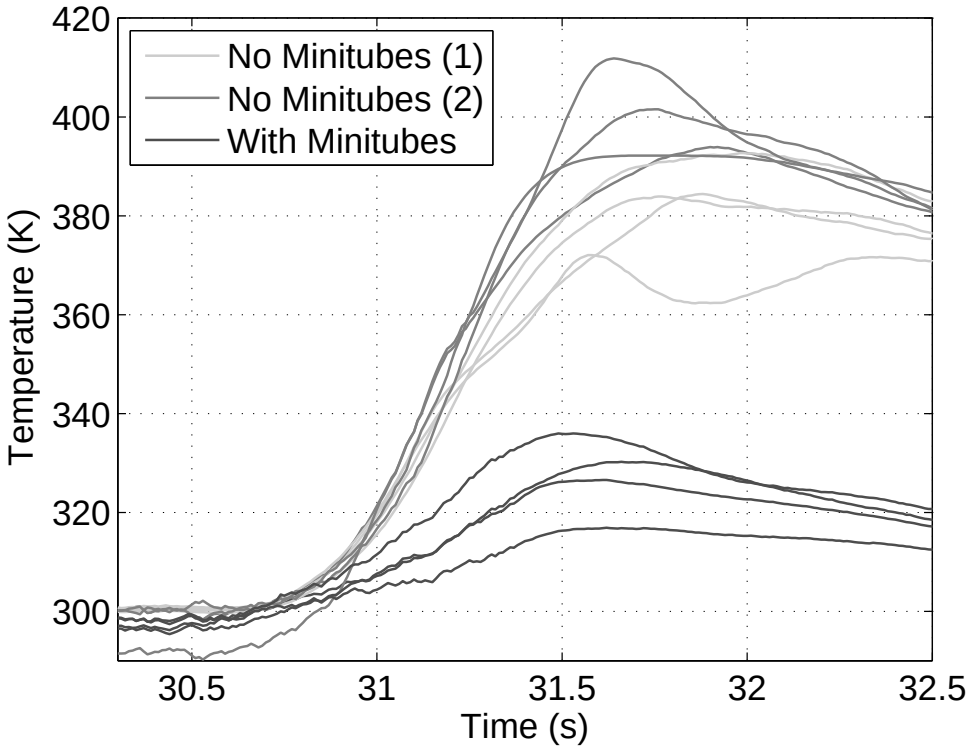

Figure 6.20: Local air temperature data during compression from the four thermocouples with and without the porous minitube array.

near, the peak of each thermocouple trace. This behavior is consistent with an inability of the thermocouples to follow the actual air temperature. As discussed in chapter 4, section 4.1, the thermocouple response time is expected to be about 0.1 seconds or greater. What is happening in figures 6.21 and 6.22 is that the thermocouple junction temperature cannot keep up with the rapidly increasing temperature, which likely peaks at nearly the same time as does the pressure, at about 31.5–31.6 seconds. Then, the air begins to cool, decreasing the temperature difference between the thermocouple junctions and the local air temperatures, and, therefore, decreasing the heat transfer rate. This can be seen by the very rounded peaks in the thermocouple data and the fact that the peaks take place later than does the pressure peak by, on average, 0.2–0.3 s. Eventually, the local temperature becomes less than the junction temperature, at which point the junction temperatures begin following the local temperatures again. Note that it cannot be said with certainty whether the thermocouples for the other trial (the case with the minitube array) follow the temperature without error, or not. However, the peak temperatures, despite being at different temperatures, occur at nearly the same time and this peak temperature is reached slightly earlier than the peak pressure is reached (by, on average, about 0.1 s). This is possibly due to the deceleration of the water interface at this point, which allowed the temperature to begin cooling, despite the fact that pressure continued to rise slowly.

6.2.2 Results from model

The Hohenberg correlation for the heat transfer coefficient, as described in chapter 3, was used in the simulation of the compression event that was without the minitube array. A constant flow rate, and, therefore, a constant interface velocity, was assumed. Initial temperature, pressure, air mass, compression ratio, and chamber geometry match the experimental parameters. The Hohenberg correlation includes two constants, C_1 and C_2, that must be tuned. Lowering C_1 by 23% to a value of 100 and lowering C_2 by 11% to 1.25 resulted in a good match in magnitude between the simulated volume-averaged air temperature and the measured volume-averaged air temperature. The results for air pressure and volume-averaged air temperature are provided in figures 6.23 and 6.24. That the experimental trials included a period of acceleration is evident from the comparison between the model results and experimental results. A gradual beginning is seen

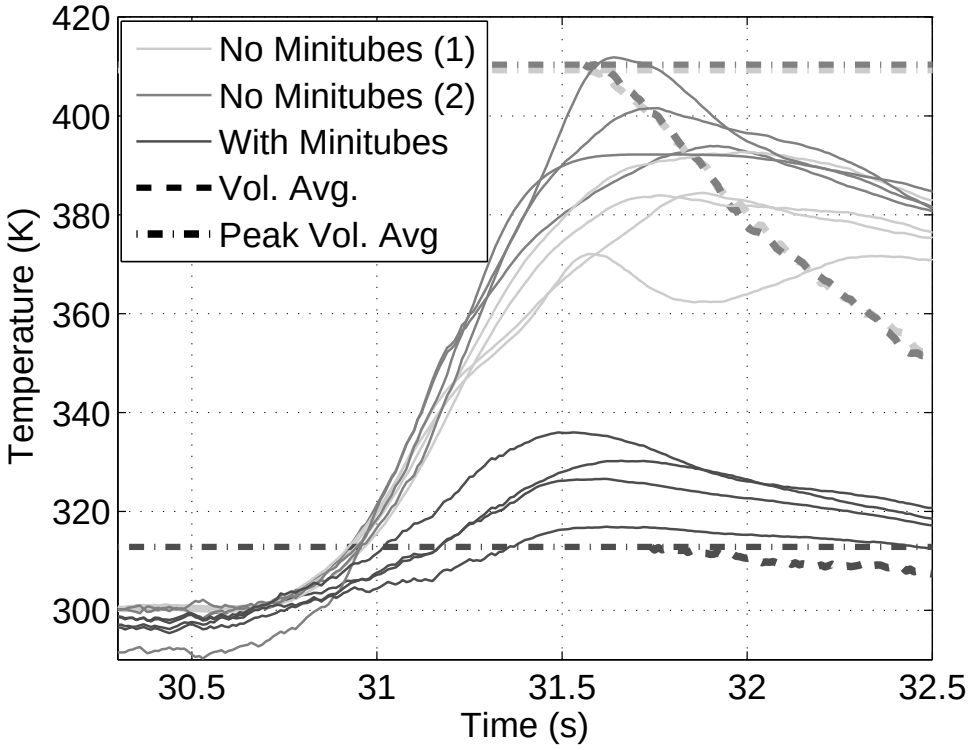

Figure 6.21: Local air temperatures from the four thermocouples (solid lines) and the volume-averaged temperature (dashed lines) during the compression event and shortly following. Results are shown with and without the porous minitube array.

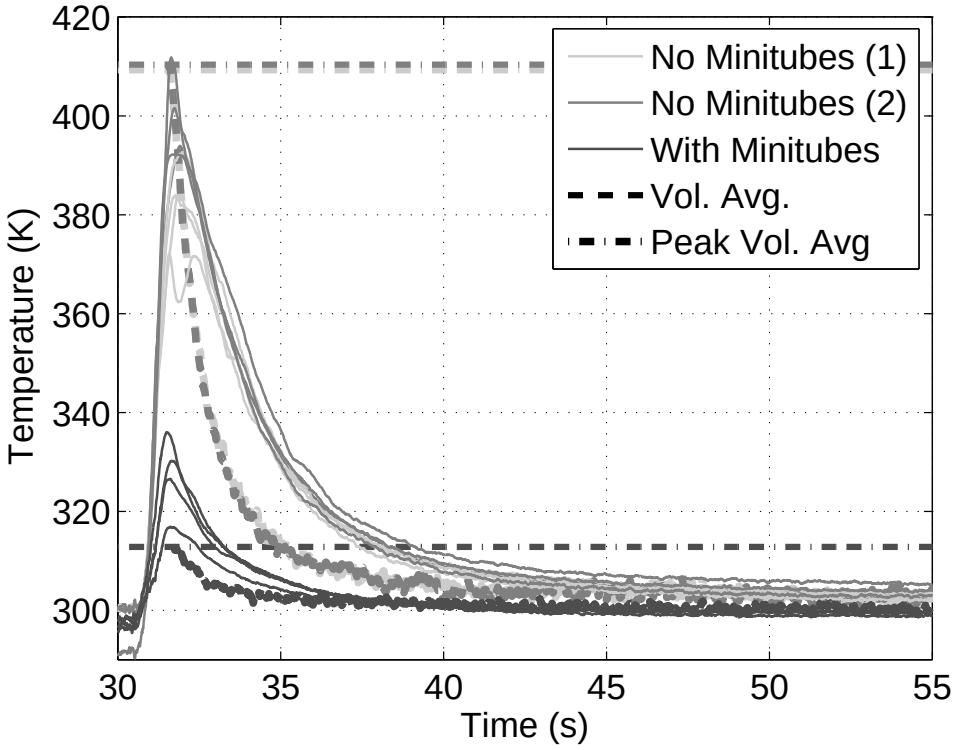

Figure 6.22: Local air temperatures from the four thermocouples (solid lines) and the volume-averaged temperature (dashed lines) during the constant-volume cooling. Results are shown with and without the porous minitube array.

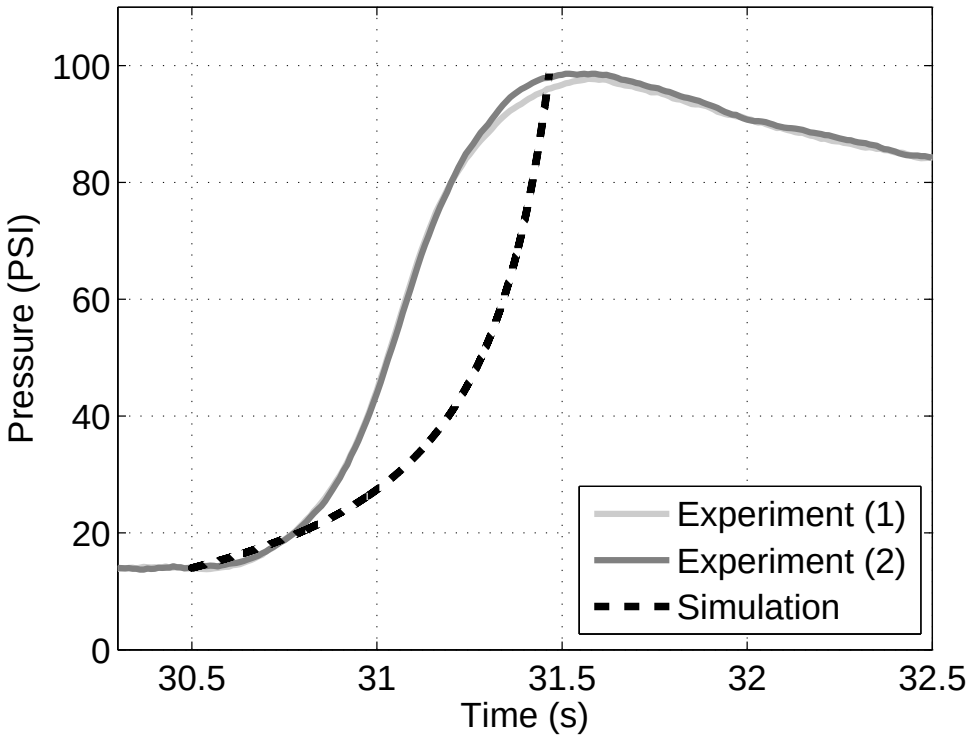

Figure 6.23: The measured pressure and simulated pressure for the compression event.

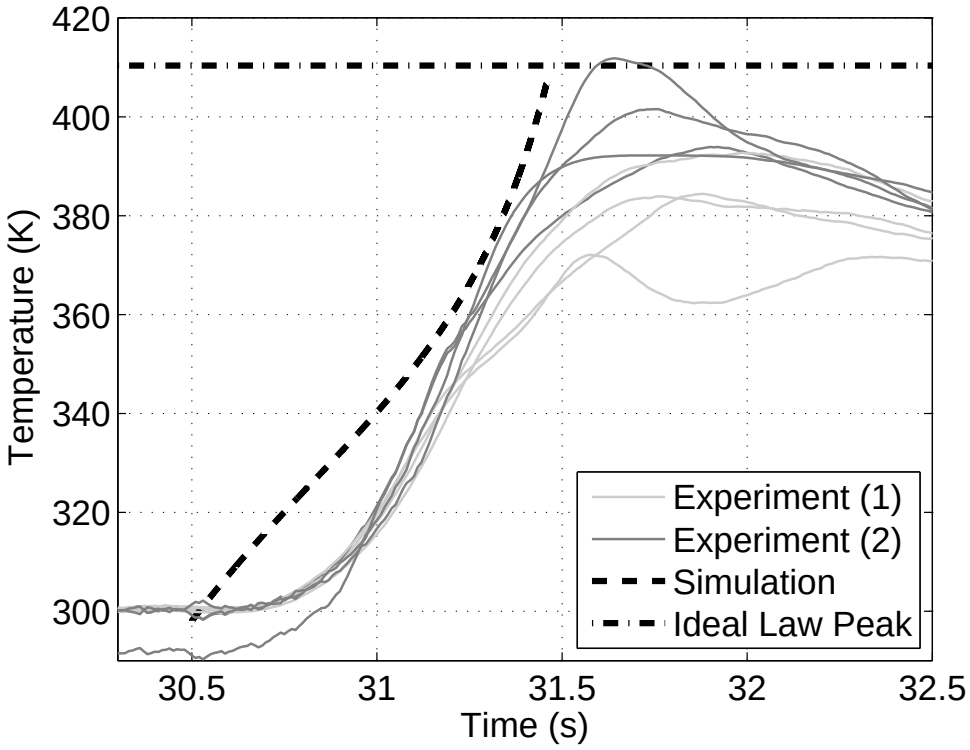

Figure 6.24: The local measured temperatures from the four thermocouples and the simulated volume-averaged air temperature and minitube temperature for the compression event. The dashed line provides the magnitude of the measured peak volume-averaged temperature.

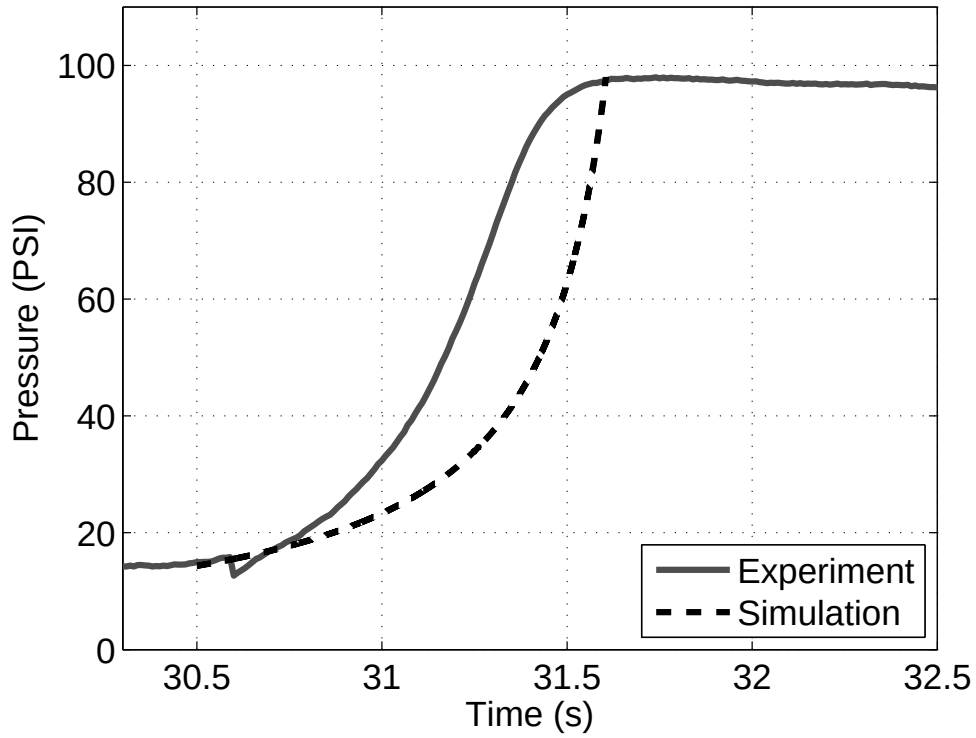

Figure 6.25: The measured pressure and simulated pressure for the compression event.

in the experimental results, whereas an immediate jump in temperature and pressure is shown in the model results.

The heat transfer model developed in chapter 3 was used in the simulation of the compression event with the minitube array. A constant and uniform interface velocity is assumed. Initial temperature, pressure, air mass, compression ratio, and chamber and minitube geometry match the experimental parameters. The simulated results for air pressure, volume-averaged air temperature, and volume-averaged minitube temperature are provided in figures 6.25 and 6.26. Figure 6.26 shows that the simulation temperature rises only to 304.6 K, whereas the magnitude of the volume-averaged temperature was measured to be 312.8 K. Recall that four different components of heat transfer were modeled: heat transfer between the air within each minitube and the inner surface of each minitube, heat transfer between the air within the interstitial space formed by a cluster of three minitubes and outer surface of the minitubes, heat transfer between the

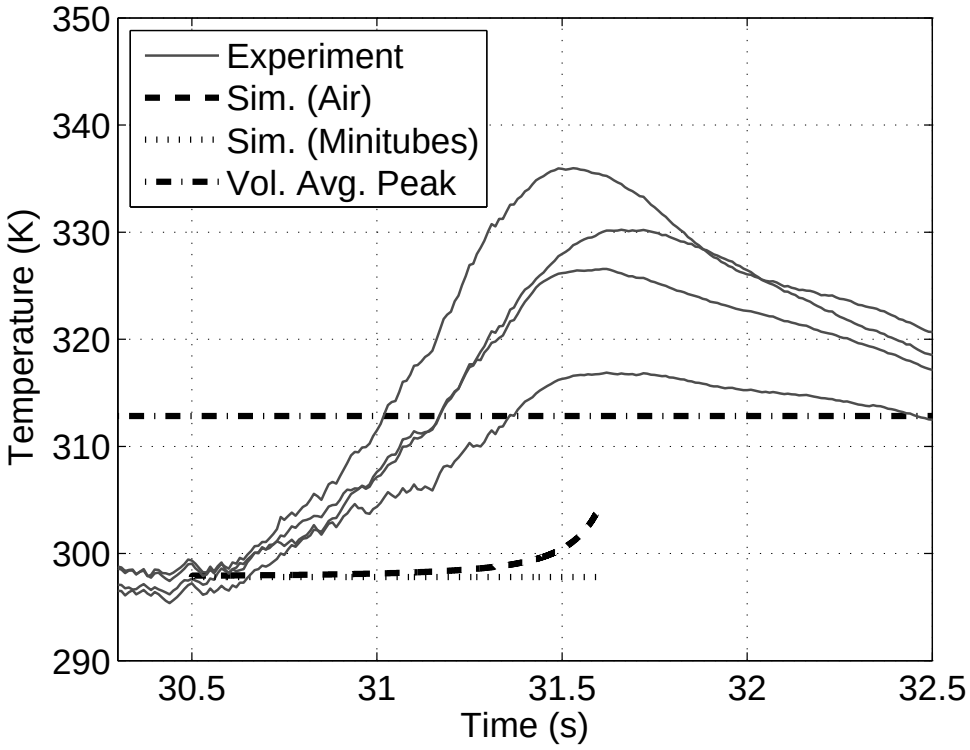

Figure 6.26: The local measured temperatures from the four thermocouples and the simulated volume-averaged air temperature and minitube temperature for the compression event. The dashed line provides the magnitude of the measured peak volume-averaged temperature.

air adjacent to the wall and the cylinder wall, and the heat transfer between the air in the plenum and the bounding surfaces of the plenum. The contribution from each of these components is shown in figure 6.27. The heat transfer to the outer surfaces of the minitubes is the dominant heat transfer path. This is due to three factors. First, the surface area is the largest, twice that of the inner surfaces. Also, because of the smaller hydraulic diameter, the heat transfer coefficient is larger outside the minitubes relative to inside the minitubes: 204 relative to 61 W/m^2-K as shown in figure 6.28. Thirdly, the model assumes a uniform air temperature, so the heat transfer rate increases as the volume-average temperature increases. The first two factors are more appropriate than the third. The temperature of the air within the minitube array, and in particular within the smallest interstitial channels, is less than the volume-averaged temperature. Thus, the model incorporates an artificially high temperature difference, which drives artificially high heat transfer rates. To compensate for this physical non-reality, an "efficiency" is assigned to the dominant heat transfer component, with a value of one equivalent to the unaltered case. It was found that the efficiency of the heat transfer to the outer surfaces of the minitubes must be decreased by 78% to achieve a final temperature equal to the measured values. The results are shown in figures 6.29 and 6.30.

Using these simulations, the work input can be calculated. For the case without the minitubes, the work in is 39.1 J, for an efficiency of 74%. For the case with the minitubes, the work in is 29.5, for an efficiency of 98%. Thus, the minitube array plus porous disks provide a 32% increase in efficiency, at nearly constant power.

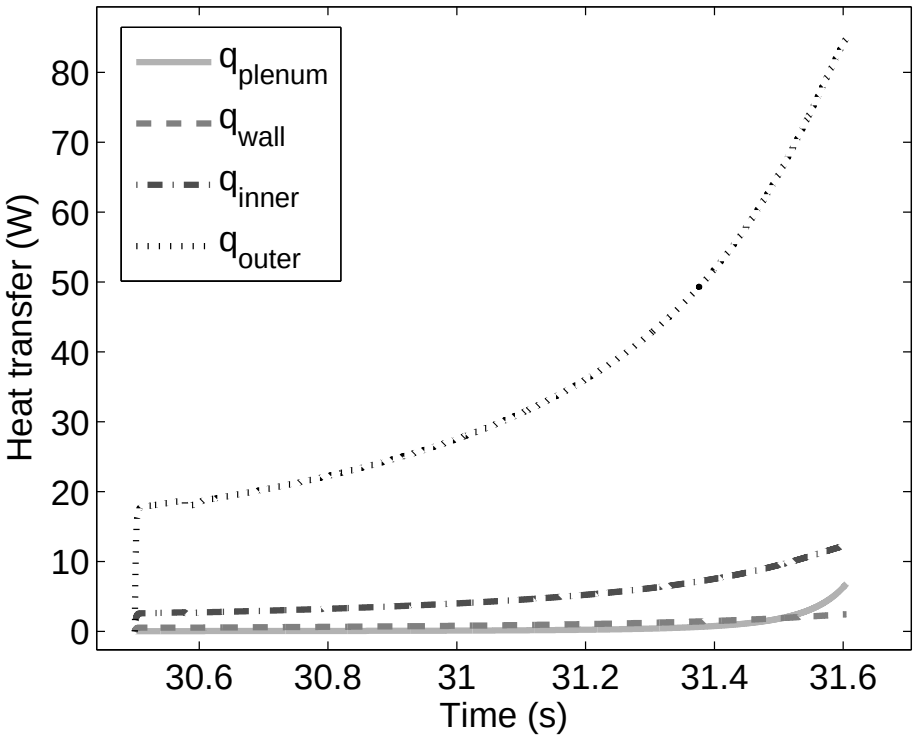

Figure 6.27: The modeled heat transfer rates as a function of time. The heat transfer to the outer surface of the minitubes is artificially high due to the uniform air temperature assumption.

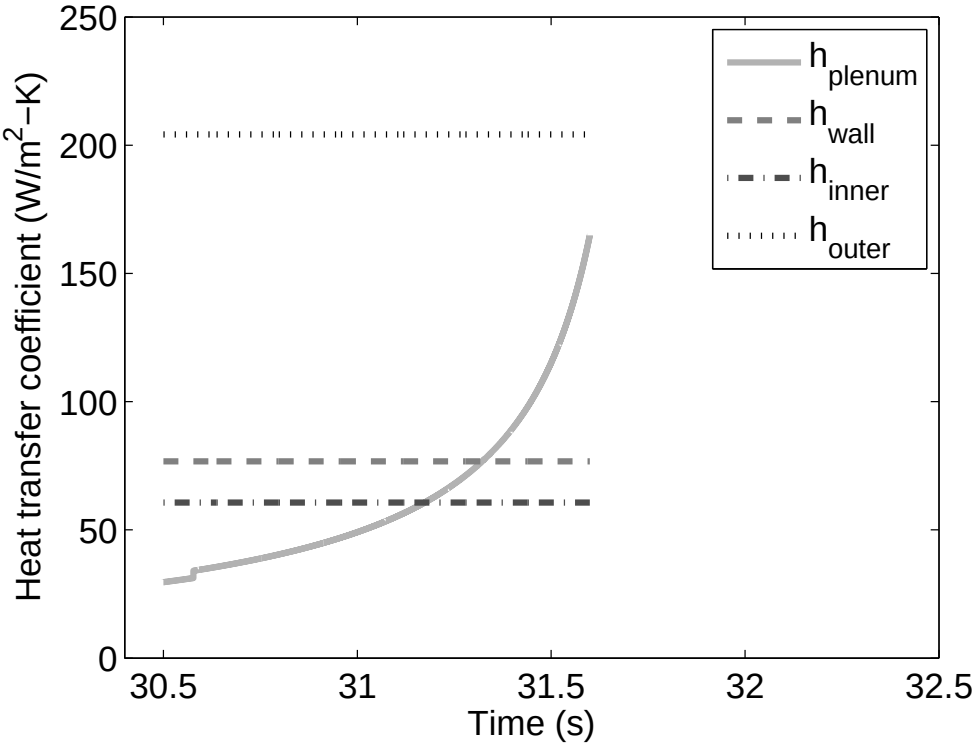

Figure 6.28: The modeled heat transfer coefficients as a function of time. The constant values are based on equations (3.43)–(3.45). The heat transfer coefficient for the plenum is based on Hohenberg's correlation as in equation (3.34).

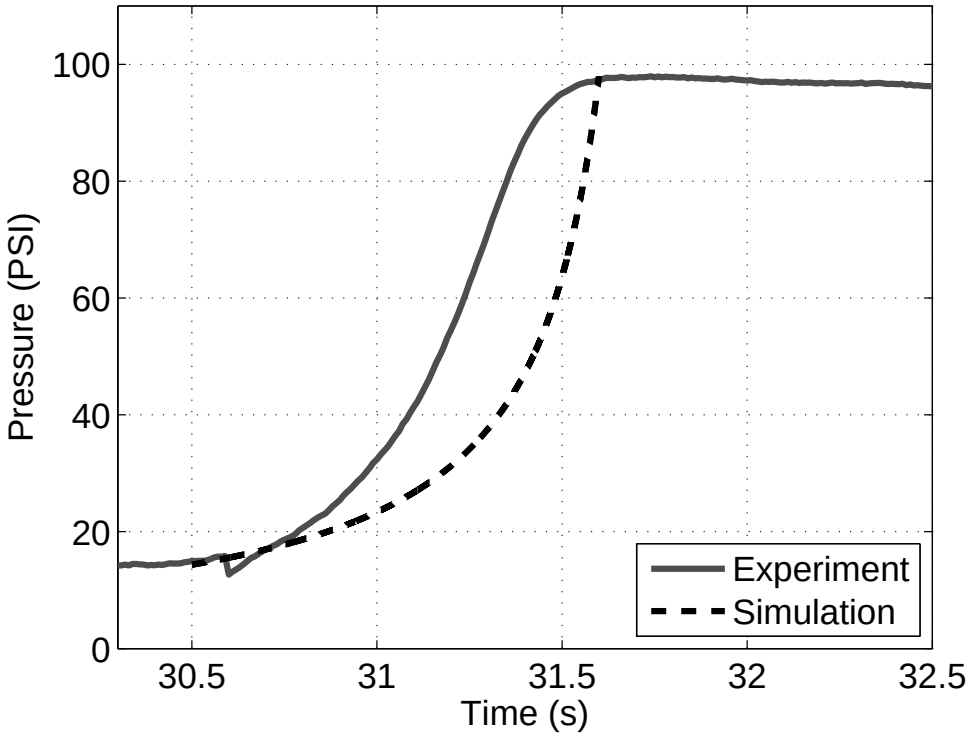

Figure 6.29: The measured pressure and modified simulated pressure for the compression event.

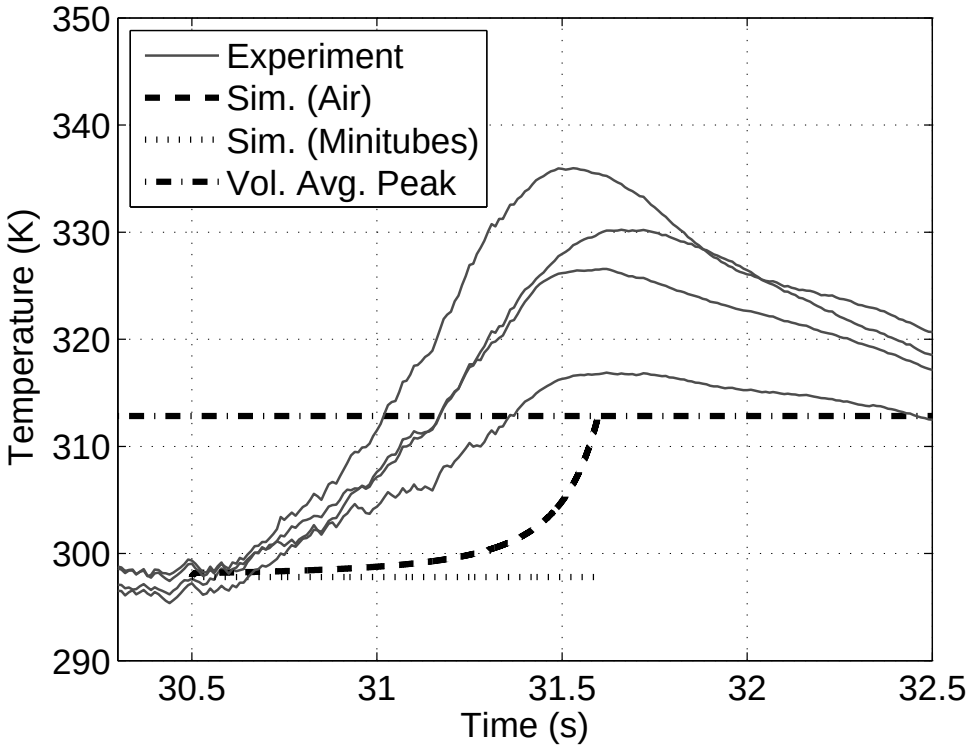

Figure 6.30: The local measured temperatures from the four thermocouples and the modified simulated volume-averaged temperature and minitube temperature for the compression event. The dashed line provides the magnitude of the measured peak volume-averaged temperature.

Chapter 7

Discussion

7.1 Mesh experiments

There are a couple observations from the results to be discussed. First, it is worth commenting on the several advantages offered by the mesh insert. First, it increases the thermal capacitance of the air space. Aluminum has a specific heat of 0.90 J/g-°C. Air has a constant volume specific heat of 0.72 J/g-°C. The mass of the air in the cylinder is initially 0.54 g, so the thermal capacitance without porous media is less than 0.5 J/°C. The thermal capacitance of the small mesh is about 1.5 J/°C, for a 300% overall improvement. The thermal capacitance of the large mesh is about 4.8 J/°C, which, combined with the thermal capacitance of the air, is over 10× the thermal capacitance of the air alone. A second benefit of the mesh is the increased surface area available for heat transfer. Without the mesh, the initial surface area is the surface area of the compression chamber, about 400 cm^2. These advantages in thermal capacitance and surface area exist despite very high porosities (over 99%). The very small total volume of a porous medium is helpful in terms of volumetric system energy density; that is, only a small mesh volume is required to obtain fairly significant effects–no supplemental or external hardware (e.g. motors, hoses, valves, etc) or power supply is necessary.

In figures 6.6 and 6.7, it is interesting to note that the magnitude of the heat transfer is very similar for the three cases, despite the fairly large differences in peak temperature. (This similarity was observed for all the trials, as may be seen in appendix E). This is likely because every case tested is relatively near isothermal compression. Compressing

the air adiabatically using a pressure compression ratio of 7 would lead to a temperature difference of 222 K. The maximum difference achieved in the experiment is 42 K.

The sample calculated instantaneous hA products and heat transfer coefficients are shown in figures 6.8 and 6.9, respectively. More figures showing the heat transfer coefficients can be found in appendix E. Due to the assumptions in estimating the mesh surface area and the noise in the signal, only general trends and order-of-magnitude conclusions should be offered. The calculated hA vs. time curve exhibits large fluctuations that are occasionally negative. The negative values are most likely due to noise in the signal since a physical interpretation requires the volume-averaged temperature to be less than the sink temperature, something that should not happen during compression. So, looking past suspicious behavior likely due to noise, the underlying trend in hA is a gradual decrease with time. However, there are exceptions, such as the trial with the big, 5.48 g mesh in figure 6.8. Considering that the heat transfer area is also decreasing with time, this trend may not be surprising. What may be surprising is that the heat transfer coefficient appears to be fairly constant over the compression process in figure 6.9. The trend for cases of other compression speeds (as may be seen in the appendix E) are less conclusive, but, in general, h's seem to be fairly steady or oscillatory before a sudden decrease near the time of peak pressure. It is interesting to note that in every case tested, the values of h with the mesh end their descent before the end of descent in meshless trials. This is likely because without the porous mesh, a larger temperature difference exists at the peak pressure, which continues to drive heat transfer; so, h must be positive longer after the peak pressure is reached than when the meshes are used.

The fitted values of h are mostly in the same range as the calculated values of h from section 6.1, quoted there to be from 15 to 50 W/m^2-K. Good quantitative agreement is seen with the 1.70 g mesh for both methods. However, the no mesh case "measured" values are somewhat smaller than the best fit h's used in the simulations. Further, the "measured" values of h are much smaller than the best fit h's for the 5.48 g mesh case. This is most likely due to the high signal-to-noise ratio (e.g. see figures E.8–E.11 in appendix E). The best fit values of h are probably the more accurate since the signal-to-noise is much better. Surprisingly, h seems to tend downward as the piston velocity increases according to the best fit constant h's used in the model. This is partly explained by the fact that the relative motion between the mesh and air does not

change very drastically, despite large changes in piston velocity. The uncertainties in the values of h are also very large. As can be seen in figure 6.13, the difference in peak temperature due to an increase in the heat transfer coefficient from 0 W/m^2-K to 0.5 W/m^2-K is much greater than the difference in peak temperature due to the increase from 10 W/m^2-K to 50 W/m^2-K. The higher the value of h, the larger a change in h must be to effect a one degree change in peak temperature. Due to the uncertainty in the temperature data, the value of h becomes even more uncertain, particularly for the larger meshes.

Nevertheless, the overall performance of the model is impressive. The simulated model results match well despite the simplicity of the model and the use of a constant h. However, it must be kept in mind that the compression speeds in the mesh experiments are very slow relative to typical compressors. While the constant h assumption fits well at these slow speeds, stronger transient effects and the increased role of turbulence may complicate the heat transfer at higher speeds. In these cases, a turbulent heat transfer correlation for a compressor may be appropriate.

7.2 Minitube experiments

There are several observations from the experimental and model results worth discussing. First, it is clear that the the compression of air using a minitube array insert offers substantial reductions in temperature. The minitube has several positive effects. First, it increases the thermal capacitance of the air space. Copper has a specific heat of 0.385 J/g-°C. Air has a constant volume specific heat of 0.72 J/g-°C. The mass of the air in the cylinder is about 0.33 g, so the thermal capacitance without porous media is less than 0.25 J/°C. The thermal capacitance of the minitube array is about 1320 J/°C. This is 5000× higher than capacitance of the air alone. Such a large high thermal capacitance is not necessary. As can be seen by the modeled minitube temperature, figure 6.26 or figure 6.30, the minitube array is essentially isothermal. Decreasing the thermal capacitance would be helpful if doing so meant the volume of the system could decrease, or air could be added instead. For example, if the minitubes were replaced with tubes with thinner walls, the total volume of the insert would decrease, and the initial volume of air would increase. Thus, in the same system volume, the total energy

increases. Further analysis is needed to optimize the thermal capacitance of the air space.

A second benefit of the minitube array is the increased surface area available for heat transfer. Without the minitube array, the initial surface area is the surface area of the compression chamber, about 200 cm^2. The initial surface area of the minitube array is about 9500 cm^2, almost a 50-fold increase. The additional surface area accounts for the vast majority of the heat transfer, as can be seen in figure 6.27. It is also implied in figures 6.26 and 6.30, where, later in the compression process when the water interface approaches the end of the minitube array, the temperature rapidly rises. Even more clearly, figure 6.21 shows that the air temperatures in the plenum are much higher than the volume-averaged temperatures. The inevitable conclusion is that, from a heat transfer perspective, the minitubes should extend even nearer the cap for even better heat transfer. If restrictions prevent this from happening, some other technique should be used to break up the relatively hot core in the plenum region. Droplet sprays would be one possibility.

As discussed in chapter 4, section 4.2, a fountaining effect was observed. Water flowing through the minitube array arrived at the end of the array at various times. The water that arrived first would jet into the plenum. The cold splashing water breaks up into droplets, adding heat transfer surface area and disturbing the flow. Doing so helped the heat transfer, but made using thermocouples in the plenum impossible. So, as discussed, porous disks were used to prevent the jetting effect. In later designs, it may be possible to manipulate the fountaining effect to the benefit of the system. However, care must be taken to prevent the fountaining water to drain into the channels still containing air. Trapping of the air is a very undesirable outcome, as work will have been expended to compress the air, but it would not be moved to the accumulator and stored. The trapped air is essentially dead volume.

Regarding the simulation results, it is observed that significant differences exist. Much of this may be attributed to difference in the volume profile. The simulation results implemented a constant interface velocity, whereas acceleration and deceleration are detected in the measured results. The modeling of heat transfer with the minitube array is more troublesome, as the discrepancy between the modeled results and the measured temperatures is significant. As observed in chapter 6, section 6.2, this is due

to the uniform-temperature assumption. The temperature of the air within the smaller channels in the minitube array is much smaller than the volume-averaged temperature, particularly toward the end of the compression event; however, the model does not recognize this difference. Thus the heat flux is over-predicted because the perceived temperature difference is greater than the real temperature difference.

A final observation worth noting occurred during compression tests without the porous minitube array. During compression, the clear polycarbonate walls of the compression cylinder became foggy and opaque. This effect appeared to be only at or near the relatively cold surface. It is probably caused by condensation as the air heats up and increases in pressure while the walls and near-wall boundary layers remain cooler.

Chapter 8

Trajectory Optimization: Problem Statement

It is desired that such compression and expansion is both energy efficient and power-dense. For given heat transfer characteristics, however, these two objectives stand in stark opposition: achieving greater efficiency requires more time. The following three chapters address the problem of optimizing the compression and expansion processes given the heat transfer characteristics. This will be done by manipulating how the air is compressed or expanded: the pressure-volume trajectory.

As explained in chapter 3, the pressure-volume trajectory is an unambiguous description of the state of the gas throughout a compression or expansion process, assuming the gas is ideal and of uniform temperature. The efficiency, defined in equation (3.5) can be determined from the pressure-volume trajectory. If the heat transfer ability of the system can be modeled, then the time, and thus power (equation (3.7)), for the process is also known. The goal, then, is to determine the PV curve that maximizes the capabilities of the heat transfer. More specifically, the goal is to determine the trajectory such that for a given efficiency, no other trajectory absorbs/provides more power, and for a given power, no other trajectory is more efficient. This situation is defined as

being Pareto optimal. Generally, the objective is to

$$\begin{aligned} \underset{\mathbf{x}}{\text{maximize}} \quad & \eta(\mathbf{x}) \\ \text{subject to} \quad & \text{Pow}(\mathbf{x}) \geq \text{Pow}^*, \\ & \mathbf{c}(\mathbf{x}) \geq \mathbf{0}. \end{aligned} \tag{8.1}$$

where Pow^* is some prescribed power requirement and $\mathbf{c}(\mathbf{x})$ are potential feasibility constraints on the variables. An equivalent problem is to maximize power for a given efficiency.

8.1 Overview of Solution Method

One conventional approach to nonlinear constrained optimization problems, such as the one proposed here, is the use of Lagrange multipliers and the Karush-Kuhn-Tucker (KKT) conditions. For an introduction to Lagrange multipliers and the KKT conditions see, e.g. [100][101][102]. For a demonstration of the use of Lagrange multipliers in a similar context, see [103] or [94]. The Lagrange multiplier method is, in essence, a process for converting a constrained problem into an unconstrained problem by moving the constraints into the objective function and multiplying each constraint by a scalar constant called the Lagrange multiplier. The Lagrange multiplier associated with a particular constraint may be interpreted as how much that constraint "hurts" the optimal solution. When the Lagrange multiplier is zero, optimization without that constraint would yield the same solution. In most cases this indicates the constraint is not "active." When the Lagrange multiplier is non-zero, the constraint is active and the magnitude of the Lagrange multiplier reflects how enforcing the constraint affects the value of the objective function.

The KKT conditions are a more general manifestation of the Lagrange multiplier method. In addition to using Lagrange multipliers to move constraints into the objective function, they also stipulate the sign of the Lagrange multiplier and enforce complementary slackness–a required characteristic of most differentiable and well-behaved constraint functions. The result is that one has a set of M differential equations and M unknowns. Solutions satisfy first order optimization criteria. Local optimality is proven by demonstrating that the solution is the appropriate extremum for the type of problem

under review. If the objective function and constraints are convex functions over the interval of interest, the local extremum is also the global extremum over that interval.

8.2 Modeling of the heat transfer

As with the experimental models, heat transfer is assumed to take the form

$$q = hA\,(T_0 - T) \tag{8.2}$$

where hA must be modeled in some way. In the present work, it is assumed that hA is a function of instantaneous air volume, V. Several studies have dealt with piston trajectory optimization before, as discussed in the literature review. However, in all those analyses, hA is constant. Notably, previous work focused on the open accumulator [94] invoked this assumption. Some studies suggest that over a limited operating range, this is an appropriate assumption [104][105]; however, this is not true in general. The heat transfer coefficient, h, can be a complicated function of gas velocities [27] [31], temperatures [39], unsteady flow features [23], boundary layer growth rates [37][38], and other factors [30]. The surface area available for heat transfer, A, is typically a function of air volume. Of these influences on hA, air volume is one of the most accessible and important. This is particularly true when the potential surface area changes dramatically, as is the case with porous media and a liquid piston (as in [16], [97], or [14]). This reasoning motivated the choice of air volume as the means by which hA will be varied. Although still much simplified, this assumption functions as an extension to the results of Sancken and Li [94], in which hA is constant.

8.3 Problem statement

The objective of this paper is to determine the Pareto optimal trajectory with respect to power and efficiency for compression from (P_0, T_0) to P_c and expansion from (P_c, T_0) to P_0, with a volume-dependent heat transfer rate $Q = hA\,(V)\,(T_0 - T)$. For a given efficiency, no other trajectory absorbs/provides more power than the Pareto optimal trajectory; for a given power, no other trajectory operates at higher efficiency. The

optimization problem can be written as

$$\text{maximize } \eta(\zeta) \qquad \text{s.t.} \quad \text{Pow}(\zeta) = \text{Pow}^* \tag{8.3}$$

where Pow^* is some prescribed power. Maximizing power for a given efficiency is an equivalent problem.

Chapter 9

Trajectory Optimization: Solution

9.1 Optimal compression and expansion trajectories

The following steps address the problem for compression only; however, the expansion problem may be solved in the same manner.

1. Consider an arbitrary compression problem with initial volume V_0. Assuming hA is a function of air volume, the volume regime over which compression takes place may be discretized into N constant-hA intervals:

$$hA = (hA)_i \quad \text{for } V_{i-1} \geq V > V_i \quad \forall i = 1, 2, \ldots N \tag{9.1}$$

where the V_i's represent the transition volumes at which the hA product changes to a new value as in figure 9.1. Over each constant-hA volume interval and for given initial and final pressures and volumes, Sancken and Li proved that the optimal trajectory with respect to work and time takes the form adiabatic-isothermal-adiabatic (AIA) [94]. To prove this, they proposed that any curve may be uniformly approximated by a series of adiabatic and isothermal steps. The work and time for a sequence of AIA steps is compared to the work and time for a sequence of Isothermal-Adiabatic-Isothermal (IAI) steps where the total compression ratios are the same. The authors demonstrate that AIA indeed takes less time than

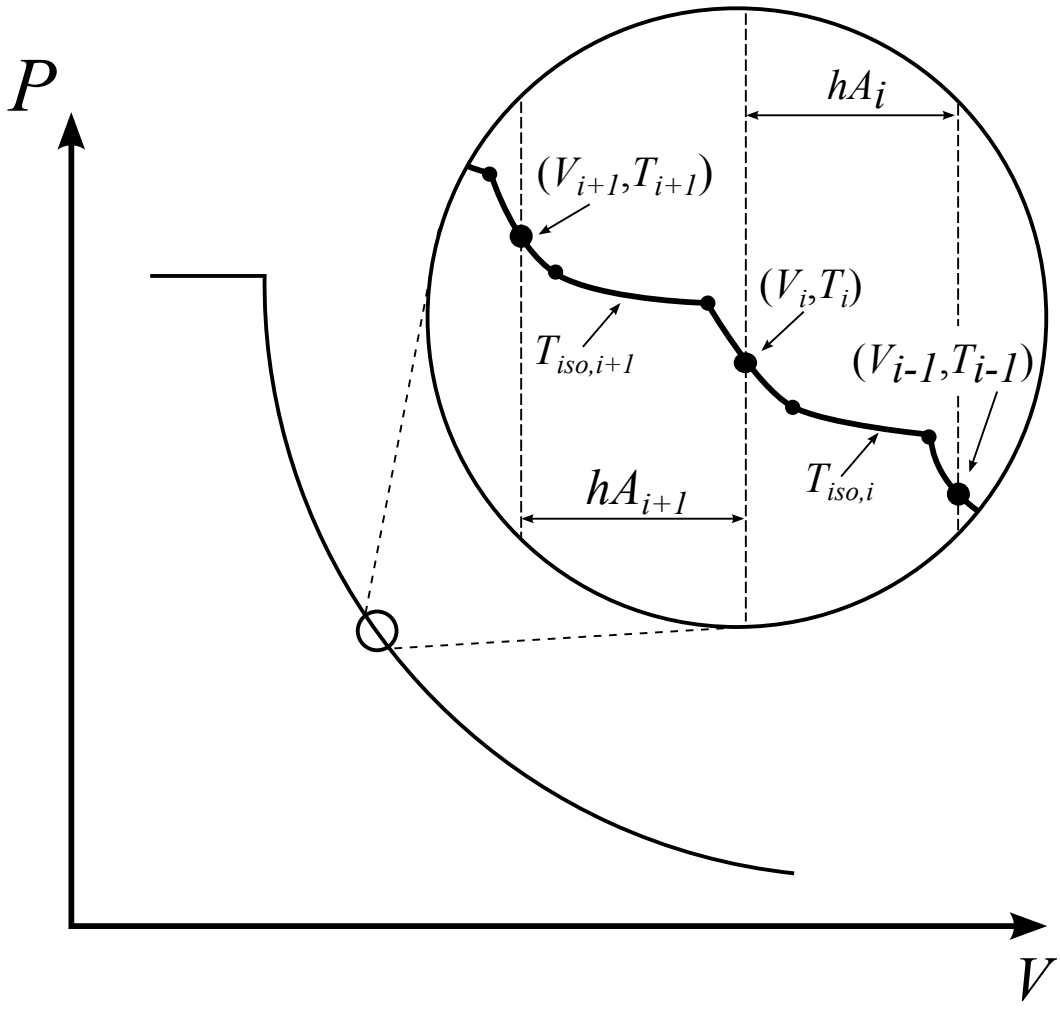

Figure 9.1: A compression trajectory is broken up into N adjacent volume intervals, each with a constant hA. Over each interval the optimal form of the compression trajectory is adiabatic-isothermal-adiabatic.

IAI with equal work. The series of adiabatic and isothermal steps can then be collapsed into a single AIA process by progressively replacing every occurrence of IAI with AIA (e.g. $IAIAIA \Rightarrow AIAAIA \Rightarrow AIAIA \Rightarrow AAIAA \Rightarrow AIA$). Appendix F offers a more thorough demonstration of the optimality of AIA for a constant hA.

2. For the repeating AIA sequence proposed above, the input work can be uniquely described by the temperatures of each isotherm, $T_{\text{iso},i}$, and the temperatures at each transition volume, T_i:

$$\frac{W_{\text{in}}}{nR} = \gamma \frac{T_c - T_0}{\gamma - 1} - \sum_{i=1}^{N} T_{\text{iso},i} \ln \left[\frac{V_i}{V_{i-1}} \left(\frac{T_{i-1}}{T_i} \right)^{\frac{1}{1-\gamma}} \right] + T_0 \left(\frac{1}{r} - 1 \right). \tag{9.2}$$

3. The compression time is also uniquely determined by the isothermal and transition temperatures. For each constant-hA stage, the time is found by integrating equation (3.27):

$$\int_{t_{i-1}}^{t_i} \mathrm{d}t = \int_{V_{i,a}}^{V_{i,b}} \frac{P \mathrm{d}V}{(hA)_i \left(T_0 - T_{\text{iso},i} \right)} \tag{9.3}$$

where $V_{i,a}$ is the volume of of the air at the beginning of the i^{th} isotherm and $V_{i,b}$ is the volume of air at the end of the i^{th} isotherm. For a nonzero hA product, adiabatic compression must be instantaneous and so does not contribute to the total time. The volumes $V_{i,a}$ and $V_{i,b}$ are related to the transition volumes and temperatures by

$$V_{i,a} = V_{i-1} \left(\frac{T_{i-1}}{T_{\text{iso},i}} \right)^{\frac{1}{\gamma-1}} \tag{9.4}$$

and

$$V_{i,b} = V_i \left(\frac{T_i}{T_{\text{iso},i}} \right)^{\frac{1}{\gamma-1}} \tag{9.5}$$

The compression time is the sum of times from each constant hA interval:

$$t_c = \sum_{i=1}^{N} t_i \tag{9.6}$$

which works out to

$$\frac{t_c}{nR} = \sum_{i=1}^{N} \frac{T_{\text{iso},i}}{(hA)_i \left(T_0 - T_{\text{iso},i} \right)} \ln \left[\frac{V_i}{V_{i-1}} \left(\frac{T_{i-1}}{T_i} \right)^{\frac{1}{1-\gamma}} \right]. \tag{9.7}$$

where $(hA)_i$ corresponds to the constant hA product between the transition volumes V_{i-1} and V_i.

4. Reformulate the optimization problem formulation (8.3) using the equations for input work and compression time:

$$\begin{aligned} \text{minimize} \quad & W_{\text{in}}\left(T_{\text{iso},1}, T_1, \ldots, T_{\text{iso},N}, T_N\right) \\ \text{subject to} \quad & t_c\left(T_{\text{iso},1}, T_1, \ldots, T_{\text{iso},N}, T_N\right) = t_c^*, \\ & T_i \leq \max\left(T_{\text{iso},i}, T_{\text{iso},i+1}\right) \quad \forall i = 1, \ldots, N, \\ & T_i \geq \min\left(T_{\text{iso},i}, T_{\text{iso},i+1}\right) \quad \forall i = 1, \ldots, N. \end{aligned} \tag{9.8}$$

Efficiency and power from the original problem statement (8.3) are transformed to work and time using equations (3.5) and (3.7). The temperature constraints force transition temperatures to lie between adjacent isothermal temperatures. Ignoring these constraints causes ambiguity when performing the Lagrange multiplier method to determine stationary points. The Karush-Kuhn-Tucker (KKT) conditions formalize the first-order optimality conditions and provide a system of differential equations. Solutions to these equations satisfy stationarity conditions, primal and dual feasibility, and complementary slackness. The stationarity conditions are

$$\begin{aligned} & nR \ln\left[\frac{V_i}{V_{i-1}}\left(\frac{T_{i-1}}{T_i}\right)^{\frac{1}{1-\gamma}}\right] \times \left(\frac{\lambda_c T_0}{(hA)_i \left(T_0 - T_{\text{iso},i}\right)^2} - 1\right) \\ & = \frac{\partial}{\partial T_{\text{iso},i}}\left[\mu_i \max\left(T_{\text{iso},i}, T_{\text{iso},i+1}\right)\right] - \frac{\partial}{\partial T_{\text{iso},i}}\left[\nu_i \min\left(T_{\text{iso},i}, T_{\text{iso},i+1}\right)\right] \quad \forall i = 1, \ldots N \end{aligned} \tag{9.9}$$

and

$$\begin{aligned} T_{\text{iso},i}\left(1 - \frac{\lambda_c}{(hA)_i\left(T_0 - T_{\text{iso},i}\right)}\right) - T_{\text{iso},i+1}\left(1 - \frac{\lambda_c}{(hA)_{i+1}\left(T_0 - T_{\text{iso},i+1}\right)}\right) \\ = \frac{T_i(1-\gamma)}{nR}\left(\nu_i - \mu_i\right) \quad \forall i = 1, \ldots N. \end{aligned} \tag{9.10}$$

The Lagrange multipliers λ_c, ν_i, and μ_i correspond to the constraints in (9.8):

$$\begin{aligned} \mu_i\left[T_i - \max\left(T_{\text{iso},i}, T_{\text{iso},i+1}\right)\right] = 0 \\ \nu_i\left[T_i - \min\left(T_{\text{iso},i}, T_{\text{iso},i+1}\right)\right] = 0 \end{aligned} \tag{9.11}$$

with $\mu_i \geq 0$ and $\nu_i \geq 0$ for all $i = 1, 2, \ldots, N$.

5. Consider when $N \to \infty$. Since $hA\,(V)$ is a differentiable function, the differences in hA and isothermal temperature between adjacent intervals become arbitrarily small

$$T_{\text{iso},i} - T_{\text{iso},i+1} \to 0 \quad \text{and} \quad (hA)_i - (hA)_{i+1} \to 0. \tag{9.12}$$

From these two statements, it can be shown that the difference in heat transfer between adjacent intervals also tends toward zero.

$$\begin{gathered} Q_i - Q_{i+1} = \\ \left((hA)_i - (hA)_{i+1}\right) T_{atm} + (hA)_{i+1} T_{\text{iso},i+1} - (hA)_i T_{\text{iso},i} = \\ \left((hA)_i - (hA)_{i+1}\right) T_{atm} + (hA)_i \left(T_{\text{iso},i+1} - T_{\text{iso},i}\right) + T_{\text{iso},i+1} \left((hA)_i - (hA)_{i+1}\right) \to 0. \end{gathered} \tag{9.13}$$

where $Q_i = (hA)_i \left(T_0 - T_{\text{iso},i}\right)$. The result is that the left hand side of equation (9.10) goes to zero. The left hand side of equation (9.10) can be rearranged to show this more clearly:

$$T_{\text{iso},i} - T_{\text{iso},i+1} + \lambda_c \left[\frac{T_{\text{iso},i+1}\left(Q_i - Q_{i+1}\right) + Q_{i+1}\left(T_{\text{iso},i+1} - T_{\text{iso},1}\right)}{Q_i Q_{i+1}}\right] \to 0. \tag{9.14}$$

So, since the left hand side of (9.10) tends to zero, $\mu_i \to \nu_i$. The KKT conditions assert that for the Lagrange multiplier, the complementary slackness must be enforced. These are reflected in statements (9.11) above. Since generally $T_{\text{iso},i} \neq T_{\text{iso},i+1}$, either ν_i or μ_i must be zero. In the $n \to \infty$ case, then all Lagrange multipliers tend toward zero, except λ_c. In the limit, equation (9.9) reduces to

$$(hA)_i \left(T_{\text{iso},i} - T_0\right)^2 = T_0 \lambda_c \qquad \forall i = 1, \ldots, N \tag{9.15}$$

and as a function of volume, to

$$hA\,(V)\left(T - T_0\right)^2 = T_0 \lambda_c. \tag{9.16}$$

It is observed that in the continuous form, the AIA sequence has been smoothed into the curve defined by equation (9.16). All interior adiabatic bursts are absorbed; however, the initial and final adiabatic sections are not negligible since the

curve defined by equation (9.16) does not necessarily intersect the prescribed initial and final temperatures. Thus, the form of the optimal compression trajectory is known. It consists of three stages: an initial adiabatic jump, an hA-dependent stage according to equation (9.16), and a final adiabatic jump, as in figure 9.2.

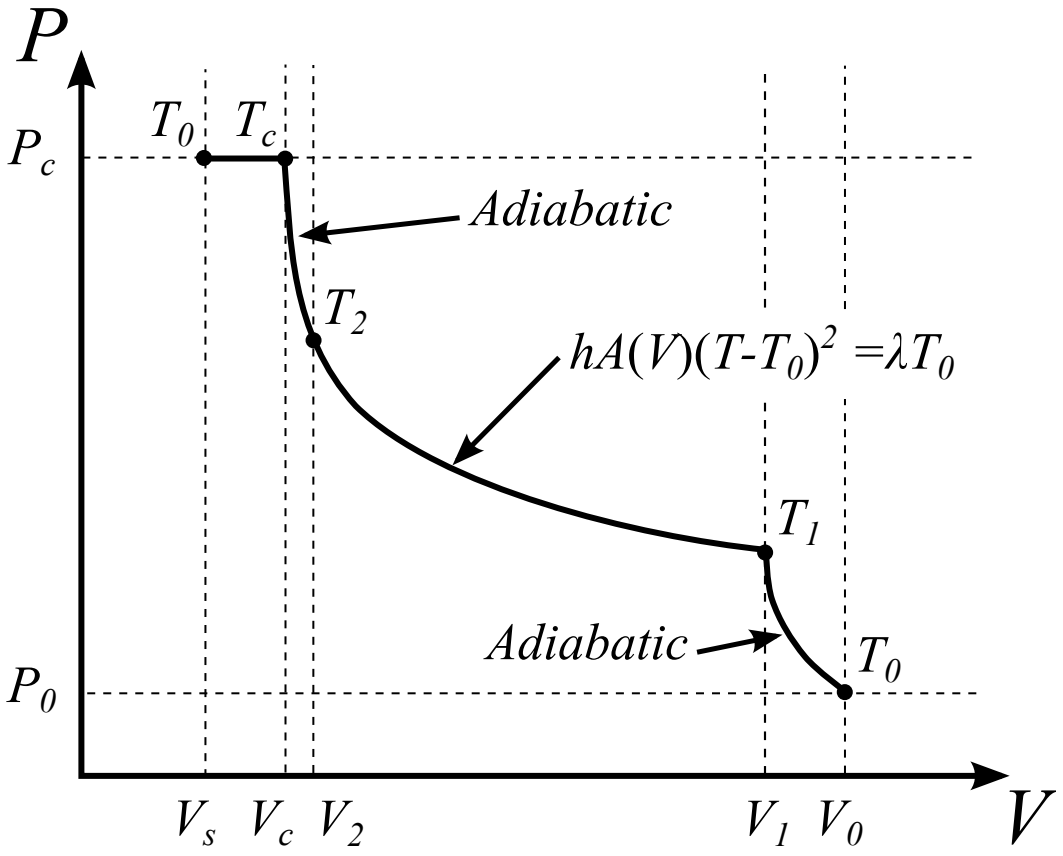

Figure 9.2: Optimal compression for a continuously varying hA product consists of three stages: adiabatic compression; hA-dependent compression; adiabatic compression. The slow hA-dependent curve is determined by the parameter λ_c. After the air is moved to the accumulator, the air volume is further reduced by isobaric cooling.

6. Reformulate expressions for work and time based on the discovered form of the optimal trajectory. Incorporating equation (9.16) allows work and time to be written as functions of T_c and λ_c, only. Let the volume and temperature at which the trajectory changes from adiabatic compression to hA-dependent compression be V_1 and T_1. Let the volume and temperature at which the trajectory changes

from hA-dependent compression to adiabatic compression be V_2 and T_2. These transition states, V_1, T_1, V_2, and T_2 are themselves dependent on λ_c and T_c. Then from the definition of W_{in}, (3.3),

$$\frac{W_{\text{in}}}{nR} = \frac{\gamma\left(T_c - T_0\right)}{\gamma - 1} - \frac{T_2 - T_1}{\gamma - 1} + T_0 \ln\left(\frac{V_1}{V_2}\right) - \sqrt{T_0 \lambda_c} \int_{V_1}^{V_2} \frac{\mathrm{d}V}{V\sqrt{hA\left(V\right)}} - T_0\left(1 - \frac{1}{r}\right) \quad (9.17)$$

and by integrating the first,

$$\frac{t_c}{nR} = -\int_{V_1}^{V_1} \frac{\mathrm{d}V}{VhA\left(V\right)} - \sqrt{\frac{T_0}{\lambda_c}} \int_{V_1}^{V_2} \frac{\mathrm{d}V}{V\sqrt{hA\left(V\right)}} + \frac{1}{2\left(\gamma - 1\right)}\left[\frac{1}{hA\left(V_1\right)} - \frac{1}{hA\left(V_2\right)}\right]. \quad (9.18)$$

As before, the adiabatic stages are instantaneous and do not contribute to the compression time.

7. Plug the new formulations for work and time into the problem statement (8.3):

$$\begin{aligned} &\text{minimize} && W_{\text{in}}\left(T_c, \lambda_c\right) \\ &\text{subject to} && t_c\left(T_c, \lambda_c\right) = t_c^*. \end{aligned} \quad (9.19)$$

With only an equality constraint, the Lagrange multiplier method may be used. It yields

$$\frac{\partial W_{\text{in}}}{\partial \lambda_c} + \beta \frac{\partial t_c}{\partial \lambda_c} = 0 \quad \text{and} \quad \frac{\partial W_{\text{in}}}{\partial T_c} + \beta \frac{\partial t_c}{\partial T_c} = 0 \quad (9.20)$$

where β is a new Lagrange multiplier. Eliminating β yields a single equation relating T_c and λ_c:

$$\frac{\partial t_c}{\partial \lambda_c}\frac{\partial W_{\text{in}}}{\partial T_c} = \frac{\partial t_c}{\partial T_c}\frac{\partial W_{\text{in}}}{\partial \lambda_c}. \quad (9.21)$$

Equation (9.21) and the constraint $t_c = t_c^*$ form a system of two equations and two unknowns which may be solved for the optimal T_c and λ_c.

The optimal trajectory is constructed using equation (9.16) with λ_c to establish the interior compression stage and adiabats passing through (T_0, P_0) and (T_c, rP_0) to form the two outer stages. This solution is similar to the constant-hA case derived by Sancken and Li in which the form is adiabatic-isothermal-adiabatic, but the temperature of the

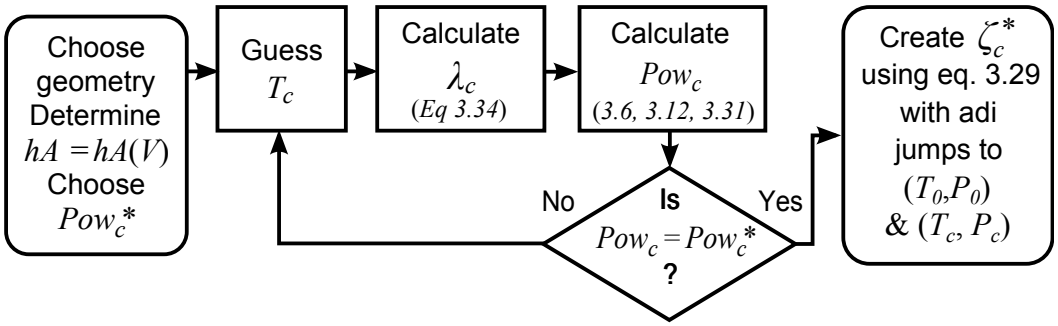

Figure 9.3: Determining the optimal trajectory for a given power

isothermal stage is independent of hA. Figure 9.3 summarizes the procedure when a power constraint is specified.

It should be noted that instantaneous adiabatic compression is not possible in real-life applications. Nevertheless, as reported in the paper by Sancken and Li, assigning a finite compression rate to the adiabatic stages on the order of the fastest compression rate during the slow stage has a minimal effect at high efficiencies [94].

The Lagrange multiplier method finds stationary points—not necessarily minima. That the proposed solution is not the worst case will become obvious in the case study. Additionally, perturbing λ_c or T_c reduces performance, indicating that the solution is, at least, locally optimal.

9.2 Optimal expansion and compression profiles

Theorem 1 ***(Compression)*** *Let P_0 and T_0 be ambient pressure and temperature. Consider an ideal gas compressed from (P_0, T_0) to (rP_0, T_c) with $r > 1$. The compression trajectory, ζ_c^*, is achieved by maintaining*

$$hA\,(V)\,(T - T_0)^2 = \lambda_c T_0$$

where λ_c is a constant parameter and hA is a differentiable function of air volume. Instantaneous adiabatic jumps connect the hA-dependent curve to the initial and final states. The work input and compression time are functions of T_c and λ_c, related by

$$\frac{\partial t_c}{\partial \lambda_c}\frac{\partial W_{\text{in}}}{\partial T_c} = \frac{\partial t_c}{\partial T_c}\frac{\partial W_{\text{in}}}{\partial \lambda_c}.$$

The trajectory ζ_c^* is Pareto optimal with respect to work and time. There does not exist a compression trajectory, ζ_c, under identical conditions such that

$$W_{\text{in}}(\zeta_c) < W_{\text{in}}(\zeta_c^*) \qquad \textit{and} \qquad t_c(\zeta_c) < t_c(\zeta_c^*).$$

(Expansion) *Let P_0 and T_0 be ambient pressure and temperature. Consider an ideal gas expanded from (rP_0, T_0) to (P_0, T_e) with $r > 1$. The expansion trajectory, ζ_e^*, is achieved by maintaining*

$$hA\,(V)\,(T - T_0)^2 = \lambda_e T_0$$

where λ_e is a constant parameter and hA is a differentiable function of air volume. Instantaneous adiabatic jumps connect the hA-dependent curve to the initial and final states. The work out and expansion time are functions of T_e and λ_e, related by

$$\frac{\partial t_e}{\partial \lambda_e}\frac{\partial W_{\text{out}}}{\partial T_e} = \frac{\partial t_e}{\partial T_e}\frac{\partial W_{\text{out}}}{\partial \lambda_e}.$$

The trajectory ζ_e^* is Pareto optimal with respect to work and time. There does not exist an expansion trajectory, ζ_e, under identical conditions such that

$$W_{\text{out}}(\zeta_e) > W_{\text{out}}(\zeta_e^*) \qquad \textit{and} \qquad t_e(\zeta_e) < t_e(\zeta_e^*).$$

Chapter 10

Trajectory Optimization: Results

10.1 Results

Results utilizing the optimal compression trajectory are plotted here for a simple cylindrical compression chamber to demonstrate the expected gains availed by the optimal compression trajectory. The significant improvements predicted by this case study are not an isolated, contrived scenario—significant gains are predicted for a variety of scenarios. See appendix G for an example of a larger scale, high-power application.

The results plotted below assume a cylindrical compression chamber and an hA product function defined as

$$hA\left(V\right) = h\left(\frac{4V}{d} + \frac{\pi d^2}{2}\right) \tag{10.1}$$

where h is a constant heat transfer coefficient, d is the diameter of the chamber, and V is the instantaneous air volume. The heat transfer coefficient is set to 100 W/m^2-K. The cylindrical chamber is has a total volume of 1 liter where the axial length is 5 times the diameter. The initial temperature and pressure are set to 298 K and 101325 Pa. The pressure compression ratio is 350. Figures 10.1, 10.2, and 10.3 show the volume, pressure, and temperature as a function of normalized compression time with three different efficiencies specified: 50%, 80%, and 99%.

Each figure depicts the initial and final instantaneous adiabatic bursts and the hA-dependent middle section. The absorbed power for each case changes by an order of magnitude. For 50% efficiency, the power is 516 W. For 80%, the power is 66 W. For

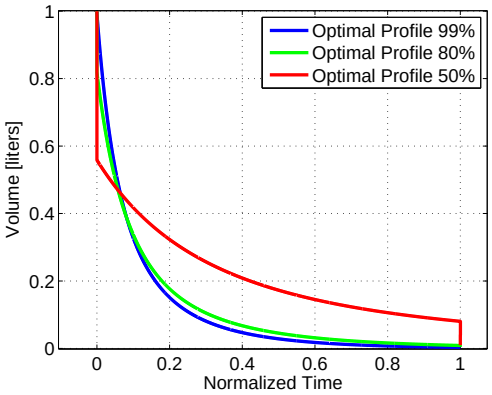

Figure 10.1: The optimal volume profile consists of an instantaneous compression, slow hA-dependent compression, then another stage of instantaneous compression. More efficient trajectories take longer and more of the compression occurs in the middle stage.

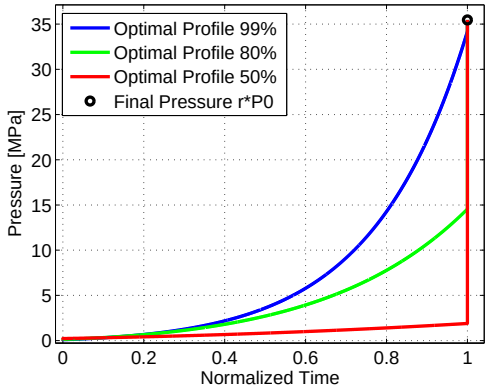

Figure 10.2: The optimal pressure profile consists of an instantaneous compression, slow hA-dependent compression, then another stage of instantaneous compression. The initial and final pressures are the same for each case, but more efficient trajectories will not include as much adiabatic compression.

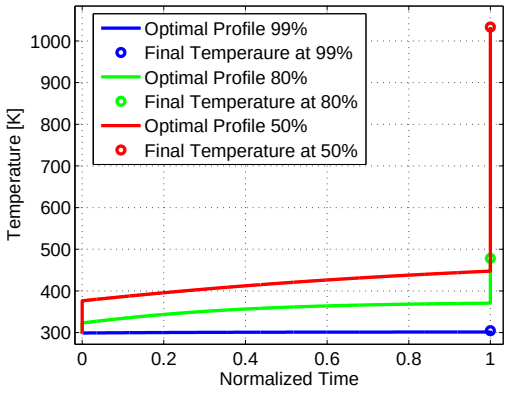

Figure 10.3: The optimal temperature profile consists of an instantaneous compression, slow hA-dependent compression, then another stage of instantaneous compression. The initial temperature is the same for each case, but the final temperature depends on the time allowed for heat transfer. More efficient trajectories take longer in general, to prevent temperatures from rising too high. The difference in final temperature can be very significant, as shown here.

99%, the power is about 2 W. Curves depicting efficiency and power as a function of the final temperature are shown in figure 10.4. As discussed earlier, deviation from isothermal leads to decreasing efficiency, although power could increase. These results match expectations. It needs to be emphasized that these results come from defining the heat tranfser characteristics as in equation (10.1). Nevertheless, these reults give one a feel for the active process during the course of the trajectory, and the effect of differing efficiencies on the profile.

Figures 10.5, 10.6, and 10.7 show the volume, pressure, and temperature as a function of normalized expansion time, each with three different efficiencies specified: 50%, 80%, and 99%. As with the compression results shown above, heat transfer is described by equation (10.1). The power provided in these three cases is 290 W, 56 W, and 2 W, respectively, where the greatest power corresponds to the trajectory with the lowest efficiency.

Curves depicting efficiency and power as a function of the final temperature are shown in figure 10.8. As with compression, it is observed that as the change in temperature increases, the power increases but the efficiency decreases.

Figure 10.9 displays the three volume profiles from figure 10.1, two volume profiles for

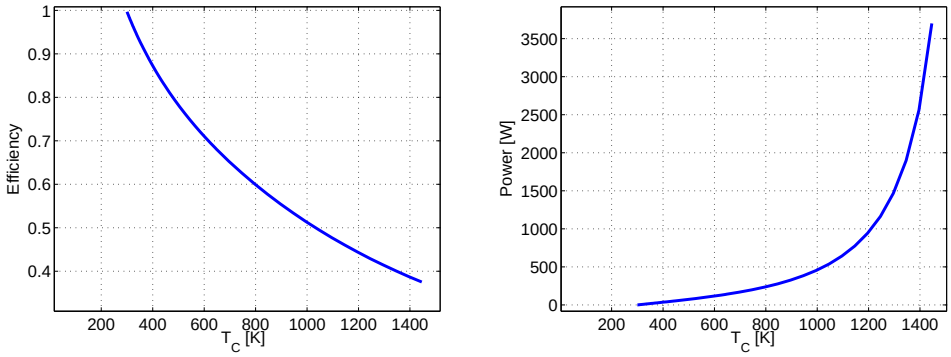

Figure 10.4: The compression efficiency, for given heat transfer characteristics, decreases as the overall temperature rise increases (left). The power absorbed during compression, for given heat transfer characteristics, increases as the overall temperature rise increases (right).

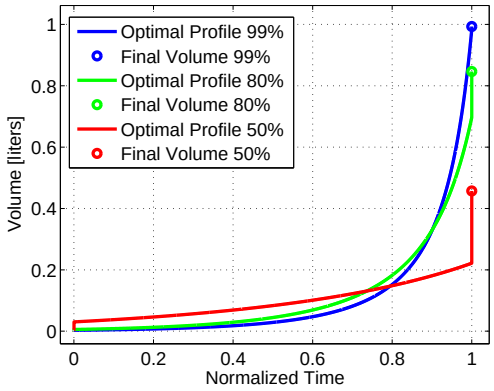

Figure 10.5: The optimal volume profile consists of an instantaneous expansion, slow hA-dependent expansion, then another stage of instantaneous expansion. The initial volume is the same for each case, but the final volumes differ depending on how the air is expanded. More efficient trajectories will be nearer to isothermal, so the final volume will be larger.

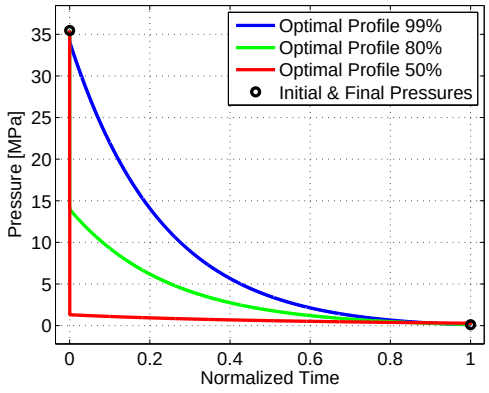

Figure 10.6: The optimal pressure profile consists of an instantaneous expansion, slow hA-dependent expansion, then another stage of instantaneous expansion. The initial and final pressure is the same for each case. Different efficiencies are due to where the expansion occurs. More efficient trajectories take longer, but at the expense of power.

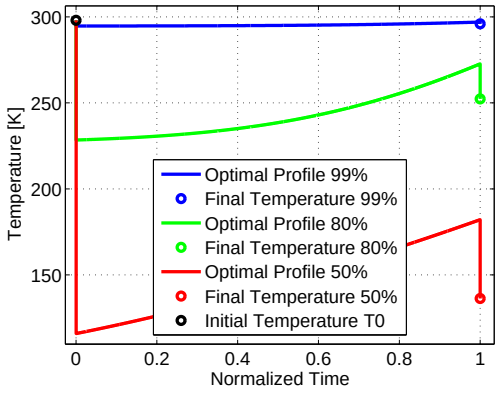

Figure 10.7: The optimal temperature profile consists of an instantaneous expansion, slow hA-dependent expansion, then another stage of instantaneous expansion. For the chosen function of hA, this profile allows the air to heat back up during the slower hA-dependent stage.

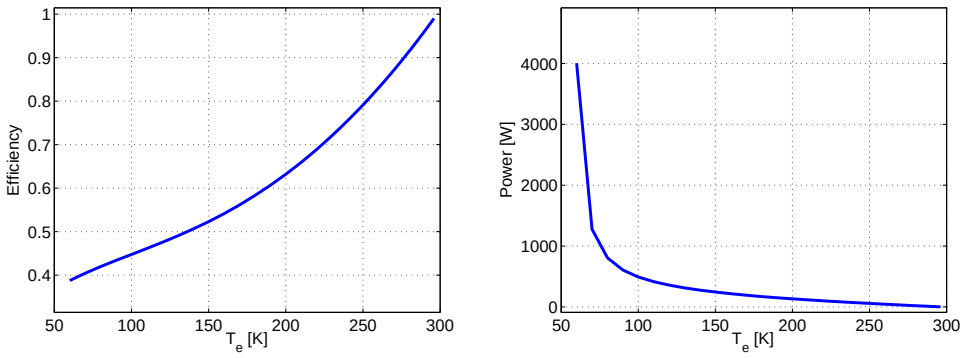

Figure 10.8: The expansion efficiency, for given heat transfer characteristics, decreases as the overall temperature change increases (left). The power provided by expansion, for given heat transfer characteristics, increases as the overall temperature change increases (right).

the constant-hA AIA solution, a sinusoidal volume profile, and a linear volume profile. The optimal profile intuitively looks more appropriate than sinusoidal or linear profiles for the chosen function of hA. At low pressures, when the required work is minimal, compress as fast as possible. Once the temperature begins to rise, slow down and take advantage of the still-large heat transfer surface area. As compression progresses, the surface area (and therefore heat transfer) diminishes, and eventually it is best to forgo the slow compression and push on to the final pressure as rapidly as possible. The same reasoning applies to expansion, but in reverse order. The expansion profiles for the optimal solution, the AIA solution, sinusoidal, and linear compression are depicted in figure 10.10.

Figure 10.11 plots compression efficiency against power absorbed for the chosen hA function and geometry. This line is sometimes called the Pareto optimal frontier. Also plotted are efficiency vs. power curves for the constant-hA AIA solution, sinusoidal, and linear compression trajectories. For any given efficiency, the optimal trajectory absorbs much more power than a linear or sinusoidal volume trajectory at the same efficiency. For example, at 90% efficiency, compression via the optimal volume trajectory absorbs 5 times the power of sinusoidal compression and 10 times the power of linear compression. There is also an improvement over the AIA trajectory, which grows less pronounced as efficiency increases. This is because as efficiency increases, both the

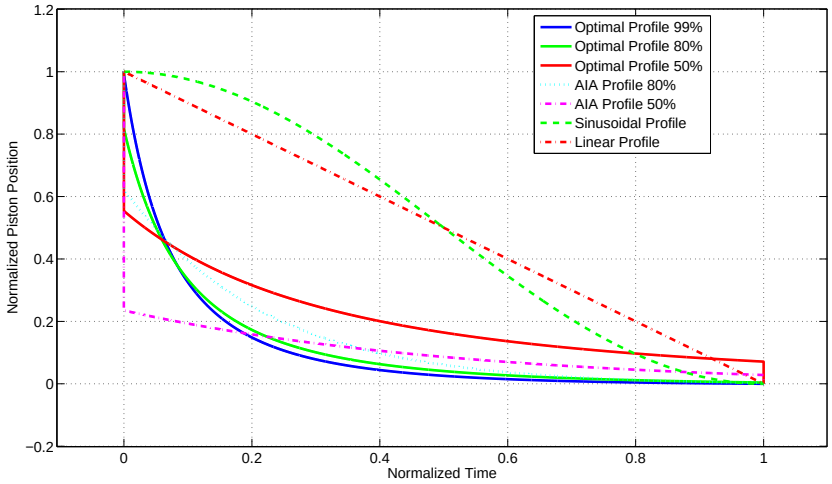

Figure 10.9: Normalized volume profiles are plotted as functions of normalized compression time. Intuition suggests that a fast-slow-fast type trajectory would be optimal.

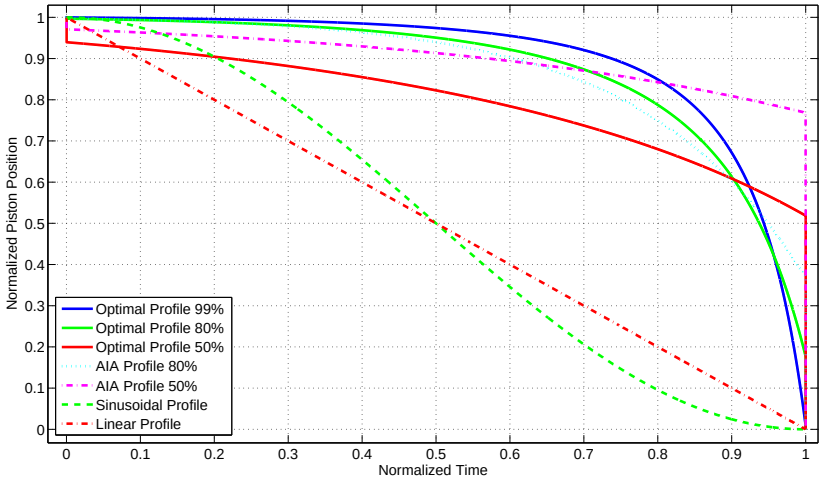

Figure 10.10: Normalized volume profiles are plotted as a function of normalized expansion time.

optimal solution described in this thesis, and the AIA solution, approach a purely isothermal compression trajectory. Figure 10.12 demonstrates that when a constant hA is assumed, the optimal trajectory becomes the AIA trajectory, as it should. Figure 10.13 plots the same trajectories for expansion, and the same conclusions may be drawn as with compression. Again, figure 10.14 shows how the optimal trajectory reduces to the AIA solution set forth by Li and Sancken [94] when hA is constant.

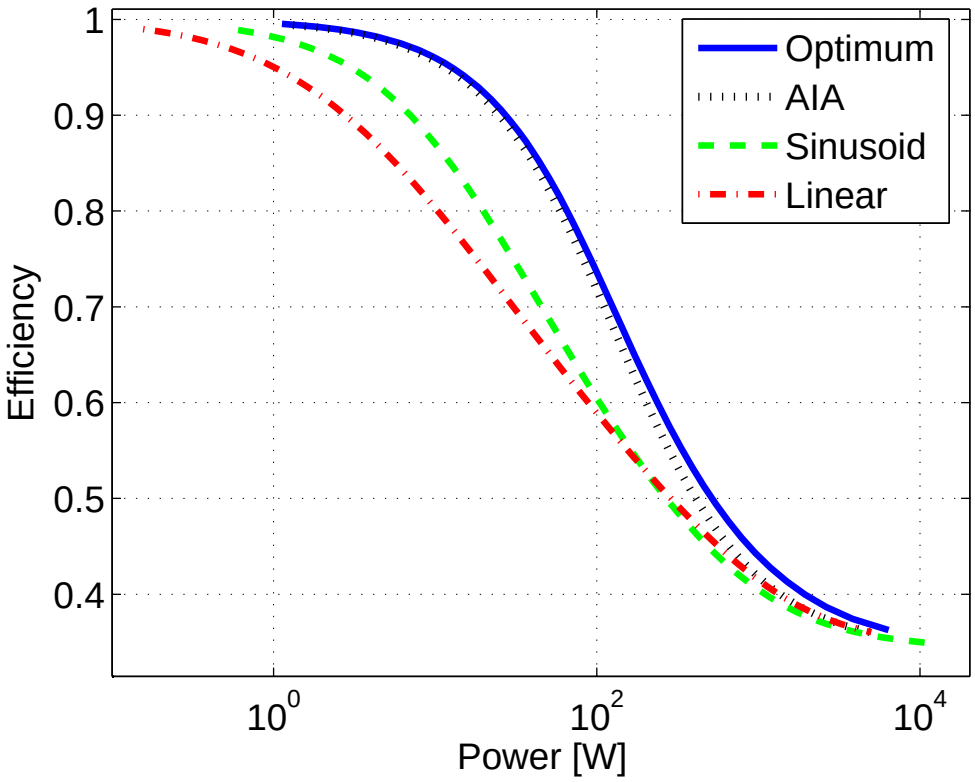

Figure 10.11: Compression efficiency is plotted as a function of power for the varying-hA optimal trajectory, constant-hA optimal trajectory, sinusoidal trajectory, and linear trajectory using the hA product defined in equation (10.1). The varying-hA optimal trajectory performs best, and is Pareto frontier for compression.

Depending on the geometry and selection of the hA function, the advantage of the optimal trajectory as described above may or may not be significantly greater than the

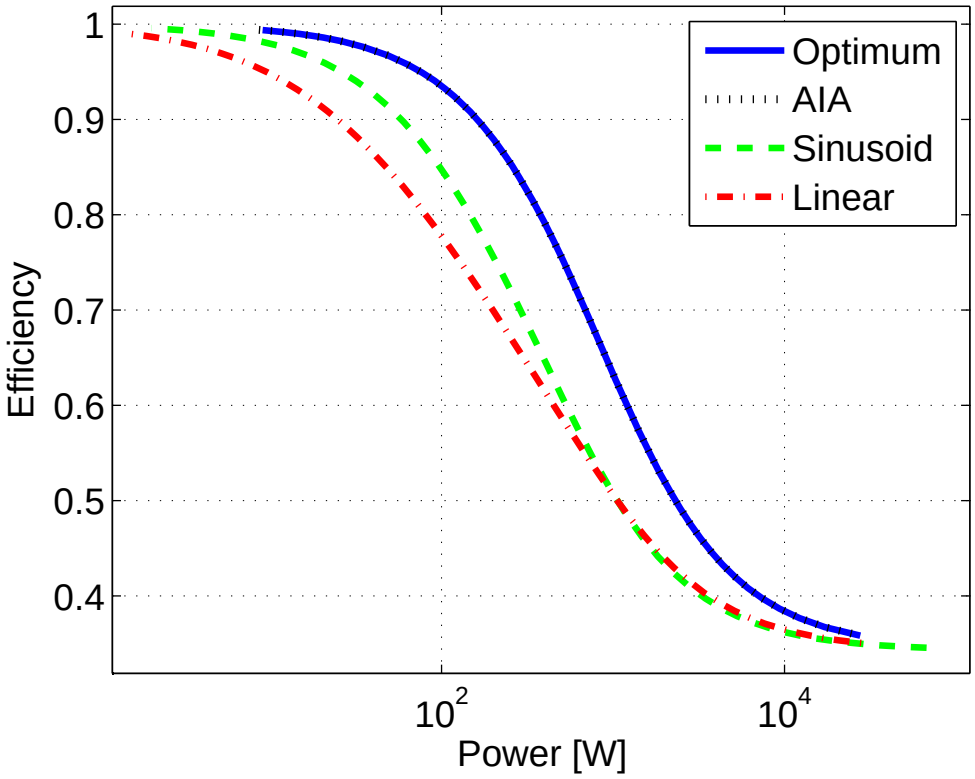

Figure 10.12: Compression efficiency is plotted as a function of power for the varying-hA optimal trajectory, constant-hA optimal trajectory, sinusoidal trajectory, and linear trajectory using a **constant** hA product. The varying-hA optimal trajectory reduces to the constant-hA optimal trajectory when hA is constant.

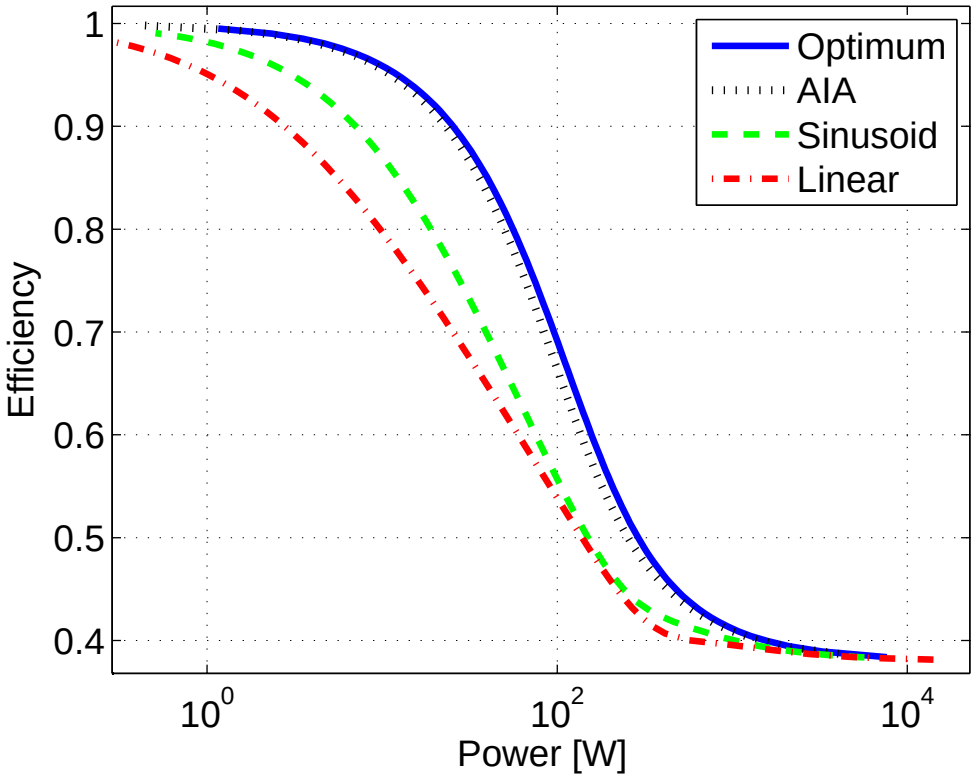

Figure 10.13: Expansion efficiency is plotted as a function of power for the varying-hA optimal trajectory, constant-hA optimal trajectory, sinusoidal trajectory, and linear trajectory using the hA product defined in equation (10.1). The varying-hA optimal trajectory performs best, and is Pareto frontier for expansion.

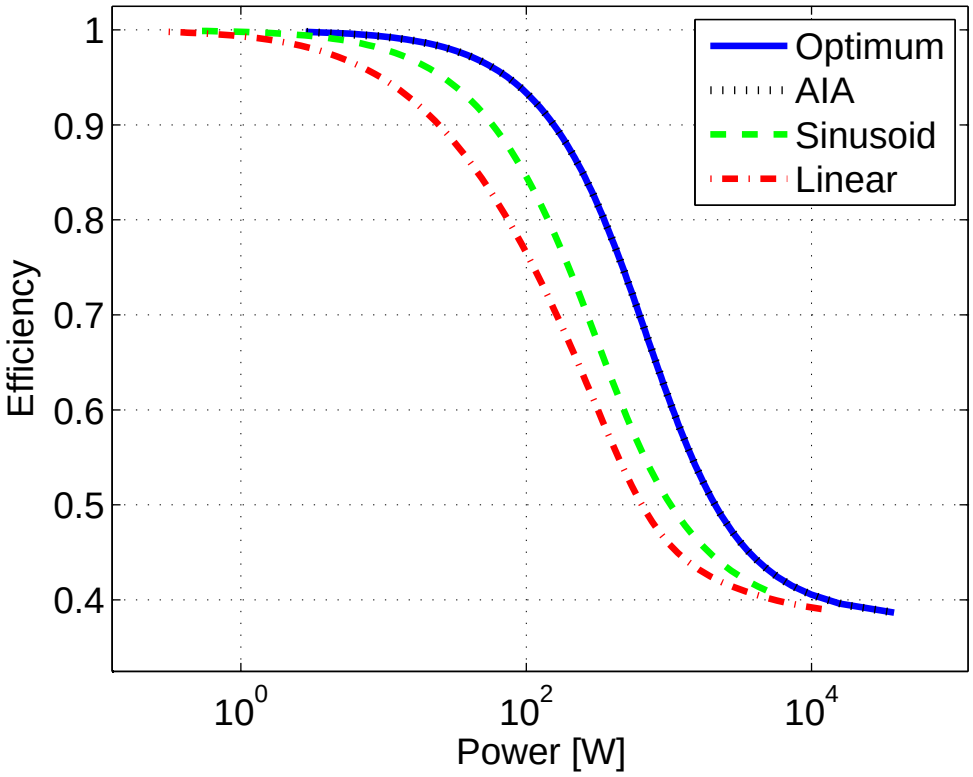

Figure 10.14: Expansion efficiency is plotted as a function of power for the varying-hA optimal trajectory, constant-hA optimal trajectory, sinusoidal trajectory, and linear trajectory using a **constant** hA product. The varying-hA optimal trajectory reduces to the constant-hA optimal trajectory when hA is constant.

simpler AIA (constant-hA) solution. In general, the less hA varies over the volume domain, the more similar the varying-hA optimal trajectory and the constant-hA optimal trajectory will be. This makes sense intuitively. For example, assuming a cylindrical compression chamber, a larger inner diameter means that the relative surface area does not change as significantly (e.g. the ratio of hA_{final} to hA_{initial} is closer to unity). Similarly, for uniformly distributed mesh with diameter d and porosity ϕ (e.g. see the example in appendix G), as d or ϕ increases, the ratio of hA_{final} to hA_{initial} gets closer to unity.

To demonstrate the effect of the geometry and hA function on the results, consider the case study examined in appendix G. Briefly, a cylindrical compression chamber with a volume of 12 m^3 and an aspect ratio of unity is uniformly filled with mesh. During compression a liquid piston gradually rises through the compression chamber and submerges the porous mesh surface area as it reduces air volume. The hA product varies with air volume as

$$hA\left(V\right) = h\left[\left(\frac{4V\left(1-\epsilon\right)}{Dd\epsilon} + \pi D\right)\frac{4V}{\pi\epsilon D^2} + \frac{\pi D^2}{2}\right] \tag{10.2}$$

where ϵ is the porosity of the mesh, d is the diameter of a single strand of the mesh, D is the diameter of the chamber, and V is the instantaneous volume of air in the chamber. Let the heat transfer coefficient be 100 $\text{W/m}^2\text{-K}$, porosity be 99.5%, and the wire diameter be 80 μm. Let the pressure compression ratio be 350. In figure 10.15, the improvement of the variable-hA solution over the constant-hA (AIA) solution is over 60%, while in the low-power case study above (figure 10.11), the improvement is only 10%.

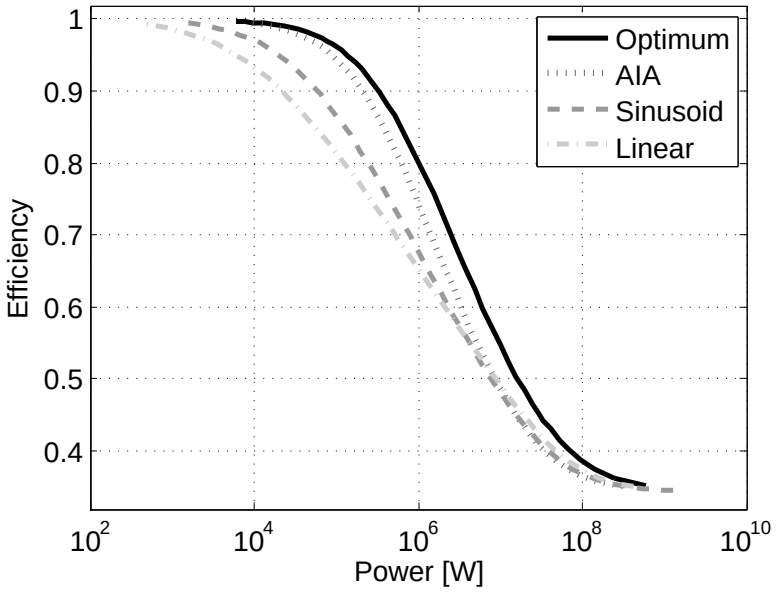

Figure 10.15: Compression efficiency vs power. The advantage of the varying-hA optimal trajectory is more significant for this case than for the simple example shown in figure 10.11

10.2 Discussion

In this analysis key assumptions were made that must be reconsidered for practical applications. Examples include a instantaneous compression speed and a negligence of friction. The difficulty of designing a controller to track the optimal trajectory based on the real-time value of hA is another issue that must be addressed in future work. Fortunately, the gains promised by the optimal trajectory are great enough that the advantage should be retained even if the trajectory can be only approximated. Future work should further generalization of hA, possibly by including temperature and/or velocity dependence. Future studies should also look into issues of practical implementation and experimental validation.

Chapter 11

Conclusion and Discussion

The objective of this thesis was to improve the energy efficiency of an air compressor without sacrificing power. Two complementary thrusts were identified as being in play. The first was to improve heat transfer rates. The second was to optimize the compression trajectory. Gains were made in both areas.

To improve heat transfer, two types of porous media would be introduced into the air space of the compressor. The first was aluminum mesh. Experiments were carried out with two meshes of 1.70 g and 5.48 g, and at piston speeds varying from 2 mm/s to 10 mm/s. Tests without any mesh were also run. All tests were run at a compression ratio of 7, starting with air at ambient conditions. It was found that even the small mesh had a measurable impact on the heat transfer rates. For trials with nearly constant power, the addition of the small mesh reduced the peak temperature change by up to 50% as compared to trials without any mesh. The addition of the larger mesh reduced the peak temperature change by up 75%. These correspond to increasing the efficiencies from the low- to mid- 90%'s to around 99%.

The second porous medium tested was a minitube array. For these tests, a free-surface liquid piston was used. This allowed the liquid, initially below the minitubes, to flow upward through the minitubes during compression, thereby compressing the air above. The compression ratio was 7 and the compression time was 1 second. It was found that the addition of the minitube array reduced the peak temperature difference by over 86% at constant power. The efficiency, determined from a model made to correlate with the experiments, increased by 32%.

The thermodynamic and heat transfer models used in conjunction with the experiments captured the important behavior, but some additional work is needed. The most significant problems occurred when modeling heat transfer rates within the narrow channels of the minitube array due to the uniform air temperature assumption. In these channels, the temperature was artificially high, and, consequently, they dominated the heat transfer throughout the compression process.

The second objective of this thesis was to optimize the pressure-volume compression trajectory. This analysis extended the work done by Sancken and Li [94] by allowing hA to vary as a function of the air volume. Previous work assumed hA was constant. It was found that the variability in hA manifested itself in the variability of the solution. For a constant hA, the optimal compression trajectory took the form adiabatic-isotherm-adiabatic. The variable hA trajectory takes the same form, but the isothermal section is replaced by hA-dependent compression in during which the temperature change is proportional to the inverse root of the hA product. Simulated results assuming a constant h and varying A demonstrated significant improvements in power absorbed over ad-hoc compression trajectories at a given efficiency. Gains over conventional linear- or sinusoidal-shaped trajectories, at the same efficiency, were seen to be $10\times$ and $5\times$, respectively, for the chosen simple test case. Similar gains were seen for expansion.

Future Work

There is still much of interest that can be investigated on both the topic of porous media inserts and trajectory optimization. In the work on heat transfer and porous media, models for the heat transfer coefficient were borrowed from engine cylinders and steady-state pipe flow. Computational fluid dynamics offers a means, in addition to experiments, to evaluate and refine these models, or perhaps suggest alternatives. Another topic of future work is the design of the porous insert. There are, of course, an infinite variety of porous media geometries, many of which will perform better than the mesh or minitube array investigated here. This thesis provides the proof of concept and launch point for future work in optimizing the geometry of the porous medium. Finally, as mentioned above, the simple, bulk-properties, model needs to be refined when used with geometries containing very different characteristic lengths in different regions. For example, it was inappropriate to use a single, volume-average temperature for the air

temperature both within the plenum and within the minitubes.

In the trajectory optimization work, many assumptions were made which could be relaxed in future studies. For example, friction was neglected. Depending on the geometry of the porous insert, this could be a poor assumption. Also, instantaneous piston motion is assumed for the adiabatic stages. This can not be implemented in real life. Future work can look at the implications of non-instantaneous adiabatic stages. Further generalization of the hA function is encouraged. Prior to this work, the compression and expansion trajectories were optimized for a constant hA. In this work, trajectories were optimized when hA is a function of air volume. Future studies could include the effects of air temperature, air pressure, and air velocity as well. Eventually, experimental and/or computational validation of the predicted gains will be important. Finally, practical implementation and control of the optimal trajectory needs to be considered.

References

[1] Robert H. Perry and Donald W. Green, editors. *Perry's Chemical Handbook for Engineer's*. McGraw-Hill, 1984.

[2] Ioannis Hadjipaschalis, Andreas Poullikkas, and Venizelos Efthimiou. Overview of current and future energy storage technologies for electric power applications. *Renewable and Sustainable Energy Reviews*, 13(6–7):1513–1522, 2009.

[3] Kyle Bradbury. Energy storage technology review. Technical report, Duke University, 2010.

[4] Zhenguo Yang, Jun Liu, Suresh Baskaran, Carl H. Imhoff, and Jamie D. Holladay. Enabling renewable energy—and the future grid—with advanced electricity storage. *Journal of the Minerals, Metals, and Materials Society*, 62(9):14–23, 2010.

[5] H. Ibrahim, A. Ilinca, and J. Perron. Energy storage systems—characteristics and comparisons. *Renewable and Sustainable Energy Reviews*, 12:1221–1250, 2008.

[6] H. Chen, T. N. Cong, W. Yang, C. Tan, Y. Li, and Y. Ding. Progress in electrical energy storage system: A critical review. *Progress in Natural Science*, 19:291–312, 2009.

[7] John P. Barton and David G. Infield. Energy storage and its use with intermittent renewable energy. *IEEE Transactions on energy conversion*, 19(2):441–448, 2004.

[8] K.C. Divya and Jacob Ostergaard. Battery energy storage technology for power systems—an overview. *Electric Power Systems Research*, 79(4):511–520, 2009.

[9] A. Arulampalam, M. Barnes, N. Jenkins, and J. B. Ekanayake. Power quality and stability improvement of a wind farm using STATCOM supported with hybrid battery energy storage. *IEE Proceedings: Generation, Transmission, and Distribution*, 153(6):701–710, 2006.

[10] Chris Bullough, Christoph Gatzen, Christoph Jakiel, Martin Koller, Andreas Nowi, and Stefan Zunft. Advanced adiabatic compressed air energy storage for the integration of wind energy. In *Proceedings of the European Wind Energy Conference*, pages 1–8, London, UK, 2004.

[11] Derk J. Swider. Compressed air energy storage in an electricity system with significant wind power generation. *IEEE Transactions on Energy Conversion*, 22(1):95–102, 2007.

[12] Jeffery B. Greenblatt, Samir Succar, David C. Denkenberger, Robert H. Williams, and Robert H. Socolow. Baseload wind energy: modeling the competition between gas turbines and compressed air energy storage for supplemental generation. *Energy Policy*, 35:1474–1492, 2007.

[13] Alfred Cavallo. Controllable and affordable utility-scale electricity from intermittent wind resources and compressed air energy storage (CAES). *Energy*, 32(2):120–127, 2006.

[14] Sylvain Lemofouet and Alfred Rufer. A hybrid energy storage system based on compressed air and supercapacitors with maximum efficiency point tracking (MEPT). *IEEE Transactions on Industrial Electronics*, 53(4):1105–1115, 2006.

[15] Perry Y. Li, James D. Van de Ven, and Caleb J. Sancken. Open accumulator concept for compact fluid power energy storage. In *Proceedings of the 2007 ASME-IMEC*, number IMECE2007-42580. ASME, 2007.

[16] James D. Van de Ven and Perry Y. Li. Liquid piston gas compression. *Applied Energy*, 86(10):2183–2191, 2009.

[17] Chad Abbey and Gézo Joos. Supercapacitor energy storage for wind energy applications. *IEEE Transactions on Industry Applications*, 43(3):769–776, 2007.

[18] A. K. Shukla, S. Sampath, and K. Vijayamohanan. Electrochemical supercapacitors: energy storage beyond batteries. *Current Science*, 79(12):1105–1115, 2000.

[19] Haichang Liu and Jihai Jiang. Flywheel energy storage—an upswing technology for energy sustainability. *Energy and Buildings*, 39(5):291–312, 2007.

[20] R. Takahashi, Li Wu, T. Murata, and J. Tamura. An application of flywheel energy storage system for wind energy conversion. In *International Conference on Power Electronics and Drives Systems, 2005*, pages 932–937, Kuala Lumpur, 2005.

[21] David Hafvenstein. Thermodynamics and heat transfer models of an open accumulator. Master's thesis, University of Minnesota, December 2009.

[22] C. A. Finol and K. Robinson. Thermal modelling of modern engines: a review of empirical correlations to estimate the in-cylinder heat transfer coefficient. In *Proceedings of the institution of mechanical engineers, part D: journal of automobile engineering*, volume 220, pages 1765–1781, 2006.

[23] Rodney J. Tabaczynski, David P. Hoult, and James C. Keck. High Reynolds number flow in a moving corner. *J. Fluid Mech.*, 42:249–255, 1970.

[24] J. Boree, D. Marc, R. Bazile, and B. Lecordier. On the behavior of a large scale tumbling vortex flow submitted to compression. In *Third International Workshop on Vortex Flows and Related Numerical Methods*, volume 7, pages 56–65, 1999.

[25] O. Le Roy and L. Le Penven. Compression of a turbulent vortex flow. *Int. J. Heat Fluid Flow*, 19(5):533–540, 1998.

[26] Ken Naitoh, Yasuo Takagi, Kunio Kuwahara, Egon Krause, and Katsuya Ishii. Computation of transition to turbulence in the compression stage of a reciprocating engine. *Fluid Dynamics Research*, 6:277–294, 1990.

[27] G. Woschni. A universally applicable equation for the instantaneous heat transfer coefficient in the internal combustion engine. *SAE Trans.*, 76, 1967. paper 670931.

[28] G. F. Hohenberg. Advanced approaches for heat transfer calculations, 1979. SAE paper 790825.

[29] K. Chen and G. A. Karim. Evaluation of the instantaneous unsteady heat transfer in a rapid compression-expansion machine. In *Proceedings of the institution of mechanical engineers, part A: journal of power and energy*, volume 212, pages 351–362, 1998.

[30] W. W. Hsieh and T. T. Wu. Experimental investigation of heat transfer in a high-pressure reciprocating gas compressor. *Experimental Thermal and Fluid Sciences*, 13(1):44–54, 1996.

[31] H. B. Faulkner and J. L. Smith. Instantaneous heat transfer during compression and expansion in reciprocating gas handling machinery. In *Proceedings of the AIAA 18th Intersociety Energy Conversion Engineering Conference*, pages 724–730, 1983.

[32] B. Lawton. Effects of compression and expansion on instantaneous heat transfer in reciprocating internal combustion engines. In *Proceedings of the institution of mechanical engineers, part A: power and process engineering*, volume 201, pages 175–186, 1987.

[33] A. A. Kornhauser and J. L. Smith, Jr. Application of a complex Nusselt number to heat transfer during compression and expansion. *J. Heat Transfer*, 116:536–542, 1994.

[34] F. J. Cantelmi, D. Gedeon, and A. A. Kornhauser. An analytical model for turbulent compression-driven heat transfer. *J. Heat Transfer*, 120:617–623, 1998.

[35] Stellan Knöös. Theoretical and experimental study of piston gas-heating with laminar energy losses. *AIAA Journal*, 9(11):2119–2127, 1971.

[36] Naotsugu Isshiki and Nobuhiko Nishiwaki. Study on laminar heat transfer of inside gas with cyclic pressure change of an inner wall of a cylinder head. In *Fourth International Heat Transfer Conference Paris-Versailles*, page FC 3.5, 1970.

[37] M. Nikanjam and R. Greif. Heat transfer during piston compression. *J. Heat Transfer*, 100:527–530, August 1978.

[38] R. Greif, T. Namba, and M. Nikanjam. Heat transfer during piston compression including sidewall and convection effects. *Int. J. Heat Mass Transfer*, 22:901–907, 1979.

[39] J. Polman. Heat transfer in a piston-cylinder system. *Int. J. Heat Mass Transfer*, 24(1):184–187, 1981.

[40] James C. Keck. Thermal boundary layer in a gas subject to a time dependent pressure. *Letters in Heat and Mass Transfer*, 8:313–319, 1981.

[41] J. Yang and J. K. Martin. Approximate solution–one-dimensional energy equation for transient, compressible, low Mach number turbulent boundary layer flows. *J. Heat Transfer*, 111:619–624, 1989.

[42] David R. Buttsworth, Abdalla Agrira, Ray Malpress, and Talal Yusaf. Simulation of instantaneous heat transfer in spark ignition internal combustion engines: unsteady thermal boundary layer modeling. *J. Engineering for Gas Turbines and Power*, 133, February 2011.

[43] Daeyup Lee and Simone Hochgreb. Rapid compression machines: heat transfer and suppression of corner vortex. *Combustion and Flame*, 114:531–545, 1998.

[44] G. W. Recktenwald, J. W. Ramsey, and S. V. Patanker. Predictions of heat transfer in compressor cylinders. In James F. Hamilton and Raymond Cohen, editors, *Proceedings of the 1986 International Compressor Engineering Conference - at Purdue*, volume 1, pages 159–174, August 1986.

[45] Gerald W. Recktenwald. *A study of heat transfer between the walls and gas inside the cylinder of a reciprocating compressor*. PhD thesis, University of Minnesota, March 1989.

[46] A. D. Gosman, R. J. R. Johns, and A. P. Watkins. Development of prediction methods for in-cylinder processes in reciprocating engines. In J. N. Mattavi and C. A. Amman, editors, *Combustion Modelling in Reciprocating Pistons*, pages 69–129. Plenum Press, 1980.

[47] A. G. Catto and A. T. Prata. A numerical study of instantaneous heat transfer during compression and expansion in piston-cylinder geometry. In *Numerical heat transfer, Part A: Applications*, volume 38, pages 281–303. Taylor & Francis, 2000.

[48] Chan-Woo Park and Massoud Kaviany. Evaporation-combustion affected by in-cylinder, reciprocating porous regenerator. *J. Heat Transfer*, 124:184–194, 2002.

[49] M. Abdul Mujeebu, M. Z. Abdullah, M. Z. Abu Bakar, A. A. Mohamad, and M. K. Abdullah. Applications of porous media combustion technology—a review. *Applied Energy*, 86:1365–1375, 2002.

[50] N. Zahi, A. Boughamoura, H. Dhahri, and S. Ben Nasrallah. Flow and heat transfer in a cylinder with a porous medium insert along the compression stroke. *J. Porous Media*, 11(6):525–540, 2008.

[51] D. R. Otis. Thermal losses in gas-charged hydraulic accumulators. In *Proceedings of the AIAA 8th Intersociety Energy Conversion Engineering Conference*, pages 198–201, 1973.

[52] A. Pourmovahed. Durability testing of an elastomeric foam for use in hydraulic accumulators. In *Proceedings of the AIAA Intersociety Energy Conversion Engineering Conference*, volume 2, pages 31–36, 1988.

[53] A. Pourmovahed, S. A. Baum, F. J. Fronczak, and N. H. Beachley. Experimental evaluation of hydraulic accumulator efficiency with and without elastomeric foam. *J. Propulsion and Power*, 4(2):185–192, 1988.

[54] M. P. Sherman and B. V. Karlekar. Improving the energy storage capacity of hydraulic accumulators. In *Proceedings of the AIAA 8th Intersociety Energy Conversion Engineering Conference*, pages 202–207, 1973.

[55] Constantinos A. Balaras. A review of augmentation techniques for heat transfer surfaces in single-phase heat exchangers. *Energy*, 15(10):899–906, 1990.

[56] A. Dewan, P. Mahanta, K. Sumithra Raju, and P. Suresh Kumar. Review of passive heat transfer augmentation techniques. In *Proceedings of the institution*

of mechanical engineers, part A: journal of power and energy, volume 218, pages 509–527, 2004.

[57] A. E. Bergles. ExHFT for fourth generation heat transfer technology. *Experimental Thermal and Fluid Science*, 26:335–344, 2002.

[58] A. E. Bergles. Heat transfer enhancement—the encouragement and accommodation of high heat fluxes. *J. Heat Transfer*, 119:8–19, 1997.

[59] J. M. Zhang, W. H. Sutton, and F. C. Lai. Enhancement of heat transfer using porous convection-to-radition converter for laminar flow in a circular duct. *Int. J. Heat Mass Transfer*, 40(1):39–48, 1997.

[60] H. Yoshida, J. H. Yun, and R. Echigo. Transient characteristics of combined conduction, convection and radiation heat transfer in porous media. *Int. J. Heat Mass Transfer*, 33(5):847–857, 1990.

[61] F. E. Megerlin, R. W. Murphy, and A. E. Bergles. Augmentation of heat transfer in tubes by use of mesh and brush inserts. *J. Heat Transfer*, 34:145–151, 1974.

[62] T. M. Kuzay, J. T. Collins, A. M. Khounsary, and Gilbert Morales. Enhanced heat transfer with metal wool filled tubes. In *ASME/JSME thermal engineering conference*, Reno, NV, 1991.

[63] Mehmet Sözen and T. M. Kuzay. Enhanced heat transfer in round tubes with porous inserts. *Int. J. Heat and Fluid Flow*, 17:124–129, 1996.

[64] Tuncer M. Kuzay and Jeffrey T. Collins. Heat transfer augmentation in channels with porous copper inserts. In S. Kakaç, A. E. Bergles, F. Mayinger, and H. Yüncü, editors, *Heat transfer enhancement of heat exchangers*, volume 355 of *NATO ASI Series E*, pages 223–247. Kluwer, 1999.

[65] H. Pahlavanzadeh, M. R. Jafari Nasr, and S. H. Mozaffari. Experimental study of thermo-hydraulic and fouling performance of enhanced heat exchanger. *International Communications in Heat and Mass Transfer*, 34:907–916, 2007.

[66] Devarakonda Angirasa. Forced convective heat transfer in metallic fibrous materials. *J. Heat Transfer*, 124:739–745, 2002.

[67] Devarakonda Angirasa. Experimental investigation of forced convection heat transfer augmentation with metallic fibrous materials. *Int. J. Heat Mass Transfer*, 45:919–922, 2002.

[68] Bogdan I. Pavel and Abdulmajeed A. Mohamad. Experimental investigation of the potential of metallic porous inserts in enhancing forced convective heat transfer. *J. Heat Transfer*, 126:540–545, 2004.

[69] Bogdan I. Pavel and Abdulmajeed A. Mohamad. An experimental and numerical study on heat transfer enhancement for gas heat exchangers fitted with porous media. *Int. J. Heat Mass Transfer*, 47:4939–4952, 2004.

[70] S. Naga Sarada, A. V. Sita Rama Raju, and K. Kalyani Radha. Experimental numerical analysis enhancement of heat transfer in a horizontal circular tube using mesh inserts in turbulent region. *European Journal of Mechanical and Environmental Engineering*, 2010-2:3–18, 2010.

[71] L. Varshney and J. S. Saini. Heat transfer and friction factor correlations for rectangular solar air heater duct packed with wire mesh screen matrices. *Solar Energy*, 62(4):255–262, 1998.

[72] C. B. Sobhan and S. V. Garimella. A comparative analysis of studies on heat transfer and fluid flow in microchannels. *Microscale thermophysical engineering*, 5:293–311, 2001.

[73] Z. Guo and Z. Li. Size effect on microscale single-phase flow and heat transfer. *Int. J. Heat Mass Transfer*, 46:149–159, 2003.

[74] Z. Guo and Z. Li. Size effect on single-phase channel flow and heat transfer at microscale. *Int. J. Heat Fluid Flow*, 24:284–298, 2003.

[75] S. Reynaud, F. Debray, J. Franc, and T. Maitre. Hydrodynamics and heat transfer in two-dimensional minichannels. *Int. J. Heat Mass Transfer*, 48:3197–3211, 2005.

[76] G. P. Celata, M. Cumo, V. Marconi, S. J. McPhail, and G. Zummo. Microtube liquid single-phase heat transfer in laminar flow. *Int. J. Heat Mass Transfer*, 49:3538–3546, 2006.

[77] J. Li, G.P. Peterson, and P. Cheng. Three-dimensional analysis of heat transfer in a micro-heat sink with single phase flow. *Int. J. Heat Mass Transfer*, 47:4215–4231, 2004.

[78] W. Owhaib and B. Palm. Experimental investigation of single-phase convective heat transfer in circular microchannels. *Experimental Thermal and Fluid Science*, 28:105–110, 2004.

[79] Bjarne Andresen, Peter Salamon, and R. Stephen Berry. Thermodynamics in finite time. *Phys. Today*, pages 62–70, September 1984.

[80] Bjarne Andresen. Current trends in finite-time thermodynamics. *Angew. Chem. Int. Ed.*, 50(12):2690–2704, 2011.

[81] Lingen Chen, Fengrui Sun, and Chih Wu. Finite time thermodynamic optimization or entropy generation minimization of energy systems. *J. Non-Equilibrium Thermodynamics*, 24(4):327–359, 1999.

[82] Peter Salamon, Abraham Nitzan, Bjarne Andresen, and R. Stephen Berry. Minimum entropy production and the optimization of heat engines. *Phys. Rev. A*, 21(6):2115–2129, June 1980.

[83] Morton H. Rubin. Optimal configuration of a class of irreversible heat engines. i. *Phys. Rev. A*, 19(3):1272–1276, 1979.

[84] Morton H. Rubin. Optimal configuration of a class of irreversible heat engines. ii. *Phys. Rev. A*, 19(3):1277–1289, 1979.

[85] Morton H. Rubin. Optimal configuration of an irreversible heat engine with fixed compression ratio. *Phys. Rev. A*, 22(4):1741–1752, 1980.

[86] Yehuda B. Band, Oded Kafri, and Peter Salamon. Maximum work production from a heated gas in a cylinder with piston. *Chemical Physical Letters*, 72(1):127–130, May 1980.

[87] Yehuda B. Band, Oded Kafri, and Peter Salamon. Finite time thermodynamics: optimal expansion of a heated working fluid. *J. Appl. Physics*, 53(1):8–28, January 1982.

[88] Peter Salamon, Yehuda B. Band, and Oded Kafri. Maximum power from a cycling working fluid. *J. Appl. Physics*, 53(1):197–202, January 1982.

[89] Michael Mozurkewich and R. Stephen Berry. Finite-time thermodynamics: engine performance improved by optimized piston motion. In *Proceedings of the National Academy of Sciences, USA*, volume 78, pages 1986–1988, April 1981.

[90] Michael Mozurkewich and R. Stephen Berry. Optimal paths for thermodynamic systems: the ideal Otto cycle. *J. Applied Physics*, 53(1):34–42, 1982.

[91] Karl Heinz Hoffman, Stanley J. Watowich, and R. Stephen Berry. Optimal paths for thermodynamic systems: the ideal diesel cycle. *J. Appl. Physics*, 58(6):2125–2134, September 1985.

[92] Lingen Chen, Fengrui Sun, and Chih Wu. Optimal expansion of a heated working fluid with phenomenological heat transfer. *Energy Conversion and Management*, 39(3):149–156, 1998.

[93] Lingen Chen, Fengrui Sun, and Chih Wu. Effect of heat transfer law on the performance of a generalized irreversible Carnot engine. *J. Phys. D: Appl. Phys.*, 32(1):99–105, 1999.

[94] Caleb J. Sancken and Perry Y. Li. Optimal efficiency-power relationship for an air motor-compressor in an energy storage and regeration system. In *Proceedings of the ASME 2009 Dynamic Systems and Control Conference*, 2009.

[95] D. Y. Peng and D. B. Robinson. A new two-constant equation of state. *Ind. Eng. Chem. Fundam.*, 15(1):59–64, 1976.

[96] Gary Borman and Kazuie Nishiwaki. Internal-combustion engine heat transfer. *Prog. Energy Combust. Sci.*, 13(1):1–46, 1987.

[97] Cecil Piya, Indraneel Sircar, James D. Van de Ven, and David J. Olinger. Numerical modeling of liquid piston gas compression. In *Proceedings of the institution of mechanical engineers, part A: journal of power and energy*, volume 218, pages 509–527, 2004.

[98] Charles Kitchin, Lew Counts, and Moshe Gerstenhaber. Reducing RFI rectification errors in in-Amp circuits. Technical report, Analog Devices, Inc, Norwood, MA, 2003.

[99] RFI rectification concepts. Technical report, Analog Devices, Inc, Norwood, MA, 2009.

[100] A. O. Converse. *Optimization*. Holt, Rinehart and Winston, Inc., New York, 1970.

[101] J. D. Lewins. Introducing the Lagrange multiplier to engineering mathematics. *Int. J. Mech. Engr. Educ.*, 22(3):191–207, 1994.

[102] R. L. Rardin. *Optimization in operations research*. Prentice Hal, Inc., Upper Saddle River, New Jersey, 1998.

[103] J. D. Lewins. Optimising and intercooled compressor for an ideal gas model. *Int. J. Mech. Engr. Educ.*, 31(3):189–200, 2003.

[104] A. Pourmovahed and D. R. Otis. The effects of thermal damping on the dynamic response of a hydraulic motor-accumulator system. *J. Dynamic Systems, Measurement and Control*, 106(1):21–26, 1984.

[105] D. R. Otis and A. Pourmovahed. An algorithm for computing nonflow gas processes in hyrdopneumatic accumulators. *J. Dynamic Systems, Measurement and Control*, 107(1):93–96, 1985.

[106] Robert Norton. *Machine Design: An Integrated Approach (3rd edition)*. Pearson Education, Upper Saddle River, NJ, 2006.

Appendix A

Nomenclature

English letter symbols

A	surface area available for heat transfer
A_{inner}	surface area of the interior of a minitube
A_{mesh}	surface area of the mesh
A_{outer}	surface area of the exterior of a minitube
A_{plenum}	surface area of the upper plenum
A_{surface}	surface area of a body
A_{wall}	surface area of the compression cylinder wall
Bi	Biot modulus
c	specific heat on a mass basis for incompressible substances
c_p	constant pressure specific heat on a molar basis
c_v	constant volume specific heat on a molar basis
d	compression cylinder bore
d_{strand}	diameter of a mesh strand
dT	differential of volume-averaged temperature
dV	differential of volume
du	differential of specific volume
dU	differential of internal energy
dU_{air}	differential change in the internal energy of the air
dU_{sink}	differential change in the internal energy of the heat sink

D_h	hydraulic diameter, $D_h = \frac{4P_{\text{wetted}}}{A_{\text{flow}}}$
E	input work required to compress the air isothermally
h	heat transfer coefficient
h_{inner}	heat transfer between the air and the inner surface of each minitube
h_{outer}	heat transfer between the air and the outer surface of each minitube
h_{plenum}	heat transfer between the air and the bounding surfaces of the plenum
h_{wall}	heat transfer between the air and the compression cylinder wall
ID	inner diameter of a minitube
k	thermal conductivity
k_w	thermal conductivity of the wall
L	Lawton's compressibility factor
L_c	characteristic length, $L_c = \frac{V_{\text{body}}}{A_{\text{surface}}}$
m	mass
m_{air}	mass of air
n	quantity of air in moles
N	number of minitubes in the minitube array
N	number of minitubes AIA sequences
Nu	Nusselt number
Nu_i	imaginary component of complex Nusselt number
Nu_r	real component of complex Nusselt number
OD	outer diameter of a minitube
P	air pressure
P_0	initial air pressure
P_c	pressure at the conclusion of compression
P_{eq}	air pressure at thermal equilibrium after isochoric cooling
P_{peak}	peak air pressure during compression
Pe_ω	oscillatory Peclet number
Pow_c	compression storage power
Pow_c^*	target compression storage power
Pow_e	expansion power
Pr	Prandtl number

q	heat transfer rate
Q	heat
r	pressure compression ratio
R	universal gas constant, $R = 8.3144621$ J/mol-K
Re	Reynolds number
t_c	compression time
t_c^*	target compression time
t_{cylinder}	wall thickness of the compression cylinder
t_i	time at which $(hA)_i$ transitions to $(hA)_{i+1}$
t_{minitube}	wall thickness of a minitube
T	volume-averaged air temperature
T_∞	adiabatic air temperature/air temperature outside the thermal boundary layer
T_0	initial volume-averaged air temperature
T_1	air temperature at transition from fast to slow compression
T_2	air temperature at transition from slow to fast compression
T_c	volume-averaged air temperature at the end of compression and before isobaric cooling
T_e	volume-averaged air temperature at the end of expansion
T_{eq}	air temperature at thermal equilibrium after isochoric cooling
T_i	air temperature corresponding to when $(hA)_i$ transitions to $(hA)_{i+1}$
$T_{\text{iso},i}$	air temperature of the isothermal stage for $(hA)_i$
T_{mesh}	temperature of the mesh
T_{minitube}	temperature of the minitube
T_{peak}	air temperature at the peak pressure during compression
T_{sink}	heat transfer sink or source, usually the compression cylinder walls or porous media
T_w	wall temperature
T_{wall}	temperature of the compression cylinder wall
u	specific internal energy, $u = \frac{U}{m}$
U	mean piston velocity or air velocity
U	internal energy
v	specific volume, $v = \frac{V}{m} = \frac{1}{\rho}$

V	air volume
$\dot{V}$	volume rate of change/flow rate
V_0	initial air volume
V_1	air volume at transition from fast to slow compression
V_2	air volume at transition from slow to fast compression
V_{body}	volume of a body
V_c	air volume at the end of compression and before isobaric cooling
V_i	air volume corresponding to when $(hA)_i$ transitions to $(hA)_{i+1}$
V_{mesh}	volume of a mesh
W	work
W_{in}	input work required to compress the air
W_{out}	output work provided by the expansion of air
Z	compressibility factor, $Z = \frac{PV}{nRT}$

Greek letter symbols

α	thermal diffusivity of air
α_0	initial thermal diffusivity of air
γ	ratio of specific heats, $\gamma = \frac{c_p}{c_v}$
δP	uncertainty in pressure measurements
$\delta Q_{\text{to air}}$	infitisimal quantity of heat transfer to the air
$\delta Q_{\text{to sink}}$	infitisimal quantity of heat transfer to the sink
δT	uncertainty in temperature measurements
δV	uncertainty in volume measurements
$\delta W_{\text{by air}}$	infitisimal amount of work done on the air
$\delta W_{\text{by sink}}$	infitisimal amount of work done on the air
ΔP	finite change in pressure
ϵ	initial porosity of air space
ζ_c	pressure-volume compression trajectory
ζ_e	pressure-volume expansion trajectory
η_c	compression efficiency
η_e	compression efficiency
λ_c	Lagrange multiplier for compression
λ_e	Lagrange multiplier for expansion
μ	dynamic viscosity of air
μ_0	dynamic viscosity of air at standard temperature and pressure
μ_i	Lagrange multiplier for $(hA)_i$
ν_i	Lagrange multiplier for $(hA)_i$
π	ratio of the circumference to the diameter of a circle
ρ_w	thernal conductivity of the wall
ρ_0	initial density of air
ω	cycle frequency

Appendix B

Establishing the flow regime in the minitube array

In the system model it was assumed that the flow through the channels was laminar. Gas velocity is known to be zero at stationary walls and equal to the piston velocity at the piston surface. Assuming the interface rose at the same velocity in every channel, it was reasoned that the gas velocity decreased almost linearly from the piston surface to the end wall. The Reynolds numbers of the highest velocity gas near the piston surface are below the transition values generally cited for flow through smooth pipes. Further, the initial acceleration of the gas and the subsequent compression enhance stability, making transition even less likely. The following calculations demonstrate that the maximum Reynolds numbers are under 2300.

Flow through pipes is an often-studied phenomenon with well-established Reynolds number thresholds corresponding to the laminar and turbulent flow regimes. Flow is laminar for Reynolds numbers less than around 2300. Flow is fully turbulent when Reynolds numbers exceed 4000. Transitional behavior occurs between 2300 and 4000. The Reynolds number for flow through a pipe is

$$\mathrm{Re} = \frac{U D_H}{\nu} \tag{B.1}$$

where U is the air velocity, D_H is the hydraulic diameter, and ν is the kinematic viscosity. The question to be addressed here is "what is the highest feasible Reynolds number seen during the compression event under the experimental conditions?"

B.0.1 Kinematic viscosity

The kinematic viscosity can be written as

$$\nu = \frac{\mu}{\rho} \tag{B.2}$$

where μ is the dynamic viscosity and ρ is the density. Density, dynamic viscosity, and kinematic viscosity change in time. The Reynolds number is proportional to density and inversely proportional to dynamic viscosity. The dynamic viscosity of air increases with temperature and so is smallest at the start time. For an isothermal process, the dynamic viscosity is constant.

The density increases as the instantaneous volume compression ratio increases, where the volume compression ratio, r_V, is defined as

$$r_V = V_0/V. \tag{B.3}$$

Here, V_0 and V are initial and instantaneous values of air volume, respectively. For adiabatic compression,

$$r_V = (P/P_0)^{\frac{1}{\gamma}} \tag{B.4}$$

where P_0 and P initial and instantaneous values of air pressure and γ is the ratio of specific heats, about 1.4 for air. For isothermal compression,

$$r_V = (P/P_0)\,. \tag{B.5}$$

Thus, at any instantaneous pressure compression ratio, an isothermal process will result in the highest density. Therefore, the density would be a maximum at the end of isothermal compression. Since dynamic viscosity is a minimum for isothermal compression, it becomes clear that the minimum value for the kinematic viscosity (and thus the largest Reynolds number) occurs at the end of isothermal compression. The value of density is

$$\rho = r\rho_0 = 7 \times 1.2 = 8.4 \quad \text{kg/m}^3 \tag{B.6}$$

where r is the pressure compression ratio and ρ_0 is the initial density of the air, approximately the density of air at standard pressure and temperature. The dynamic viscosity is constant for the isothermal process.

$$\mu = 1.98e^{-5} \quad \text{kg/m-s} \tag{B.7}$$

B.0.2 Hydraulic diameter

Water flowing through the packed cylinder array has its choice of channels. Options include traveling through the inner diameter of each minitube, the regularly shaped interstitial spaces between three packed minitubes, the regularly shaped interstitial spaces between two packed minitubes tubes and the wall, or the scattered irregularly shaped interstitial spaces. The hydraulic diameter, D_h, of the regular shapes can be calculated by

$$D_h = \frac{4A_{\text{flow}}}{P_{\text{wetted}}} \tag{B.8}$$

where A_{flow} is the flow cross-section and P_{wetted} is the wetted perimeter. The hydraulic diameter is constant throughout the compression process. Figure B.1 depicts the regular, repeating channels seen in the packed minitube array. The ideal packing arrangement imitates a honeycomb pattern. The hydraulic diameter inside the small tubes (the shaded region labeled A in the figure) works out to be the inner diameter.

$$D_h = ID = 1.55 \quad \text{mm.} \tag{B.9}$$

The hydraulic diameter of the smallest spaces (as in B) becomes

$$D_h = OD\left(\frac{2\sqrt{3}}{\pi} - 1\right) = 0.33 \quad \text{mm.} \tag{B.10}$$

The space between two minitubes and a wall (C in the figure) is similar, and is

$$D_h = OD\left(\frac{4}{\pi} - 1\right) = 0.87 \quad \text{mm.} \tag{B.11}$$

The hydraulic diameters of the irregular spaces will range from 0.33 mm to perhaps 2–3× the inner diameter 1.55 mm. It may also be useful to calculate the "average" hydraulic diameter based on the total flow area and wetted perimeter. This is

$$D_h = \frac{4\epsilon A_{CS}}{\pi D + N\pi OD} = 0.94 \quad \text{mm.} \tag{B.12}$$

where ϵ is the initial porosity. The hydraulic diameter is a constant value along the length of each parallel channel.

The Reynolds number is proportional to hydraulic diameter, so the highest Reynolds numbers will most likely be found in the largest irregularly shaped interstitial spaces.

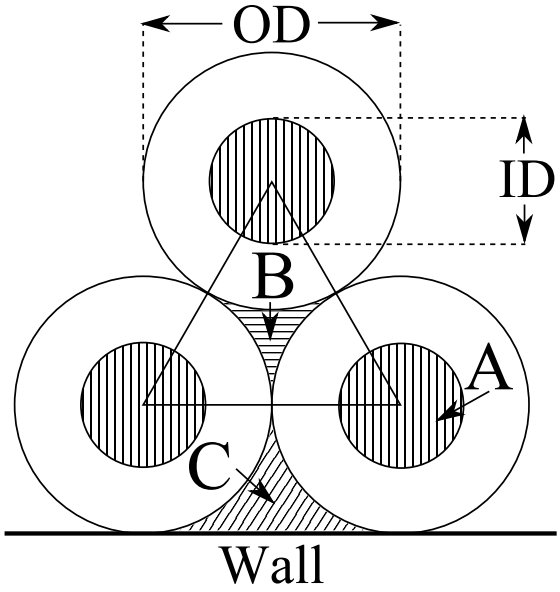

Figure B.1: A diagram of a representative packing arrangement in the minitube array. Three different flow channels, labeled A, B, and C, are shaded.

From visual inspection of the minitube array used in the experiments, it is estimated the hydraulic diameter for the largest flow channel is about three times the inner diameter of a single minitube.

$$D_H = 3 \times 0.00155 \text{ m} \tag{B.13}$$

B.0.3 Air velocity

The bulk air velocity is expected to be largest at the piston surface, and decrease to the stationary boundary condition at the cap. For the water piston, the water-air interface is broken up by the many cylinders packed into the chamber. Due to the different cross-sections of the various channels through the cylinder array, the water interface will rise at a different speeds in different channels, but for the purposes of this calculation it is assumed that the interface rises uniformly.

The average interface speed may be determined by the overall flow rate of water into the chamber. The flow rate is approximately constant, equal to about 250 cc/s. Given

that the porosity, ϵ, is about 35%, the average interface velocity through the pipes is

$$U_{\text{avg}} = \frac{Q_{\text{flow/rate}}}{A_{\text{flow/area}}} = \frac{Q_{\text{flow/rate}}}{\epsilon A_{\text{chamber/area}}} = 36 \quad \text{cm/s.} \tag{B.14}$$

B.0.4 Calculating Re

Using these estimates for velocity, kinematic viscosity, and hydraulic diameter, the conservative estimate for the maximum Reynolds number is

$$\text{Re}_{\text{max}} = \frac{\left(7 \times 1.2 \text{ kg/m}^3\right)(0.36 \text{ m/s})(3 \times 0.00155 \text{ m})}{1.98 \times 10^{-5} \text{ kg/m-s}} = 710 \tag{B.15}$$

which, for a smooth pipe, is below the transition Reynolds number of 2300. It should be noted that typical values of Reynolds numbers will be significantly lower. For example, even assuming isothermal compression, flow through the inner diameter at the beginning of the compression process, the Reynolds number is expected to be

$$\text{Re}_{\text{initial}} = \frac{\left(1.2 \text{ kg/m}^3\right)(0.36 \text{ m/s})(0.00155 \text{ m})}{1.98 \times 10^{-5} \text{ kg/m-s}} = 34. \tag{B.16}$$

It should also be noted that even if flow through a channel does begin to transition, it will not affect the gross description of heat transfer in the minitube array.

B.0.5 The effect of various interface velocities

Given that there are several flow channels of different cross-sections, the interface will actually rise at different velocities, according to the flow resistance. If the velocity scales with the square of hydraulic diameter and the total flow rate is 250 cc/s, the velocities through the various channels, assuming regular channel geometries, may be calculated. Through the smallest channels, the velocity is about 2.3 cm/s. For flow through the minitubes, the velocity is about 51.7 cm/s, about 25 times faster.

Appendix C

Apparatus detail

C.1 Mesh Experiments

C.1.1 Appartus details

The hydraulic oil used was Synative ES 2964 from Cognis Corporation, selected for, among other things, a high flash point.

The Parker OilDyne miniature piston pump had a fixed displacement of 0.156 cc/rev (0.0095 in^3/rev) and provided continuous operation until 24 MPa (3500 psi). A 24VDC/6.5 TDK-Lambda HK150A-24/A power supply provided power to the motor and pump. The voltage from the supply wass regulated by an H-bridge circuit controlled by a computer to achieve varying flowrates.

The Haldex G. C. Series gear pump had a fixed displacement of 6.36 cc/rev (0.388 in^3/rev) and provided continuous operation until 11 MPa (1600 psi). The gear pump was driven by a variable speed permanent magnet DC motor, a MicroMo GNM4125. A 24VDC/20A Mean Wells SP-480-24 power supply provided power to the motor. The voltage wass also regulated by an H-bridge circuit controlled by a computer.

The Vickers DG4V-3 from Eaton offered a maximum pressure of over 20.7 MPa (3000 psi) and maximum flow of 83 l/min (22 GPM). The electrically-controlled 3-2 valve is from Hydraulic Controls, Inc. part number 4WE6D6X/EG12N9Z5L.

The compression cylinder was cut from a length of extruded polycarbonate tubing. The inner diameter of the tubing is 50.8 mm (2.0 inches) and the outer diameter is 57.2

mm (2.25 inches). Using a digital caliper accurate to within 0.1 mm, the maximum deviation in the diameter was measured to be 0.25 mm (0.01 inches)—well within the 1 mm manufacturer's tolerance. The length of the cylinder was measured to be 25.4 cm with an uncertainty of 0.05 cm. The polycarbonate cylinder fit between the mount and the top end cap. A second cylinder of the same inner and outer diameter fit between the mount and the lower end cap. Threaded steel rods connect the caps to the mount, as can be seen in figures 4.3 or 4.5. Nuts are tightened at the cap to seal the air space and can be removed to take off the cap (see figure 4.7).

The 25.4 cm polycarbonate cylinder was fit into a 4130 alloy steel cylinder to create a compound wall. The steel cylinder had an outer diameter of 63.5 mm (2.5 inches) and an inner diameter of 57.4 mm (2.26 inches). The inner diameter was sized such that a near press-fit was obtained between the polycarbonate cylinder and the steel cylinder. Six oval windows, each 28 mm long and 10 mm wide, were cut from the steel cylinder on either side, allowing visual inspection of the interior of the compression chamber. Two additional larger windows, 28 cm long by 18 mm wide, were placed near the top of the cylinder to aide visualization near the end of the compression stroke. The steel cylinder extended the length of the chamber, minus 5 mm clearance on either end. A photograph of the piston system is shown in figure 4.5. The upper cylinder is clad in the steel "exoskeleton."

The steel exoskeleton encasing the polycarbonate compression cylinder significantly improves the safety of the system. The 25.4 cm compression cylinder is designed to operate at pressures up to 3.45 MPa (500 psi). If a conservative factor of safety of 10 is desired, the polycarbonate tube itself would be insufficient. Failure could occur due to radial stress, axial stress, or tangential (hoop) stress. Of these, the tangential stress is the most probable failure mode. The tangential stress is found by [106]

$$\sigma_t = \frac{r_i^2 P_i - r_o^2 P_o}{r_o^2 - r_i^2} + \frac{r_i^2 r_o^2 \left(P_i - P_o\right)}{r^2 \left(r_o^2 - r_i^2\right)} \tag{C.1}$$

where P_i is the internal pressure, P_o is the external pressure, r_i is the inner radius, r_o is the outer radius, and r is the radius of the point of interest. The maximum pressure occurs when $r = r_i$. The chamber can be expected to fracture due to tangential stress

when the tangential stress equals the ultimate tensile strength of the material, $\sigma_t = S_{ut}$

$$P_{i,fracture} = \frac{S_{ut}\left(r_o^2 - r_i^2\right) + 2P_o r_o^2}{r_i^2 + r_o^2} \tag{C.2}$$

where S_{ut} is the ultimate tensile strength.

For extruded polycarbonate, the ultimate tensile strength is 63–72 MPa (9180–10500 psi). For an inner diameter of 50.8 mm and outer diameter of 57.2 mm, fracture occurs at 7.5 MPa (1093 psi). For alloy steel, the ultimate tensile strength is 450–1965 MPa (65300–285000 psi). For an inner diameter of 57.4 mm and outer diameter of 63.5 mm, fracture is expected to occur no sooner that 45 MPa (6574 psi), a factor of safety of 13.

The mass of each mesh was determined using an Escali Professional Scale Model #L125 with 0.01 gram resolution.

C.1.2 Instrumentation details

The Kulite ETM-375 pressure transducer was placed with the diaphragm (force collector) flush with the surface of the end cap. The sensing element is a piezoresistive material. The output is amplified to 0–5 volts, corresponding to absolute pressures of 0–1.72 MPa (0–250 psi). A small sealed vacuum establishes the absolute pressure. The bandwidth is DC to 4 kHz, which is more than ample for this application. This pressure sensor replaced an older Kulite pressure transducer, model XTL-123B-190-1000SG, which measured gauge pressures 0–6.89 MPa (0–1000 psi) with a 0–100 mV output. The older sensor was replaced so the the range of pressures would be more appropriate and because of calibration issues.

The Omega PX309 series pressure transducer is amplified to 0–5 volts, corresponding to absolute pressures of 0–6.89 MPa (0–1000 psi). The accuracy is reported to be +/- 0.25% Full-scale best-straight-line (BSL) at 25° C, including linearity, hysteresis, and repeatibility. The response time is less than 1 millisecond.

The MTS Tempsonics C-Series core sensor uses magnetostriction to determine the location of the piston. The uncertainty of the sensor is reported to be 0.15 mm non-linearity, 25 microns repeatability, and 25 microns hysteresis. The original calibration was determined by determining two points and assuming the volume was linear with piston position. However, the uncertainty of this method was deemed too large, particularly at the end of the stroke where the manufacturers report the greatest non-linearity.

To obtain a more accurate calibration, a burette was filled with oil and connected to a hole in the end cap with a hose. The piston began at the top was lowered by way of small incremental steps, slowly drawing oil into the chamber. At each step, the voltage and displaced oil were recorded so a direct voltage to volume calibration curve was created. The uncertainty of this calibration is 1 cc.

C.2 Minitube Array Experiments

C.2.1 Apparatus

Water was drawn from the water tap through a flexible hose to the pump. The water pressure varied between 620–690 kPa (90–100 PSI).

The D-10-I series Hydra-Cell positive displacement diaphragm pump from Wanner Engineering, Inc had a maximum flow rate of 0.25 l/s (4 gpm). The maximum output pressure was 6.9 MPa (1000 psi). The pump was driven by a 1.5 hp Dayton 3N550 electric motor at 1740 rpm. The water passed through a Danfoss Power Pack Valve type VPH 15 E which housed both a relief valve and directional control valve. The pressure relief valve had a breaking pressure of 2.5 MPa (363 psi). A pressure switch determined the state of the directional control valve. The pressure switch was set to about 1 MPa (150 psi). The valve was powered by a Mean Well RS-150-12 12VDC/12.5A power supply.

The Bürkert proportional solenoid control valve Type 6223 was used to control the flow rate to the compression cylinder. The valve's pressure range was from 50 kPa to 1 MPa (7 to 145 psi). The maximum line pressure was maintained at 1 MPa (150 psi) using the pressure switch since the relief valve's pressure was too high. Future tests using this facility will benefit from a new spring which enables the mechanical relief valve to open 1 MPa (150 psi) and so provides more reliable operation. The flow coefficient, C_v was 5.8 when the valve was fully open, allowing the maximum flow from the pump to pass. The flow coefficient is defined for water as

$$C_v = 42\dot{V}\sqrt{1/\Delta P} \tag{C.3}$$

Here, $\dot{V}$ is the flow rate in l/s and ΔP is the pressure drop in kPa. The flow was controlled electronically by a 0–5 volt analog input. This valve was powered by the

same Mean Well RS-150-12 12VDC/12.5A power supply as the relief valve.

Two compression cylinders were cut from a length of extruded polycarbonate tubing. The inner diameter of the tubing was 50.8 mm (2.0 inches) and the outer diameter was 57.2 mm (2.25 inches). The length of one was measured to be 33.7 cm and the other 35.4 cm, with an uncertainty of 0.05 cm. The difference in length is not important. The fracture pressure for polycarbonate tubes of these dimensions was calculated in section 4.1 to be 7.5 MPa (1093 psi), which is a factor of safety of over 10. Since a liquid piston replaces the solid tandem piston, a thick rubber sheet sealed the bottom of the aluminum mount where the lower cylinder was attached. The cap was made of aluminum and was held firmly to the polycarbonate cylinder using threaded rods as can be seen in figure 4.11.

The 33.7 cm polycarbonate tube contained the minitube array. The minitubes were purchased in lengths of 1.83 m (6 ft), which were each divided into six 30.5 cm (1 foot) sections by grinding through the copper walls. The surfaces were lightly sanded to remove burrs. The maximum length variation is 3 mm, which is 1% of the total length.

C.2.2 Instrumentation

The pressure sensors details are found in section C.1.

The Omega KMQSS thermocouples have an exposed, beaded junction and 304 stainless steal sheath. The sheath diameter is 0.010 inches (0.254 mm) and the thermocouple wire diameter is 0.0015 inches (0.0381 mm). The thermocouple materials meet or exceed the special limits of error, corresponding to accuracy within 1.1 K or 0.4%, whichever is greater.

Appendix D

Thermocouple data

Thermocouple data were taken using the very fine thermocouples for the empty compression chamber (no mesh) and a compression ratio of about 6.8 for various compression speeds using the mesh experiment facilities as described in chapter 4, section 4.1. The thermocouple junction was located about 2.5 cm away from the cap and near the axis of the compression chamber. The results are shown in figure D.1 for four chamber inlet flowrates (i.e. piston speeds). Four each test, compression begins at 30 seconds. Compression ends when the final pressure reaches 6.9 MPa (100 psi). The pressurized air is allowed to expand after the air temperature had returned to the initial air temperature. The thermocouple data are noisy and irregular, and only very general correspondence with physical reality can be identified. This is partly due to the noisy environment and partly the real irregularity of the local temperature. The magnitude of the thermocouple measurements are of the same order as expected values, but generally quite a bit less than the calculated volume-averaged temperatures as seen in chapter 4, section 6.1. The thermocouple does record a speedy return to near thermal equilibrium after compression and expansion, a somewhat surprising finding attested to throughout the entire experimental program.

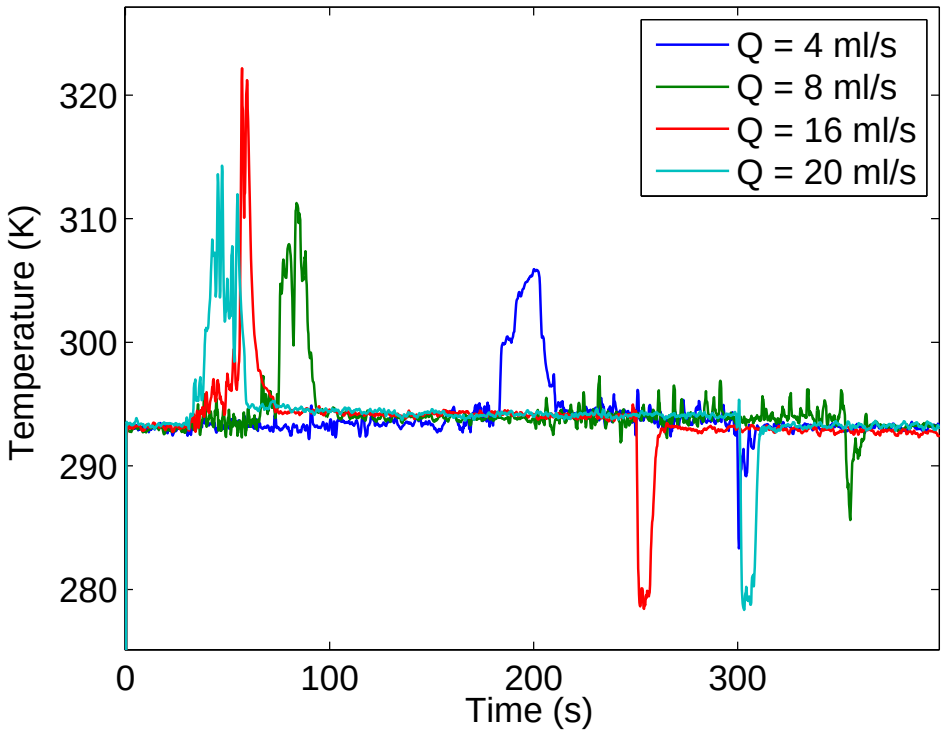

Figure D.1: Temperature vs time traces taken by a single thermocouple (wire diameter 0.001 inches) at a location 2.5 cm from the cap near the centerline.

Appendix E

Additional Results

E.0.3 Experimental results

This appendix is an extension of the results for the mesh experiments. Chapter 6, section 6.1 provides representative samples. The plots herein are a supplement to that section. Plots are provided for temperature vs. time, heat transfer rates vs. time, hA vs. time, and h vs. time.

Temperature

Figures E.1, E.2, E.3, and E.4 show temperature vs. time for which the compression speed in each plot is the same. The different curves reveal the dependence on mesh mass on temperature. Figures E.5, E.6, and E.7 show temperature vs. time data for which the mesh mass in each plot is the same. The different curves reveal the dependence of temperature on compression speed.

Heat Transfer Coefficient

Figures E.8 through E.11 show the instantaneous heat transfer coefficient vs. time for which the compression speed in each plot is the same. The different curves reveal the dependence of instantaneous heat transfer coefficient on mesh mass.

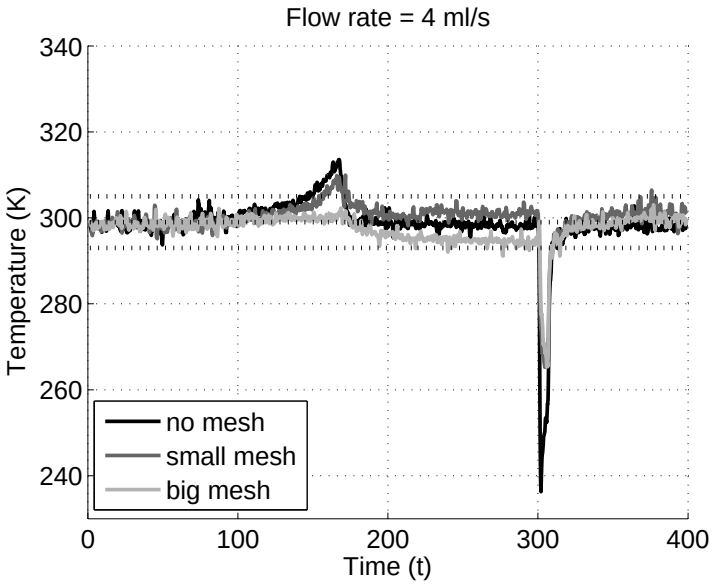

Figure E.1: Calculated temperature profiles with a flow rate of 4 cc/s during compression. Compression begins at 60 seconds and ends at about 170 seconds.

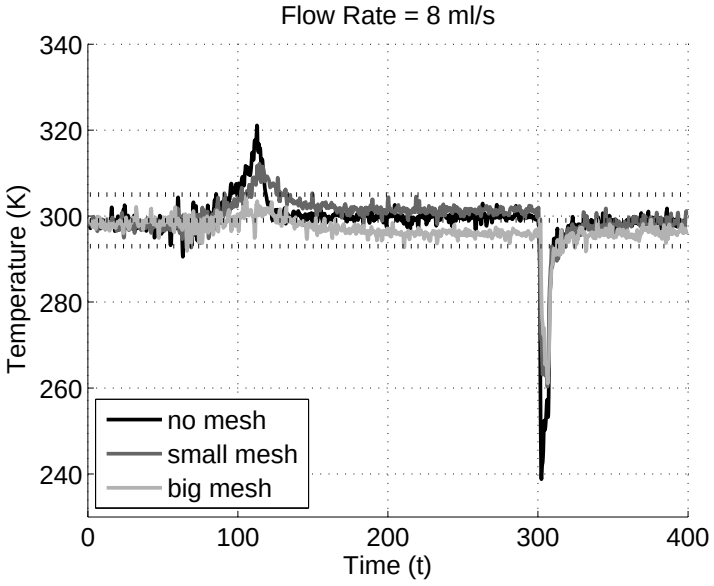

Figure E.2: Calculated temperature profiles with a flow rate of 8 cc/s during compression. Compression begins at 60 seconds and ends at about 115 seconds.

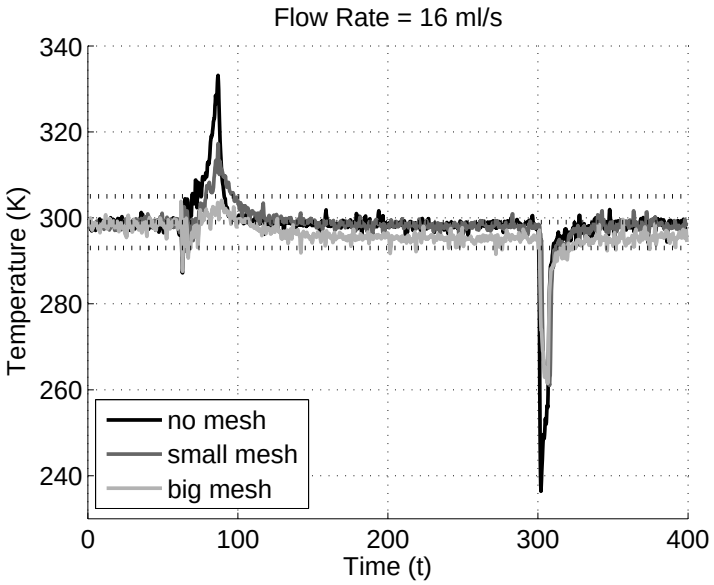

Figure E.3: Calculated temperature profiles with a flow rate of 16 cc/s during compression. Compression begins at 60 seconds and ends at about 87 seconds.

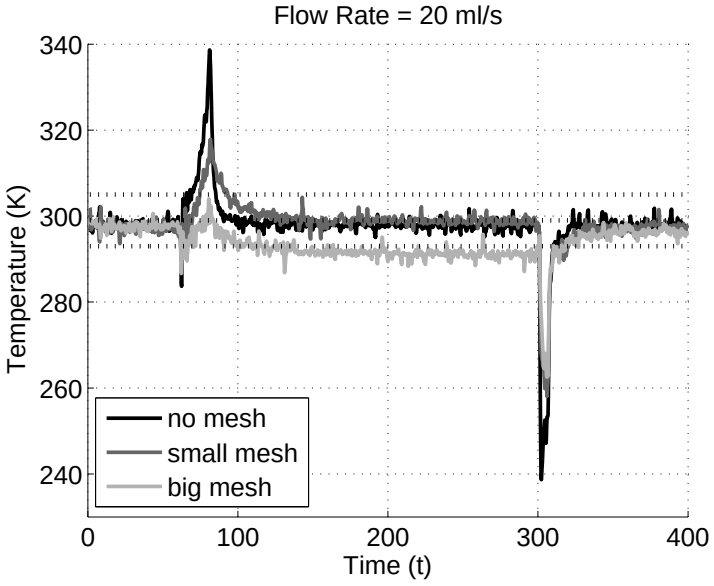

Figure E.4: Calculated temperature profiles with a flow rate of 20 cc/s during compression. Compression begins at 60 seconds and ends at about 81 seconds.

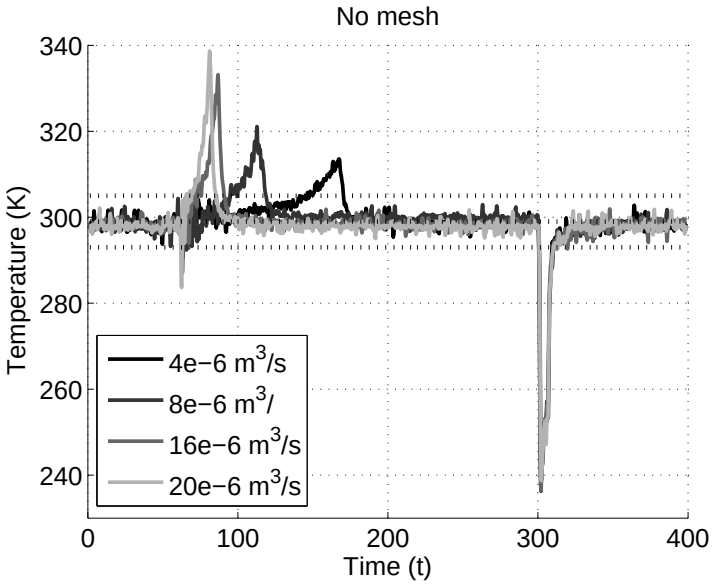

Figure E.5: Calculated temperature profiles with no mesh. Compression begins at the 60 second marker. The four ending times are approximately 81, 86, 115, and 167 seconds.

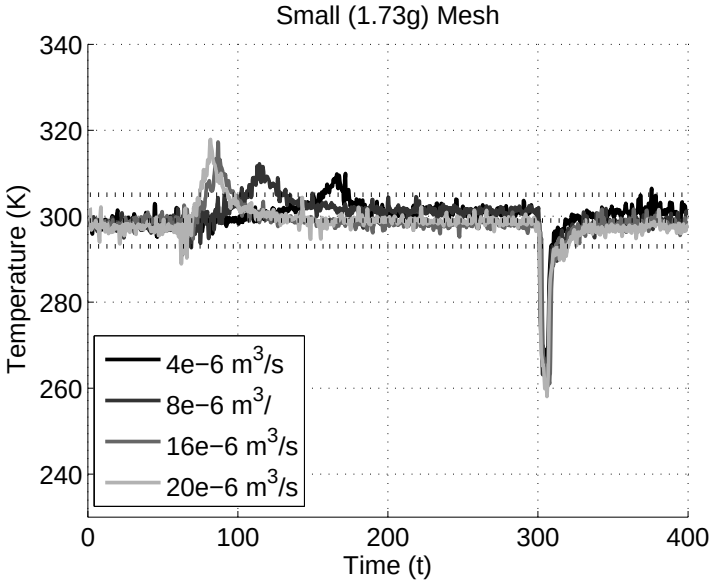

Figure E.6: Calculated temperature profiles with a 1.7 g mesh. Compression begins at the 60 second marker. The four ending times are approximately 81, 87, 115, and 167 seconds.

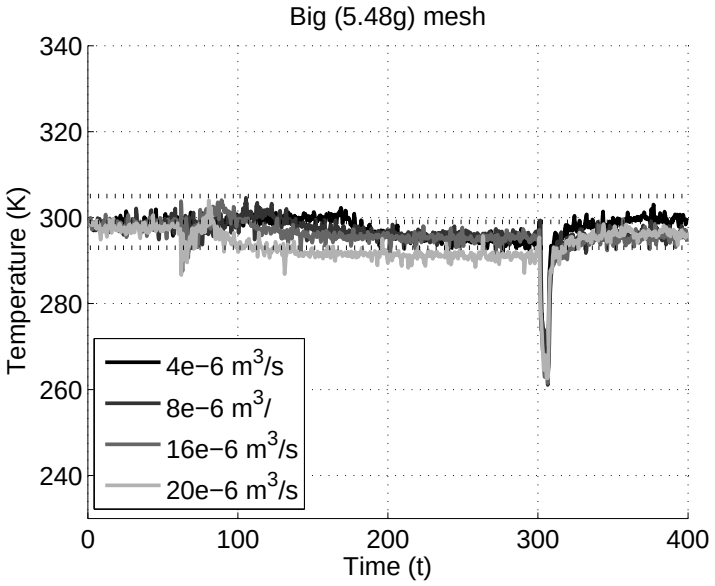

Figure E.7: Calculated temperature profile with a 5.48 g mesh. Compression begins at the 60 second marker. The four ending times are approximately 81, 87, 116, and 172 seconds.

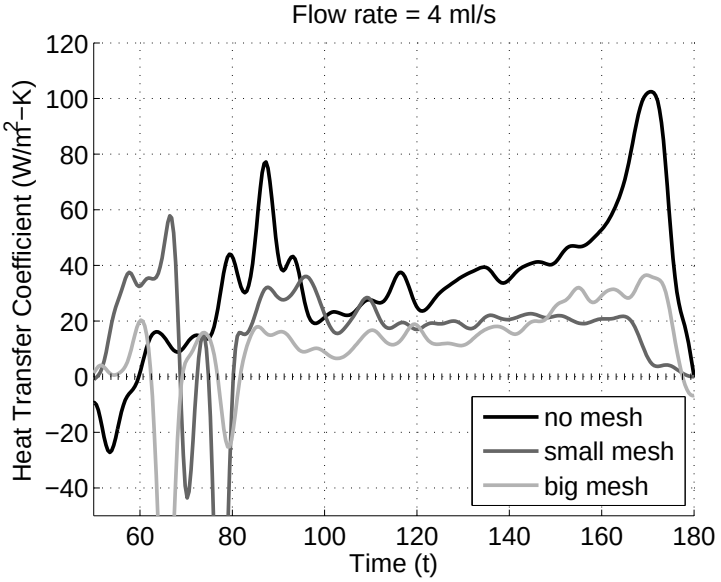

Figure E.8: Calculated heat transfer coefficient as a function of time with a flow rate of 4 cc/s during compression. Compression begins at 60 seconds and ends at about 170 seconds.

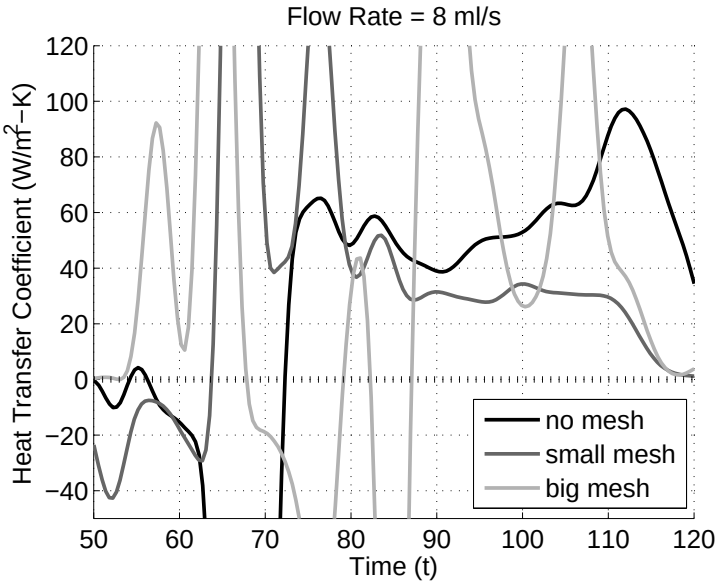

Figure E.9: Calculated heat transfer coefficient as a function of time with a flow rate of 8 cc/s during compression. Compression begins at 60 seconds and ends at about 115 seconds.

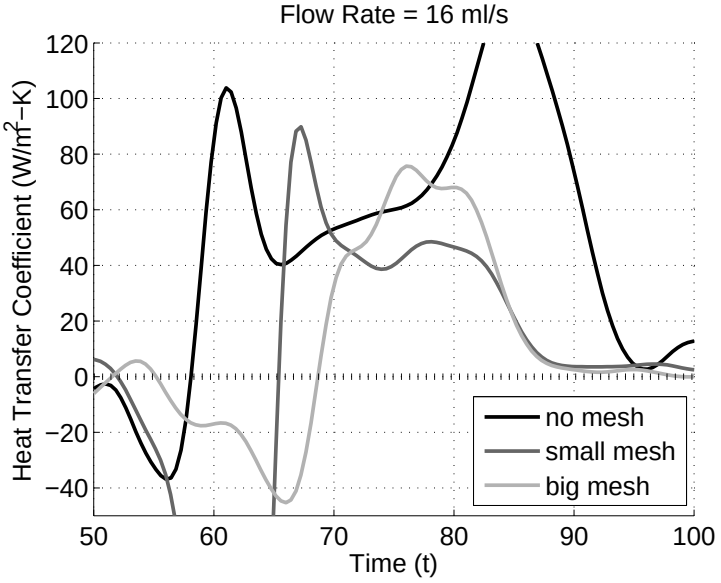

Figure E.10: Calculated heat transfer coefficient as a function of time with a flow rate of 16 cc/s during compression. Compression begins at 60 seconds and ends at about 87 seconds.

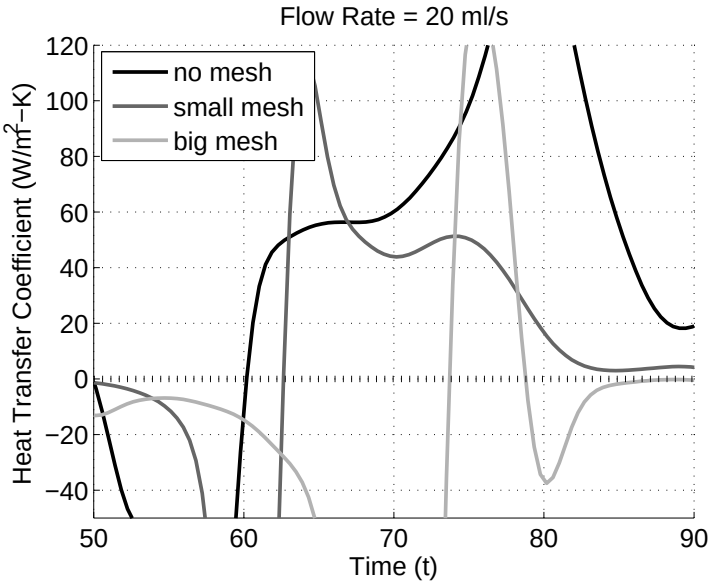

Figure E.11: Calculated heat transfer coefficient as a function of time with a flow rate of 20 cc/s during compression. Compression begins at 60 seconds and ends at about 81 seconds.

Comparison

Figures E.12–E.23 show the temperature plots for each trial, including the simulated best fitting h.

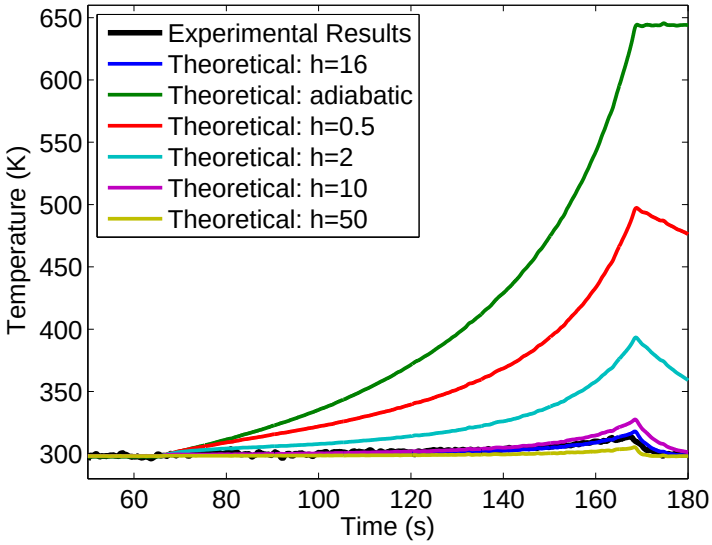

Figure E.12: Calculated air temperature vs time with no mesh and 4 cc/s flowrate. Experimental data compared to simulation output for various constant h's.

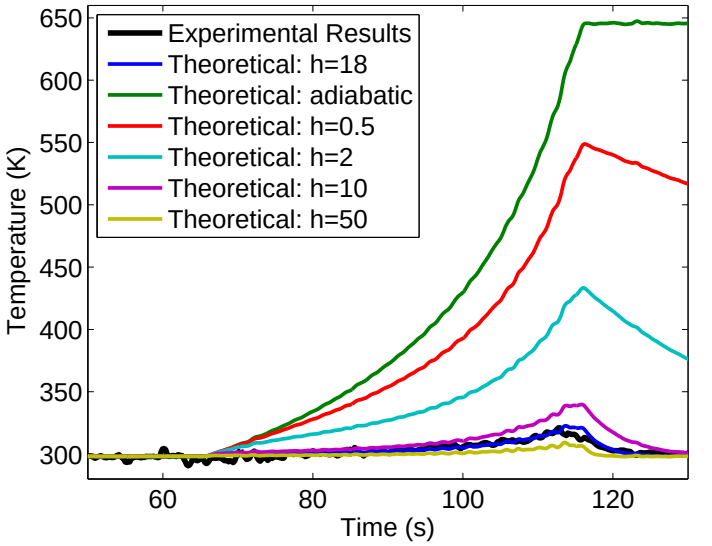

Figure E.13: Calculated air temperature vs time with no mesh and 8 cc/s flowrate. Experimental data compared to simulation output for various constant h's.

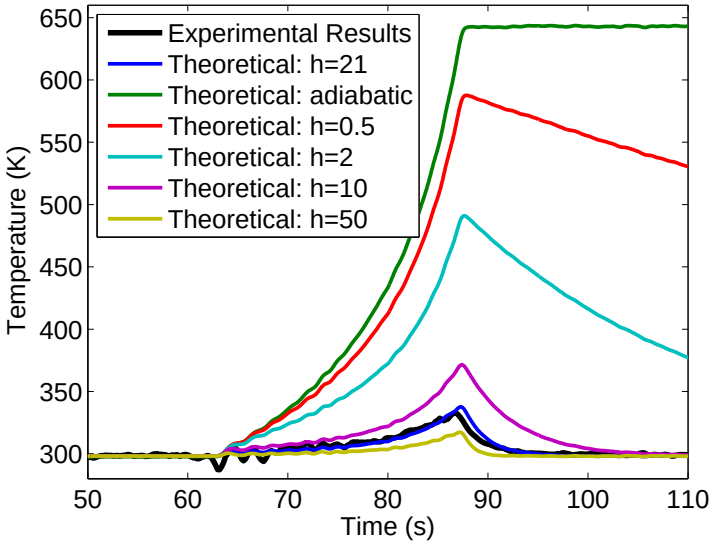

Figure E.14: Calculated air temperature vs time with no mesh and 16 cc/s flowrate. Experimental data compared to simulation output for various constant h's.

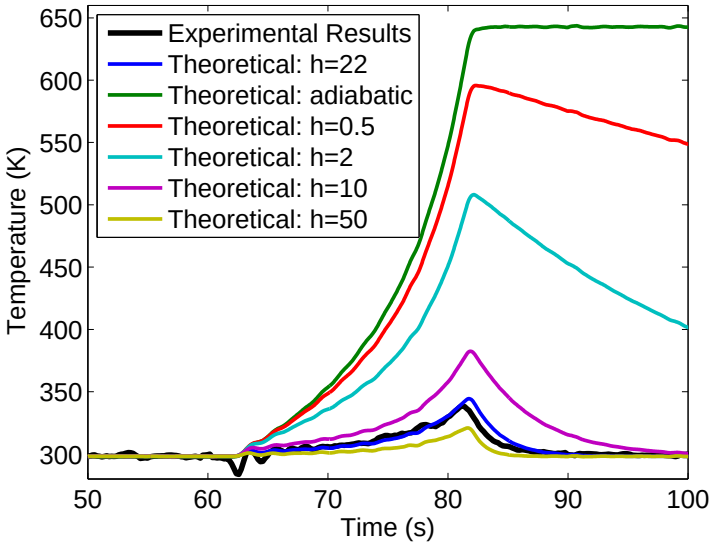

Figure E.15: Calculated air temperature vs time with no mesh and 20 cc/s flowrate. Experimental data compared to simulation output for various constant h's.

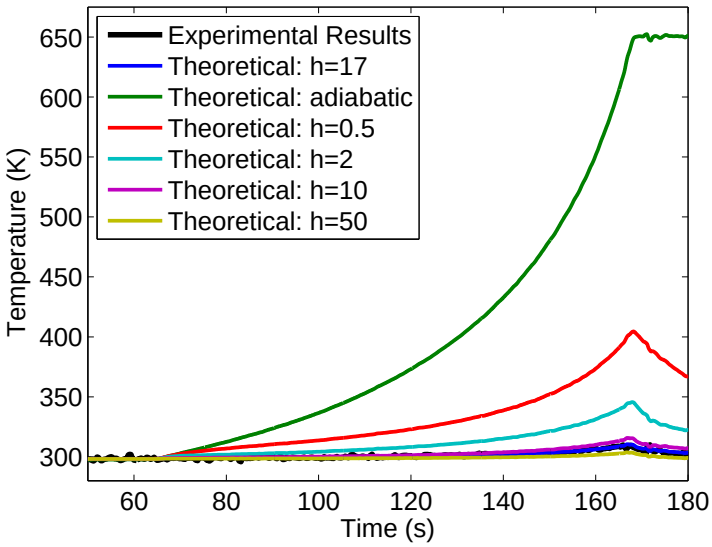

Figure E.16: Calculated air temperature vs time with the 1.70 g mesh and 4 cc/s flowrate. Experimental data compared to simulation output for various constant h's.

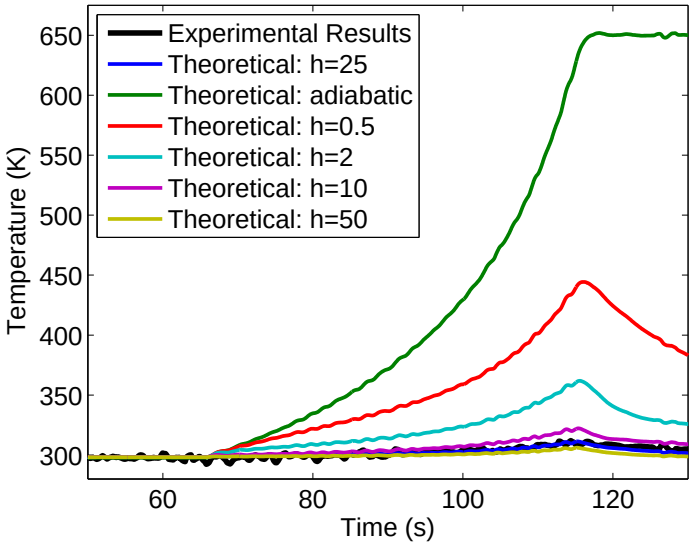

Figure E.17: Calculated air temperature vs time with the 1.70 g mesh and 8 cc/s flowrate. Experimental data compared to simulation output for various constant h's.

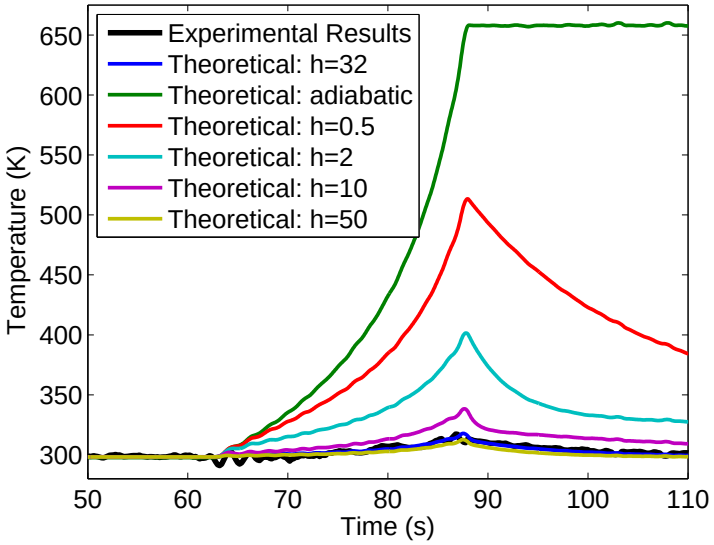

Figure E.18: Calculated air temperature vs time with the 1.70 g mesh and 16 cc/s flowrate. Experimental data compared to simulation output for various constant h's.

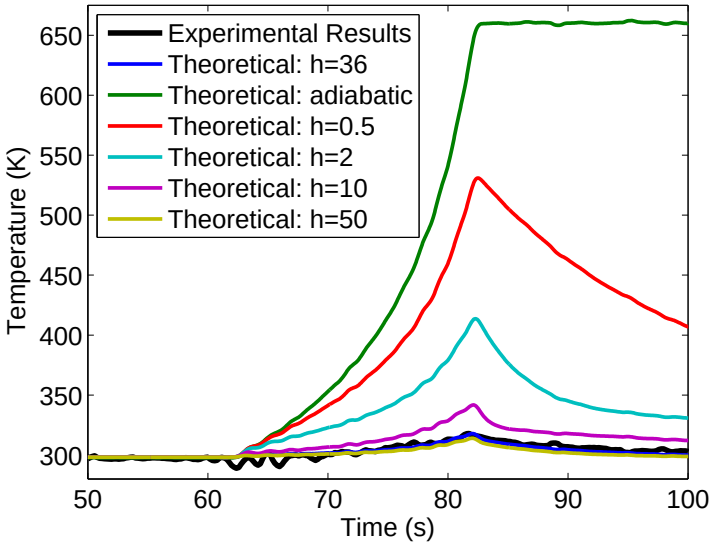

Figure E.19: Calculated air temperature vs time with the 1.70 g mesh and 20 cc/s flowrate. Experimental data compared to simulation output for various constant h's.

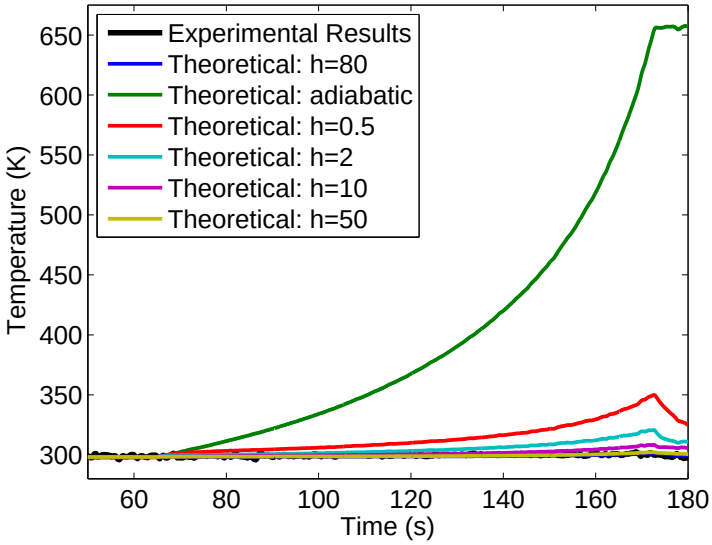

Figure E.20: Calculated air temperature vs time with the 5.48 g mesh and 4 cc/s flowrate. Experimental data compared to simulation output for various constant h's.

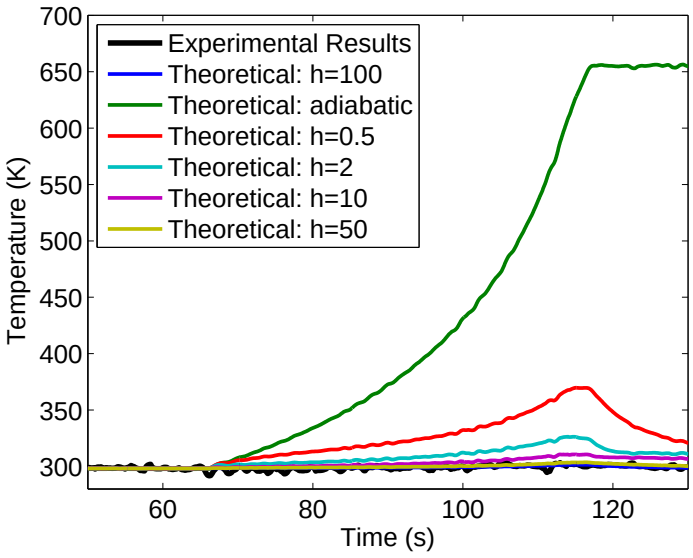

Figure E.21: Calculated air temperature vs time with the 5.48 g mesh and 8 cc/s flowrate. Experimental data compared to simulation output for various constant h's.

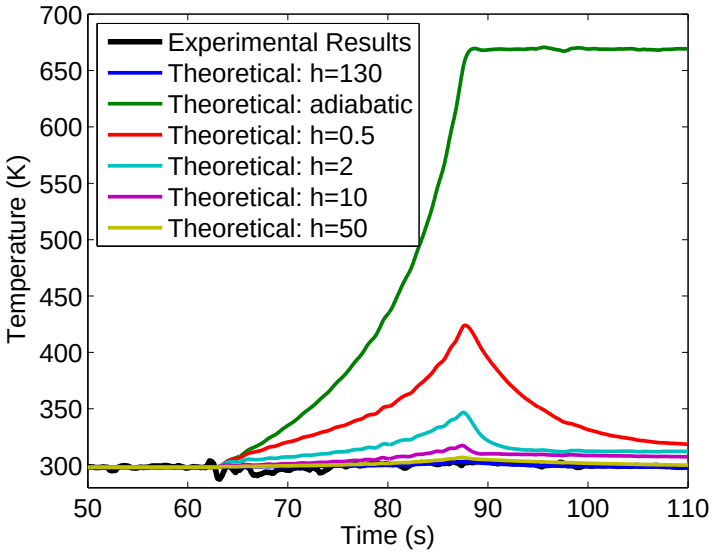

Figure E.22: Calculated air temperature vs time with the 5.48 g mesh and 16 cc/s flowrate. Experimental data compared to simulation output for various constant h's.

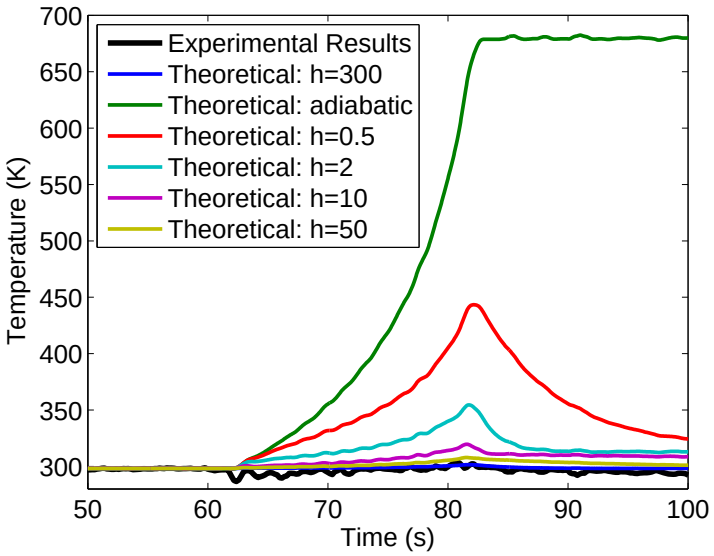

Figure E.23: Calculated air temperature vs time with the 5.48 g mesh and 20 cc/s flowrate. Experimental data compared to simulation output for various constant h's.

Appendix F

Optimal compression trajectory for a constant hA product

F.0.4 Introduction

Chapters 8–10 addressed the problem of determining the optimal compression trajectory for a given set of assumptions. In the solution provided in chapter 9, it was claimed that the optimal trajectory for the same set of assumptions, but with constant-hA was previously determined to be in the form "adiabatic-isothermal-adiabatic." The objective of this appendix is to prove that claim. This work is adapted from Sancken and Li [94].

F.0.5 Sketch of Proof

Assume h is constant and nonzero. Any curve may be uniformly approximated by a series of isothermal and adiabatic steps, where a truly adiabatic step must necessarily take place in zero time. As in figure F.1, two unique sequences (trajectories) are proposed to traverse states A and D: 1) isothermal-adiabatic-isothermal (IAI), that is A-B-C-D, called ζ and 2) Adiabatic-Isothermal-Adiabatic (AIA), that is A-E-F-D, called ζ^*. At equal work, $W(\zeta^*) = W(\zeta)$, it can be shown that an AIA trajectory takes less time than an IAI trajectory, $t(\zeta^*) < t(\zeta)$. To show this, let

$$r_I \equiv \frac{P_B}{P_A} \cdot \frac{P_D}{P_C} = \frac{P_F}{P_E} \tag{F.1}$$

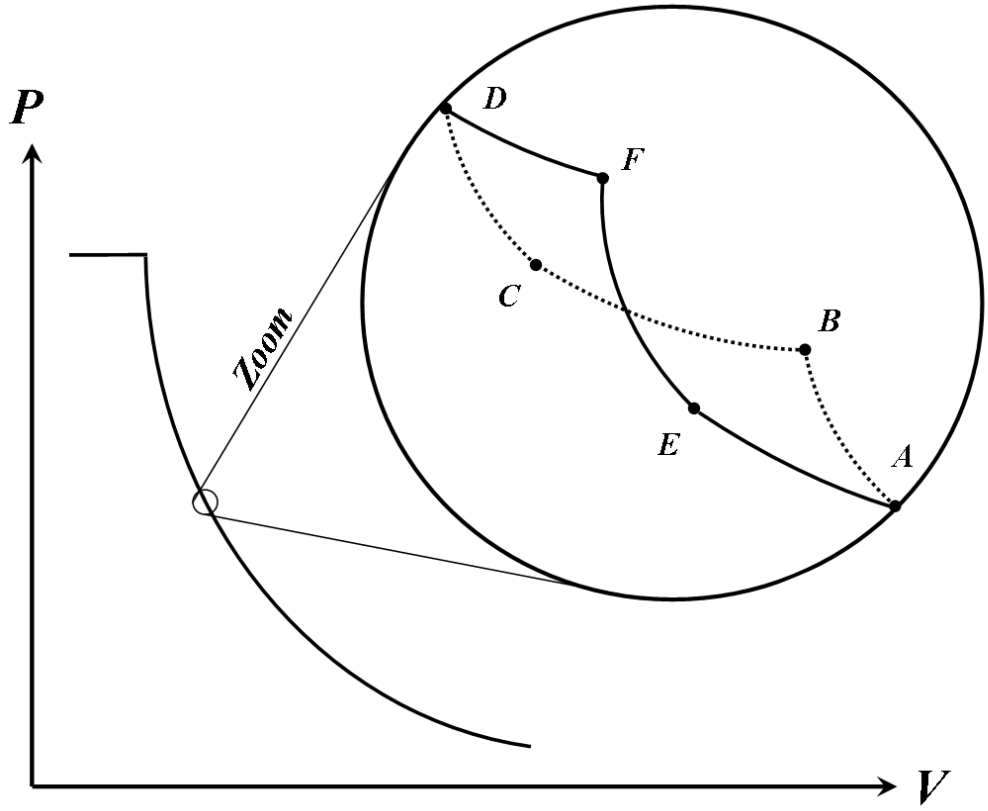

Figure F.1: Diagram of isothermal-adiabatic-isothermal (ζ) and adiabatic-isothermal-adiabatic (ζ^*) profiles.

be the total isothermal compression ratio, and let x be such that

$$\frac{P_B}{P_A} = r_I^x \qquad \text{and} \qquad \frac{P_D}{P_C} = r_I^{(1-x)}. \tag{F.2}$$

Calculating the work required for each trajectory and setting them equal yields the relation

$$T_E = xT_A + (1-x)T_D \tag{F.3}$$

Let s be the time difference normalized by the AIA time:

$$s\left(\zeta^*, \zeta\right) = \frac{t\left(\zeta\right) - t\left(\zeta^*\right)}{t\left(\zeta^*\right)}. \tag{F.4}$$

Time is calculated by equations (3.27) and (8.2) with $\dot{T} = 0$ and $T =$ constant. Substituting (F.3) and rearranging, a form of s is obtained with three factors that may take positive or negative values: a term in parenthesis $(*)$, a term in brackets $[*]$, and x.

$$s\left(\zeta^*, \zeta\right) = xT_0\left(1 - \frac{T_A}{T_E}\right)\left[\frac{1}{T_A - T_0} - \frac{1}{T_D - T_0}\right] \tag{F.5}$$

There are eight scenarios summarized in table F.1. Pluses indicate that the factor is positive for the selected ranges of r_I and x. Minuses indicate the factor is negative. In every case s is positive, demonstrating that for the same work, AIA takes less time than IAI.

	$r_I > 1$	$r_I < 1$
$x > 1$	+ / + / +	+ / - / -
$0 < x < 1$ with $P_D > P_A$	+ / + / +	+ / + / +
$0 < x < 1$ with $P_D < P_A$	+ / - / -	+ / - / -
$x < 0$	- / + / -	- / - / +
Format: "sign of x" / "sign of $(*)$" / "sign of $[*]$"		

Table F.1: The sign of s is determined from the sign of three factors. In all eight scenarios, s is positive.

A series of adiabatic and isothermal steps used to traverse two states can be collapsed into a single AIA process by progressively replacing every occurrence of IAI with AIA (e.g. $IAIAIA \Rightarrow AIAAIA = AIAIA \Rightarrow AAIAA = AIA$). Any compression or expansion process can be completed with the same work but less time using an adiabatic-isothermal-adiabatic trajectory, so only AIA trajectories need be considered as candidates for the Pareto optimal solution when hA is constant.

Appendix G

A high-power case study

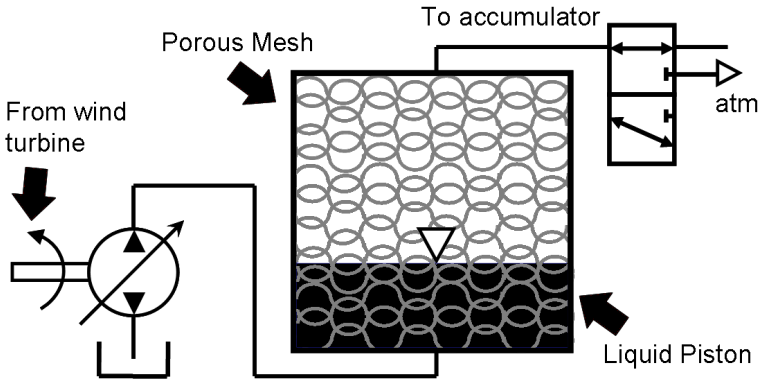

Figure G.1: Schematic of the compressor with liquid piston and porous mesh for the case study.

Offshore wind is becoming more prevalent as a renewable energy source. One issue with wind power is its intermittent nature. A promising remedy is energy storage. Suppose the Open Accumulator infrastructure is used to capture and store energy as efficiently as possible for a specific geometry and hypothetical volume-dependent heat transfer function. How might the piston trajectory look for various power and efficiency requirements? Suppose the compression chamber geometry be that of a 12 m^3 cylindrical drum, with an aspect ratio of unity. To improve the heat transfer, uniformly fill the chamber with a perfectly conducting metallic mesh bonded to isothermal chamber walls and use a liquid piston with a direct liquid-to-air interface as in figure G.1. During

compression the liquid will gradually fill the compression chamber and submerge the porous mesh surface area as it reduces air volume. If, for simplicity, it is assumed that h is 100 W/m^2-K and constant, then the hA product will vary with air volume as

$$hA\left(V\right) = h\left[\left(\frac{4V\left(1-\epsilon\right)}{Dd\epsilon} + \pi D\right)\frac{4V}{\pi\epsilon D^2} + \frac{\pi D^2}{2}\right] \tag{G.1}$$

where ϵ is the porosity of the mesh, d is the diameter of a single strand of the mesh, D is the diameter of the chamber, and V is the instantaneous volume of air in the chamber. Let porosity be 99.5% and the wire diameter be 80 μm. Let the pressure compression ratio be 350. Set the storage power to be 1 MW. The procedure outlined in the flow chart in figure 9.3 determines the optimal trajectory. Selected outputs are tabulated in below.

Pow_c	1.00×10^6 W	η_c	0.803
t_c	5.88 s	W_{in}	7.33×10^6 J
T_0	298 K	T_1	309 K
T_2	379 K	T_c	539 K
λ_c	1.04×10^5 W		

Now consider different target efficiencies. Figure G.2 displays normalized volume trajectories throughout compression for two different efficiencies: 90% and 60%. They each have a instantaneous stage, a slow stage, and a final instantaneous stage. Higher efficiency trajectories have shorter adiabatic compression stages, as can be seen in the figure. Recall that isothermal compression is the most efficient. Adiabatic-isothermal-adiabatic (AIA) volume trajectories are plotted in figure G.2 as well using the same efficiencies. When the hA product is constant, the AIA trajectory is optimal. When hA is not constant, as in this case study, the AIA trajectory absorbs less power than the variable-hA optimal trajectory at the same efficiency. Also plotted for purposes of comparison are linear and sinusoidal profiles. Conventional crank driven pistons often use sinusoidal trajectories. The optimal profile intuitively looks more appropriate than sinusoidal or linear profiles for the chosen function of hA. At low pressures, when the required work is minimal, compress as fast as possible. Once the temperature begins

to rise, slow down and take advantage of the still-large heat transfer surface area. As compression progresses, the surface area (and therefore heat transfer) diminishes, and eventually it is best to forgo the slow compression and push on to the final pressure as rapidly as possible. The same reasoning applies to expansion, but in reverse order.

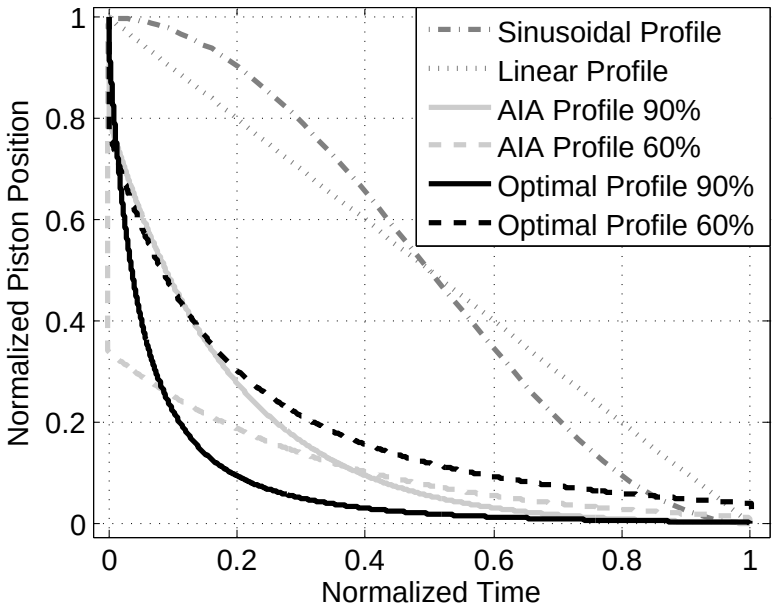

Figure G.2: Sample profiles of the optimal trajectory for various efficiencies. Volume, normalized by the maximum volume, is shown as a function of time, scaled by total compression time. Sinusoidal, linear, and AIA trajectories are provided for comparison.

Figure G.3 demonstrates the benefits of the optimal compression trajectory over ad hoc approaches. In the figure, compression efficiency is plotted against power absorbed. At any efficiency, the optimal trajectory absorbs more power than any other trajectory. For example, at 90% efficiency, compression via the optimal trajectory absorbs over 5 times the power of sinusoidal compression and over 15 times the power of linear compression. Compared to the adiabatic-isothermal-adiabatic solution, the optimal trajectory absorbs 60% more power, also at 90% efficiency. It needs to be emphasized, however, that these numbers are for a specific case. Figure G.4 plots expansion efficiency against power output. Again, the curve representing optimal expansion demonstrates superior power for any efficiency.

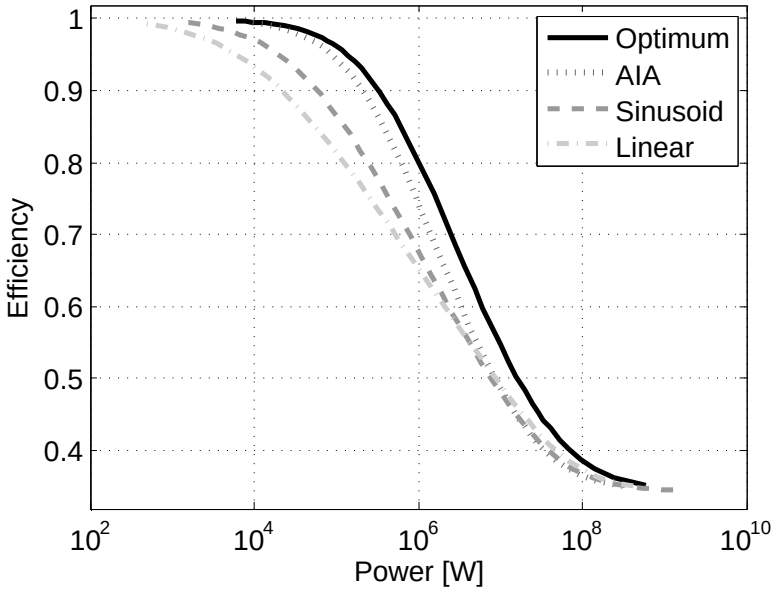

Figure G.3: Compression efficiency vs power. There is no other trajectory that allows more power to be absorbed at a given efficiency than the optimal trajectory. Sinusoidal, linear, and AIA trajectories are provided for comparison.

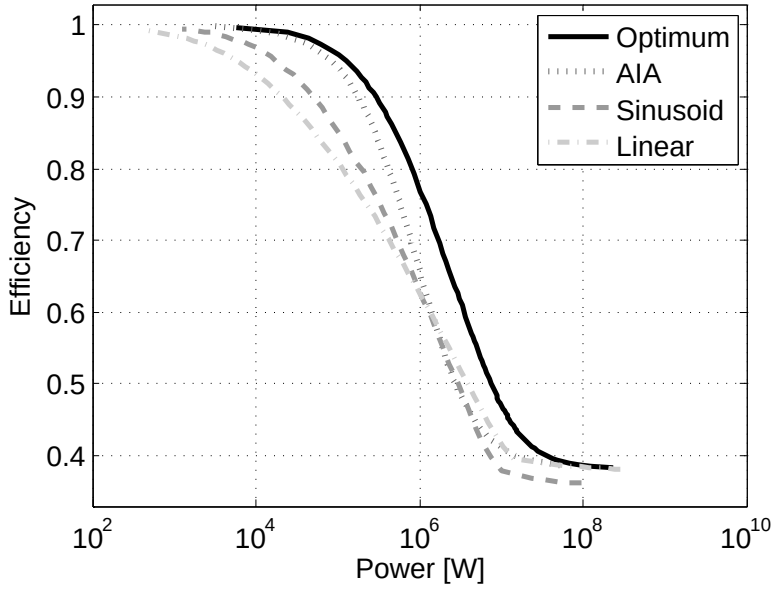

Figure G.4: Expansion efficiency vs power. There is no other trajectory that allows more power to be produced at a given efficiency than the optimal trajectory. Sinusoidal, linear, and AIA trajectories are provided for comparison.